EVALUATING AND SCHEDULING EXOPLANET DIRECT IMAGING MISSIONS

A Dissertation

Presented to the Faculty of the Graduate School

of Cornell University

in Partial Fulfillment of the Requirements for the Degree of

Doctor of Philosophy

by

Dean Robert Keithly

December 2021

EVALUATING AND SCHEDULING EXOPLANET DIRECT IMAGING MISSIONS

Dean Robert Keithly, Ph.D.

Cornell University 2021

Future exoplanet direct imaging instruments will be capability of detecting and spectrally characterizing Earth-like exoplanets, but which stars to observe, how long they should be observed, or how to follow up the detection of an exoplanet that appears Earth-like are still open questions. In this dissertation, I validate the probability based yield estimation technique, called completeness, for estimating single-visit blind search yield of the Nancy Grace Roman Space Telescope by simulating a Monte Carlo of full mission simulations. I show the Roman Coronagraphic Instrument (CGI) is largely sensitive to gas giants, planets that move relatively slowly in planet-star separation (s) and planet star difference in magnitude (Δmag) space over the instruments detection limits. Since future telescopes, like HabEx, have smaller inner working angles and a larger limiting Δmag, they are capable of detecting planets moving faster in (s,Δmag) space. Since the traditional completeness does not account for planetary motion, I created the *exodetbox* software package and *Integration Time Adjusted Completeness* to account for this planetary motion. I found that a design reference mission optimized with traditional completeness overestimates yield by 9.61% compared to Integration Time Adjusted Completeness. Once integration time adjusted completeness is calculated for a target star, dynamic completeness can be computed an order of magnitude faster than the traditional method.

Post detection follow-up requires classification ways to compute temporal

revisit parameters. I show how, even in our own solar system, an Earth-like planet can be confused with up to 6 other solar system planets. I present a method for computing the probability a planet is from a given sub-population. Since there are few methods to determine limiting or ideal times to follow-up the first detection, I also present methods to determine when to revisit as well as how long to revisit for.

The exodetbox powered methods I introduce are computationally fast, provide a rich array of planet population data, and is a versatile backbone to planning revisits.

BIOGRAPHICAL SKETCH

Dean Keithly graduated from Rochester Adam High School in a distant suburb of Detroit in 2011 after serving two successive years at the captain of the Adambots FIRST robotics team. Immediately out of high school, he undertook a position at Re-Sol as their sole programmer. He concurrently attended both Oakland University and Oakland Community College while working; taking additional responsibility over Oakland University's Formula SAE ergonomics components. He also found the time to start and mentor the FIRST Tech Challenge team at Van Hoosen Middle School called the Tech Vikes. The following summer he undertook his first research position under National Science Foundation funding to develop a data acquisition system for an automatic shifting bicycle with a continuous gear transmission. He subsequently transferred to Michigan Technological University and joined their Formula SAE team. In the next summer, he worked for Hilite International in the year that they became awarded powertrain supplier of the year. Nearing the end of that summer, he received a fortuitous call from an individual at the NASA Langley Research center to work on balloon interferometry which was promptly missed because he (stupidly) took a few minutes to consult others before making the decision on accepting the offer. As Dean's luck goes, the very next day he was called to work in the NASA Langley Research Center computational fluid dynamics (CFD) group and was ecstatic to undertake this endeavour he found so fascinating. It was in those hallways that he found a glowing passion in the eyes of his 30 doctorate coworkers, people who loved their work. This place had a stark contrast from the automotive engineering field in which he had become accustomed. The people in this place had unending passion in their hearts for their work; they inspired and drove each other to do great things.

Dean set forth the goal to enter the Aerospace Industry. After a semester spent working on an Autonomous Rendezvous and Docking rig design for an Europa undersea rover with his pedantic pal Sean Hurd; Dean was to join the Aerospace Enterprise, where he took up the mantle of Thermal Team Lead on the Oculus-ASR nanosatellite and did undergraduate research on Robotic Falconry. He graduated from Michigan Technological University in May of 2015 with a Bachelors of Science in Mechanical Engineering and a minor in Aerospace Engineering.

Dean found his way back into the NASA family at the Marshall Space Flight Center, working on a manned extravehicular activity vehicle for space operations called Flexcraft. He continued his education at Cornell University, pursuing a Masters of Engineering in Systems Engineering, taking on a special project called Robosquid with Dr. Shepherd and Dr. Peck. Cornell provided such a rewarding experience and the educational opportunities so rich that he decided to stay and pursue a doctoral degree.

In 2016, he began his PhD program in mechanical engineering at Cornell University, working with Professor Dmitry Savransky and the Space Imaging and Optical Systems Lab.

Over the course of his PhD, he had the opportunity to work at the Jet Propulsion Laboratory, Air Force Research Lab, and Ball Aerospace in various aspects of mission planning, optimization, and design.

ACKNOWLEDGEMENTS

I am grateful for having Dmitry Savransky as an advisor for the great many things he has taught me. One of the most important being: *take the time to say what you want to say*. So I shall take the time to thank the people who must be thanked for helping form me into who I am and helping me get here.

There are three individuals of irreplaceable importance to the culmination of this work; Dmitry and my parents. Thank you for the many seen and unseen contributions you have made both to this work and my personal growth. I would not be where I am today doing the good work I am doing without your invaluable assistance.

There are some K12 educators who went above and beyond their job description provide a stellar educational environment including, but not limited to, James Taylor, Warren Hildebrandt, Paul Jakey, and Christine Deyo as well as the extracurricular mentoring from the Drummers.

There are many collegiate and industry mentors who have played an important role in my decision to pursue higher education, fuel my passion for space exploration, and provided a myraid of opportunities. Peter Kaub, Dr. Osama Rawashdeh, Dr. Christopher Rumsey, Van Karsen, Dr. Mo Rastgaar, Charlie Dischinger, David Seal, Dr. Rolf Danner, and Dr. Robert Shepherd.

I would also like to thank my close friends and fellow lab members for their advice, help and fun times along this journey including Tanay, Steven, Jason, Ben, Rich, Kris, Doga, Arnaldo, Alex, Gabe, Jacob, Corey, Daniel, and Christian.

The work in this dissertation is a product of multiple funding sources including the NASA Space Grant Graduate Fellowship from the New York Space Grant Consortium, NASA Grant Nos. NNX14AD99G (GSFC), NNX15AJ67G (WFIRST Preparatory Science), NNG16PJ24C (WFIRST Science Investigation

Teams) and the Science Investigation Team of the Nancy Grace Roman Space Telescope under NASA Grant NNX15AB40G.

This research made use of a multitude of online databases and open-source code resources. This research has made use of the NASA Exoplanet Archive, which is operated by the California Institute of Technology, under contract with the National Aeronautics and Space Administration under the Exoplanet Exploration Program. This research has made use of NASA's NAIF planetary data system kernels. This research has made use of the Washington Double Star Catalog maintained at the U.S. Naval Observatory. This research made use of Astropy, a community-developed core Python package for Astronomy (Astropy Collaboration, 2018) and OR-Tools, an optimization utility package made by Google Inc. with community support. This research has made use of the Imaging Mission Database, which is operated by the Space Imaging and Optical Systems Lab at Cornell University. The database includes content from the NASA Exoplanet Archive, which is operated by the California Institute of Technology, under contract with the National Aeronautics and Space Administration under the Exoplanet Exploration Program, and from the SIMBAD database, operated at CDS, Strasbourg, France.

I also need to thank the hundreds or thousands of Stack Overflow and Stack Exchange contributors who answer those oddly specific coding questions.

LIST OF SYMBOLS

Throughout this work, we use some common subscript conventions and notation discussed here. We use a generic variable X to describe these conventions. The subscript k, like in X_k or $X_{x,k}$, is referring to a X or X_x of an individual planet. The subscript i, like in X_i or $X_{x,i}$, is referring to a X or X_x of a individual target star. The subscript min, like in X_{min} or $X_{x,\mathrm{min}}$ describes that this parameter is a minimum of X or X_x; this extends to the max subscript. We use bold variables like $\mathbf{X}$ when we are referring to a set or collection of something. We use underlines like $\underline{X}$ to identify position vectors and $\hat{X}$ to identify unit vectors.

We make use of common variables differentiated by their subscript or boldness to differentiate between what they specifically refer to. All ϵ parameters are related to efficiency of something. Lower case a refers to a semi-major axis related parameter. Lower case p refers to an albedo related parameter. Lower case c refers to a completeness. Lower case r refers to a direction or position vector. t variables are all time related. s refers to a planet-star separation related value. a refers to a semi-major axis related value. R refers to a planet radius related value

Table 1: Table of Symbols

α_i	SAG13 planet population parameter in Table 2.1
β_i	SAG13 planet population parameter in Table 2.1
$\gamma(\lambda, WA)$	intensity transmission of extended background sources see Figure A.1

Continued on next page

γ_i	SAG13 planet population parameter in Table 2.1
$\Gamma(\lambda, WA)$	area of the Full Width Half Maximum region of the planet Point Spread Function
$\Delta\mathrm{mag}$	difference in brightness between the planet and star in magnitudes
$\Delta\mathrm{mag}_{\mathrm{lim}}$	observatory limiting planet-star magnitude
$\Delta\mathrm{mag}_0$	planet-star magnitude used to calculate integration time cut-off for filter
$\Delta\mathrm{mag}_{\mathrm{min},i}$	lower limit of integration for $\Delta\mathrm{mag}$ for the i^{th} star
$\Delta\lambda$	observing wavelength bandwidth
$\epsilon_q(\lambda)$	detector quantum efficiency see Figure A.2
ϵ_{inst}	attenuation due to optics specific to the science instrument
ϵ_{syst}	attenuation due to optics specific to the coronagraph e.g. polarizer, Lyot stop, extra flat mirror
ϵ_{PC}	photon counting efficiency applied to planet signal
ϵ_{pp}	post processing efficiency
ε	$\mathrm{d}c_i/\,\mathrm{d}t_i$ the derivative of completeness w.r.t t for a subset of stars
ε^*	the optimal ε
η	expected number of planets per star
η_{KL}	η for the Kepler Like planet population
η_{SAG13}	η for the SAG13 planet population
σ_e	Rayleigh parameter for eccentricity

Continued on next page

λ	wavelength
$\nu_i(\lambda)$	i^{th} star visual magnitude in B-V color
$\mu_{Z_{\min}}$	mean magnitude of minimum zodiacal light intensity of stars in $\mathbf{I}$
$\mu_{Z_{\max}}$	mean magnitude of maximum zodiacal light intensity of stars in $\mathbf{I}$
μ	without subscripts, this is gravitational parameter for the sun
μ_{det}	mean number of detections
μ_e	mean eccentricity
$\Psi(\lambda, WA)$	core mean intensity see Figure A.1
A	pupil area
$a_{85,\text{norm}}$	$f_{\overline{a}}$ integrated over $a_{0.8}$ to a_{85}
$a_{0.8}$	semi-major axis for a 0.8 day orbital period planet around a sun mass star
a_{85}	semi-major axis for an 85 day orbital period planet around a sun mass star
a_{knee}	planet semi-major axis occurrence drop-off knee
a_{norm}	normalization factor for $f_{\overline{a}}$
BV_i	color of the star as a difference between B and V bands in magnitudes
$C_{sr,i}$	starlight residual count rate
$C_{z,i}$	zodiacal light count rate
C_{ez}	exozodiacal light count rate

Continued on next page

C_{dc}	dark current count rate
C_{cc}	clock induced charge count rate
C_{rn}	readout noise count rate
$C_{p,i}$	planet signal electron count rate of the i^{th} planet in s^{-1}
$C_{b,i}$	background noise electron count rate of the i^{th} planet in s^{-1}
$C_{sp,i}$	speckle spatial structure of the system in s^{-1}
$C_{\mathcal{F}_0}(\lambda)$	spectral flux density as a function of λ
K_i	intermediate constant of the SAG13 planet population
$\mathbf{C}_{p0}$	a vector of $C_{p,i}$ used for calculation of $\mathbf{c}_0$
$\mathbf{C}_{sp0}$	a vector of $C_{sp,i}$ used for calculation of $\mathbf{c}_0$
$\mathbf{C}_{b0}$	a vector of $C_{b,i}$ used for calculation of $\mathbf{c}_0$
$c_{3,i}$	planned completeness of target i to be observed
$c_{t_{obs},i}$	completeness of target i observed in a survey simulation
$c_i(t_i)$	completeness for the i^{th} target star at integration time t_i
$c_{\infty,i}$	theoretical maximum completeness for the i^{th} target star for this instrument
$c_{0,i}$	nominal completeness for the i^{th} target used in Algorithm 1
c'	speed of light in a vacuum
$\mathbf{c}(\mathbf{t})$	$\{c_i(t_i) \; \forall \; i \in \; \mathbf{I}\}$
$\mathbf{c}_0$	a vector of $c_{0,i}$
$\mathrm{d}c_i(t_i)/\mathrm{d}t_i$	the derivative of c with respect to integration time for the i^{th} target star

Continued on next page

$\mathrm{d}t$	infinitesimally small amount of time
d_i	sun to target star distance
EZ	Exo-Zodiacal light intensity in magnitudes
ENF	excess noise factor
e	planet eccentricity
$e_{\min}$	minimum allowed eccentricity
$e_{\max}$	upper 95^{th} percentile for e
e_k	eccentricity of the k^{th} planet
$\mathcal{F}_0$	zero-magnitude flux at λ see Eq. A.1
f_{Z0}	local zodiacal light surface brightness in intensity
f_{EZ0}	exo-zodiacal light surface brightness in intensity
$f_{Z,i}$	local zodiacal light of the i^{th} target star
$f_{\overline{R}}$	SAG13 planetary radius probability density function
$f_{\overline{a}}$	planet semi-major axis occurrence distribution for Kepler Like planets
$f_{\overline{a}\|R}$	planet semi-major axis occurrence distribution given R for SAG13 planets
$f_\lambda(\log_{10}(\lambda))$	zodiacal light wavelength correction factor
$\mathbf{f}_{Z,\min}$	$\{\min(f_{Z,i}(t)) \; \forall \; i \in \; \mathbf{I}\}$
h	planck constant
IWA	inner working angle
$\mathbf{I}$	list of target stars to observe
i	index referring to the i^{th} star
k	index referring to the k^{k} planet

Continued on next page

N	number of target stars in $\mathbf{I}$
N_p	number of planets generated in a universe
N_{pix}	number of pixels
N_q	number of planets in planetary radius bin q
$NCTE$	is the net charge transfer efficiency
n	uniform random variable between 0 and 1
OWA	outer working angle of the instrument
PPL	is the number of pixels per lenslet and is simply the lenslSamp^2
PS	is the detector pixel scale in arcsec per pixel
q	index for each bin in Figure 7 of Ref. 25
$\underline{r}_{k/i}$	position vector from star i to planet k
$\underline{r}_{i/SC}$	vector from the spacecraft position to the i^{th} target star
$\underline{r}_{\odot/SC}$	vector from the spacecraft to the sun
$\underline{r}_{Body/SC}$	vector from the spacecraft to the planetary body
$\hat{r}_{i/SC}$	unit vector from the spacecraft to the target star i
$\hat{r}_{\odot/SC}$	unit vector from the spacecraft to the sun
R	general planetary radius
$R_\oplus$	radius of the Earth
$R_{\text{vals},q}$	planet occurrence frequency for q^{th} bin of $\mathbf{R}_{\text{vals}}$
$\mathbf{R}$	vector of planet radii with length N_p
$\mathbf{R}_{85}$	vector of planet radius occurrence frequency values[25]
$\mathbf{R}_{\text{vals}}$	$\mathbf{R}_{85}$ normalized and scaled by $a_{85,\text{norm}}$
$\mathbf{R}_q$	set of N_q randomly generated R from $R_{\text{vals},q}$

Continued on next page

SNR	signal to noise ratio of the planet signal
t_c	the current mission time
t_∞	an infinite integration time
$t_{0,i}$	nominal integration time for the i^{th} target used in Algorithm 1
t_i	integration time for observation of the i^{th} target star
$\mathbf{t}_0$	a vector of $t_{0,i}$
$\mathbf{t}_2$	optimal integration time solutions to Algorithm 2
$\mathbf{t}_3$	a binary vector output solution to Algorithm 3
$\mathbf{t}_{f_{Z,\min}}$	times past t_c when $\mathbf{f}_{Z,\min}$ occur
$T(\lambda, WA)$	instrument core throughput at λ and WA see Figure A.1
T_{OH}	time per observation needed for the CGI to dig the dark hole and reach thermal equilibrium at the new spacecraft attitude
$T_{settling}$	time per observation for necessary observatory upkeep
$T_{\max}$	maximum amount of time to spend observing
WA_0	working angle used to calculate integration time cut-off for filter
WA_{int}	WA used for integration time calculations
x_i	binary decision variable to include the i^{th} target in target list in Algorithm 1
$\mathbf{x}_1^*$	optimal binary vector output solution to Algorithm 1
$\mathbf{x}_2^*$	optimal binary vector output solution to Algorithm 2
$\mathbf{x}_3^*$	a binary vector output solution to Algorithm 3

Continued on next page

Z	Zodiacal light intensity in magnitudes

There are many common variable forms used which are simply summarizable. Any variable $\underline{x}$ refers to a 3D vector in X, Y, and Z coordinates of something. We use $\mathbf{x}$ to indicate an array of variables, specifically used when referring to multiple roots of a polynomial. $|\overline{AB}|$ refers to the length of line segment $\overline{AB}$. Line segment $\overline{AB}$ is treated as a vector. C' is a projection of point C.

There are multiple different subscripts with different meanings used in this paper. A subscript with x_i refers to the index of a host star (out of some whole, nondescript, star catalog). A subscript x_k refers to an individual planet out of the whole large set of planets. A subscript of $x_{\min}$, $x_{\max}$, x_{lmin}, and x_{lmax} are a descriptor on the individual variable x which indicates the variable is associated with the minimum, maximum, local minimum, or local maximum respectively. When solving for the distance between point inside and ellipse and the vertices or co-vertices of that ellipse with semi-major axis a, we use the shorthand notation of the form $s_{a+x,y}$ (this is specifically the distance between point (x,y) and ($-a$,0)).

We denote coefficients of the polynomials of the four methods which solve the quartic in this paper as $A_{\#}$.

In Figure 5.4 we reference many points on the 3D elliptical orbit and 2D projection of this orbit into the plane of the sky. Points on the original 3D ellipse are labeled B, H, P, C, K, O, D, A, B',H',P',C',K',O',D',A'.

In 5.1 we use p_0 through p_{11} as intermediate constants for simplifying the full quartic expression. P, D, and Δ (by itself and only in the appendix) are intermediate constants derived from quartic coefficients for determining the sign of the quartic solutions.

K_0 through K_9 are intermediate simplifying coefficients used in representing Eqn. 5.22, Eqn. 5.23, and Eqn. 5.24 in Section 5.2.1.

LIST OF ABBREVIATIONS

Table 2: Table of Acronyms

AYO	Altruistic Yield Optimization[96]
CGI	Coronagraphic Instrument[53]
DRMs	Design Reference Missions
ExoPAG	Exoplanet Program Analysis Group
EXOSIMS	Exoplanet Open-Source Imaging Mission Simulator[83]
HabEx	Habitable Exoplanet Observatory[100]
IWA	Inner Working Angle
LUVOIR	Large Ultra-Violet-Optical-Infrared Surveyor[87]
MET	Mission Elapsed Time
NASA	National Aeronautics and Space Administration
OWA	Outer Working Angle
SLSQP	Sequential Least Squares Quadratic Programming[47]
SAG13	ExoPAG Study Analysis Group 13[8]
TPF-C	Terrestrial Planet Finder Coronagraph
WFIRST	Wide-Field Infrared Survey Telescope
SNR	Signal to Noise Ratio
IAC	Integration time Adjusted Completeness
MCMC	Markov Chain Monte Carlo
MC	Monte Carlo
OFTI	Orbits For The Impatient
SIOSlab	Space Imaging and Optical Science Lab

Table of Contents

List of Tables

List of Figures

CHAPTER 1

INTRODUCTION

Simply stated, in this work I present new tools and techniques of my own design to plan, schedule, and predict yield of exoplanet direct-imaging missions in the search for nearby, habitable, Exo-Earths.

In this chapter, I outline the motivations for seeking out Exo-Earths, contextualize the importance of such a discovery, provide a brief explanation of other exoplanet discovery techniques, provide background for why the work in this dissertation is relevant and important to this endeavour, why now is the proper timing for this work to be conducted, and present and outline of this work.

1.1 Motivation For Finding Exo-Earths

At present, the only planet, known with certainty, to be capable of supporting human life is the one we live on, Earth. So far, the explored planetary space has been found to be inhospitable. There is a logical train of thought that concludes there must be another habitable Earth-like exoplanet out there.

Our Earth orbits the Sun. The Sun is a star. There are many stars in the night sky. It can therefore be reasoned that some of these stars in the night sky may have planets around them. Of these planets, some of them may be *sufficiently similar* to Earth to harbor life like that found on our own planet.

It is this author's opinion that the general public has a persistent level of interest in finding other habitable Earth-like exoplanets. It stems from the frequency of news articles about "Earth 2.0" or "potentially habitable planets"[99,

76, 66] and the persistence of life on other planets in popular culture.[106, 107, 6, 55, 77, 72]

This interest extends to the science community as well. In 2021, NASA spent 27.6% of its Science budget on Earth Science[67]; funding dedicated towards understanding the planet we live on. But Earth is our only datapoint! Some scientists are interested in finding more and opening up a new field of study in comparative planetology. Comparative planetology is the identification of trends between planet insolation, density, and mass with composition, structure, temperature, and other attributes just as has been done with the identification of the star "main sequence" in their mass-luminosity relationship. [49] Since Mars and Venus are considered the two extremes of Earth's future habitability, discovering other planets in between could paint a portrait of what Earth will look like thousands, millions, or billions of years from now. To acquire this portrait, spectral characterizations of these discovered planets need to be taken. **High resolution spectral characterizations of nearby Earth-like exoplanets can only really be acquired through direct-imaging techniques.**[98]

The interest in Earth-like exoplanets is further substantiated by current studies of future, large-scale, exoplanet direct-imaging observatories. These studies enumerated their primary motivations in their reports. The leading and pervasive question they seek to answer and I am interested in is "Are we alone?"[100] The science team for the Habitable Exoplanet Observatory (HabEx) recasts this question into a series of answerable questions:

- Is there at least one Earth-like exoplanet?
- Are Earth-like exoplanets common?
- Do these other Earth-like exoplanets have signs of life?

These studies simultaneously influence and are influenced by the upcoming 2020 Astrophysics Decadal Survey which is expected to have substantial exoplanet and Earth-like exoplanet interest.

The scientific motivation for part of the work in this dissertation is formally derived from NASA's two 2010 Decadal Surveys. The Planetary Decadal Survey: Vision and Voyages is interested in "how the solar system fits into a vast collection of other planetary systems" [18]. The Astrophysical Decadal Survey "New Worlds, New Horizons" is interested in answering whether "[the] Solar System is a commonplace occurrence or a cosmic rarity" [75]. While these questions can only be answered by dedicated surveys, I can model and simulate a universe of stars as solar systems and demonstrate the ability of planned observatories to answer these questions.

These decadal surveys are important touchstones for planned and current missions because they are an indicator of the various areas of interest to the scientific community and what NASA should fund in the coming decade. An example of this is all New Frontiers and Discovery class missions funded in the last decade have top level science objectives directly derivative of the scientific questions posed in the decadal survey. It is expected that exoplanet science, specifically related to habitable Earth-like exoplanets, will take a prominent role in the 2020 decadal survey. This implies that astrophysics funding and missions will be aimed towards making these discoveries.

1.2 Overview of Different Exoplanet Detection Techniques

Perryman [74] contains a complete review and description of all current exoplanet direct imaging techniques employed to discover, detect, and measure exoplanet properties. Figure 1.1[74] graphically depicts the diversity of exoplanet detection techniques employed to date as well as the current projected planet-mass detection capabilities of these techniques, the number of exosystems detected with these techniques and the number of exoplanets discovered.

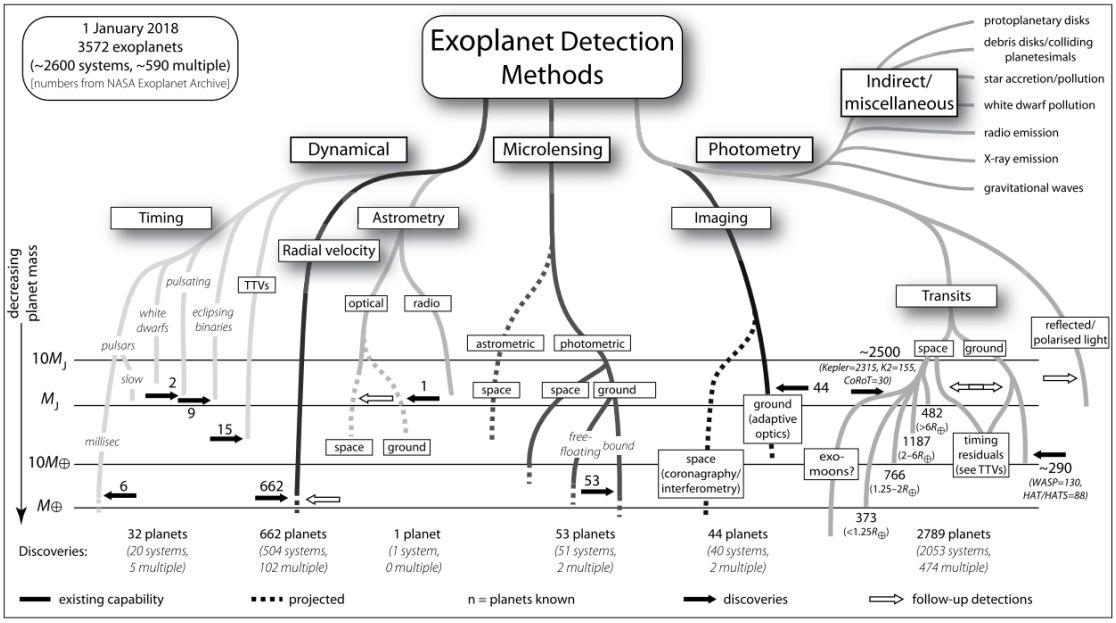

Figure 1.1: An overview of exoplanet discovery capabilities for various techniques. The current and future-potential planet-mass discoveries of techniques are shown on the left-hand side. The number of discoveries are enumerated for each discovery method.

The first indirect discovery of an exoplanet was made with the existing Arecibo radio telescope. While Arecibo was observing a pulsar, it found variations in its timing which was explained by the existence of a planetary system.[109] Detections made using this technique are rare and not possible for sun-like stars.

Today, the most exoplanet detections are made using transit or radial velocity techniques. There is additional promise for the microlensing technique, but it is still an indirect method and not used on nearby stars. There are many other indirect techniques capable of indirectly detecting exoplanets, but these are all incapable of providing the high resolution spectra of Earth-like exoplanets.

In this section, I discuss the two most prevalent exoplanet detection techniques and their limitations for finding habitable Earth-like exoplanets.

1.2.1 Transit Technique

The transit technique is uses the apparent dip in the light curve of an observed star to indirectly identify the existence of a transiting exoplanet as shown by the circular orbit in Figure 1.2. When more eccentric orbits with marginal inclinations are considered, either the transit or occultation side may not exist.

Transit Detections Miss Multi-planetary Systems

Of all 4521 detections made, a large number (3414) of them are made by the transit technique. Of all the exoplanets detected, many of them are in single planet exosystems as shown in Table 1.1.

If multiple planets in a star system, it is because we have not established a long enough baseline to detect multiple transits associated with long period planets. For example; Jupiter's orbital period is 11.862 years meaning a Jupiter-like planet cannot be detected twice in Kepler's 6 year long mission.

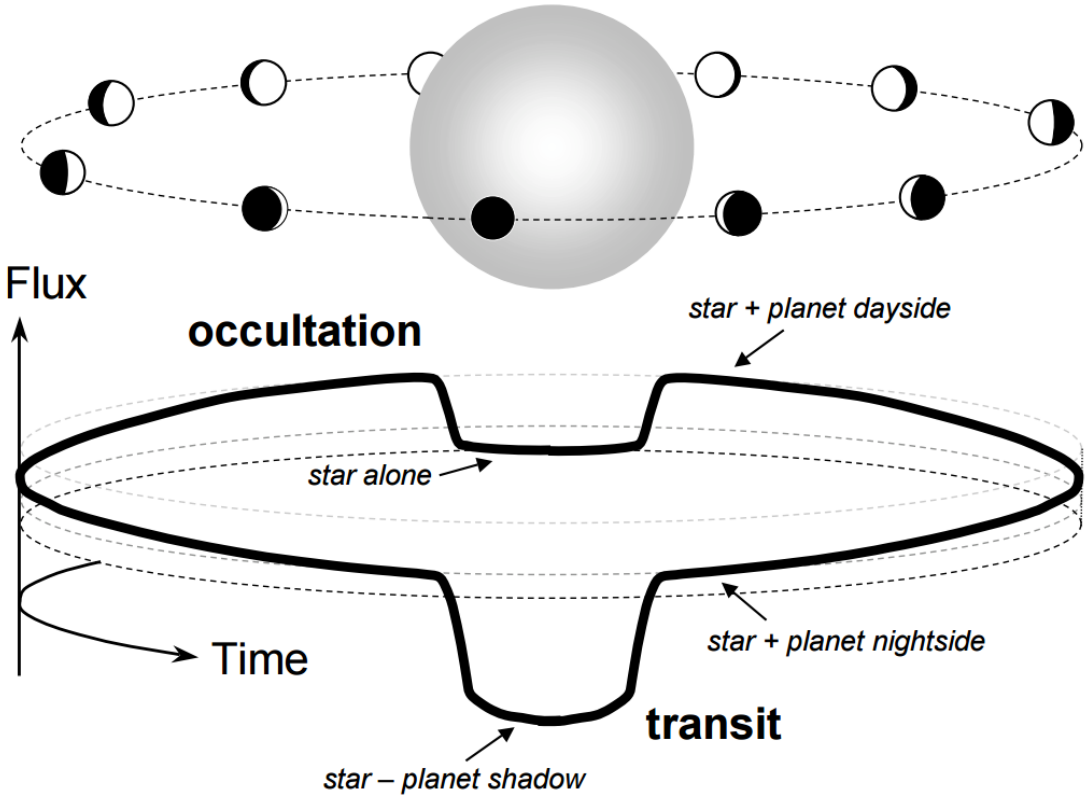

Figure 1.2: An illustration of transits and occultations from Winn [108] for a circular orbit. Variations in flux are substantially exaggerated for clarification purposes.

Over enough time, the dust cloud surrounding a forming star will aggregate into a common inclination of the orbital plane. The solar system planets *mostly* lie in a common orbital plane as indicated in Table 2.2 where the planet inclinations are given relative to Earth's orbital plane. In Figure 1.3, I plotted the maximum out of plane inclination a planet can have at its peak out-of-plane position in our solar system and still transit the sun (black line). I then plotted the inclinations of solar system planets relative to the common solar system angular momentum plane (blue dots). This shows that an external observer observing our own solar system would not be able to detect all the planets with the transit technique (with the exception of the fraction of cases where the solar system planets right ascension of the ascending node align appropriately). It

Table 1.1: The number of multiplanetary exosystems discovered with all techniques. (Sept 23, 2021[38])

Number of Exoplanets	Number of Star Systems
1	2576
2	515
3	161
4	61
5	25
6	8
7	1
8	1

would be difficult to detect even one of our solar system planets with the transit technique.

Transit Detections of Habitable Exoplanets Bias M Dwarfs

Our star, the sun, is a G type star. However, the coolest main sequence stars in the Harvard spectral classification system are the M Dwarfs.

The stellar effective temperature of these stars changes the habitable zone around them. For main sequence stars, the respective luminosity and stellar effective temperature are coupled; an increase in luminosity is proportional to an increase in stellar effective temperature to the 4^{th} power. The smaller semi-major axis limit of a conservative habitable zone around sun-like stars is 0.95 AU (CO_2 cloud formation).[41] The distances of the habitable zone around a star is scaled by the luminosity of the target star, so the habitable zone around sun-like stars can scaled to a fainter M star ($L = 0.395L_{\odot}$) to 0.25 AU. This results in planets in the habitable zone with much shorter periods. Because transit surveys are biased towards short period planets, transit surveys are more likely to detect

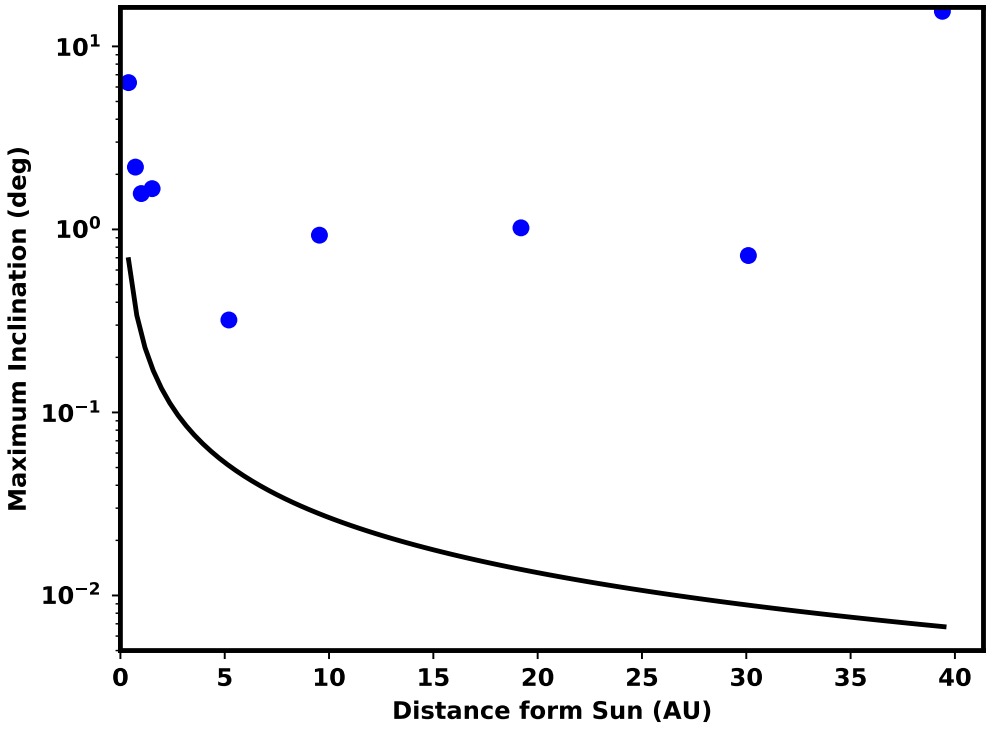

Figure 1.3: The black line is the maximum out-of-plane inclination a planet can have from the system angular momentum plane and still appear as a transit detection as a function of semi-major axis. Only planets with inclination below the black line can be detected with the transit technique. The blue dots are solar system planet inclinations relative to system angular momentum plane.

exoplanets in the habitable zone around low stellar effective temperature stars like M dwarfs than FGK type stars.

This limitation particularly effects shorter missions like Kepler, where multiple longer baselines are more difficult to establish.

Transit Biasing of Smaller Semi-major Axis Planets

I plotted the estimated semi-major axis and planetary radius of all exoplanets detected with various techniques to date in Figure 1.4. The solar system plan-

ets are also plotted, along with the population of planets detected by Roman through 1000 mission simulations. The solar system planets have distinctly smaller planetary radii and larger planet-star separation than the exoplanets detected with the transit, timing variations, orbital brightness modulation, or astrometry. A few exoplanets that have been directly imaged have similar planet radii and semi-major axis to solar system planets. The broad generalization I can draw from Figure 1.4 is that the Roman CGI is sensitive to exoplanets in a distinct region of planet radius and semi-major axis phase space

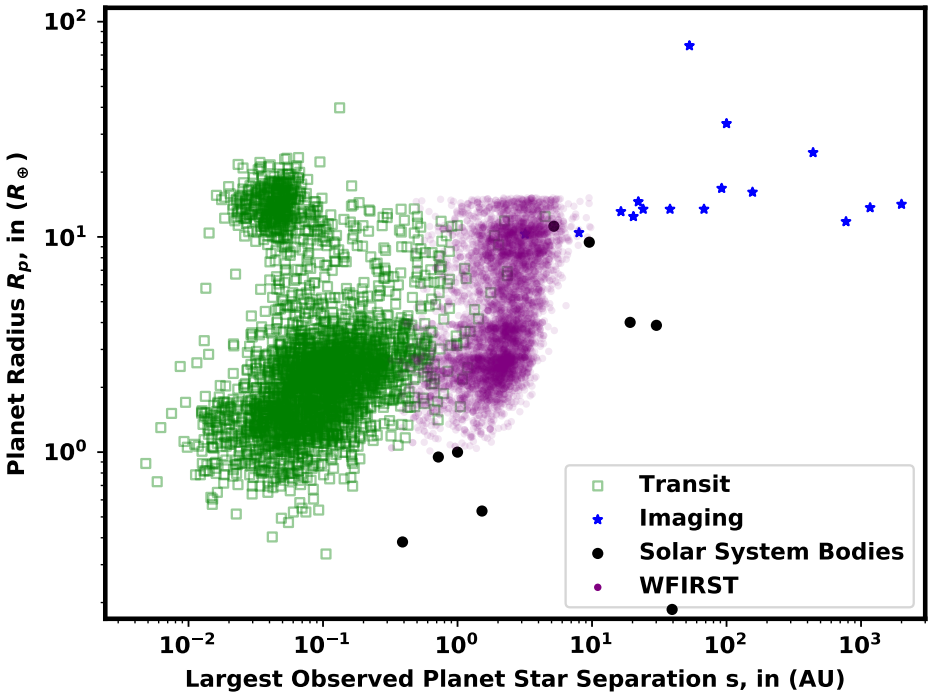

Figure 1.4: Plotted are the planet radius and semi-major axis of exoplanets detected with various detection techniques[38], the population of exoplanets detectable by the Roman CGI (for $R < 22.6R_\oplus$) taken from 1000 MC simulations (purple), and solar system planets are plotted as black dots.

1.2.2 Radial Velocity Technique and Limitations

The primary limitation of the radial velocity technique is the narrow population range of exoplanets it can detect. Since this technique is most sensitive to large mass exoplanets inclined in edge-on orbits, is has difficulty detecting the relatively low mass Earth-like exoplanets or systems that are more face-on. In Figure 1.5, I plotted the $M\sin(i)$ of exoplanets detected with the radial velocity technique. Of the 879 detections, only 39 of them occur within < 30 pc and have minimum planet mass within the upper limit Earth-like classification of 2.743 $M_{\oplus}$[100]. The upper limit of Earth-like planets used in Team [100] has a planet mass of 2.743 $M_{\oplus}$. I plotted the exoplanets that can have Earth-like mass and are within 30 pc of the sun in $M\sin(i)$ vs semi-major axis in Figure 1.6, the largest planet detected has a semi-major axis of 0.243 AU. These detections are distinctly far from the Earth-like planet population.[74]

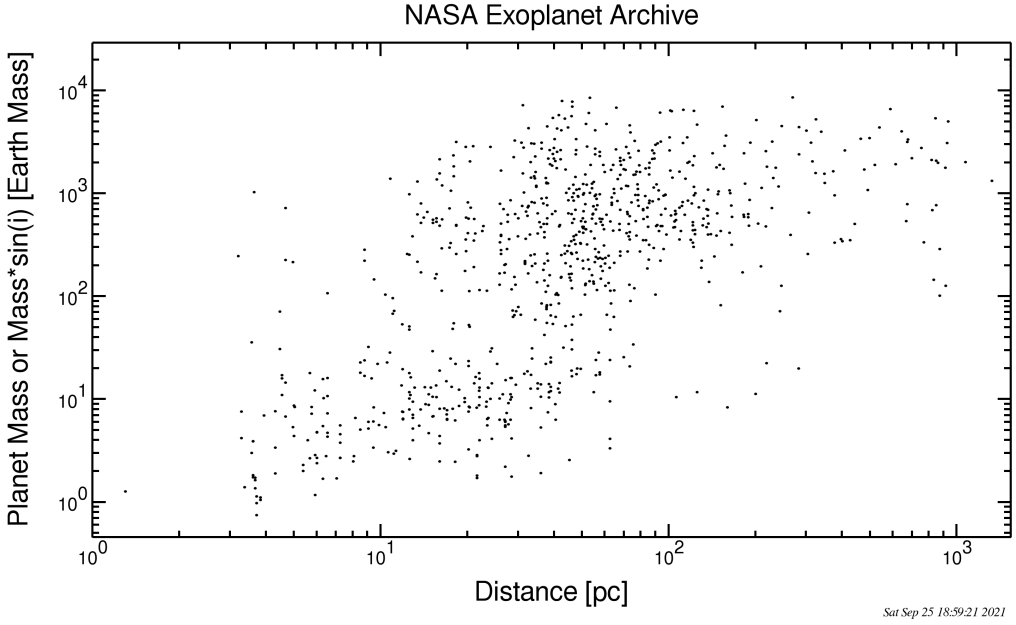

Figure 1.5: $M\sin(i)$ vs star distance of exoplanets detected with the radial velocity technique.

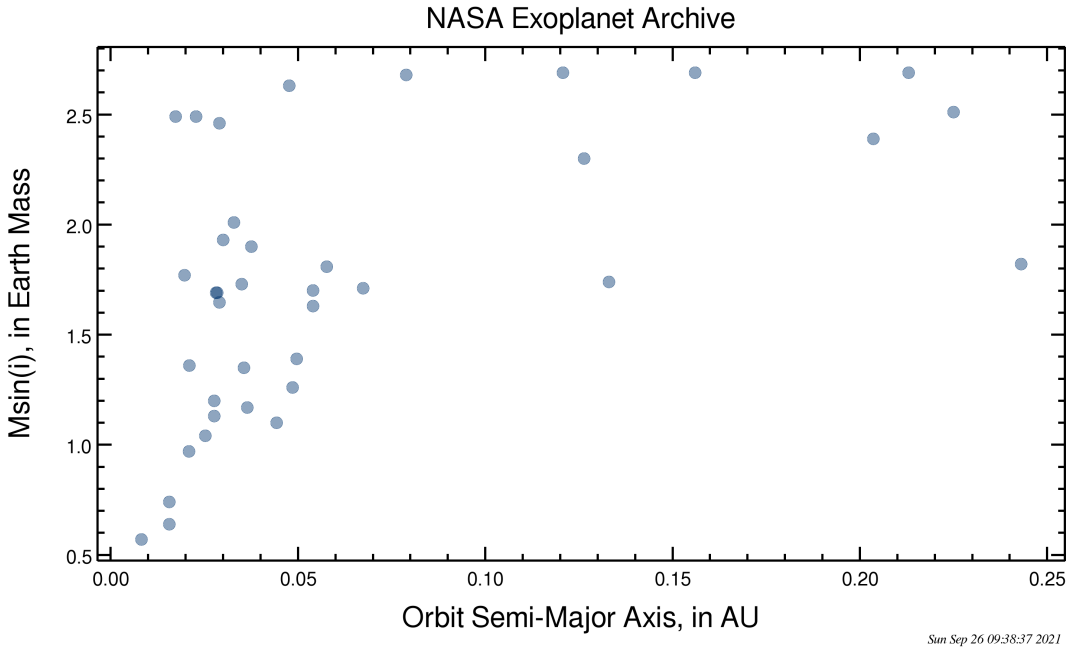

Figure 1.6: $M\sin(i)$ vs semi-major axis of exoplanets detected with the radial velocity technique around stars within 30 pc and potential Earth mass ($M < 2.743M_{\oplus}$).

1.2.3 Direct-Imaging

Direct-Imaging of exoplanets is a technique where the CGI collects and measure photons reflected off a planet orbiting a host star while suppressing the light emitted by the host star using a coronagraph. The first version of a coronagraph was invented by Bernard Lyot in order to observe the sun's corona without waiting for a solar eclipse. A coronagraph is even aboard the Hubble Space Telescope (HST). While the HST's primary mirror is big enough to detect exoplanets, the coronagraph was not designed to directly image exoplanets around other stars. Figure 1.7 contains the visual magnitudes of various objects in the sky with the left-most being the brightest in the sky and the right being the faintest. Normally, exoplanet brightness is looked at as brightness relative

to their host star.To the far right in Figure 1.7 are a faint collection of red dots indicating the visual magnitudes of exoplanets around a sun-like star.

The Gemini Planet Imager (GPI) saw first light in 2013 and has been directly imaging the space around nearby stars for gas giants. One of these such images from Marois et al. [62] is shown in Figure 1.8 with the primary astrometric features of a direct image overlayed; the minimum planet-star separation caused by the inner working angle of the coronagraph, the maximum planet-star separation limited by the outer working angle of the coronagraph, and the observed planet-star separation.

The Detection Mode

Images taken with the aim of discovering new exoplanets are detection observations. Detection observations collect light over a broader portion of the visible spectrum than spectral characterizations to maximize the number of photons collected per unit time ($\lambda = 565$ nm and $\Delta\lambda = 56.5$ nm). The visible spectrum is the ideal portion of the spectrum to make these observations in because the 19 solar system planetary bodies cataloged in Madden and Kaltenegger [60] have peak spectral responses in the visible portion of the spectrum. Making observations in this portion of the spectrum is where the planet-star flux ratio is maximized.

The primary purpose of a detection mode observation is to discover whether a planet exists. After discovery, detection mode observations are used to constrain a *sufficient* amount of a planet's orbital parameters to make a the high time cost spectral characterization.

The standards definition and evaluation team final report (SDET)[65] represents the current published state of the art in scheduling and planning exoplanet direct imaging missions. The SDET outlines revisit cadence best practices for missions scheduled in EXOSIMS, where they found "a newly detected habitable zone planet can be characterized with 3-4 detections separated by 2-6 months"[65]. This best practice is substantiated by simulations results in Figure 7, 8, and 9 in the SDET[65] which shows Keplerian Orbital Elements being reliably constrained to within 10% after 3-4 detections.

These orbit determination observations are necessary because of the substantial amount of time a mission can spend performing spectral characterizations. In Figure 17 of the SDET[65], the scheduled mission spend 22.7% of the time making detection observations and 26.6% of the time making spectral characterizations.

Spectral Characterization

The main advantage, and primary goal, of taking direct images of exoplanets is to acquire a spectral characterization of the planets which determines if there is water and biosignature gases in the atmosphere of the planet. These biosignature gases are indicators that processes occur on the surface which are creating chemical species at a different rate than what would exist because of solar abundances alone.

Scientists are interested in the measurement of the H_2O, O_3, O_2, CH_4, and O_4 spectral lines[100]. These are most readily apparent in Figure 7 of Turnbull et al. [104] which shows the Earthshine spectrum. This spectrum contains rela-

tive reflectance vs wavelength and calls out the specific wavelengths associated with different chemical species. Table 1.2 contains the wavelength range and the spectral resolution required to constrain atmospheric abundance column densities. Figure 17 of Morgan et al. [65] shows a a nominal mission timeline for HabEx 4H with spectral characterizations (300 nm- 1500 nm spectra at $Rs = 140$ to SNR$= 10$) that take anywhere between a few days and ≈ 50 days. At the narrowest of these wavelengths, the HabEx design has a $\Delta\lambda$ of 2.1 nm.

Some of the missions simulated in EXOSIMS in the SDET[65] filter out targets with *characterization completeness* less than 10% and integration times longer than 60 d.

Table 1.2: HabEx spectral resolution and wavelength measurement objectives from Table 6.3-1 and Table 5.1-2 of Team [100]

Rs	λ	Objective
5	0.53 μm-0.66 μm	F3.4 O_3
50	0.57 μm	F3.6 O_4
40	0.63 μm	F3.6 O_4
35	0.72 μm	F2 H_2O
70	0.75 μm-0.78 μm	F3.4 O_2
35	0.82 μm	F2.3 H_2O
8	0.8 μm	F6 H_2
100	0.87 μm	F6 CO_2
32	0.88 μm	F3.4 CH_4
17	0.94 μm	F2.3 H_2O
11	1.59 μm	F3.6 CO_2

There is currently work in measuring exoplanet spectral composition through transit spectroscopy, a technique where the difference in spectrum of a star is measured as an exoplanet transits in front of the host star.[7] A major difficulty in current transit spectroscopy is that different instruments cover different wavelengths meaning the separate spectra measured must be stitched together with the underlying issue being variations in baseline stellar flux being

different for observations taken at different times.[7] This is an issue because the time for a planet to transit the host star is small. The time for Mercury to transit the Sun (if observed as a transit detection of an exosystem) is approximately 0.33 d ($= 0.0093\text{AU} \times \frac{88\text{d}}{2\pi 0.387\text{AU}}$). This represents a maximum amount of observing time you can have to make an observation of the system, meaning multiple narrow band images must be spread across multiple exposures resulting in variable baselines.

1.3 State of The Art Gap in Mission Modeling

In the ideal world, an exoplanet direct imaging mission would be implemented in such a manner as to maximize the number of Earth-like exoplanets orbit fit and spectra measured over biosignature absorption bands. Currently, various levels of heuristics are used in the computation of this maximum number and dynamic mission planning. The work in this paper validates some heuristics and introduces new heuristics.

1.3.1 Integration Time Adjustment of Completeness

The broadest heuristic is the probability based yield estimate, called completeness, originating from Brown [13]. **Completeness is the probability of detecting an exoplanet around a star should one exoplanet exist.** Completeness can be used to calculate expected exoplanet yield by multiplying with the exoplanet occurrence rate. This can be used to estimate the yield of a *single-visit* exoplanet direct imaging mission. Brown [13] identifies a set of additional work that must

be completed in order to implement a mission. This includes a formalism comprised of a planning and scheduling algorithm to identify the next best target to observe, a computer orrery for tracking exoplanet motion in time, and a full accounting of telescope time-related costs like overhead time. In chapter 3, I present and discuss the EXOSIMS[83] mission modeling tool and how it is used to address each of these points of additional work.

1.3.2 Orbit Fitting

Section 3.2.5 and section 1.2.3 provide the motivation for orbit fitting exoplanets after detection. We want a sufficient orbit fit, less than 10% uncertainty according to Morgan et al. [65], before an expensive spectral characterization of a target is produced. This is because a series of detection observations is less time-expensive than a full spectral characterization observation. Each detection observation depends on the previous one and scheduling tools are needed to determine when the best time is to make the next observation.

Orbit fitting and scheduling are interrelated, but I will talk to orbit fitting first. A fast computational tool for orbit fitting astrometric data exists called Orbits For the Impatient (OFTI)[10]. OFTI is multiple orders of magnitude faster at orbit fitting than a conventional MCMC. In a particular case, OFTI converged after 134 minutes and the MCMC approach was still unconverged after 30 hours.[10] While this is quite fast (and potentially fast enough to use in a real mission), it is not fast enough to use in a Monte Carlo of mission simulations that will detect 100's of stars and needs to be run 1000 times (100 detections $\times 1000$ sims $\times 134$ min per detections $/1440$ min per day $\sim$

9305 days).

The OFTI method generates a Monte Carlo of planets from priors, scales-and-rotates, and then rejection samples. It has been used for orbit fitting directly imaged exoplanets like GJ 504, but it does not currently use photometry. While I have been told that photometric priors can be added to OFTI from private correspondence with Eric Neilsen, I have not tried implementing them. Generally, the astrometric calculations of Keplerian Orbits are faster than the photometric calculations due to non-linearity in the photometric calculation. The addition of photometric priors will further extend the computation time. **In chapter 5 and chapter 8, I present a faster method of orbit fitting than OFTI which incorporates photometry of two direct images.**

For 3 direct images and beyond, orbit fitting the Keplerian Orbital Elements should be done with OFTI. When photometry is used in Orbit fitting, assumptions about the planet's phase curve must be made. A phase curve the the fraction of light reflected by the body depending on the star-planet-observer angle; like the phases of the moon. In chapter 2, I show the broad diversity of even solar system phase curves. The Earth's phase curve is, on average, represented closely by the quasi-Lambert phase function[4] as I show in chapter 2. It is difficult to justify using the average Earth phase function because Figure 1 of Luger et al. [59] shows the substantial variation of a "Mock" Earth's phase function over the time of year and even time of day.

The uncertainty reduction in an orbit fit that can be achieved at varying epochs and uniform wait times between revisits is shown in Guimond and Cowan [32]. The first two detections (epochs) assume a simplified posterior distribution for semi-major axis for the orbit fit. All subsequent detections use

a full MCMC for the orbit determination. The most import part of this paper is the uncertainty reduction in semi-major axis for the uniform eccentricity distribution over time. Averaged over 100 random planets, the orbit fit precision is, on average, ~ 0.4 AU. The computational time required to achieve this is potentially longer than the 30 hr MCMC unconverged orbit fit identified in Blunt et al. [10]. In chapter 8, **I demonstrate my method of orbit fitting, that is faster than OFTI and incorporates orbit fitting specifically targeting two detections that can achieve uncertainty reduction in semi-major axis to below 10%.**

1.3.3 Scheduling

Currently, Morgan et al. [65] represents the state of the art for exoplanet direct imaging mission modeling. While the current EXOSIMS simulations in Morgan et al. [65] do some scheduling of 6 detection observations and a spectral characterization, the entirely probabilistic based approach, Altruistic Yield Optimization (AYO), does not.

Under some special circumstances, Morgan et al. [65] states scheduling has a minimal impact on coronagraph single-visit yield, but **I show scheduling of even the first detection has an impact on single-visit yield caused by variations in the local zodiacal dust in chapter** 3. There can be additional implications of when to schedule the first visit within a star's keep-out visibility window if a rapid-revisit is desired. As I show in section 7.1.3, **the telescopes solar and solar panel keep-outs can limit the maximum wait time to visit a target in the same visibility window.**

Depending on what instruments are used and the circumstances of the sys-

tem being observed (like exo-zodi levels, zodiacal light, keepout constraints, external occulters used), Morgan et al. [65] says scheduling can have a varying degree of impact on mission yield. Sections of Morgan et al. [65] citing orbit fitting work from Horning, Morgan, and Nielson [35] shows substantial variation in the orbit fit uncertainty reduction for various wait times if an Earth with a 45° inclined orbit. If such variation in semi-major axis uncertainty reduction exists for a planet with a narrowly defined orbit, then there should be a similar or greater variation when the broader population of orbits is considered. **Chapter 8 shows some variation in orbit fit as a function of wait time for a broader population of Earth-like exoplanets, further substantiating the importance of scheduling.**

Simulations in Morgan et al. [65] frequently assume only Exo-Earths exist in the simulation and effectively assume the detection of any Exo-Earth can be translated into a spectral characterization. In chapter 6, I show how planets within our own solar system can be confused with one another and that confusion is prolific between different planet types in the limited solar system diversity. This indicates planet confusion will be prolific in a broader planet population like SAG13. An important way planets of different types can be distinguished from one another is by scheduling a rapid-revisit.

The most important scheduling work I conduct is the analysis tools for scheduling of a rapid-revisit in chapter 7. Effectively, gas giants move differently in (s,Δmag) space than Earth-like exoplanets, but they can be confused with one another if too much time elapses between detections if multiple exoplanets are detected. Performing a rapid-revisit ensures the astrometry and photometry of the second detection can be associated with the first detection

with a high degree of confidence. I do not want the revisit to be so soon that the planet appears in the same region of phase space; I want the exoplanet to move *substantially* between detections so I get a better orbit fit. Chapter 7 explores the nuances of the minimum revisit time such that a planet is *distinctly distinguishable* and *still detectable*, how the (s,Δmag,$\Delta\theta$) measurable vary in time, and what some ideal revisit times may be.

There is some additional scheduling work conducted in chapter 5 associated with dynamic completeness. The original formulation of dynamic completeness in Brown and Soummer [14] assumes no detection was made but a planet exists around the host star. It investigates how revisit completeness changes in time. The improvement made is in computation time, where my unoptimized exo-det-box powered method can compute dynamic completeness $7\times$ faster than Brown's original method.

1.3.4 Phase Function Assumption

Since Brown [13], exoplanet direct imaging missions have been primarily modeled assuming the planets being imaged have isotropic scattering by assuming they have the lambert phase function.[82, 27, 16, 65, 37, 100, 32, 33, 103, 35, 14, 96]

Work in [86] tries to move away from the commonly used Lambert phase function[91], but they are not widely adopted. This includes works like Agol [4], Luger et al. [59] , and Mallama and Hilton [61]. In chapter 4, I investigate the impact on single-visit yield when optimizing assuming the Lambert phase function, quasi-Lambert phase function, and Earth's average phase function and try

observing a universe of planets with a different phase function.

1.4 Thesis Outline

In this dissertation, I presented a series of methods which can improve the yield of the general exoplanet direct imaging mission through more efficient operations and planning.

In chapter 2, I present the various planet populations used throughout this work and include methods of probabilistically classifying a (s,Δmag) detection. In chapter 3, I outline the method of optimizing a single-visit design reference mission and the ideal times to make these detection observations. It also includes my method of validating the probabilistic yield estimate approach by simulating a Monte Carlo of mission simulations considering the dynamics of the exoplanets, telescope orbit, and solar system planets. Chapter 4 use the Monte Carlo of simulations approach to test the validity of the commonly assumed Lambert phase function as compared to the quasi-Lambert phase function or Earth's phase function. In chapter 5, I present a series of methods to calculate the time(s) when a planet has a particular s or Δmag which I then use to calculate an Integration Time Adjusted Completeness.

After a detection, new (s,Δmag) information is obtained about the exoplanet. In chapter 6, I consider our solar system, the best understood multi-planetary system with a habitable exoplanet, as an exosystem. I show that many systems can have coincidence and that planets that appear Earth-like may be another exoplanet.

I also present tools for planning the second and third detection. In chapter 7, I present a method of calculating the minimum revisit time for performing a rapid revisit producing a detection that is distinctly distinguishable. I describe a second ideal revisit time where the fraction of Earth-like exoplanets distinctly distinguishable and still detectable to SAG13 planets distincitly distinguishable and still detectable is maximized. In chapter 8, I present and exodetbox powered approach to orbit fitting which incorporates the photometry to provide an orbit fit with as few as two detections.

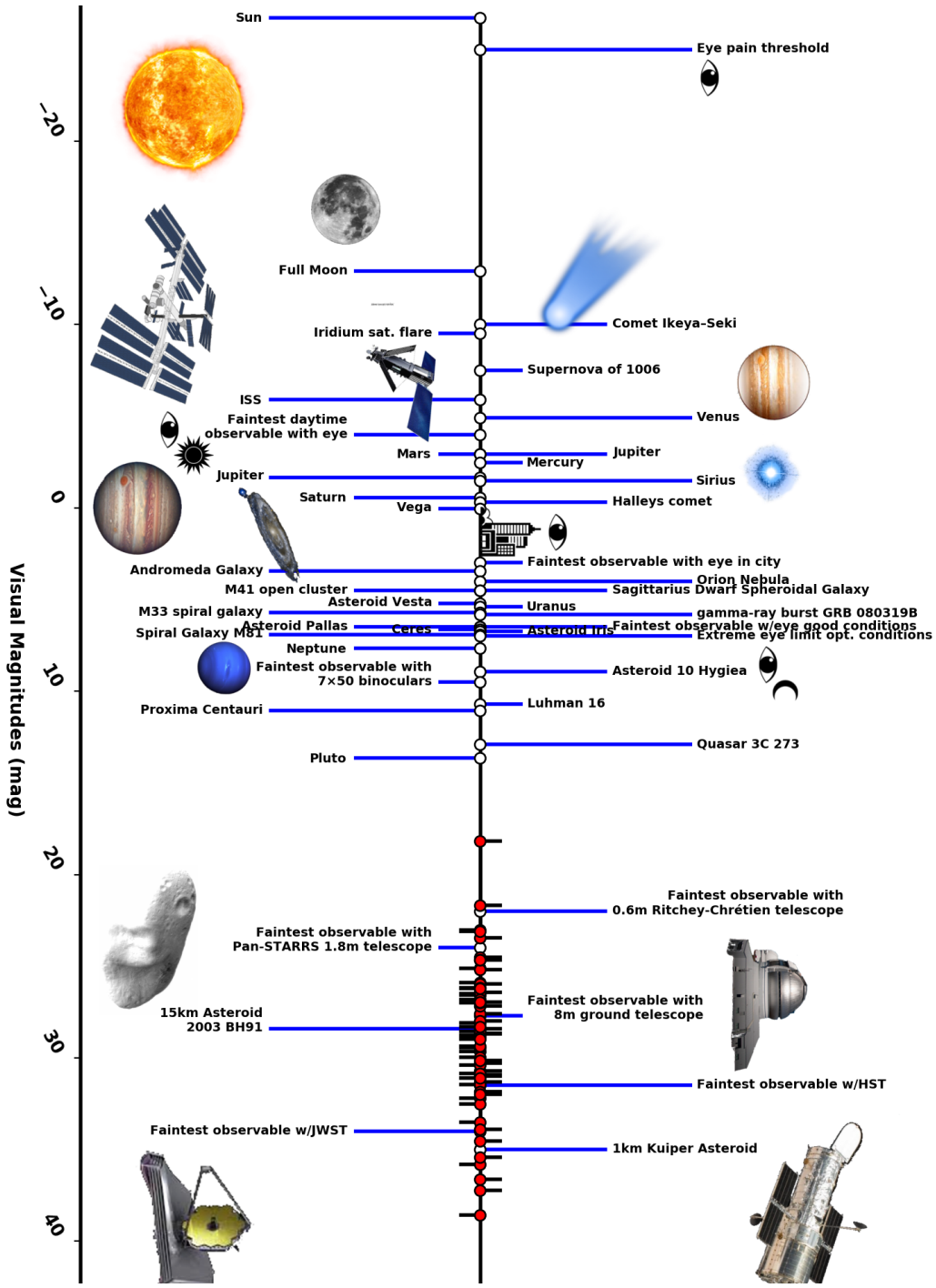

Figure 1.7: Exoplanets on a visual magnitude scale of objects in the sky with the brightest being the Sun and faintest an exoplanet. Despite Hubble and JWST being able to see objects as faint as exoplanets, the exoplanets depicted require a specialized coronagraph capable of suppressing the starlight of their host to see the faint light reflected by the planet.

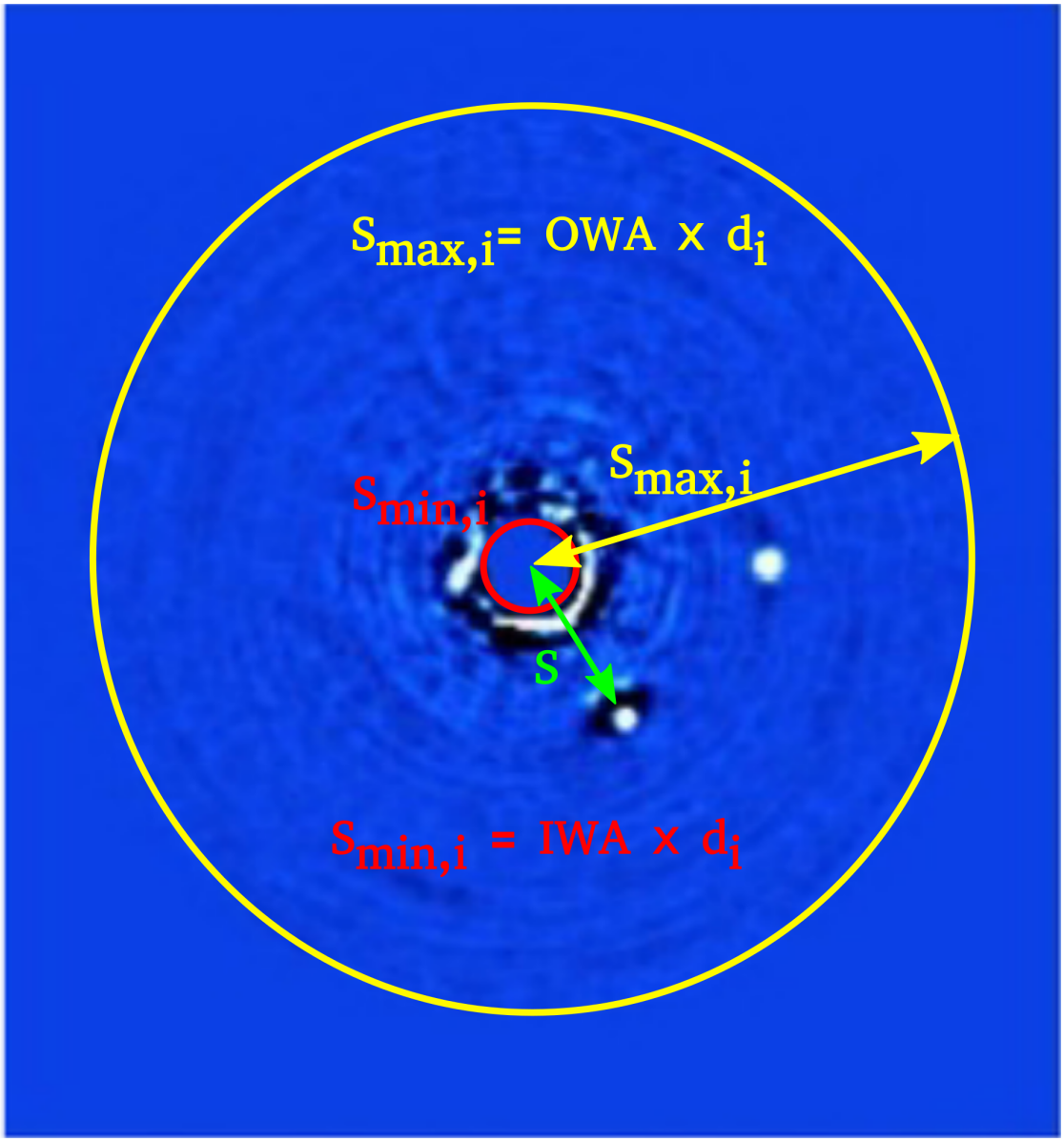

Figure 1.8: An example of a directly imaged exoplanet and synthetically simulated exoplanet from Figure 4 of Marois et al. [62].

CHAPTER 2

PLANET POPULATIONS

I make use of a variety of planet populations in this work for various reasons. The purpose of this chapter is to consolidate and present the planet populations used in this text. I additionally add a section related to the computation of the probability a detected exoplanet is of a particular type.

In general, our knowledge of exoplanets is constantly evolving as more time is spent observing the planet phase space around stars. The Kepler-like planet population is the originator of the majority of exoplanets detected via the transit technique employed by the Kepler Telescope.

The Kepler-like planet population represents one of the earliest planet populations based on a substantial volume of data. The issue with this planet population is that the transit technique inherently biases closer in planets and has not likely done a good job finding multiplanetary star systems (see Figure 1.3). Issues with reaction wheels ended the Kepler mission prematurely, but even if executed for its extended design life of 6 years, it would not be able to detect long period planets like Jupiter or Saturn over multiple epochs. The design life of a spacecraft is typically limited to ≈ 13 years.[78] This limitation is imposed by the design limitation of the components aboard the spacecraft and when they exceed their design life. NASA is constantly working to produce longer lifespan components by running continuous durability tests in basements of various NASA centers. If we want a component to demonstrate functionality for longer missions, it needs to be tested under expected loads well beyond the design life (i.e. tested for the "equivalent" of 13 years).

The Gemini Planet Imager followed up on an exponential relationship between exoplanet occurrence rate and semi-major axis indicated by Kepler data.[19, 71] This direct imaging telescope did not find the abundance of large planets expected by the exponential relationship (albeit with a small sample size) and instead indicated a breakpoint in this exponential occurrence rate curve.Fernandes et al. [24] We adapted the Kepler-like planet population to use this observed semi-major axis "knee".

There are many more exoplanet techniques each sensitive to exoplanets with different characteristics and stemming from different fields of study as seen in Figure 1.1. This prompted NASA to direct a working group, SAG13, to arrive at a current best estimate of occurrence rate model combining the different data around 2018. They arrived at the occurrence rate model we use most commonly in this paper, the SAG13 planet population. As new transit data comes out from missions like TESS, this planet population may be updated in the future.

In order to simplify simulations and arrive at idealized yield estimates of Earth-like exoplanets, various planet populations of Earth-like exoplanets have been created. Generally, the Earth-twin simulates exoplanets with the same properties as Earth (but with a Lambert phase function).

2.1 Kepler Like

2.1.1 Planetary Semi-major Axis and Radii

For the Kepler Like planet population, we adopt a power-law distribution for semi-major axis (a) modified from the power law fit in Cumming et al. [19] to be of the form

$$f_{\overline{a}}(a) = \frac{a^{-0.62}}{a_{\rm norm}} \exp\left(-\frac{a^2}{a_{\rm knee}^2}\right) \tag{2.1}$$

where -0.62 is adopted from Moorhead et al. [63]. In this model, we include an exponential decline in semi-major axis past a "semi-major axis knee" ($a_{\rm knee}$). This "knee" is motivated by a lack of giant planet discoveries by the Gemini Planet Imager which indicates the RV-based power-law planet occurrence rate from Cumming et al. [19] approaches 0 between 10 and 100 AU.[71] Using giant planet radial velocity data, Fernandes et al. [24] fit many period break points to the giant planet occurrence rate power-law model. We assume an intermediate knee equivalent to $a_{knee} = 10$ AU. The normalization factor is given by integrating the non-normalized distribution over a specific a range

$$a_{\rm norm} = \int_{a_{\rm min}}^{a_{\rm max}} a^{-0.62} \exp\left(-\frac{a^2}{a_{\rm knee}^2}\right) {\rm d}a \,, \tag{2.2}$$

where we consider values of a range in $a_{\rm min} = 0.1$ AU to $a_{\rm max} = 30$ AU, again based on the paucity of wide-separation planets discovered to date. The per-simulation average distribution of $\mathbf{a}$ is shown in the histogram above Figure 3.12 (a). We note that $a_{\rm min} < \min(s_{{\rm min},i})$ for Roman and this planet population. Since the closest target list star has distance $\min(d_i) = 2.63$ pc and has the smallest observable planet star separation $\min(s_{{\rm min},i}) \approx IWA \times \min(d_i)$, then Roman's inner working angle (IWA) of 0.15 arcsec means the smallest planet-star

separation observable by Roman is 0.394 AU. By assuming a maximum planet eccentricity $(e_{\max}) = 0.35$, the smallest observable semi-major axis $a_{\min}$ from $s_{\min}) \approx a_{\min}(1 + e_{\max}) = 0.292AU$.

We base our Kepler Like planetary radii (R) based off Figure 7 in Fressin et al. [25]. We define the bin counts in Figure 7 of Fressin et al. [25] as $\mathbf{R}_{85}$. These bins range from $R_{\min} = 1\ R_{\oplus}$ to $R_{\max} = 22.6\ R_{\oplus}$ and are based solely on data from planets with periods greater than 0.8 d, but less than 85 d. To properly tune the overall Kepler Like planet occurrence rates (η_{KL}) starting with $\mathbf{R}_{85}$, we first use Eq. 2.2 evaluated at $a_{\min} = a_{0.8}$ to $a_{\max} = a_{85}$ to get $a_{85,\text{norm}}$. Here, $a_{0.8}$ and a_{85} are the semi-major axes corresponding to periods of 0.8 d and 85 d around a sun mass star. We then scale $\mathbf{R}_{85}$ by Eq. 2.2 and $a_{85,\text{norm}}$ to get the adjusted planetary radii occurrence rates,

$$\mathbf{R}_{\text{vals}} = \mathbf{R}_{85}\frac{a_{\text{norm}}}{a_{85,\text{norm}}}. \tag{2.3}$$

We multiply the last 5 bins in $\mathbf{R}_{\text{vals}}$ by 2.5 to account for longer orbital baseline data and more closely match the larger period orbit distributions available from radial velocity surveys at the time when this distribution was first derived[19, 36]. Even with this multiplication, the right hand side histogram of Figure 3.12 (a) shows the characteristic drop-off in planetary radius clearly observable in Figure 7 of Fressin et al. [25]. The Kepler Like planet occurrence rate per star is $\eta_{KL} = \sum \mathbf{R}_{\text{vals}} = 2.375$ over the specific a and R ranges discussed in this section.

How many planets do we generate of a given radius?

When we simulate a universe of Kepler Like planets, we first calculate the number of planets to generate for each planet radius bin (N_q) for all bins in $\mathbf{R}_{\text{vals}}$.

This is given by

$$N_q = N_p \left\lceil \frac{R_{\text{vals},q}}{\sum \mathbf{R}_{\text{vals}}} \right\rceil . \tag{2.4}$$

In this paper, N_p is the number of planets to generate. In our Monte Carlo completeness calculations, we generate 10^8 planets. We take N_q samples from a log-uniform distribution over the q^{th} bin range in $\mathbf{R}_{\text{vals}}$ to get a set of planets radii ($\mathbf{R}_q$).[25] Finally, we randomly select N_p radii from the collective 9 sets of planetary radii to get $\mathbf{R} = \bigcup_{q=1}^{9} \mathbf{R}_q$. At the same time, we use an inverse transform sampler to generate $\mathbf{a} = \{a_k \,\forall\, k \;\in\; 1..N_p\}$ based on Eq. 2.1.

How do we sample semi-major axis for a planet with a given radius?

To generate a planet from the probability distributions in this section, we first sample Eq. 2.8 using a single variable inverse transform sampler to get a set of planetary radius, $\mathbf{R}_p$. We also use a single variable inverse transform sampler to sample Eq. 2.9 and get $\mathbf{a}$. The $a_{\min}$ and $a_{\max}$ used in the SAG13 population are the same as in the Kepler Like planet population. SAG13's a frequency distribution is included above Figure 3.12 (b). The 2D contour plot and associated grid values in Figure 3.12 (b) shows $\mathbf{R}$ and $\mathbf{a}$ interdependence.

2.1.2 Eccentricity

We assume a Rayleigh distribution for orbital eccentricities in both the Kepler Like and SAG13 planet populations as done in Moorhead et al. [63], such that the eccentricity (e_k) of the k^{th} simulated planet is

$$e_k = \sigma_e \sqrt{-2 \ln \left[\exp\left(\frac{-e_{\min}^2}{2\sigma_e^2} \right) - n \left(\exp\left(-\frac{e_{\min}^2}{2\sigma_e^2} \right) - \exp\left(-\frac{e_{\max}^2}{2\sigma_e^2} \right) \right) \right]}, \tag{2.5}$$

where n is a uniform random variable between 0 and 1, σ_e is the Rayleigh parameter for eccentricity, $e_{\min}$ is the minimum allowed eccentricity, defined as 0, and $e_{\max}$ is the upper 95^{th} percentile for e. The mean eccentricity $\mu_e = \sigma_e\sqrt{\pi/2}$. In Moorhead et al. [63], the authors fit the Rayleigh distribution to radial velocity-detected planets and found $\mu_e \approx 0.225$ to be a best fit with p-value of 0.5. They additionally found $0.125 < \mu_e < 0.25$ has a p-value above 0.05 and placed strict limits of $\mu_e < 0.35$ and $\mu_e > 0$[63]. For this work, we use $\mu_e = 0.175$ (splitting the difference between 0.225 and 0.125) as done in Fressin et al. [25] and adopt their independence of star spectral type assumption.

2.1.3 Planet Albedo from Semi-major Axis

In both the Kepler Like and SAG13 planet population, we calculate albedo (p), using a cubic 2D interpolant over metallicity and a using the V-band column from Table 4 of Cahoy, Marley, and Fortney [16]. The individual values in Table 4 from Cahoy's work are based off the atmospheric modeling of Jupiter and Neptunes at a from 0.8 AU to 10 AU over varying metallicity ranging from $1\times$ solar abundances to $30\times$ solar abundances. To accommodate these restrictions for each p_k interpolated, we use the randomly generated a_k truncated to be between 0.8 and 10 AU. This means any planets with $a_k < 0.8$ AU will be treated as having 0.8 AU in the interpolant and conversely and planets with $a_k > 10$ AU will be treated as having 10 AU in the interpolant. Jupiters at 0.8 AU in Cahoy's work were found to be cloud-free, resulting in a geometric albedo of 0.322 which is comparable to Earth's geometric albedo. We assume a uniform random planet metallicity multiplication factor between $1\times$ and $30\times$. Metallicity of a planet is a descriptor for the abundance of elements heavier than hydrogen or

helium in that planet. The least reflective planet would be a Neptune at 0.8 AU with $30\times$ solar abundance metallicity which is slightly larger than the geometric albedo of Mercury and the Moon. The most reflective planet would be a Jupiter at 2 AU with $3\times$ solar abundance. Planets formed through different processes will have varying metallicity representative of the planet's atmospheric metallic composition relative to solar abundances.

2.2 SAG13

When we sample the SAG13 distribution, the semi-major axis and planet radius are jointly sampled and the albedo is jointly sampled with semi-major axis. The eccentricity and angular Keplerian Orbital Elements are independently sampled. In the SAG13 distribution, only the joint distribution of planetary radius and semi-major axis are different from the Kepler like planet population in section 2.1.

2.2.1 SAG13 Planetary Radii and Semi-major Axis

The SAG13 planet population represents a significant update on the Kepler Like population, incorporating all available Kepler data circa 2017. The occurrence rate model presented in Belikov et al. [8] is a power-law model fit as a function of $\ln P$ and $\ln R$, but does not include an occurrence rate turnover indicated in giant planet occurrence rates from radial velocity studies[24] and the lack of detections of large a planets by subsequent Gemini Planet Imager survey results.[71] We need an occurrence rate model that is in terms of linear Keplerian

orbital elements and decreases occurrence rates for large a planets so our extrapolation of the model beyond the bounds in Belikov et al. [8] does not produce substantially more large a planets than expected. We include a full derivation of the SAG13 occurrence rate model implemented[28, 29] in EXOSIMS in section 2.2, but summarize the steps, important components, and results here.

We start with the original occurrence rate model fit from Belikov et al. [8] included as Eq. 2.10 and convert from ($\ln P, \ln R$) to (P, R) resulting in Eq. 2.11. We reconstructed the occurrence rate grid from the linear model in Figure 2.1 (a). When directly compared to the occurrence rate grid for G type stars in Belikov et al. [8], we see a maximum deviation of 0.74 ($100\times$ planets per bin occurrence) and maximum percent deviation of 13%. We then convert Eq. 2.11 from period (P) space to a space using Eq. 2.12 and Eq. 2.13 assuming a solar mass star to arrive at Eq. 2.14. We compare the analytical integral over a space of this new occurrence rate model to arrive at Figure 2.1 (b) which shows identical occurrence rates in each of their counterparts grid spaces in Figure 2.1 (a). We now append a semi-major axis "knee" to decay occurrence rates of larger a planets to 0 which results in Eq. 2.15. We calculate the overall SAG13 exoplanet occurrence rate per planet (η_{SAG13}) by performing the double integral over the entire a and R space as in Eq. 2.16. The SAG13 model parameters in Table 2.1 are split at 3.4 $R_\oplus$, so we use the notation $i = 0$ for $R_{\mathrm{min}} = 0.666\ R_\oplus \leq R < 3.4\ R_\oplus$ and $i = 1$ for $3.4\ R_\oplus \leq R < 17.086\ R_\oplus = R_{\mathrm{max}}$. An intermediate simplification of the double integral in the calculation of η_{SAG13} is

$$\eta_{\mathrm{SAG13}} = \frac{\gamma_0 K_0}{\alpha_0}[R_{\mathrm{max}}^{\alpha_0} - (3.4\ R_\oplus)^{\alpha_0}] + \frac{\gamma_1 K_1}{\alpha_1}[(3.4\ R_\oplus)^{\alpha_1} - R_{\mathrm{min}}^{\alpha_1}]. \tag{2.6}$$

Where γ_i, β_i, and α_i are constants from Table 2.1. The α_i in the denominator and $(\alpha_i - 1)$ to α_i exponent are a result of the indefinite integral over R. The four R terms are the result of evaluating the indefinite integral over R_{min} to $3.4\ R_\oplus$ to

$R_{\max}$. Finally, K_i is an intermediate calculation representing the marginalization of Eq. 2.15 over a written as

$$K_i = \int_{a_{\min}}^{a_{\max}} \left(2\pi\sqrt{\frac{a^3}{\mu}}\right)^{(\beta_i-1)} \left(3\pi\sqrt{\frac{a}{\mu}}\right) \exp\left(-\frac{a^3}{{a_{\text{knee}}}^3}\right) \mathrm{d}a. \tag{2.7}$$

Here, μ is the gravitational parameter assuming a solar mass star. We use the same $a_{\text{knee}} = 10$ AU in the SAG13 planet population that we use for the Kepler Like planet population. The average number of planets generated per star in the EXOSIMS implemented SAG13 universe over the range specified is $\eta_{\text{SAG13}} = 5.62$.

Table 2.1: Parametric fit parameters for the SAG13 planet population implemented in EXOSIMS[8]

Parameter	$[i = 0, i = 1]$
β_i	$[0.26, 0.59]$
α_i	$[-0.19, -1.18]$
γ_i	$[0.38, 0.73]$

2.2.2 Planetary Radius, R_p

In order to generate planets with R and a from the occurrence rate model, we still need a joint probability density function $f_{\overline{R}_p,\overline{a}}(R, a)$ as well as a single variable probability density function and conditional probability density function. By normalizing Eq. 2.15 by η_{SAG13}, we get the joint probability distribution in Eq. 2.17. From here, we calculate the probability distribution of R for the SAG13 planet population by marginalizing Eq. 2.17 over a only. This gives us the planetary radius distribution

$$f_{\overline{R}}(R) = \frac{\gamma_i K_i}{\eta_{\text{SAG13}}} R^{(\alpha_i-1)}. \tag{2.8}$$

This probability density function inherits the parametric conditions of the joint probability density function. Since $f_{\overline{R}}(R)$ is a marginalization over the joint probability density function, the integral of $f_{\overline{R}}(R)$ over the range $R_{\min} \leq R \leq R_{\max}$ is 1. The distribution of generated planets in $\mathbf{R}$ is shown in the right side histogram of Figure 3.12 (b). We now calculate the conditional probability distribution $f_{\overline{a}|\overline{R}}(a)$ using $f_{\overline{R},\overline{a}}(R,a)$, $f_{\overline{R}}(R)$, and Bayes rule. The conditional probability distribution is a simple division of the joint probability density function by the marginalized probability density function to get

$$f_{\overline{a}|\overline{R}_p}(a) = \frac{1}{K_i}\left(2\pi\sqrt{\frac{a^3}{\mu}}\right)^{(\beta_i-1)}\left(3\pi\sqrt{\frac{a}{\mu}}\right)\exp\left(-\frac{a^3}{a_{\text{knee}}^3}\right). \tag{2.9}$$

We now have the tools to sample semi-major axis and planetary radius.

2.2.3 SAG 13 Occurrence Rate Derivation

At some point, we need to convert occurrence rate models from period (P) space into semi-major axis (a) space. We chose to do this at the probability distribution level so we may arrive at a distribution of $\Delta\mathrm{mag}$ vs s, which will be a function of a.[**Garret2018b**] In this section, we convert the joint probability density function of planet occurrence rate in $\ln P$ and $\ln R$ space from the study analysis group 13 model in Belikov et al. [8] to a and R space. The parametric fit exoplanet occurrence rate model they present is

$$\frac{\partial^2\eta(R,P)}{\partial\ln R\partial\ln P} = \gamma_i R^{\alpha_i}P^{\beta_i} = \begin{cases} \gamma_0 R^{\alpha_0}P^{\beta_0} & R \leq 3.4R_\oplus \\ \gamma_1 R^{\alpha_1}P^{\beta_1} & R > 3.4R_\oplus \\ 0 & \text{else} \end{cases}. \tag{2.10}$$

Here, P refers to the planet period in years which is defined in the SAG 13 model over the range $10 \leq P \leq 640$ d. R must be in units of $R_\oplus$ and P must be in units of years. The constants γ_i, α_i, and β_i all refer to constants from Belikov et al. [8] included in Table 2.7, where i in this instance refers to whether $i = 0$ or $i = 1$ is used. We would like to transform this occurrence rate distribution into linear functions of R and a.

We first need to convert this parametric model fit from log-scaled distributions like $\partial\ln R$ and $\partial\ln P$ to linear scale distributions of the form ∂R and ∂P. The general expression $y = \ln x$ has derivative $x\mathrm{d}y = \mathrm{d}x$ which we can apply to both of these separable parameters since the γ_i, α_i, and β_i terms are all constant.

We arrive at the linear distribution of occurrence rates over R and a as

$$\frac{\partial^2 \eta(R,P)}{\partial R \partial P} = \gamma_i R^{\alpha_i - 1} P^{\beta_i - 1} = \begin{cases} \gamma_0 R^{\alpha_0 - 1} P^{\beta_0 - 1} & R \leq 3.4 R_\oplus \\ \gamma_1 R^{\alpha_1 - 1} P^{\beta_1 - 1} & R > 3.4 R_\oplus \\ 0 & \text{else} \end{cases}. \tag{2.11}$$

We now need to convert from an occurrence rate model in terms of P to a. This conversion exists in Vallado [105] as

$$P = 2\pi \sqrt{\frac{a^3}{\mu}}. \tag{2.12}$$

Here, $\mu = GM_s$ where M_s is the mass of the sun and G is the gravitational constant. M_s is close to the average mass of G spectral type stars, the spectral type the SAG 13 occurrence rate model is defined for. We assume the SAG 13 model extends to stars of all spectral types. To replace ∂P we calculate the partial derivative of Eq. 2.12 with respect to a as

$$\partial P = \partial \left(2\pi \sqrt{\frac{a^3}{\mu}} \right) = 3\pi \sqrt{\frac{a}{\mu}} \partial a. \tag{2.13}$$

Substituting this into the linear occurrence rate model in Eq. 2.11 gives the linear SAG 13 occurrence rate model in terms of R and a of

$$\begin{aligned} \frac{\partial^2 \eta(R,a)}{\partial R \partial a} =& \gamma_i R^{\alpha_i - 1} \left(2\pi \sqrt{\frac{a^3}{\mu}} \right)^{\beta_i - 1} \left(3\pi \sqrt{\frac{a}{\mu}} \right) \\ =& \begin{cases} \gamma_0 R^{\alpha_0 - 1} \left(2\pi \sqrt{\frac{a^3}{\mu}} \right)^{\beta_0 - 1} \left(3\pi \sqrt{\frac{a}{\mu}} \right) & R \leq 3.4 R_\oplus \\ \gamma_1 R^{\alpha_1 - 1} \left(2\pi \sqrt{\frac{a^3}{\mu}} \right)^{\beta_1 - 1} \left(3\pi \sqrt{\frac{a}{\mu}} \right) & R > 3.4 R_\oplus \\ 0 & \text{else} \end{cases}. \end{aligned} \tag{2.14}$$

The Keck Planet Search used radial velocity observations of exoplanets to describe an occurrence rate as a power-law in planet mass and orbital period,

but was limited to planets with $P < 2000$ d ($a < 14.4$ AU).[19] However, subsequent direct imaging surveys by the Gemini Planet Imager discovered the power-law did not extend throughout the entirety of the instrument's sensitivity range and supports that planet occurrence rates approach 0 between 10 and 100 AU.[71] Fernandes et al. [24] introduces a period break to describe giant planet occurrence turnover in radial velocity data and presents many possible knee values ranging from ≈7 AU to ≈15 AU depending on the model fit being used. We transform their period break into a similar semi-major axis knee value of $a_{knee} = 10$ AU making the adjusted SAG 13 exoplanet occurrence rate model

$$\frac{\partial^2 \eta(R,a)}{\partial R \partial a} = \gamma_i R^{\alpha_i - 1} \left(2\pi\sqrt{\frac{a^3}{\mu}}\right)^{\beta_i - 1} \left(3\pi\sqrt{\frac{a}{\mu}}\right) \exp\left(-\frac{a^3}{a_{\rm knee}^3}\right). \tag{2.15}$$

The total planet occurrence rate (η_{SAG13}) over an assumed planet range is given by marginalizing over both parameters of the SAG 13 occurrence rate model with the appended a_{knee} to get

$$\eta_{\rm SAG13} = \int_{R_{\rm min}}^{R_{\rm max}} \int_{a_{\rm min}}^{a_{\rm max}} \frac{\partial^2 \eta(R,a)}{\partial R \partial a} {\rm d}a{\rm d}R. \tag{2.16}$$

It is important to note that a cubic form of the roll-off on the semi-major axis distribution is used, rather than the quadratic form from the Kepler Like case (c.f., Eq. 2.1). This is motivated by recent limits placed on wide-separation planets by direct imaging and longer-baseline radial velocity data.[24] We now calculate the joint probability density function of a and R by normalizing based

on the integral over the occurrence rate parametric model to arrive at

$$f_{\overline{R}_p,\overline{a}}(R,a) = \frac{1}{\eta_{\mathrm{SAG13}}} \times \begin{cases} \gamma_0 R^{\alpha_0 - 1} \left(2\pi\sqrt{\frac{a^3}{\mu}}\right)^{\beta_0 - 1} & \\ \left(3\pi\sqrt{\frac{a}{\mu}}\right) \exp\left(-\frac{a^3}{a_{\mathrm{knee}}^3}\right) & R \leq 3.4R_\oplus \\ \gamma_1 R^{\alpha_1 - 1} \left(2\pi\sqrt{\frac{a^3}{\mu}}\right)^{\beta_1 - 1} & \\ \left(3\pi\sqrt{\frac{a}{\mu}}\right) \exp\left(-\frac{a^3}{a_{\mathrm{knee}}^3}\right) & R > 3.4R_\oplus \\ 0 & \text{else} \end{cases} . \tag{2.17}$$

The integral of this joint probability distribution over the a and R range is 1.

Previous work in Garrett and Savransky [28] that originally derived the equations in this section showed that independently sampling R and sampling a marginalization over R of Eq. 2.17 could achieve less biased sampling of the exoplanet distribution. We marginalize Eq. 2.17 over a to arrive at an intermediate constant

$$K_i = \int_{a_{\min}}^{a_{\max}} R^{\alpha_i - 1} \left(2\pi\sqrt{\frac{a^3}{\mu}}\right)^{\beta_i - 1} \left(3\pi\sqrt{\frac{a}{\mu}}\right) \exp\left(-\frac{a^3}{a_{\mathrm{knee}}^3}\right) \mathrm{d}a. \tag{2.18}$$

We use K_i to find the probability density function of semi-major axis conditional on R of

$$f_{\overline{a}|\overline{R}_p=R}(a|R) = \begin{cases} \frac{1}{K_0} \left(2\pi\sqrt{\frac{a^3}{\mu}}\right)^{\beta_0 - 1} \left(3\pi\sqrt{\frac{a}{\mu}}\right) \exp\left(-\frac{a^3}{a_{\mathrm{knee}}^3}\right) & R \leq 3.4R_\oplus \\ \frac{1}{K_1} \left(2\pi\sqrt{\frac{a^3}{\mu}}\right)^{\beta_1 - 1} \left(3\pi\sqrt{\frac{a}{\mu}}\right) \exp\left(-\frac{a^3}{a_{\mathrm{knee}}^3}\right) & R > 3.4R_\oplus \\ 0 & \text{else} \end{cases} . \tag{2.19}$$

We can independently sample the planetary radius distribution and subsequently sample the probability density function of semi-major axis conditional on the sampled R.

We demonstrate the similitude and differences between our EXOSIMS implementation of the SAG 13 model from Belikov et al. [8] in Figure 2.1. In Figure 2.1 (a), we directly replicate linear exoplanet occurrence rate model around G spectral type stars from Belikov et al. [8] included in Eq. 2.11. The purple numbers represent $100\times$ the double integral over their respective bin areas. The largest absolute difference of these numbers from those in Belikov et al. [8] is 0.74 in the range of $2.2 \leq R < 3.4$ and $320 \leq P < 640$. The largest percent difference of these numbers is 13.8% in the range of $11 \leq R < 17$ and $20 \leq P < 40$. We transformed these into percentages which sum to 100% over the whole grid. The occurrence rates and percentages of Figure 2.1 (b) are calculated by integrating over the transformation of the SAG13 grid to a space with Eq. 2.14. The integrated values in each bin are identical to their counterpart in Figure 2.1 (a). Finally, Figure 2.1 (c) is the probability density function used in EXOSIMS with the "knee" included. The coloring difference between (c) and (a) or (b) is because (c) is a per bin area density and the bin areas of the top right bin is several orders of magnitude larger than the bottom left bin in both (a) and (b).

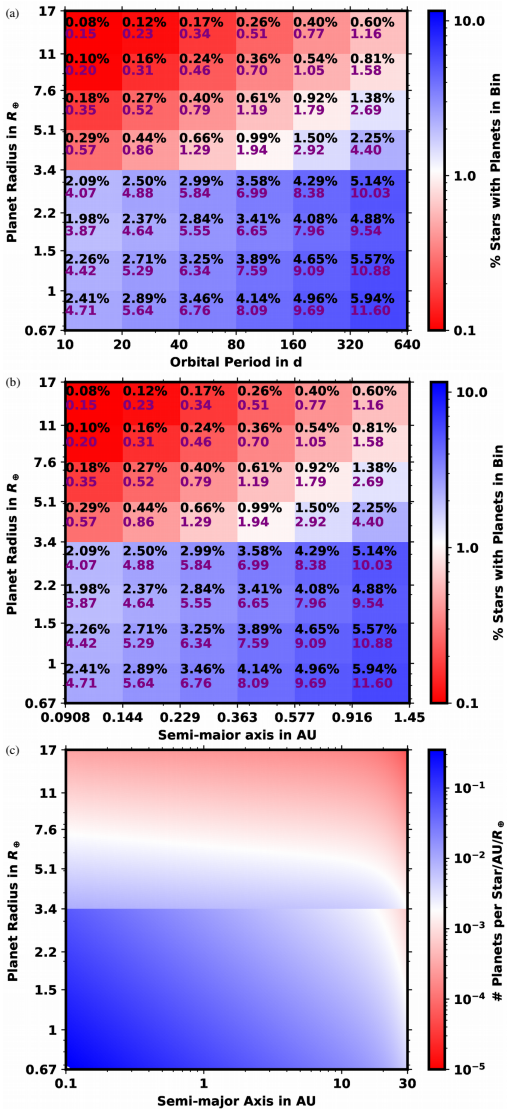

Figure 2.1: We replicate the SAG13 exoplanet R vs T occurrence rate distribution from Belikov et al. [8] in (a) showing per-bin occurrence rates (purple) and percentage rates (black). We reformulated as R vs a in (b). We show the joint probability distribution of R and a from Eq. 2.17 implemented in EXOSIMS in (c) which is extrapolated beyond the range of (a) and includes the semi-major axis "knee". The apparent difference in color gradient between (a) or (b) and (c) is due to the logarithmic scale of (c); the top right bins are orders of magnitude larger in area than the bottom left bins.

2.3 The Solar System

2.3.1 Planet Properties

Table 2.2: Tabulated volumetric mean radius (R), semi-major axis (a), geometric albedo (p), eccentricity (e), and inclination (i) of Solar System planets.

Planet Name	R (km) [5]	$a \times 10^{-9}$ (m) [89]	p [89]	e [90]	i (°) [89]
Mercury (☿)	2439.7	57.91	0.142	0.20563069	7.00487
Venus (♀)	6051.8	108.21	0.689	0.00677323	3.39471
Earth (⊕)	6371.0	149.6	0.434	0.01671022	0
Mars (♂)	3389.92	227.92	0.150	0.09341233	1.85061
Jupiter (♃)	69911	778.57	0.538	0.04839266	1.30530
Saturn (♄)	58232	1433.53	0.499	0.05415060	2.48446
Uranus (♅)	25362	2872.46	0.488	0.04716771	0.76986
Neptune (♆)	24622	4495	0.442	0.00858587	1.76917

For this analysis, we make several simplifying assumptions about the Solar System planets. First, we assume the planets are spherical, allowing us to use their volumetric mean radius (R). Second, we assume the combination of the geometric albedo (p) and phase function to be sufficient to describe the fraction of incident light reflected. We use the high order polynomial model fit planetary phase functions from Mallama and Hilton [61] to account for the unique reflective properties of each body. Third, we assume the planets have circular orbits. As we can see from Table 2.2, with the exception of Mercury, the eccentricities (e) are small ($\lesssim 0.05$). An eccentricity of 0.05 would change apoastron and periastron by $\sim 5\%$ thus maximally changing the net planetary flux by $\sim 10\%$. Assuming circular orbits allows substantial simplification of the s and Δmag functions. Fourth, we assume all planets lie in a common system angular momentum plane. Table 2.2 contains the inclinations of Solar System planets from the ecliptic, each varying by a few degrees. This would affect some (s,Δmag)-

coincidences, particularly between interior and exterior planets. We include a summary of the planet parameters used in this work in Table 2.2.

2.3.2 Solar System Planet Phase Function Equations

The high order, parametric, polynomial fit phase functions from Mallama and Hilton [61] cover a large portion of the phase angle space for most planets. Where the polynomial fit would be extrapolated beyond measured data and is therefore unreliable, we substitute in the Lambert phase function from Eqn. 4 of Brown [13] first presented in Sobolev [91]. To make these parametric phase functions usable in a continuous optimization method, we "meld" the phase functions together using parameterized hyperbolic tangent functions. The smallest phase angle where melding between the planet's phase function and the Lambert phase function occurs is 130°, for Jupiter. The phase functions of inner Solar System planets span nearly the entire range of phase angles. The limits of the model fit planet phase functions are included in 2.3.

We selected the hyperbolic tangent function to join parametric phase function components together because it allows us to create a melded phase function with smooth transitions and is differentiable over the entire range. The $\tanh$ is a curve ranging from $-\infty < x < \infty$ where $\lim_{x\to\infty} \tanh(x) = 1$, $\lim_{x\to-\infty} \tanh(x) = -1$, and $\tanh(x = 0) = 0$. We convert this into two separate equations used to transition between the "start" and "end" of a individual parametric model. The first is modified to ensure $\lim_{x\to-\infty} f(x) = 0$ and $\lim_{x\to\infty} f(x) = 1$; used to "start" a model. The second is modified to ensure $\lim_{x\to-\infty} f(x) = 1$ and $\lim_{x\to\infty} f(x) = 0$; used to "end" a model. We also add

two constants unique to each planet in order shift the model transition mid-point with A and adjust the transition slope with B to get

$$f_{\text{start}}(x, A, B) = 0.5 + 0.5 \tanh\left(\frac{x - A}{B}\right) \tag{2.20}$$

$$f_{\text{end}}(x, A, B) = 0.5 - 0.5 \tanh\left(\frac{x - A}{B}\right). \tag{2.21}$$

The melding of phase functions introduces small, negligible errors at $\beta = 0°$ and $\beta = 180°$. The melded phase functions are shown in Figure 2.2 along with the typically used Lambert phase function.

Here, we combine the phase functions extracted from the model fit visual magnitude functions (V_{mag}) of each Solar System planet in Mallama and Hilton [61] using the parameterized hyperbolic tangent functions to meld parametric phase functions into a continuous phase function. In β ranges where a phase curve model for the planet is unavailable, we "fill in the gaps" by substituting in the Lambert phase function, Eqn. 4 from Brown [13].

In general, we have knowledge of the phase function over most of the β range for Earth and planets interior to Earth. The phase date we have for planets exterior to Earth are limited to the phase angles observable by Earth and the ranges imaged via various flybys. The regions generally requiring melding with the Lambert phase function to span the β range are in excess of $130°$ and are where the planet is dimmest and least detectable.

Mercury

Mercury's phase function is given by

$$-2.5 \log_{10}\left(\Phi_{\mathbin{\mathrlap{\mathsf{Q}}\mathsf{\Psi}}}(\beta)\right) = 6.3280 \times 10^{-2}\beta - 1.6336 \times 10^{-3}\beta^2 + 3.3644 \times 10^{-5}\beta^3 - 3.4265 \times 10^{-7}\beta^4 + 1.6893 \times 10^{-9}\beta^5 - 3.0334 \times 10^{-12}\beta^6. \tag{2.22}$$

It spans the entire β range and does not require melding.

Venus

Venus's phase function is separated over two regions. The first,

$$\Phi_{\text{int},\venus,1}(\beta) = 10^{-0.4(-1.044\times10^{-3}\beta+3.687\times10^{-4}\beta^2-2.814\times10^{-6}\beta^3+8.938\times10^{-9}\beta^4)}, \tag{2.23}$$

is defined from $0^\circ \leq \beta \leq 163.7^\circ$. The second,

$$\Phi_{\text{int},\venus,2}(\beta) = 10^{-0.4(-2.81914\beta+8.39034\times10^{-3}\beta^2))}, \tag{2.24}$$

is defined over the region $163.7^\circ \leq \beta \leq 179^\circ$. The parametric phase functions have minor discontinuities which we account for by adding a constant to and scaling the second parametric phase function into

$$\begin{aligned}\Phi_{\text{int},\venus,3}(\beta) = \\ \Phi_{\text{int},\venus,1}(163.7^\circ)\Bigg(1 + \frac{\Phi_{\text{int},\venus,2}(\beta)\Phi_{\text{int},\venus,1}(163.7^\circ)}{\Phi_{\text{int},\venus,2}(163.7^\circ) - \Phi_{\text{int},\venus,2}(179^\circ)} - \\ \frac{\Phi_{\text{int},\venus,2}(163.7^\circ)\Phi_{\text{int},\venus,2}(163.7^\circ)}{\Phi_{\text{int},\venus,2}(163.7^\circ) - \Phi_{\text{int},\venus,2}(179^\circ)}\Bigg).\end{aligned} \tag{2.25}$$

Finally, we meld $\Phi_{\text{int},\venus,1}(\beta)$ and $\Phi_{\text{int},\venus,3}(\beta)$ together using the hyperbolic tangents to arrive at Venus's melded phase function

$$\begin{aligned}\Phi_{\venus}(\beta) =& f_{\text{end}}(\beta, A = 163.7^\circ, B = 5^\circ)\Phi_{\text{int},\venus,1}(\beta) \\ &+ f_{\text{start}}(\beta, A = 163.7^\circ, B = 5^\circ) f_{\text{end}}(\beta, A = 179^\circ, B = 0.5^\circ)\Phi_{\text{int},\venus,3}(\beta) \\ &+ f_{\text{start}}(\beta, A = 179^\circ, B = 0.5^\circ)\Phi_L(\beta) + 2.766 \times 10^{-4}.\end{aligned} \tag{2.26}$$

Earth

The phase function for Earth spans the range of β and is

$$\Phi_{\oplus}(\beta) = 10^{-0.4(-1.060\times10^{-3}\beta+2.054\times10^{-4}\beta^2)}. \tag{2.27}$$

Mars

Mars's phase function is separated over two regions. The first,

$$\Phi_{\text{int},\mathord{\male},1}(\beta) = 10^{(-0.4(0.02267\beta - 0.0001302\beta^2))}, \tag{2.28}$$

is valid from $0° \leq \beta \leq 50°$. The second,

$$\Phi_{\text{int},\mathord{\male},2}(\beta) = 10^{(-0.4(-0.02573\beta + 0.0003445\beta^2))}, \tag{2.29}$$

is valid over $50° < \beta \leq 180°$. We need to normalize $\Phi_{\text{int},\mathord{\male},2}(\beta)$ to account for discontinuities between the two phase functions and arrive at the corrected second phase function of

$$\Phi_{\text{int},\mathord{\male},3}(\beta) = \Phi_{\text{int},\mathord{\male},1}(50°)/\Phi_{\text{int},\mathord{\male},2}(50°)\Phi_{\text{int},\mathord{\male},2}(\beta). \tag{2.30}$$

Combining these two phase functions, we get Mars's melded phase function

$$\begin{aligned}\Phi_{\mathord{\male}}(\beta) =& f_{\text{end}}(\beta, A = 50°, B = 5°)\Phi_{\text{int},\mathord{\male},1}(\beta) \\ &+ f_{\text{start}}(\beta, A = 50°, B = 5°)\Phi_{\text{int},\mathord{\male},3}(\beta)\end{aligned} \tag{2.31}$$

In the original formulation from Mallama and Hilton [61], both parametric V_{mag} functions of Mars vary depending upon the rotational and orbital longitude of the planet. We assume the average of these correction terms which are both 0.

Jupiter

The phase function for Jupiter is defined over two separate regions. The first is

$$\Phi_{\text{int},\mathord{\jupiter},1}(\beta) = 10^{(-0.4(-3.7\times10^{-4}\beta + 6.16\times10^{-4}\beta^2))}. \tag{2.32}$$

The second is

$$\begin{aligned}\Phi_{\text{int},\mathord{\jupiter},2}(\beta) = 1 - 1.507(\beta/180°) - 0.363(\beta/180°)^2 - 0.062(\beta/180°)^3 \\ + 2.809(\beta/180°)^4 - 1.876(\beta/180°)^5.\end{aligned} \tag{2.33}$$

We offset $\Phi_{\text{int},♃,2}(\beta)$ accounting for the the last valid value of $\Phi_{\text{int},♃,1}(\beta)$ to arrive at the modified second phase function of

$$\Phi_{\text{int},♃,3}(\beta) = \Phi_{\text{int},♃,1}(12^\circ) - \Phi_{\text{int},♃,2}(12^\circ) + \Phi_{\text{int},♃,2}(\beta). \tag{2.34}$$

We then combine the phase functions for Jupiter to get

$$\begin{aligned}\Phi_{♃}(\beta) =& f_{\text{end}}(\beta, A = 12^\circ, B = 5^\circ)\Phi_{\text{int},♃,1}(\beta) \\ &+ f_{\text{start}}(\beta, A = 12^\circ, B = 5^\circ) f_{\text{end}}(\beta, A = 130^\circ, B = 5^\circ)\Phi_{\text{int},♃,3}(\beta) \\ &+ f_{\text{start}}(\beta, A = 130^\circ, B = 5^\circ)\Phi_L(\beta).\end{aligned} \tag{2.35}$$

Saturn

The phase function for Saturn is complicated by measurements of the planet obfuscated and augmented by the rings which have a unique phase function from the planet. The phase function of Saturn without the rings is defined over two separate regions. The first,

$$\Phi_{\text{int},♄,1}(\beta) = 10^{(-0.4(-3.7\times10^{-4}\beta+6.16\times10^{-4}\beta^2))}, \tag{2.36}$$

is based on Earth observations valid from $0^\circ \leq \beta \leq 6.5^\circ$. The second,

$$\Phi_{\text{int},♄,2}(\beta) = 10^{(-0.4(2.446\times10^{-4}\beta+2.672\times10^{-4}\beta^2-1.505\times10^{-6}\beta^3+4.767\times10^{-9}\beta^4))} \tag{2.37}$$

is defined over the range $6^\circ \leq \beta \leq 150^\circ$. By properly adjusting the discontinuity between the first and second phase function, we arrive at

$$\Phi_{\text{int},♄,3}(\beta) = \Phi_{\text{int},♄,1}(6.5^\circ) - \Phi_{\text{int},♄,2}(6.5^\circ) + \Phi_{\text{int},♄,2}(\beta). \tag{2.38}$$

We combine the phase functions for Saturn to get

$$\begin{aligned}\Phi_{♄}(\beta) =& f_{\text{end}}(\beta, A = 6.5^\circ, B = 5^\circ)\Phi_{\text{int},♄,1}(\beta) \\ &+ f_{\text{start}}(\beta, A = 6.5^\circ, B = 5^\circ) f_{\text{end}}(\beta, A = 150^\circ, B = 5^\circ)\Phi_{\text{int},♄,3}(\beta) \\ &+ f_{\text{start}}(\beta, A = 150^\circ, B = 5^\circ)\Phi_L(\beta)\end{aligned} \tag{2.39}$$

Uranus

Uranus has a unique phase function due to the inclination of the pole's rotational axis, but only has one phase function. We assume a sub-solar latitude of -82° which makes Uranus as bright as possible by adding a 0.0689 correction to the phase function (the minimum correction occurs at 82° and adds -0.0689). The phase function for Uranus is

$$\Phi_{\text{int},\sphericalangle\bigcirc}(\beta) = 10^{(-0.4(0.0689+6.587e-3\beta+1.045e-4\beta^2))}, \tag{2.40}$$

valid over the range $0^\circ \leq \beta \leq 154^\circ$. The combined phase function model for Uranus is

$$\begin{aligned}\Phi_{\sphericalangle\bigcirc}(\beta) =& f_{\text{end}}(\beta, A = 154^\circ, B = 5^\circ)\Phi_{\text{ind},\sphericalangle\bigcirc}(\beta) \\ &+ f_{\text{start}}(\beta, A = 154^\circ, B = 5^\circ)\Phi_L(\beta)\end{aligned} \tag{2.41}$$

Neptune

Neptune has two phase functions, one based on Earth measurements which cover such a small range of phase angles that we ignore it and use the phase curve from Voyager 2 radiometer measurements. Neptune's one phase functions is

$$\Phi_{\text{int},\Psi\bigcirc}(\beta) = 10^{-0.4(7.944\times10^{-3}\beta+9.617\times10^{-5}\beta^2)}, \tag{2.42}$$

and is valid over the range $0^\circ \leq \beta \leq 133.14^\circ$. The combined phase function for Neptune is therefore

$$\begin{aligned}\Phi_{\Psi\bigcirc}(\beta) =& f_{\text{end}}(\beta, A = 133.14^\circ, B = 5^\circ)\Phi_{\text{int},\Psi\bigcirc}(\beta) \\ &+ f_{\text{start}}(\beta, A = 133.14^\circ, B = 5^\circ)\Phi_L(\beta).\end{aligned} \tag{2.43}$$

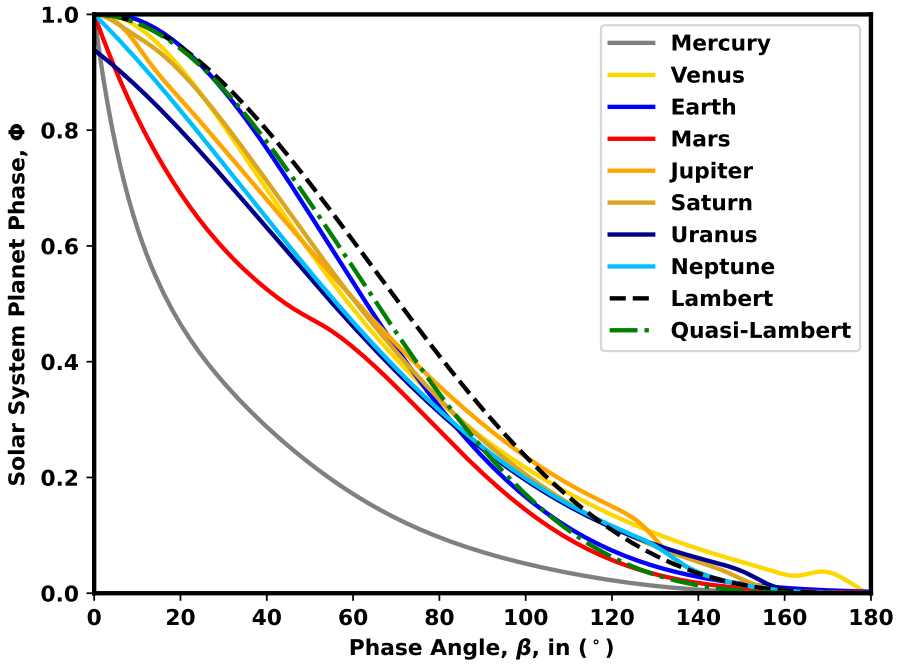

Figure 2.2: Melded Solar System planet phase functions.

2.3.3 Jupiter and Saturn Melded Phase Functions Compared to Published Data

The phase functions in [61] that we based our "melded" phase functions off of was called into question at some point because they are model fits of the planet's phase curves in the visible spectrum of the planet. We took planet albedo data vs wavelength and phase angle directly from [57] and [21] which we integrated over portions of the visible spectrum and plotted this data in Figure 2.3 and Figure 2.4. Our model fit phase functions are quite close to the data presented in these models. At maximum, a 5% difference occurs at $20°$. Furthermore,

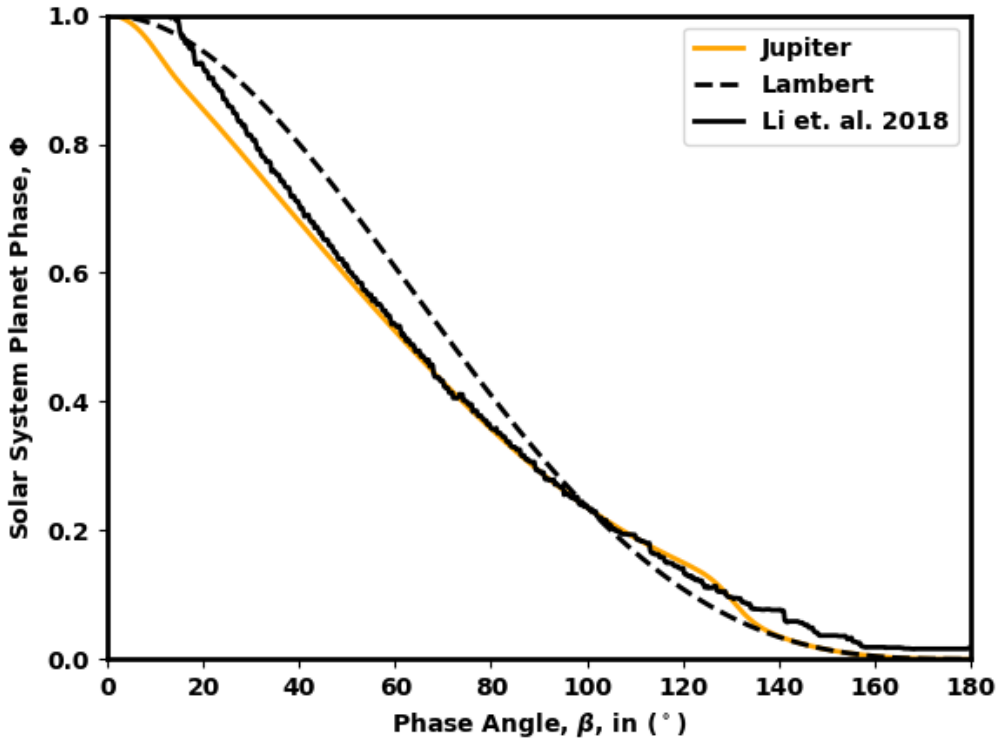

Figure 2.3: A direct comparison of the "melded" phase function for Jupiter with Jupiter's phase function in the visible spectrum based off various collections of flyby data accumulated in [57].

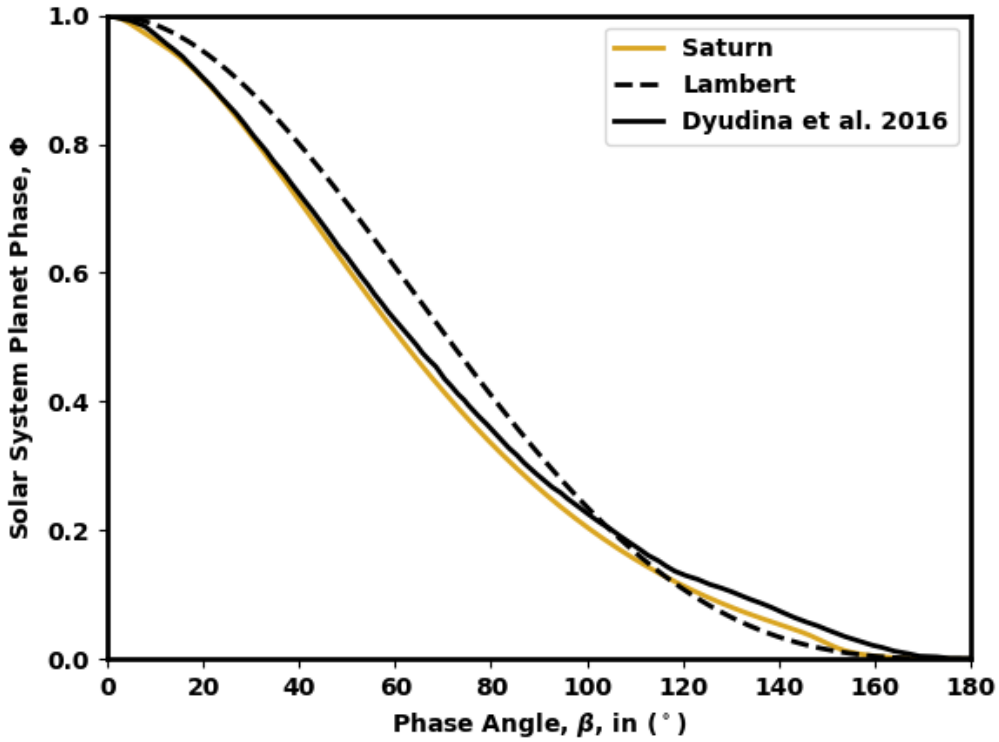

Figure 2.4: A direct comparison of the "melded" phase function for Saturn with Saturn's phase function in the visible spectrum based off Cassini flyby data accumulated in [21].

2.4 Guimond and Cowen 2019

The Guimond and Cowan [32] planet population isn't a *realistic* planet population. This planet population uses a uniform eccentricity distribution as well as a uniform natural log semi-major axis distribution. I include their full list of planetary parameters used in Table 2.3. I make use of this planet population to make a direct comparison between two detection orbit fitting with exodetbox and the MC method in Guimond and Cowan [32].

Table 2.3: Planet population parameters from Guimond and Cowan [32]

Name	Sym.	Prior distribution	Prior range	Input
Semi-major axis	a	Uniform in natural log	[0.01, 50] AU	[0.95, 1.70] AU
Eccentricity	e	Beta ($\sigma = 0.081$) or uniform	[0,1)	[0,1)
Inclination	i	Uniform in cosine	[0,π)	[0,$\pi/2$)
Argument of periapsis	ω_p	Uniform	[0,2π)	[0,2π)
Longitude of the ascending node	Ω	Uniform	[0,2π)	[0,2π)
Mean anomaly at first epoch	M_0	Uniform	[0,2π)	[0,2π)

2.5 Habitable, Earth-like, and Earth Twin Sub-populations

We are most interested in detecting exoplanets that lie within the *habitable zone*. This is traditionally defined as the region around a star where a rocky planet with a CO_2, H_2O, and N_2 atmosphere planet can *sustain* liquid water on the surface.[51, 41] However, the definition of habitability is scientifically fungible in definition rigor because we have only **1** datapoint of a certifiably habitable

Earth-like planet (the Earth we live on).

The vast variability in definition of the habitable zone stems from the wide variety of surface models, atmospheric models, and forms of heat transfer considered in each publication. The habitable zone can be further extended by considering planets with transient surface water. Planets with a highly eccentric orbit would experience larger extremes in planet temperature. Close in and eccentric planets with water vapor could condense into liquid water at or around apoapsis. Similarly, far away and eccentric planets with water ice could melt into liquid water at or around periapsis.

We use a definition of Earth-Like exoplanet similar to that used in Team [100] which is a conservative definition of the Habitable zone. The most conservative definition of habitable zone is the KOE region around a star where liquid water can persist on the planet's surface and there is a $CO_2/H_2O/N_2$ atmosphere.[41] We use a more conservative planetary radius range $0.9R_\oplus \leq R \leq 1.4R_\oplus$, consistent the standard definition and evaluation team final report.[65] We use the flux-at-planet range $0.3586 \leq L_{\text{plan}} \leq 1.1080$.[41]

When we classify a planet as Earth-like with some KOE, we use the time-averaged incident flux on the planet calculated by

$$L_{\text{plan}} = \frac{L_*}{(a + \frac{ae^2}{2})^2}. \tag{2.44}$$

This allows for more eccentric orbits to be considered Earth-like.

I would be remiss to overlook the ways in which we can simulate Earth-like exoplanets. While the definition of Earth-like is vague, it does not stop us from creating many different populations of Earth-like exoplanets. In Horning, Morgan, and Nielson [35], a specific Earth is used to find revisit heuristics because

this assumption simplifies the problem. There are more conservative definitions of habitable zone that are narrower and less conservative ones which are more generous. I would want to use the conservative definition to build confidence in capability, but the less conservative model to demonstrate potential performance. In others still, like Guimond and Cowan [32], a simple Earth-like planet population is presented for their particular study making assumptions in occurrence rate models that are convenient for them.

Earth Twin

In some cases, we specifically refer to the Earth Twin planet population. When we do this, we are talking about the "EarthTwinHabZone2" planet population in EXOSIMS with $R = R_\oplus$, $p = 0.367$, $0.7 \leq a \leq 1.5$, $0 \leq e \leq 0.9$, and $\eta_\oplus = 0.1$ with the semi-major axis and eccentricity sampled randomly from uniform distributions. While the eccentricity range here is wide, it is constrained to the semi-major axis range such that the only kind of $a = 1.5$ AU planet that can be simulated is one with $e = 0$. When generating this planet population, we first randomly sample semi-major axis and subsequently sample a constrained

2.6 General Exoplanet Sub-type Classifications

For the purposes of classifying exoplanets, we use two separate methods; one for classifying exoplanets generally and one for classifying Earth-like exoplanets. The first classification method introduced in Ref. [50] is recreated in Figure 2.5 overlaying the SAG13 R vs a joint probability density function. The blue lines are chemical equilibrium condensation lines for H_2O, CO_2, and CH_4 from left to right. The planetary radius generally dictates the types of species that

accumulate on the planet. For example, Mercury has too low of a mass to hold onto any atmosphere of substance due to the hydrodynamic[111] and thermal escape velocity of particles at the surface temperature of the planet [17]. Figure 1 of [111] shows the hydrodynamic and thermal escape velocity curves for various chemical species for a given planets escape velocity and insolation distance. In Figure 1 of [111], any planet above and to the left of a chemical species escape velocity curve cannot sustain an atmosphere of that particular composition. We remind the reader that the escape velocity of a particle from a planet is determined by the planet's mass and that mass will generally have a positive scaling with planetary radius. Both the host star's activity, planet mass, and atmospheric composition of the planet determine the particle escape velocity rate and ultimately, what the composition of the planet's atmosphere is. Figure 5.4 of [17] shows the escape speed of particles at various planet surface temperatures. The closer the planet is to the host star, the higher the surface temperature will be and the faster particles will be moving.

The bounding limits on Figure 2.5 are based on where planets generally do not have sufficient gravity to hold onto any atmosphere, $R < 0.5R_{\oplus}$, and where planets begin producing their own internal heat (Brown Dwarfs), $R > 14.3R_{\oplus}$.

When we generate a population of planets, we can classify each planet in that population as a particular sub-type from Kopparapu et al. [50] and create a series of JPDFs ($f_{ij}(s, \Delta\mathrm{mag})$) for each classification scheme. These such JPDFs are shown in Figure 2.5. We can calculate the probability an exoplanet detected

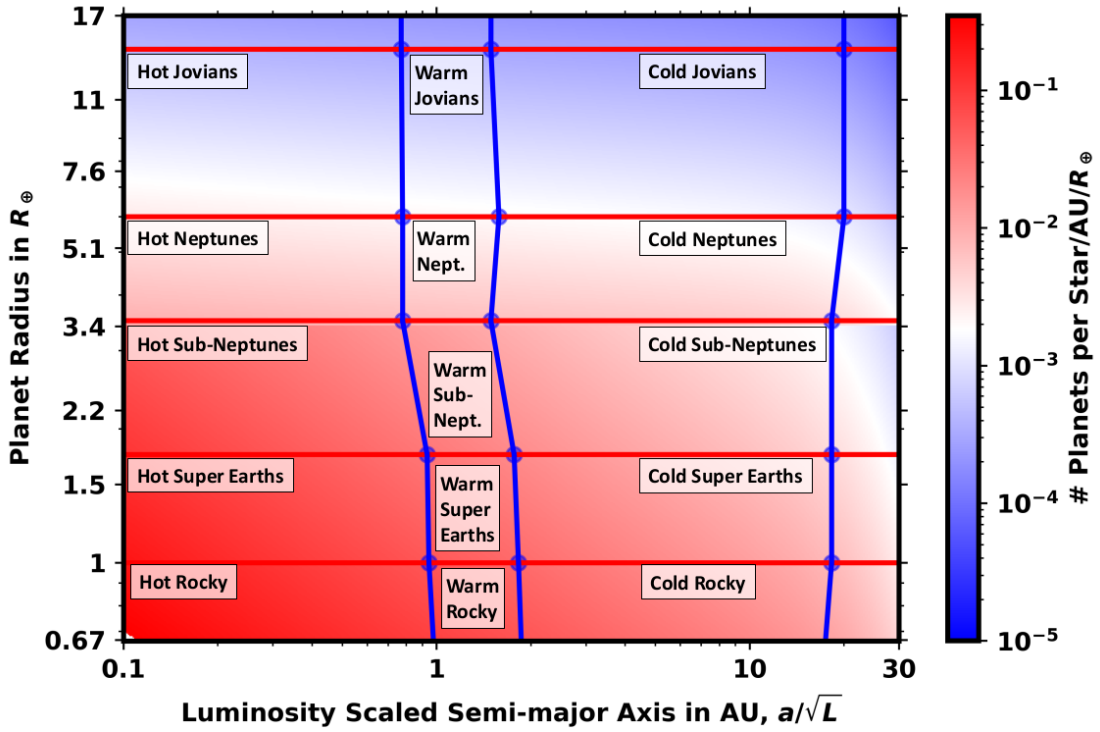

Figure 2.5: The SAG13 planet population R vs a joint distribution with the Kopparapu classification grid overlayed.

at (s,Δmag) is of type ij using

$$P(ij, s, \Delta\text{mag}, \sigma_s, \sigma_{\Delta\text{mag}}, n) = \int_{\Delta\text{mag}-n\sigma_{\Delta\text{mag}}}^{\Delta\text{mag}+n\sigma_{\Delta\text{mag}}} \int_{s-n\sigma_s}^{s+n\sigma_s} f_{meas}(s, \Delta\text{mag}) f_{ij}(s, \Delta\text{mag}) \delta s \delta \Delta\text{mag}, \quad (2.45)$$

where we assume independence between the photometric and astrometric measurement to get

$$f_{meas}(s, \Delta\text{mag}) = f_s(s) f_{\Delta\text{mag}}(\Delta\text{mag}) = \frac{\exp -\frac{1}{2}\left(\frac{s-\mu_s}{\sigma_s}\right)^2}{\sigma_s\sqrt{2\pi}} \frac{\exp -\frac{1}{2}\left(\frac{\Delta\text{mag}-\mu_{\Delta\text{mag}}}{\sigma_{\Delta\text{mag}}}\right)^2}{\sigma_{\Delta\text{mag}}\sqrt{2\pi}}. \quad (2.46)$$

We extend this further by normalizing the classification probability to get

$$P_n(ij, s, \Delta\text{mag}, \sigma_s, \sigma_{\Delta\text{mag}}, n) = \frac{P(ij, s, \Delta\text{mag}, \sigma_s, \sigma_{\Delta\text{mag}}, n)}{\frac{N_{ij}}{N_{tot}}}. \quad (2.47)$$

N_{tot} is the total number of planets simulated in the MC and N_{ij} are the total number of planets in the particular sub-type bin.

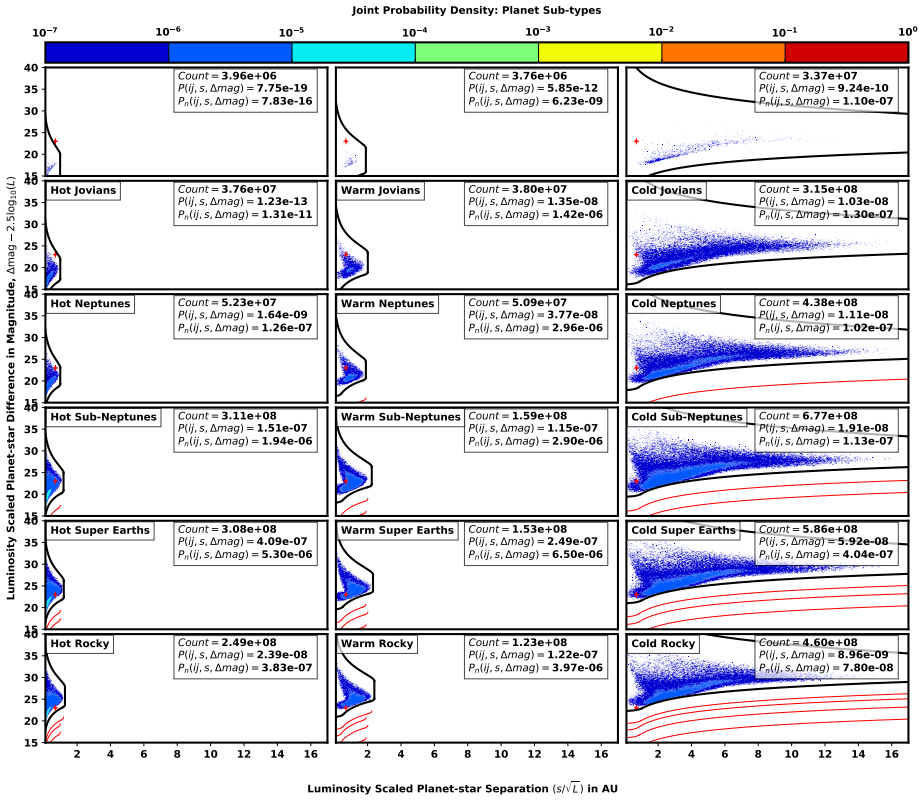

Figure 2.6: The SAG13 planet population dissected into planet sub-types according to the Kopparapu classification scheme. Black lines are analytical limits from Garrett and Savransky [27]. Red lines are analytical limits of the other populations in the same column. Red cross is the location and the 1σ uncertainty of an Earth-like exoplanet detected with (s=0.7 AU,Δmag=23) and a detection with $\sigma_{\Delta\text{mag}} = 0.023$ and $\sigma_s = 5$ mas at 10 pc. $P(ij, s, \Delta\text{mag}, \sigma_s, \sigma_{\Delta\text{mag}}, n)$ and $P_n(ij, s, \Delta\text{mag}, \sigma_s, \sigma_{\Delta\text{mag}}, n)$ shown for the detection in each bin.

For the Earth Analog with (s=0.7 AU,Δmag=23) and a detection with $\sigma_{\Delta\text{mag}} = 0.023$ and $\sigma_s = 5$ mas at 10 pc, we see the largest P_n ij classification bin is first the Warm Super Earths followed by the Hot Super Earths, Warm Neptunes, Warm Sub-Neptunes, and Hot Sub-Neptunes. **This classification correctly identifies the detected planet having the highest probability of coming from the planet population is actually belongs to.**

An additional method of orbit fitting can be to use the exodetbox methods presented in chapter 5 to the narrow 1σ detection box and find the fraction of planets of all planets detected that are of a particular type.

2.7 Conclusion

In this chapter I included a collection of planet populations and two methods for probabilistically classifying the detected exoplanet sub-type. These planet populations can be used on any of the generalized methods in this dissertation and are discussed here so they do not provide a lengthy detraction from the methods or results found in those chapters.

The important result from this chapter is that the detected planet classification method I presented correctly identifies the detected planet having the highest probability of coming from the planet population is actually belongs to.

CHAPTER 3

OPTIMAL SCHEDULING OF EXOPLANET DIRECT IMAGING SINGLE-VISIT OBSERVATIONS OF A BLIND SEARCH SURVEY

The overall Earth-like exoplanet yield (both orbit characterization and spectral characterization) of a direct imaging mission should theoretically be proportional to the blind-search single-visit yield; calculable using only probabilistic methods like completeness. This approach is appropriate when we magically guess the exact amount of time used on single-visit blind search, orbit characterization images, and the spectral characterization. According to the SDET[65], "we should treat completeness-based yields as somewhat optimistic". However, the SDET goes on to use AYO based yields to represent the yields of nearly every telescope design in the SDET, briefly stating that average yields of a Monte Carlo of mission simulations is a pessimistic yield limited by mission scheduling algorithms. In this work, we demonstrate that the EXOSIMS Monte Carlo of simulations yield in a single-visit blind search is close to the probabilistic yield in an optimally executed mission and how to execute that mission.

In this chapter we present an algorithm, effective over a broad range of planet populations and instruments, for optimizing integration times of an exoplanet direct imaging observation schedule, to maximize the number of unique exoplanet detections under realistic mission constraints. Our planning process uses "completeness" as a reward metric and the non-linear combination of optimal integration time per target and constant overhead time per target as a cost metric constrained by a total mission time. We validate our planned target list and integration times for a specific telescope by running a Monte Carlo of full mission simulations using EXOSIMS, a code base for simulating telescope

survey missions. These simulations encapsulate dynamic details such as time-varying local zodiacal light for each star, planet keep-out regions, exoplanet positions, and strict enforcement of observatory use over time. We test our methods on the Nancy Grace Roman Space Telescope (Roman) Coronagraphic Instrument (CGI). We find that planet, sun, and solar panel keep-out regions limit some target per-annum visibility to less than 28%, and that the mean local zodiacal light flux for optimally scheduled observations is 22.79 mag arcsec^{-2}. Both these values are more pessimistic than previous approximations and impact the simulated mission yield. We find that the Roman CGI detects 5.48 ± 0.17 and 16.26 ± 0.51 exoplanets, on average, when observing two different planet populations based on Kepler Q1-Q6 data, and the full Kepler data release, respectively. Optimizing our planned observations using completeness derived from the more pessimistic planet population (in terms of overall planet occurrence rates) results in a more robust yield than optimization based on the more optimistic planet population. We also find optimization based on the more pessimistic population results in more small planet detections than optimization with the more optimistic population.

3.1 Introduction

The 2010 astronomy and astrophysics decadal survey highly prioritized exoplanet bulk population statistics and inventorying planets around nearby stars (within 30 pc)[68]. The Roman space telescope (Roman)[88], prioritized by the 2010 decadal survey, will include a coronagraphic instrument (CGI) capable of directly imaging and detecting new exoplanets unobservable by modern radial velocity or transit techniques. The expected performance of CGI in blind

search surveys can be estimated through probabilistic methods using completeness.[13, 96] An alternative method is to execute a Monte Carlo of full survey simulations on simulated universes. This process creates an ensemble of design reference missions (DRMs) containing a list of target stars observed, the integration time used for each star, when the simulated observations occurred, and the simulated outcome of each observation. Such a collection of DRMs, produced by our method, effectually certifies the ability of the instrument to make the expected number of detection observations claimed in a probabilistic evaluation like completeness. It is important to note that both methods are still equally limited in their overall prediction accuracy by the assumptions made about the true population of exoplanets to be discovered.

Detailed DRMs enable requirement definition and design iteration optimization for future telescopes including the large-scale mission concepts under development by science and technology definition teams for NASA's 2020 decadal survey. Both the Habitable Exoplanet Observatory (HabEx)[100] and the Large UV-Optical-Infrared Surveyor (LUVOIR)[31] mission concepts contain a significant exoplanet direct imaging component with HabEx reserving 1.95 years for coronagraph science operations and LUVOIR reserving 50% of the total mission time for exoplanet science. While target revisits and spectral characterizations could represent a substantial portion of the executed mission, we purposefully omit optimization with revisits or characterizations due to the complexity of that problem. We do include the rare spectral characterization in our Roman mission simulations. In our optimization process, we focus solely on delivering an estimate of the maximum possible number of uniquely detected exoplanets under realistic mission constraints by evaluating the number of detections made through single-visit observations of stars, henceforth referred to as yield.

We leave the inclusion of revisits, orbit characterizations, and spectral characterizations in full survey optimization for future work.

Brown[13] introduced single-visit completeness to estimate the number of extrasolar planets potentially discoverable with the Terrestrial Planet Finder (TPF-C), an earlier direct imaging mission concept. Single-visit completeness, hereafter referred to as completeness, is the probability of detecting a planet, drawn from a particular population, using a particular instrument, should one exist about a given target star[13, 27, 96]. When completeness is evaluated for each star in a full target list, summed, and scaled by the expected number of planets from that population per star (η), we arrive at the expected number of planets to be detected from that population by that mission[30]. While this technique can be used to quickly evaluate a mission's performance, it abrogates temporal constraints and uncertainties such as target visibility, variable overhead times, changing local zodiacal light intensity, and unscheduled characterizations of newly detected planets. Solely using completeness to evaluate a mission can therefore only provide an upper bound for expected performance.

Completeness has previously been used as a reward metric for multiple observation integration time optimizations. Brown demonstrated a method for finding the group $\Delta\mathrm{mag}$ (difference in brightness between the planet and star in magnitudes), and number of target trade-off point by optimizing a target list subset $\Delta\mathrm{mag}$ against the number of targets in that subset assuming different fixed mission times[13]. While this method approximates the reward gradient for achieving a specific group $\Delta\mathrm{mag}$, it overlooks the gain made by customizing $\Delta\mathrm{mag}_i$ for each individual star, i. Hunyadi et al.[37], advanced Brown's work by maximizing summed completeness over all targets assuming a fixed mission

time and using integration times as the decision variables. In this new approach, star integration times are optimized to equivalent slopes beyond the completeness vs log integration time inflection point and the highest completeness per integration time of these targets is then selected. To practically achieve this, the authors of that study discretized integration times into 1 hour increments and calculated completeness values for each integration time. Their final target list contained the set of highest completeness per integration time targets. Hunyadi et al. specifically investigated Earth-analogue planets in the habitable zone (as also done in Brown[13]), but also explored Jupiter and Saturn-analogues. Alternatively, a limiting search observation, as defined by Brown [14], would observe a target for the fixed exposure time sufficient to achieve the system's limiting planet-star magnitude, $\Delta\mathrm{mag}_{\mathrm{lim}}$, for each target. The creation of the final observation schedule in Brown[14] involved selecting the subset of targets with precalculated integration times and overhead time per observation that fit within the total observing time. While Brown implemented target revisits, which can improve yield, the use of precalculated $\Delta\mathrm{mag}_{\mathrm{lim}}$ makes the resulting target list sub-optimal. While optimization of integration times and inclusion of revisits mark improvements in yield and target list planning realism, the omission of overhead times and discretization of integration times limits the ability to practically implement the desired observations within a finite span of time and under dynamic mission constraints.

A refinement of Brown and Hunyadi's work—altruistic yield optimization (AYO)[96]— uses completeness vs integration time as a figure of merit as in Brown and Soummer [14] to incrementally sacrifice stars from a target list and re-allocate the integration time, t_i, from star i to the largest $\mathrm{d}c_j(t_j)/\mathrm{d}t_j$ star j in increments of $\mathrm{d}t$. At its core, this represents a form of "greedy optimiza-

tion" which incrementally converges each observation to a constant slope similar to that described in Hunyadi[37]. This method does not allow for the reintroduction of targets stars to the target list, a necessity of a dynamically evolving mission schedule. Finally, the original AYO method does not fully account for overhead times in the calculation of integration times but rather states that the addition of time can occur after the fact and the use of a finite $\mathrm{d}t$ parameter results in a loss of potential completeness.

None of these yield optimization processes use optimization with continuous integration times or test the ability to schedule observations via full mission simulations accounting mission elasped time (MET). Brown stressed that Monte Carlo simulations of the mission as a whole should be used to produce confidence in the proposed mission's integrity[13]. Brown's work seeded the founding pillars of our well book-kept full mission survey simulator to include:

1. tracking individual exoplanets around target stars vs MET
2. tracking spacecraft position vs MET
3. accounting for solar system body locations and keep-out regions vs MET
4. accounting for variations in local zodiacal light vs MET
5. potential restriction of telescope observations to prescribed observing blocks and time-sharing with other observatory instruments vs MET

The EXOSIMS[83] code base was specifically developed to book-keep these parameters across MET. In EXOSIMS and this paper, we account for the locations of individual exoplanets around target stars vs MET, the tracking of our observatory on a nominal L2 Halo orbit[23] vs MET, solar system body locations vs MET from ephemeridies, keep-out occlusion of target stars vs MET, changes in

local zodiacal light intensity vs MET, and possesses the capability to account for cordoned off observing blocks reserved for other instruments at varying MET, and portion of mission life reserved for observatory science.

This paper describes our process for producing a set of planned observations maximizing unique exoplanet detection yield and subsequently validating this prediction under realistic mission conditions. The observation planning process incorporates a combination of filters applied to a planet population and star catalog, described in Section 3.2.1 and Section 3.2.2, completeness calculations detailed in Section 3.2.3, and our optimization algorithms with Binary-Integer Programming (BIP)[58] and Sequential Least Squares Quadratic Programming (SLSQP)[11], discussed in Section 3.2.4. Our validation process is outlined in Section 3.2.5 where we discuss the framework of EXOSIMS[83, 84, 85, 45] survey simulation as well as incorporation of time-varying keep-out regions (Section 3.2.5), time-varying local zodiacal light noise (Section 3.2.5), and the convergence of our Monte Carlo simulation (Section 3.2.5). We then show practical application on Roman in Section 3.3 where we discuss attributes of the observing plan, and a comparison of planet populations input vs instrument capabilities vs detected planet population.

3.2 Methods

3.2.1 Planet Population Joint Density Functions

To calculate completeness for each target for a specific instrument, we first generate a joint probability density function of $\Delta\mathrm{mag}$ and planet-star separation

projected onto the image plane, s, using Monte Carlo as in Brown [13] for an assumed planet population. We use the two planet populations in section 2.2 and section 2.1 for this work; one is derived from Kepler's detections from Q1-Q6 data[25] (Kepler Like)[81] and another derived from NASA's Exoplanet Program Analysis Group (ExoPAG) Study Analysis Group 13 (SAG13)[50, 28]. The Kepler Like and SAG13 populations both share the same eccentricity and albedo distributions, but differ in their occurrence rates, semi-major axis, and planetary radii distributions. The final output necessary for calculating completeness is the joint probability distribution of $\Delta\mathrm{mag}$ and s which is found by sampling the respective planet population and fitting a rectilinear bivariate spline. We use the same sampling methods and distributions for both calculating the joint probability distributions, and generating planets in our simulated universes.

Joint Probability Density Function

The final remaining parameters needed to describe planets at the time of an observation are the physical location of the planets relative to their host stars ($\underline{r}_{k/i}$) which is defined by Eq. (1) in Savransky, Cady, and Kasdin [82]. We assume that the direction of the orbit eccentricity vector is uniformly distributed in space, so that the orbit inclination is sinusoidally distributed between 0 and π, while the remaining Keplerian Elements (longitude of the ascending node, argument of periapsis, and mean anomaly) are all uniformly distributed from 0 to 2π[82].

We sample all of the parameters above for each planet which is sufficient information to calculate a projected planet-star separation (s_k) and difference in magnitude between the host star and the planet $(\Delta\mathrm{mag})$. We calculate the

projected planet-star separation as

$$s_k = \left| \underline{r}_{k/i} - \underline{r}_{k/i} \cdot \frac{\underline{r}_{i/SC}}{|\underline{r}_{i/SC}|} \right|. \tag{3.1}$$

We calculate $\Delta\mathrm{mag}_k$ using Eq. (4) from Garrett and Savransky [27] and adopt their use of a Lambert phase function.

Sampling all of the parameters described above for $N_p = 10^8$ planets allows us to calculate the joint probability density of projected separation and star-planet magnitude difference, $f_{\bar{s},\overline{\Delta\mathrm{mag}}}(s, \Delta\mathrm{mag})$. As in Eq. (7) in Garrett and Savransky [27] we assume independence between all parameters, except for semi-major axis and planet radius in the SAG13 population as well as the planet albedo dependence on planet radius. We bin these planets into a 1000 by 1000 grid and fit a rectilinear bivariate spline to the resulting 2D histogram. This rectilinear bivariate spline consists of integrable high order polynomials with total volume under the surface of 1. The resulting $f_{\bar{s},\overline{\Delta\mathrm{mag}}}(s, \Delta\mathrm{mag})$ densities for the two populations are shown in Figure 3.1.

3.2.2 Star Catalog

We need a list of target stars, along with their positions on the sky, distance (d_i), and apparent brightness in B and V bands for our calculations of completeness and integration time. We derive the list of targets stars from the EXOCAT-1 star catalog discussed in Turnbull [102], which contains a variety of targets out to a distance of approximately 30 pc. Some of these stars are missing photometric values including; the luminosity, absolute magnitude, V band bolometric correction, and the apparent VBHJK magnitudes, all of which we attempt to fill in

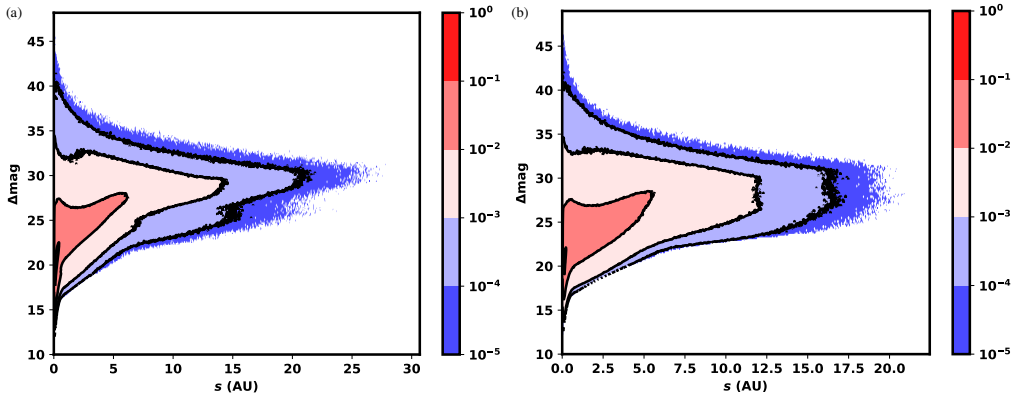

Figure 3.1: Joint probability density functions of projected separation and Δmag based on Kepler Like (a) and SAG13 (b) Planet Populations. The Kepler Like distribution produces larger orbital radii (and therefore projected separations) than SAG13 for the same a_{knee} values due to the use of the quadratic and cubic semi-major axis rollover functions (see Eq. 2.1 and 2.7).

by interpolating a table of standard stars by spectral type in Pecaut and Mamajek [73].

From the $N = 2396$ targets we have an initial set of target stars $\mathbf{I}$ which we pare down through a series of filters. There are many stars in the EXOCAT-1 star catalog with "not a number" data entries which can propagate through our equations so we remove targets with these kinds of data entries. Not all of these entries are absolutely necessary so some targets may have been unnecessarily filtered. Some of these star systems are binary systems which we do not account for in our equations so we omit them from $\mathbf{I}$. Additionally, some stars have low apparent visual magnitudes so we filter any target stars we know would take excessively long to achieve a reasonable $\Delta\mathrm{mag}$ on.

Missing Data Filter removes 429 targets with any fields containing a "Not a Number" value within the set of IPAC fields {hip_name, st_spttype, parx,

st_vmag, st_j2m, st_h2m, st_vmk, st_dist, st_bmv, st_mbol, st_lbol, coords, st_pmra, st_pmdec, wds_sep} as well as whenever we could not fill in a missing photometric value of a star

Binary Star Filter removes 164 targets using the Washington Double Star catalog (filters targets with companion stars within less than 10 arcseconds)[110]

Integration Time Cut-off Filter removes 1436 targets with integration times $t_i > 30\mathrm{d}$, where t_i is calculated assuming local zodiacal light to be $Z = 23.0$ mag arcsec^{-2}, exo-zodiacal light with magnitude $EZ = 22.0$ mag arcsec^{-2}, $\Delta\mathrm{mag}_0 = 22.5$ (used on the $t_i(\Delta\mathrm{mag})$ equations in Nemati [69] and Stark et al. [96]), and a working angle $WA_0 = 0.28$ arcsec. This WA results in reasonable Core Mean Intensity and Throughout combination based on inspection of the instrument parameter files in Figure A.1 (a) and (c).

After paring down **I** using a missing data filter, binary star filter, and integration time cut-off filter, **I** is reduced down to 651 targets (the filters are not mutually exclusive). Our initial filtering of target stars reduces the number of degrees of freedom in the optimization process and increases computation time. Larger telescopes will result in larger target lists with less candidate stars removed via the initial integration time filter. The statically optimized target list is included in Table B.1. This optimized target list contains mainly FGK type stars and 8 A type stars. All of these targets are located within 20 pc.

3.2.3 Calculating Completeness

Completeness is calculated for the i^{th} target by integrating over the joint probability density function of s and Δmag[84],

$$c_i = \int_0^{\Delta\text{mag}_i} \int_{s_{\min,i}}^{s_{\max,i}} f_{\overline{s},\overline{\Delta\text{mag}}}(s, \Delta\text{mag})\ \mathrm{d}s\,\mathrm{d}\Delta\text{mag}. \tag{3.2}$$

The limits on the inner integrand are strictly obscurational. For star i, at a distance d_i from the sun, the minimum planet-star separation observable is $s_{\min,i} = \text{IWA}\ \mathrm{d}_i$ and the maximum planet-star separation is $s_{\max,i} = \text{OWA}\ \mathrm{d}_i$ where IWA and OWA are the instrument's inner and outer working angles, respectively. For the outer integrand, we use the fundamental lower limit on $\Delta\text{mag}_{\min,i} = 0$ as opposed to the analytical lower bound in Eq. (18) of Garrett and Savransky [27]. The upper limit on Δmag relates the completeness to the integration time. Typically, integration times (t_i) are defined as a function of a limiting Δmag and background flux levels, which are functions of the assumed instrument operating characteristics (i.e., throughput, contrast, etc.)[69, 96]. We invert the integration time model based on Nemati [69] to find Δmag as a function of integration time to find

$$\Delta\text{mag}_i(t_i) = -2.5\log_{10}\frac{SNR\sqrt{\frac{C_{b,i}}{t_i} + C_{sp,i}^2}}{C_{\mathcal{F}_0}10^{-0.4\nu_i(\lambda)}T(\lambda, WA)\epsilon_{PC}}. \tag{3.3}$$

Here, $\nu_i(\lambda)$ is the target star's B-V color, implemented as an empirical fit to data from Pecaut and Mamajek [73], which is accurate to about 7% in the wavelength range 400 nm $<\ \lambda\ <$1000 nm as discussed in Traub et al. [101].SNR is the signal to noise ratio threshold chosen for determining planet detections[13]. ϵ_{PC} is the photon counting efficiency of the system and is used to give the ideal planet count rate. $T(\lambda, WA)$ is the instrument's core throughput.T is a function

of WA, and by extension s so the integral over $\Delta\mathrm{mag}$ is not separable unless we assume a single representative WA at which to evaluate each star. Assuming a WA substantially speeds up calculations, but may not be representative of instruments with strong $\Delta\mathrm{mag}_{\mathrm{lim}}$dependence on WA. $C_{b,i}$ is the net background count rate, and $C_{sp,i}$ is the net speckle residual count rate, including all post-processing assumptions. We use the calculations of $C_{p,i}$, $C_{b,i}$, and $C_{sp,i}$ from Nemati [69].The spectral flux density is given by

$$C_{\mathcal{F}_0}(\lambda) = \mathcal{F}_0(\lambda)A\Delta\lambda\epsilon_q(\lambda)\epsilon_{inst}\epsilon_{syst}. \tag{3.4}$$

Here, $\mathcal{F}_0$ is the zero-magnitude flux calculated as in Eq. A.1 and presented in Traub et al. [101], A is the pupil area, $\Delta\lambda$ is the spectral bandwidth, $\epsilon_q(\lambda)$ is the detector quantum efficiency from Figure A.2, ϵ_{inst} is the optical attenuation due to the science instrument, and ϵ_{syst} is the optical attenuation due to the coronagraph, treated separately since a single instrument can have multiple coronagraphs. By integrating Eq. 3.2 with the limiting $\Delta\mathrm{mag}_i$ from Eq. 3.3, we arrive at a formulation for completeness as a direct function of integration time, $c_i(t_i)$.

The theoretical maximum completeness for the i^{th} target ($c_{\infty,i}$) is found by integrating Eq. 3.2 to the upper limit of $\Delta\mathrm{mag}_i$ at t_∞ (this assumes an infinite observing time is available). Using the Roman parameters, we see a universal upper limiting $\Delta\mathrm{mag}_i$ of 23.137. It is important to note that the inclusion of speckle residuals means that integrating past a certain point will not produce any improvements in the achieved SNR, meaning there is a specific time for every target past which it makes no sense to integrate further.

While the equations derived thus far are sufficient to perform continuous integration time optimization, gradient-based solvers, such as the ones we employ below, all perform significantly better with analytical gradient functions.

To expedite the optimization process in section 3.2.4, we calculate the derivative of completeness with respect to integration time as a function of integration time. As in Savransky, Delacroix, and Garrett [84], the derivative of Eq. 3.3 with respect to time is

$$\frac{\mathrm{d}\Delta\mathrm{mag}_i}{\mathrm{d}t_i}(t_i) = \frac{5C_{b,i}}{4\ln(10)}\frac{1}{C_{b,i}t_i + (C_{sp,i}t_i)^2}, \tag{3.5}$$

and the derivative of completeness with respect to integration time is therefore

$$\begin{aligned}\left.\frac{\mathrm{d}c_i}{\mathrm{d}t_i}\right|_{t_i} &= \frac{\mathrm{d}}{\mathrm{d}t_i}\left[\int_0^{\Delta\mathrm{mag}_i(t_i)}\int_{s_{\min,i}}^{s_{\max,i}} f_{\overline{s},\overline{\Delta\mathrm{mag}}}(s,\Delta\mathrm{mag})\,\mathrm{d}s\,\mathrm{d}\Delta\mathrm{mag}\right]\Bigg|_{t_i} \\ &= \frac{\mathrm{d}}{\mathrm{d}\Delta\mathrm{mag}_i}\left[\int_0^{\Delta\mathrm{mag}_i(t_i)}\int_{s_{\min,i}}^{s_{\max,i}} f_{\overline{s},\overline{\Delta\mathrm{mag}}}(s,\Delta\mathrm{mag})\,\mathrm{d}s\,\mathrm{d}\Delta\mathrm{mag}\right]\left.\frac{\mathrm{d}\Delta\mathrm{mag}_i}{\mathrm{d}t_i}\right|_{t_i} \\ &= \left[\int_{s_{\min,i}}^{s_{\max,i}} f_{\overline{s},\overline{\Delta\mathrm{mag}}}(s,\Delta\mathrm{mag}(t_i))\,\mathrm{d}s\right]\left.\frac{\mathrm{d}\Delta\mathrm{mag}_i}{\mathrm{d}t_i}\right|_{t_i}.\end{aligned} \tag{3.6}$$

We now have all the analytical expressions needed to optimize our planned observing schedule and have filtered down the original >2,000 degrees of freedom represented by the required integration times for each star in the input catalog to 651 (see section 3.2.2). Input decision variables $\mathbf{t} = t_i \;\forall\; i \;\in \mathbf{I}$ of 651 degrees of freedom is still quite large and could take a long time to compute, especially given the non-convexity of the sigmoid-shaped $c_i(t_i)$ curves. In order to ensure fast convergence of the nonlinear optimization, we need to provide a feasible starting guess preferably close to the final solution. We know from experimentation with AYO[96] that an optimal observation schedule will converge to a fixed $\varepsilon = \mathrm{d}c_i/\mathrm{d}t_i \;\forall\; i \in \mathbf{I}$. By combining Eq. 3.6 with Eq. 3.3 and inverting, we can find integration time as a function of $\mathrm{d}c_i/\mathrm{d}t_i \equiv \varepsilon$.

To derive this, we start from Eqn. 3.5, we state

$$\frac{\mathrm{d}\Delta\mathrm{mag}_i}{\mathrm{d}t_i}(t_i) = \varepsilon \tag{3.7}$$

We now solve for t_i by first completing the square containing t_i.

$$\varepsilon = \frac{5C_{b,i}}{4\ln(10)} \frac{1}{(C_{sp,i}t_i + \frac{C_{b,i}}{2C_{sp,i}})^2 - \frac{C_{b,i}^2}{4C_{sp,i}^2}} \tag{3.8}$$

After solving above eqn for t.

$$t = \frac{1}{C_{sp,i}} \sqrt{\frac{5C_{b,i}}{4\varepsilon\ln(10)} + \frac{C_{b,i}^2}{4C_{sp,i}^2}} - \frac{C_{b,i}}{2C_{sp,i}} \tag{3.9}$$

Pull out 1/4

$$t = \frac{1}{2C_{sp,i}} \sqrt{\frac{5C_{b,i}}{\varepsilon\ln(10)} + \frac{C_{b,i}^2}{C_{sp,i}^2}} - \frac{C_{b,i}}{2C_{sp,i}} \tag{3.10}$$

Pull out 1/sqrt(ln(10))

$$t = \frac{1}{2C_{sp,i}\sqrt{\ln(10)}} \sqrt{\frac{5C_{b,i}}{\varepsilon} + \frac{C_{b,i}^2\ln(10)}{C_{sp,i}^2}} - \frac{C_{b,i}}{2C_{sp,i}} \tag{3.11}$$

Pull out 1/e**2

$$t = \frac{1}{2\varepsilon C_{sp,i}\sqrt{\ln(10)}} \sqrt{5C_{b,i}\varepsilon + \frac{C_{b,i}^2\ln(10)\varepsilon^2}{C_{sp,i}^2}} - \frac{C_{b,i}}{2C_{sp,i}} \tag{3.12}$$

Pull out 1/Csp**2

$$t = \frac{1}{2\varepsilon C_{sp,i}^2\sqrt{\ln(10)}} \sqrt{5C_{b,i}\varepsilon C_{sp,i}^2 + C_{b,i}^2\ln(10)\varepsilon^2} - \frac{C_{b,i}}{2C_{sp,i}} \tag{3.13}$$

Bring outside term into the square root to find integration time as a function of $\mathrm{d}c_i/\,\mathrm{d}t_i \equiv \varepsilon$.

$$t_i = \frac{1}{2\varepsilon C_{sp,i}^2\sqrt{\ln(10)}} \left(-C_{b,i}\varepsilon\sqrt{\ln(10)} + \sqrt{5C_{b,i}\varepsilon C_{sp,i}^2 + C_{b,i}^2\ln(10)\varepsilon^2}\right), \tag{3.14}$$

which allows us to solve for integration time of all targets in a specific sub-group of **I** at ε[84]. This provides us with everything we need to both formulate the optimization problem and find a good initial solution, as described in the next section.

3.2.4 Optimization Process

Our goal is to maximize the number of unique detections throughout a blind-search survey. We evaluate the reward potential of a target using the completeness metric and the cost as the integration time required to achieve that completeness. In our optimization formulation, we seek to maximize the summed completeness that fits within the rigid mission time constraints coupled with an additional time cost per observation. Maximizing summed completeness with fixed overhead per observation in a time constrained mission is the full non-linear optimization problem we aim to solve in this section.

Our optimization process is broken down into 3 major steps.

The first is the calculation of an initial feasible solution via a Binary Integer Program (BIP).

The second is a scalar minimization problem solving the target subset and collective derivative using Brent's Method wrapped around a BIP (similar to Hunyadi, Shaklan, and Brown [37]).

The third step uses the output from the first or second step depending on which produces a higher summed completeness as an initial solution to optimize the solution by adding, removing, and finely tuning integration times via SLSQP.

Both step 1 and step 2 enable the solving of the full non-linear optimization problem in step 3. Step 3 can be seeded with any "good" initial guess (an initial solution sufficiently close to an optimal solution). A "good" initial guess for SLSQP can even be an infeasible solution (i.e. In the case of an unexpected

reduction in total observing time, we can seed step 3 with the previous solution to step 3). Optimization step 3 is fundamentally important because it allows individual adjustment of each t_i, individual removal of targets, and individual addition of targets (something Stark et al. [96] cannot do) while conforming to all time related constraints of the full non-linear optimization problem.

Mission Time Constraints

We formulate the summed completeness maximization problem to ensure any non-zero, fractional, observation incurs the observatory overhead and instrument settling time costs of making an observation. Settling time, $T_{settling}$, is time required by the observatory to start a new observation. This includes waiting out transient vibrations from the slew, time needed to reach thermal equilibrium, and time for the initial generation of the high-contrast region, either by "digging the dark hole" for a coronagraph, or by completing the precision alignment required by an external starshade. Overhead time, T_{OH}, on the other hand, is any additional time required by the observatory during the science integration. This includes time reserved for momentum dumping and orbit maintenance (if these operations will interrupt science data collection), dark hole maintenance for coronagraphs, and stationkeeping burns for starshades. The inclusion of $T_{settling}$ and T_{OH} makes it difficult to find an initial feasible solution in most cases, as the overhead time required for observing every target in the target list is typically greater than the total amount of mission time available. In the specific case of the Roman CGI explored here, we have over 650 days of overhead time associated with observing the full target list, and less than 100 days of allotted exoplanet observing time. This means that we cannot simply

evenly distribute our available time between targets to get an initial state for the optimization, as this would generate a constraint-breaking total required time. In general, initializing gradient-based optimizations on non-linear and non-convex search spaces (like the completeness vs integration time sigmoids) leads to poor optimizer performance and frequently results in no feasible solution being found.

Step 1: The Binary Integer Program

Step 1 is designed to create a guaranteed initial feasible solution to the non-linear optimization problem and uses reasonable inputs. Step 1 uses an initial calculation of background count rate ($\mathbf{C}_{b0}$), and residual speckle count rate ($\mathbf{C}_{sp0}$) using f_{Z0}, f_{EZ0}, and WA_{int}.f_{Z0} is the zodiacal light surface brightness, in arcsec^{-2}, calculated using

$$f_{Z0} = 10^{-0.4Z}, \tag{3.15}$$

where the default Z we use in Step 1 is a static 23.0 mag arcsec^{-2}[13]. f_{EZ0} is the exo-zodiacal light surface brightness in arcsec^{-2} calculated using

$$f_{EZ0} = 10^{-0.4\mathrm{EZ}}, \tag{3.16}$$

where the default EZ we use in Step 1-3 is 22.0 mag arcsec^{-2}[96]. WA_{int} is the working angle used for calculating integration times (this sets the specific values of instrument contrast, throughput and other angular-separation dependent terms) and is $2\times$IWA. We use 0.3 arcsec for all targets in Step 1 which is near a maximum balance of core mean intensity and throughput at $\lambda = 565$ nm based on Figure A.1 (a) and (c). The aforementioned parameters are used to calculate an initial $\mathbf{c}_0$ and $\mathbf{t}_0$. We additionally impose a constraint on the total time spent using $T_{\max}$ as the maximum amount of time to spend observing and

$T_{OH} + T_{settling}$ as a fixed overhead time for making any observation. We use the Coin-OR Branch and Cut solver[58], as provided by Google OR-Tools to solve our BIPs, as described in Algorithm 1. This gives us an initial feasible solution of targets, denoted by $\mathbf{x}_1^*$, with integration times, $\mathbf{t}_0$, and summed completeness, $\mathbf{x}_1^*\mathbf{c}_0$.

Algorithm 1: Binary Integer Program - $\mathbf{x}_1^* = \mathrm{BIP}(\mathbf{c}_0, \mathbf{t}_0)$

Input: $\mathbf{I}$, $\mathbf{c}_0$, $\mathbf{t}_0$, T_{OH}, $T_{settling}$, $T_{\max}$, and an optimization time limit maximum of 5 minutes

Output: $\mathbf{x}_1^*$, the list of binary values signaling to keep (1) or remove (0) each target

$$\mathbf{x}_1^* = \min_{\mathbf{x}} \quad -\sum_{i=0}^{N-1} x_i c_{0,i}$$

$$\text{s.t.}$$

$$\sum_{i \in \mathbf{I}} x_i (t_{0,i} + T_{OH} + T_{settling}) \leq T_{max} \quad ,$$

$$x_i \in \{0, 1\}, \qquad \forall\, i \ \in \mathbf{I}$$

Step 2: Scalar Minimization with group dc/dt

In Step 2, we reuse $\mathbf{C}_{p0}$, $\mathbf{C}_{b0}$, and $\mathbf{C}_{sp0}$ specifying a solution tolerance of 10^{-2} on a bounded scalar minimization problem with bounds on ε of [0,7]. We know ε at $t = \infty$ and $t = 0$ is 0, but we have determined from software experiments that 7 works well as an upper bound in this case. Realistically, this upper bound on ε should be $\max[dc_i/dt_i \ \forall\ i \ \in \ \mathbf{I}]$, but only 1 target could achieve that value and the optimization fail so the upper bound on ε must be reachable by multiple targets. This minimization in Step 2 uses the Python implemented scipy "minimize scalar" function, as described in Algorithm 2. Successful execution of this procedure produces a separate, feasible solution, distinct from the solu-

tion arrived at in Step 1. By varying the ε and solving the BIP sub-problem in section 3.2.4, we achieve a different set of targets $\mathbf{x}_2^*$ with integration times $\mathbf{t}_2$.

Algorithm 2: Bounded Scalar Minimization Wrapping Binary Integer Program

Input: $\mathbf{I}$, $\mathbf{C}_{p0}$, $\mathbf{C}_{b0}$, $\mathbf{C}_{sp0}$, T_{OH}, $T_{settling}$, $T_{\max}$, and an optimization time limit maximum of 5 minutes

Output: ε^*, the value of $\mathrm{d}c/\,\mathrm{d}t$ evaluated for each target which maximizes yield

Output: $\mathbf{t}^*$, integration times for each target evaluated at ε^*

Output: $\mathbf{x}_2^*$, the list of binary values signaling to keep or remove each target

$$\begin{aligned}\varepsilon^* = \min_{\varepsilon} \quad & -\sum_{i\in\mathbf{I}} \mathrm{BIP}(c_i(t_i^*(\varepsilon)), t_i^*(\varepsilon), T_{OH}, T_{settling}, T_{\max})_i c_i(t_i^*(\varepsilon)) \\ & \text{s.t.} \\ & \varepsilon \leq 7, \\ & -\varepsilon \leq 0\end{aligned}$$

$\mathbf{t}_2^* \Leftarrow [t_i^*(\varepsilon^*),\ \forall\, i\ \in\ \mathbf{I}]$

$\mathbf{x}_2^* \Leftarrow [\mathrm{BIP}(c_i(t_i^*(\varepsilon^*)), t_i^*(\varepsilon^*), T_{OH}, T_{settling}, T_{\max}),\ \forall\, i\ \in\ \mathbf{I}]$

Step 3: SLSQP Minimization

In Step 3, we formulate the SLSQP optimization process with an initial solution seeded with $\mathbf{x}_1^*\mathbf{t}_0$ or $\mathbf{x}_2^*\mathbf{t}_2^*$, whichever produces a larger summed completeness. In practice, we could take any $\mathbf{xt}$ as a good initial guess and resolve with new mission time constraints based on new information. This seeded solution should prove sufficiently close to an optimal solution such that the $\mathbf{c}(\mathbf{t})$ sigmoid-like inflection point is exceeded. We now replace our previous assumed f_{Z0} with a more optimistic surface brightness. We calculate zodiacal light surface brightness every ≈1/3 of a day for a year, interpolating the lookup tables from Leinert et al. [56] as shown in Figure 3.6. For our optimization, we specifically use the per annum minimum, $\mathbf{f}_{Z,\min}$ for all targets excluding $f_{Z,i}$ in keep-out regions

shown in Figure 3.4 (a). This is crucial as the $f_{Z,i}$ intensity of targets with 0° heliocentric ecliptic latitude, (b) have local zodiacal light minimum within 56° of the observatory's anti-solar point (see Figure 3.6), a region not visible to Roman due to solar panel pointing requirements in Table 3.2.

Algorithm 3: SLSQP Optimization

Input: $\mathbf{I}$, $\mathbf{f}_Z$, $\mathbf{t}$, T_{OH}, $T_{settling}$ and $T_{\max}$
Output: $\mathbf{t}_3^*$, the integration times to spend on each star

$$\begin{aligned}
\mathbf{t}^* = \min_{\mathbf{t}} \quad & -\sum_{i=0}^{N-1} c_i(t_i) \\
\text{s.t.} \quad & \\
& t_i < T_{\max}, \quad \forall\, i \in \mathbf{I}, \\
& -t_i < 0, \quad \forall\, i \in \mathbf{I}, \\
& \sum_{i \in \mathbf{I}} x_i (T_{OH} + T_{settling}) + t_{0,i} < T_{\max}
\end{aligned}$$

The output $\mathbf{t}_3^*$ is an optimal allocation of integration times to each target accounting for the non-linear overhead time assignment. This optimal allocation encodes our observation priority over all possible targets and means each target in the target list is equivalently important to observe to achieve the expected summed completeness. In the validation section, we choose the minimum zodiacal light intensity target selection metric to complement our optimization assumptions. The drawback is, if variations occur in the total mission time for any reason, high reward targets might not be observed. There are technically infinite "near-optimal" solutions. Equivalent maximum summed completeness target lists can be achieved for a range of different numbers of target stars. This is directly caused by the increasing number of approximately equivalent target stars at further stellar distances. These integration times are used as inputs to our validation process discussed in section 3.2.5 and implemented in EXOSIMS

which runs a Monte Carlo of full mission survey simulations, observing each target for the integration times prescribed in $\mathbf{t}_3^*$ and bookkeeping all dynamic aspects of the mission.

Optimization Performance

By breaking our optimization problem into 3 distinct parts, we see some benefits from each part. The BIP guarantees an optimal solution based on the input and has a sub-second solve time. The scalar minimization problem solves within a few seconds and achieves $\approx 99\%$ of the maximum completeness we achieve. The SLSQP part on Roman seeded with the scalar minimization solution marginally improves the summed completeness and takes a little over a minute. The solution arrived at by SLSQP is almost certainly a local minimum and not a global optimum.

In this paper, rows 1, 2, and 3 in Table 3.1 are how we solved for the optimal observation target list and integration times, using $f_{Z,0}$ as input to 1 and 2 of the optimization problem. We contrast optimizing with $f_{Z,0}$ to $\mathbf{f}_{Z,\min}$ in rows 4, 5, and 6 of Table 3.1 which causes a marginal decrease in summed completeness for the BIP and scalar minimization problems. Row 7 is optimization seeded with $\mathbf{t}_3^*$ from row 6 and a slightly longer total observing time which solves in a shorter time than the from scratch optimization process. Rows 8, 9, 10, 11, and 12 are based on a substantially larger telescope which is reflected in the higher overall summed completeness. Solve times are strictly larger on the Big Telescope than for Roman, but we see row 11 and 12, which are seeded with the optimal solution from row 10 have substantially shorter solve times than row 10.

Table 3.1: Optimization method solve times and summed completeness for Roman using different input zodiacal lights and solving with different maximum mission times.

		Opt. Method	**Solve Time (sec)**	$\sum x_i c_i$	f_Z	$T_{\max}$
Roman	1	BIP	0.019	1.92	$f_{Z,0}$	$T_{\max}$
	2	Scalar Min.	5.468	2.33	$f_{Z,0}$	$T_{\max}$
	3	SLSQP	70.16	2.35	$f_{Z,\min}$	$T_{\max}$
	4	SLSQP	16.88	2.33	$f_{Z,\min}$	$0.9 \times T_{\max}$
	5	SLSQP	9.432	2.35	$f_{Z,\min}$	$1.1 \times T_{\max}$
Roman	6	BIP	0.109	1.89	$f_{Z,\min}$	$T_{\max}$
	7	Scalar Min.	5.739	2.31	$f_{Z,\min}$	$T_{\max}$
	8	SLSQP	65.34	2.35	$f_{Z,\min}$	$T_{\max}$
Big Telescope	8	BIP	0.929	105.79	$f_{Z,\min}$	$T_{\max}$
	9	Scalar Min.	7.23	179.21	$f_{Z,\min}$	$T_{\max}$
	10	SLSQP	638.7	180.36	$f_{Z,\min}$	$T_{\max}$
	11	SLSQP	258.8	183.29	$f_{Z,\min}$	$1.1 \times T_{\max}$
	12	SLSQP	182.0	180.05	$f_{Z,\min}$	$0.9 \times T_{\max}$

In the course of optimizing these target lists, Figure 3.2 is an example of the targets being optimized to a constant dC/dT as intended in these algorithms. We see that all targets have a maximal dC/dT (which could be either blue or black but always located at the peak of a red curve). Where the targets have a dC/dT greater than the dC/dT to be optimized to, the optimal integration time will increase from the point of maximum to along the apparent black line of dots.

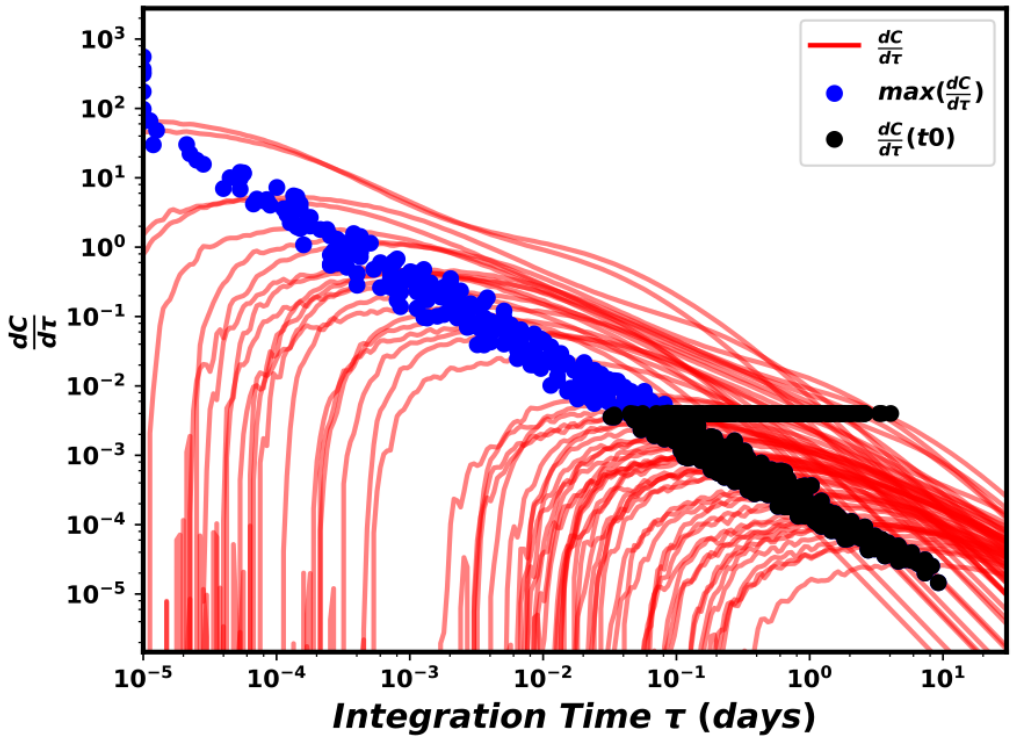

Figure 3.2: An example of the optimization process described in this work applied to a large number of targets. The black dots represent the optimized time and associated dC/dT of the individual targets. The apparent horizontal line of black dots is the optimal time and associated dC/dT. The black and blue dots appearing at the maximum of the red curves are the time and value of maximum dC/dT for that particular planet. The blue dots represent the location of maximum dC/dT of a target that was us

3.2.5 Validation

We validate the ability to schedule our optimized integration times from section 3.2.4, and listed in Table B.1 of Appendix B.1, via a Monte Carlo of full survey simulations using the EXOSIMS code base, detailed in Savransky and Garrett [85]. This software allows us to bookkeep dynamic aspects of the mission while scheduling observations on randomly generated planetary systems about a real set of target stars. By using EXOSIMS, we account for exoplanet, solar system planet, and observatory orbit propagation as well as recalculating look vectors, keep-out regions, and local zodiacal light noise.

At the start of each survey simulation, we randomly generate planets around stars; drawn from the Kepler Like or SAG13 planet populations discussed in section 3.2.1 using sampling methods described in Savransky and Garrett [85]. To define the observable times of individual stars, we combine solar system planet locations with instrument specific keep-out angles and observatory look vectors for each target in the star catalog throughout the duration of the mission. These solar system planet locations are taken from the Horizons Ephemeris System furnished by NASA's Navigation and Ancillary Information Facility (NAIF)[3, 2] based on an assumed mission start modified julian date (60634 for Roman). The EXOSIMS framework default observatory orbit is a quasi-periodic, stable, halo orbit at the second Earth-Sun Lagrange point with period of ≈ 180 days based on Kolemen, Kasdin, and Gurfil [48]. We stitch the observatory position along the orbit using a 1D spline interpolant and propagate the observatory along the interpolant throughout MET assuming a general observatory start location on the Halo orbit when the Earth is at the Earth-Sun equinox (60575.25 MJD for Roman). The starting location of the observatory for

a single-visit blind search survey coronagraph mission has negligible impact on yield. We discuss the calculation of keep-out regions in section 3.2.5. In each simulation, we incrementally filter available targets, simulate observations and their outcomes, and propagate orbits as shown in Figure 3.3.

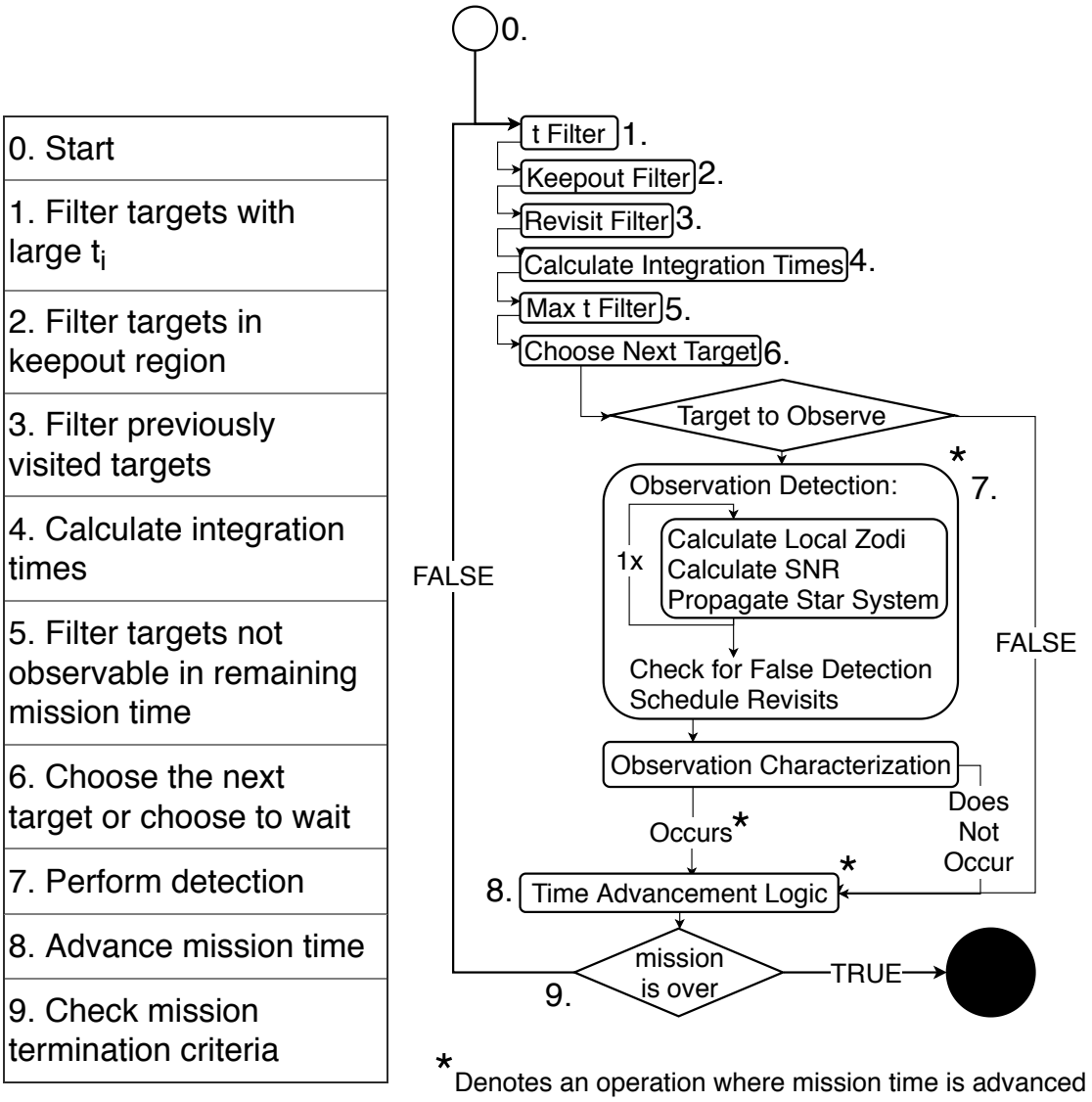

Figure 3.3: EXOSIMS survey simulation simplified flowchart depicting major filtering steps discussed in section 3.2.2, calculating integration time, selecting the next target, making the detection observation, making the characterization observation, and advancing time. EXOSIMS is additionally capable of strictly adhering to pre-defined observing blocks, but this functionality was not used for the results presented here.

At the start of each main loop depicted in Figure 3.3 (Steps 1 - 9), filters remove targets with too long of integration times ($t_i > 30$ d); targets currently in keep-out regions of planetary bodies; previously observed stars not currently scheduled for revisits; and filters targets not observable within the nearest time constraint. In this paper, we do not revisit targets, so we filter out any targets that have been observed during the mission. We then use an intelligent method of choosing the next target at the current mission time, t_c. Several selection metrics have been studied in Savransky, Delacroix, and Garrett [84], 45, and 46, but we choose to observe targets at their minimum zodiacal light intensity. Here, our method of selecting targets for observation advances time by the smallest amount min($t_c - \mathbf{t}_{f_{Z,\min}}$). $\mathbf{t}_{f_{Z,\min}}$ are the mission times when targets in $\mathbf{I}$ have their next local zodiacal light minimum, $\mathbf{f}_{Z,\min}$. This identifies target star i which we proceed to observe for the pre-calculated time t_i from the method described in section 3.2.4. We divide the observations into discrete time intervals and calculate the signal and noise at each interval, calculate the total achieved SNR, and propagate planets around the star as well as the observatory and solar system planets. Splitting up observations into time intervals enables us to approximate the achieved SNR via Riemann sum using the new location of the observatory, planets, and simulated exoplanets along with the associated zodiacal light, planet phase angle, planet position in the instrument working angle. We divide our observations into two equal intervals over the duration of the integration time, t_i, which are all strictly less than 2 days in this case. We then advance the mission time by $t_i + T_{OH} + T_{settling}$ and check if the mission is over.

The EXOSIMS framework relies upon probabilistic planet generation and random draws, however, our Python implementation is capable of not only replicating results, but also fully reproducing each survey simulation run by re-

setting the simulation from the simulation's random seed. EXOSIMS also keeps track of all inputs required to replicate the simulation.

Keep-out Regions

Roman has keep-out regions specified in Table 3.2. We define these keep-out regions as a subset of the sky which cannot be entered by the telescope look vector throughout an observation. Our strict accounting for time and geometry in simulations enables us to ensure any observation's look vector ($\underline{r}_{i/SC}$) does not start, stop, or pass through a keep-out region. Nominally, each solar system body in Table 3.2 has a minimum keep-out region the telescope cannot look within. The sun has a maximum keep-out region of 124° the telescope cannot look outside of. This is set by the minimum incidence angle of light on the spacecraft's solar panels to power the observatory and CGI. The bore-axis vector of Roman cannot point farther than 124° away from the spacecraft sun vector ($\underline{r}_{\odot/SC}$) in order to meet spacecraft power requirements. There is an additional minimum solar panel keep-out angle at 56° which was not modeled. Since our implementation in EXOSIMS in this specific case enforces observations at local zodiacal light minimum indicated by the black squares shown in Figure 3.6, these observations either occur near the spacecraft anti-solar point or edge of the maximum solar panel keep-out region.

We cache a keep-out map to substantially increase simulation speed. This keep-out map spans the duration of the mission and is discretized into small time bins (1 day in this paper) and encodes the visibility of each star in the catalog. The keep-out map encodes the visibility status of targets at each point in time by calculating the angular distance between $\underline{r}_{i/SC}\ \forall\ i \in \mathbf{I}$ and the

Table 3.2: Keep-out regions for Roman defined as the (minimum angle between $\underline{r}_{Body/SC}$ and $\underline{r}_{i/SC}$, maximum angle between $\underline{r}_{Body/SC}$ and $\underline{r}_{i/SC}$)

Body	**Keep-out Angle (**deg**)**
Earth	$45°$
Moon	$45°$
Sun	$45°$
Small Bodies	$1°$
Solar Panels	$124°$[88]

observatory to planet vectors. If the formed angle is less than the minimum keep-out angle or greater than the maximum keep-out angle for that body, the target star is marked as not visible. In Figure 3.4 (a), we see the target visibility for 100 stars in the star catalog ordered by right ascension with their visible times (white) and obstructing bodies. The sun (yellow) is the major contributor to keep-out regions with the Earth (blue) being the second largest contributor. Star occultation by Mars, Venus, or Jupiter keep-out regions is nearly negligible. Figure 3.4 (b) also shows some targets are visible less than 28% of the time while others are visible all of the time. We can conclude from these plots that increasing Roman's maximum solar keep-out angle or decreasing the minimum keep-out angle can increase the amount of time a target is visible by maximally ≈ 2 d per change in degree.

Local Zodiacal Light

The local zodiacal light intensity ($f_{Z,i}$) is the largest, known, time varying noise source we account for and manifests itself in the background noise count rate introduced in Eq. 3.3. Variations in local zodiacal light can vary the summed completeness by up to 10%[45, 46, 44].

Calculation of local zodiacal light is broken down into two major compo-

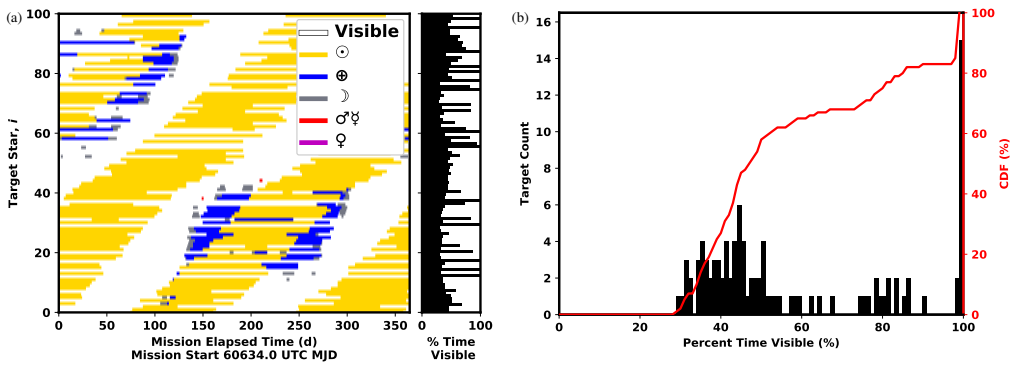

Figure 3.4: Keep-out map of Roman/targets over the first mission year showing visible times of targets (white) and different sources of keep-out occlusion including the Sun (yellow), Earth (blue), Moon (grey), Mercury/Venus (red). The horizontal histogram shows percentage of time each target is visible (a). The keep-out map filter is implemented in EXOSIMS at the Step 2 shown in Figure 3.3. The histogram and cumulative distribution of visibility of all targets is shown (b). Minimum target visibility is 28%.[94, 92]

nents: an intensity wavelength dependence correction factor, $f_\lambda(\lambda)$, and intensity at the spacecraft centered look vector, $f_\beta(\underline{r}_{i/SC})$.

For f_β, we know the zodiacal dust cloud has structure, but the degree to which structure and phase/scattering properties contribute to the zodiacal light intensity from a general observer location in space is currently uncertain (although missions have been proposed to model such a dust cloud[93]). Knowing the degree of contribution determines whether the anti-solar point of Table 17 of Leinert et al. [56] should be modeled as fixed relative to the Earth or fixed relative to the observer. To simplify our work, we assume the latter so $\lambda - \lambda_0 = 0°$ when $\underline{r}_{i/SC} = \underline{r}_{\odot/SC}$ and the corresponding anti-solar point is when $\underline{r}_{i/SC} = \underline{r}_{SC/\odot}$ and $\lambda - \lambda_0 = 180°$.

To calculate local zodiacal light, we first find the position of the observatory

in the heliocentric ecliptic frame $\underline{r}_{SC/\odot}(t_c)$. We then calculate

$$l_{SC/\odot}(t_c) = \text{sgn}(\underline{r}_{SC/\odot}(t_c) \cdot \hat{\underline{y}}) \cos^{-1}\left(\frac{\underline{r}_{SC/\odot}(t_c) \cdot \hat{\underline{x}}}{|\underline{r}_{SC/\odot}(t_c)|}\right). \tag{3.17}$$

We get the longitude of the sun relative to the spacecraft in the heliocentric frame $l_{\odot/SC} = (l_{SC/\odot} + 180)\%360$. We find the position vector describing the star position in the heliocentric true ecliptic frame $\underline{r}_{i/\odot}$ and calculate the star position with respect to the observatory $\underline{r}_{i/SC} = \underline{r}_{i/\odot} - \underline{r}_{SC/\odot}(t_c)$. We then transform $\underline{r}_{i/SC}$ into spherical coordinates using Astropy's SkyCoord and extract the target star's latitude ($b_{i/SC}$) and longitude ($l_{i/SC}$) relative to the spacecraft. We then convert to absolute values for interpolation in the latitude and longitude range of Figure 3.6 ($0° < b_i < 90°$ and $0° < l < 180°$) by $b_i = |b_{i/SC}|$ and $l_i = |((l_{i/SC} + 180°) \bmod 360°) - 180°|$ respectively. This l and b are used in $f_\beta(l, b)$, a linear gridded interpolation of Table 17 in Leinert et al. [56] and by extension $f_Z(l, b, \lambda)$ in Eq. 3.18.

To assess the validity of our spacecraft centered vs geocentric ecliptic frame, we need to assess how much the angular position of zodiacal light intensity interpolant inputs would differ. Since Roman is on a L2 Halo orbit, its out of ecliptic motion is < 0.004 AU and orbital distance from the Sun is ≈ 1.010 AU, resulting in a geocentric ecliptic frame interpolation input deviation of $\Delta b < 0.22°$. When $\underline{r}_{i/SC}$ is $180°$ or $0°$ from $\underline{r}_{\odot/SC}$, the l and b used for interpolation is correct, however, interpolating for a target at say $l = 90°$ has the value somewhere between $89° < l < 90°$ due to the actual position of the spacecraft at the L2 Halo orbit and not Earth. We expect $\Delta l < 1°$ for a Sun-Earth L2 orbit. We now make note that the smallest griddspacing of the input data is $5°$ meaning Δl and Δb are within these bounds. It is also important to note the accuracy of this Zodiacal light model is, at best, 10%[56]. The final component necessary to complete

Eq. 3.18 is $f_\lambda(\lambda)$, a wavelength correction factor. Which has a detailed explanation in Leinert et al. [56].

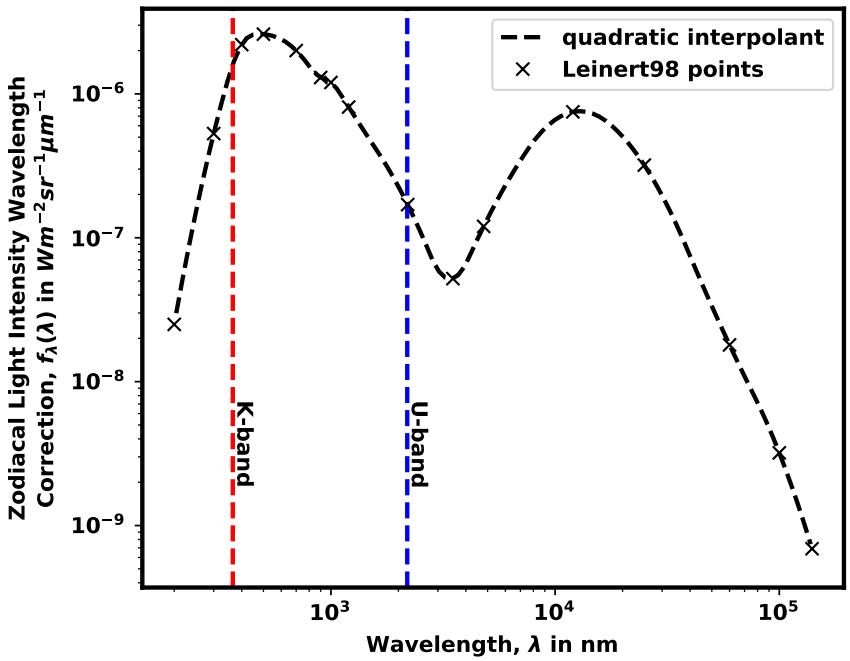

Figure 3.5: Local zodiacal light correction factor from Table 19 of Leinert et al. [56] with region of high accuracy between 200 nm (red dashed line) and 2.0 μm (blue dashed line) and decreasing accuracy at larger wavelengths due to infrared and scattering parity in contribution.

In section 3.2.4, for Step 1 for our integration time optimization, we use a static Z_0 of 23.0 mag arcsec^{-2} as done in Stark et al. [96]. However, in Step 3, we optimize our final integration times using $\mathbf{f}_{Z,\min}$ (or equivalently $\mathbf{Z}_{\max}$) which implies specific times of the year when these observations can be made, as shown by the black lines in Figure 3.6. The black points in Figure 3.6 is curved at low l, this is directly caused by the large anti-solar keep-out region which marginally inhibits observation at $f_{Z,\min}$.

There is a distinction between the $f_{Z,i}$ used in the integration time optimization and the $f_{Z,i}$ used in the Monte Carlo validation. When we evaluate

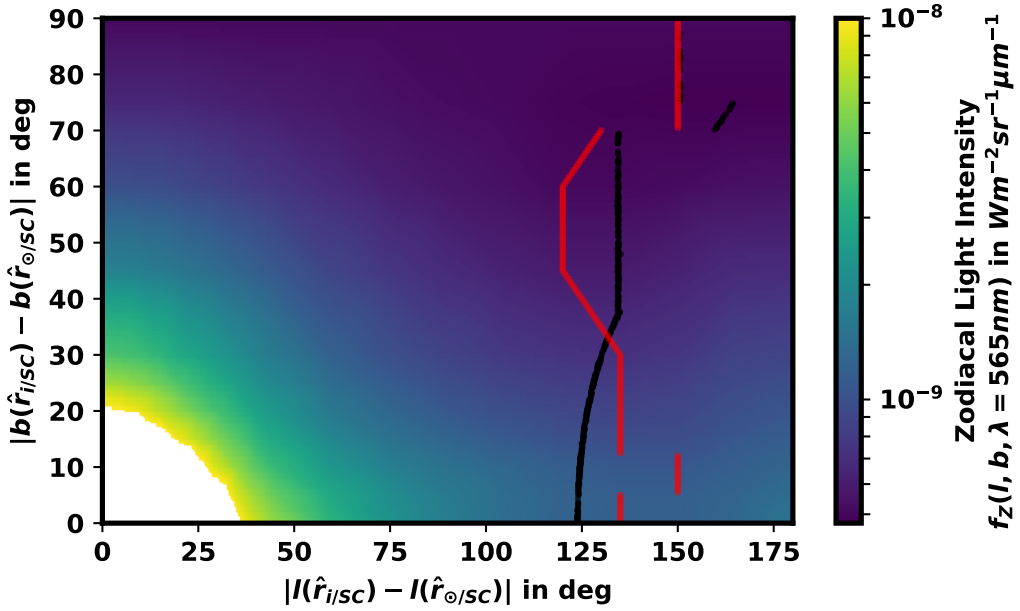

Figure 3.6: Local zodiacal light intensity interpolant ($f_Z(l, b, \lambda)$ of Eq. 3.18) at target star-spacecraft heliocentric ecliptic longitude ($l(\hat{r}_{i/SC})$) relative to the sun-spacecraft heliocentric ecliptic longitude ($l(\hat{r}_{\odot/SC})$) and target star heliocentric ecliptic latitude ($b(\hat{r}_{i/SC})$) relative to spacecraft heliocentric ecliptic latitude ($b(\hat{r}_{\odot/SC})$), and $\lambda = 565$ nm. The minimum zodiacal light intensity ($f_{Z,\min}(b)$) for each b is indicated by densely packed red squares which appear to form lines caused by using a linear interpolant and the coarseness of the underlying datapoints. Our implementation makes observations only when target stars are coincident with black squares, the minimum f_Z with keep-out restrictions ($b < 37°$). Note Leinert et al. [56] is significant to 3 decimal places but the interpolant introduces machine precision numbers, the red and black dots have functionally equivalent values for $b > 37°$. Only one quadrant is shown as the data is assumed to be reflection symmetric.

whether a detection has been made at the top of Step 7 in Figure 3.3, we calculate the planet SNR using $f_{Z,i}$ based on $\underline{r}_{i/SC}(t_c)$ where t_c is the current time in the simulation. We calculate the interpolant in Figure 3.6 using Eq. 3.18, a 2D linear interpolation of intensity from Table 17 of Leinert et al. [56] ($f_\beta(l, b)$), a quadratic interpolation of wavelength dependence from Table 19 in Leinert

et al. [56] ($f_\lambda(\log_{10}(\lambda))$), and applying a sun color correction of $\mathcal{F}_0(\lambda)$ to get

$$f_Z(l, b, \lambda) = \frac{f_\lambda(\log_{10}(\lambda)) f_\beta(l, b)}{hc' \mathcal{F}_0(\lambda)}. \tag{3.18}$$

Here, h and c' are the planck constant and speed of light in a vacuum, and $f_\lambda(\log_{10}(\lambda))$ is a quadratic 1D interpolant of Leinert et al. [56] data in Figure 3.5.Since the Table 17 from Leinert et al. [56] is in the geocentric ecliptic coordinates, but the spacecraft will physically be located on an Earth-Sun L2 orbit, we assume the table's $b = 0°$ and $l = 0°$ is coincident with $\underline{r}_{\odot/SC}$ and the additional distance of the spacecraft from the Sun has no effect.

Since the statically optimized integration time assumes a fixed zodiacal light which coincides with a specific time of year and our actual observation takes into account the local zodiacal light conditions, our target selection method has an impact on the zodiacal light of the target we observe. In previous work, we tested different target selection metrics incorporating completeness, integration time, and deviations from the maximum or minimum zodiacal light intensity.[84, 45, 46] For a statically optimized target list, we found the strategy observing at minimum zodiacal light to be most effective. However, this assumes we have all the observing time allotted. If we included instrument degradation due to radiation or possibly early mission terminations, other selection metrics which preferentially select higher performing targets may become more attractive.

Using the 2D interpolation of Figure 3.6 combined with instrument specific filters in section 3.3, and optimization process in section 3.2.4, we can plot the histogram of minimum (black dots in Figure 3.6) and maximum (at edge of solar keep-out) local zodiacal light intensity in Figure 3.7. Depending on the time of year observations are made, the variation in zodiacal light intensity changes

(excluding when targets are in keep-out) by upwards of 2 magnitudes. We also see using an estimated Z_0 of 23.0 mag arcsec^{-2} is an overly optimistic approximation of the local zodiacal light noise. Realistically, for our filtered set of target stars, the appropriate $\mu_{Z_{\min}} \approx 22.79$ mag arcsec^{-2} and $\mu_{Z_{\max}} \approx 21.59$ mag arcsec^{-2}. Since $f_{Z,\min}$ and $f_{Z,\max}$ in Figure 3.7 includes the instrument specific keep-out regions for Roman, increasing the maximum solar keep-out could decrease $f_{Z,\min}$ and decreasing the minimum solar keep-out angle would increase $f_{Z,\max}$.

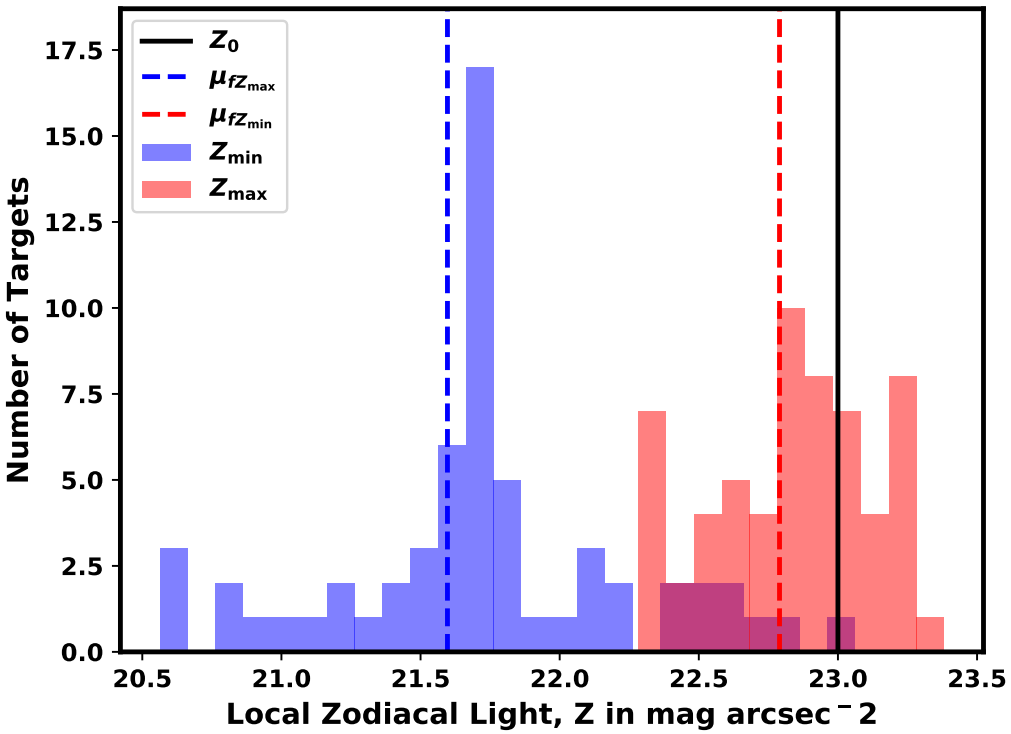

Figure 3.7: A histogram of Zodiacal Light intensity in mag arcsec^{-2} (Z), for stars at the minimum observed intensity ($Z_{\max}$), and stars at maximum observed intensity ($Z_{\min}$), taking into account Roman keep-out regions. Z_0 is corresponds to the optimistic zodiacal light intensity in mag arcsec^{-2} used by Stark in Stark et al. [96] and Brown in Brown [13]. Dashed lines represent target list $\mu_{Z_{\min}} = 22.79$ mag arcsec^{-2} and $\mu_{Z_{\max}} = 21.59$ mag arcsec^{-2}.

Detection and Characterization Observations

When making a detection observation of a planet, we do not use the same parameters as in the optimization process. Our algorithm for confirming a detection is also different. In a survey simulation, we define a planet as being detected when the collected $SNR_k > 5$. We calculate this SNR using Nemati's SNR model from Nemati [69].The planet signal is,

$$S = C_p t_i / N_{\mathrm{d}t} \tag{3.19}$$

and the noise is

$$N = \sqrt{C_b t_i / N_{\mathrm{d}t} + C_{sp}^2 (t_i / N_{\mathrm{d}t})^2}. \tag{3.20}$$

These equations are treated as a riemann summation over the whole integration time (t_i) broken into $N_{\mathrm{d}t} = 2$ segments. The riemann summation approximates variations in local zodiacal light, exozodiacal light, planet phase angle, and changes in planet WA as well as the new resulting $T(\lambda, WA)$, $\Gamma(\lambda, WA)$, $\Psi(\lambda, WA)$, and $\gamma(\lambda, WA)$. The count rates we calculate here, C_p, C_b, and C_{sp}, use the same equations in section 3.2.3 but with inputs specific to the planet. WA_k is updated based on the planet position at the current time propagated using the Kepler state transition matrix. The new, physical, $\Delta\mathrm{mag}_k$ is calculated using Eq. (4) from Garrett and Savransky [27] and the new planet phase angle calculated from a Lambert phase function. $f_{Z,i}$ is updated based on the new observatory position along the halo orbit. We use a different calculation of f_{EZ} following from Savransky, Kasdin, and Cady [79], where

$$f_{EZ,k} = 2 \times 10^{-0.4(V_{\mathrm{mag},i} - 4.83 + EZ)} (2.44 - 0.0403 \mathrm{supp}(I_k) + 0.00269 \mathrm{supp}(I_k)^2) / \|\underline{r}_{k/i}\|^2. \tag{3.21}$$

Here, EZ is the visual magnitude of the exozodiacal light scaled relative to the Sun. $\mathrm{supp}(I_k)$ is the supplementary angle to the planet's orbital inclina-

tion (in degrees) resulting in a range from $[0^\circ, 90^\circ]$ and is mirrored in the range $[90^\circ, 180^\circ]$ based on personal communication with D. Lindler in 2008. In multi-planetary systems, we assume the exozodiacal light of each planet has the inclination of each planet. The inverse $\|\underline{r}_{k/i}\|^2$ term accounts for the decreasing exozodiacal light contribution with increasing distance from the planet and star, as discussed in Stark et al. [96].

We include spectral characterization observations in our survey simulations, but not in our optimization process. This is due to both the rarity in finding a strong enough planet signal to make characterization of with Roman and the high mission value placed on acquiring spectral characterizations. We do not model characterizations in our optimization process because it adds complexity and we have no good method of weighting new planet detections to spectral characterizations. We attempt to immediately perform a spectral characterization upon successfully detecting any new exoplanet. We calculate integration times for this characterization observation using the measured $\Delta\mathrm{mag}_k$, WA_k, $f_{EZ,k}$, and $f_{Z,i}$ at the current time as well as the characterization mode parameters.We check if the new integration time plus overhead would exceed the total mission time, would enter into a keep-out region, or would exceed the 30 d integration cutoff filter. In the vast majority of cases, a SNR of 10 is not achievable given what we know about the exoplanet from a single detection. Additionally, we make observations at local zodiacal light minimum immediately before a planet enters keep-out or immediately after a planet exits keep-out causing approximately half of the successfully detected planets to enter keep-out immediately following their observation.

Convergence

We determine the required number of simulations to ensure the accuracy of our results by executing 10,000 simulations of a generic input specification similar to that used in section 3.3. By assuming the true mean yield is equivalent to the mean yield over 10,000 simulations ($\mu_{det,10000}$), we can demonstrate convergence of $\mu_{det,i}$ to $\mu_{det,10000}$, where i in this section is the number of simulations in the ensemble. We calculate the mean yield from a subset of ensembles incrementally for each i using Eqn. 38 from Savransky [80]. We then calculate the percent deviation between $\mu_{det,i}$ and $\mu_{det,10000}$ shown in Figure 3.8. Figure 3.8 shows the mean number of unique detections converges for a sufficiently large number of simulations.

By assuming the mean number of detections per run are normally distributed, we show the 1σ, 2σ, and 3σ confidence intervals of the mean in Figure 3.8. In reality, the ensembles are some form of gamma distribution because the numbers are all positive and priors are exponentially distributed. This normal distribution assumption fits better for high yield telescopes. The absolute percent errors for varying confidence intervals for 100 and 1000 simulations are presented in Table 3.3. Absolute percent errors represent the uncertainty in the mean number of unique detections. Excluding Table 3.3 and Figure 3.8, all results in this paper are derived from single simulations or ensembles of 1000 simulations. We use the 3σ confidence interval to make comparisons and determine whether a result is significant. We can say a general mean number of unique detections is accurate to within $\pm 3.19\%$ at 3σ for 1000 simulations.

Table 3.3: Absolute percent error confidence intervals for 100 and 1000 simulations. This table references data created using runs from Dean22May18RS09CXXfZ01OB01PP01SU01 and file convergenceDATA_ Dean22May18RS09CXXfZ01OB01PP01SU01 _2019_04_09_01_23_.txt

# Sims	Confidence Interval	Absolute Percent Error (%)
1000	1σ	1.16
1000	2σ	2.33
1000	3σ	3.19
100	1σ	3.45
100	2σ	6.95
100	3σ	9.58

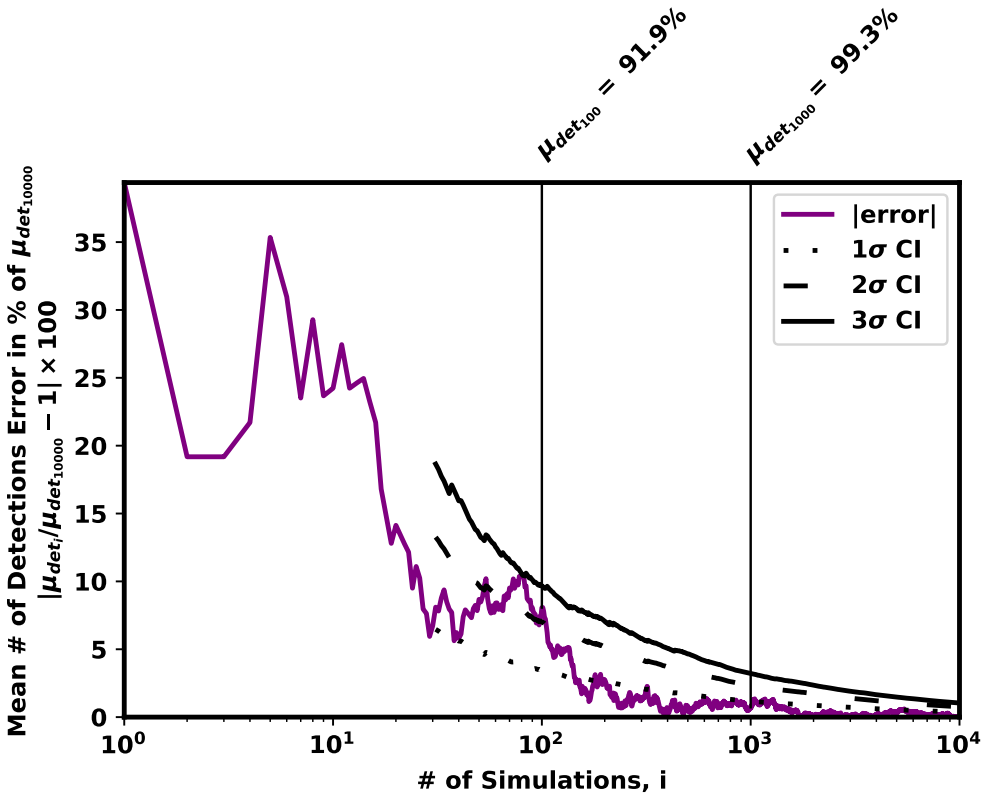

Figure 3.8: Absolute percent error from $\mu_{det_{10000}}$ convergence combined with 1σ, 2σ, and 3σ confidence intervals.

3.3 Roman Results

The results in this section are generated using all previously discussed assumptions and parameters as well as the parameters in Table A.1 based on the cycle 6 description of the CGI.[53]

3.3.1 Completeness and Planned Observations

By applying the optimization process from section 3.2.4 to the target list filtered in section 3.2.2 and assuming a Kepler Like planet population with per observation $T_{OH} = T_{settling} = 0.5$ d and maximum observing time of $T_{\max} = 91.3125$ d (3 months), we get the integration times in Table B.1 in Appendix B.1. The planned summed completeness of this target list is $\sum c_i(t_{3,i}) = 2.35$. Since completeness is the probability of detecting planets from a population around a star, multiplying $\sum c_i$ by the population occurrence rate (η_{KL} from section 3.2.1) gives the expectation value of planets detected, in this case equal to 5.58 detections. We calculate the ultimate completeness[14] for all 651 potential targets by evaluating $\sum c_i$ at an infinite integration time (t_∞) to get $\sum c_i(t_\infty) = 9.01$ and an expectation value of 21.40 exoplanets detected. We note here that the theoretical maximum summed completeness, if there were no $\Delta\mathrm{mag}$ or WA constraints, for all 651 target stars is 651. The summed ultimate completeness of only the targets in Table B.1 is $\sum c_i \; \forall \; i \; \in \; \mathbf{I} = 2.99$ with an expectation value of 7.10 exoplanets detected. The ratio $2.35/9.01 \times 100 = 26.1\%$ is a measure of planned target list yield to the maximum theoretical summed completeness observing all 651 targets with t_∞. The ratio $2.35/2.99 \times 100 = 78.6\%$ is a measure of the summed completeness of the planned target list to the maximum theoretical summed com-

pleteness of only the target stars observed with t_∞. These ratios represent the fraction of planet phase space about all scheduled targets that could be probed in the assumed, finite, total mission time. We can conclude from these results that, in the short amount of time allocated for Roman, our optimized target list is capable of observing 78.6% of the summed ultimate completeness it could possibly gather.

There is a non-negligible difference between the planned completeness, $c_{3,i}$, and the completeness actually observed $c_{t_{obs},i}$. The planned observations and Monte Carlo simulations entirely based on the Kepler Like population are shown in Figure 3.9. Note the loss of 1 observation between the planned and actual observations, which we attribute to accumulation of machine precision errors and our strict adherence to the $T_{\max}$ upper bound on observing time as well as the allowance of characterizations in the implemented survey. The loss of an observation is evident by the single red square without an associated blue circle in Figure 3.9. The $\sum c_i$ actually observed in this particular simulation of the Monte Carlo was 2.33. For each observation made in a survey simulation, observed completeness (blue circles) coincident with planned completeness (red squares) indicate each simulated observation occurs under optimal conditions for a single visit. Because we are observing targets solely at the local zodiacal light minimum and do not modify integration times, all observations made are optimal. If targets were observed at sub-optimal zodiacal light levels, the $c_{t_{obs},i}$ would be below the $c_{0,i}$ as shown in Keithly et al. [45].

From the combined time varying limit in Eq. 3.3 applied to Eq. 3.2 we get the black sigmoid-like lines in Figure 3.9, specifically plotting $c_i(t_i)$ for the top 10, median, and lowest completeness optimized targets in the target list. The

median and lowest $c_i(t_i)$ lines are characteristic for the majority of similar low completeness targets and the addition of targets will typically be below the lowest completeness target in this list. The $c_i(t_i)$ and completeness side histogram shows a clustering of targets at lower completeness values, which can be attributed to the increased number of targets at larger d_i. The upper limit of completeness lines are consistent with the theoretical maximum completeness values.

Demonstrating the importance of including overhead and settling times in observations are the max c_i/t_i diamonds in Figure 3.9. These are universally located at some small integration time ($t_i < 10^{-3}$ d, $\forall\, i \in \mathbf{I}$) and small completeness meaning any optimized target list maximizing $\sum \frac{c_i(t_i)}{t_i}$ without overhead constraints will have strictly non-zero $t_i > 0$, $\forall\, i \in \mathbf{I}$. This means optimizing summed completeness without T_{OH} and $T_{settling}$ results in an observation target list of length N (651 in the case of Roman), which cannot be executed under realistic conditions. Similarly, observing at $\Delta\mathrm{mag}_{\mathrm{lim}}$ would result in sub-optimal individual target completeness and also leaves a substantial amount of unobserved phase space around each target.

Calculating completeness using the SAG13 planet population shows the summed ultimate completeness of all 651 targets is 13.538. The summed ultimate completeness of the observed targets is 3.641. The minimum completeness of these targets has increased due to the increased likelihood of larger $\Delta\mathrm{mag}$ planets at larger s in the SAG13 distribution in Figure 3.1 (b). As in the Kepler Like optimized target list, we see a single target is not being observed due to strict enforcement of observing time constraints. The major difference from Figure 3.9 to Figure 3.10 is the change in shape of the $c_i(t)$ lines. The SAG13

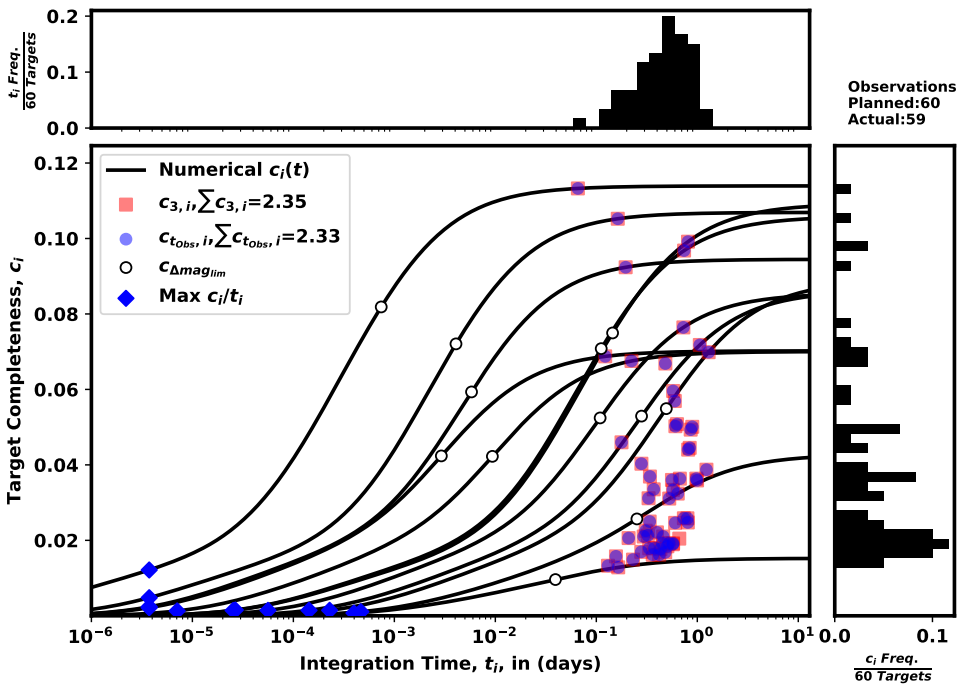

Figure 3.9: Completeness as a function of integration times calculated using the Kepler Like distribution, EXOCAT-1 star catalog, Nemati SNR model[69], and Leinert Table Zodiacal Light[56]. Black lines show completeness vs integration time for the 10 highest planned completeness targets, the median completeness target, and the lowest completeness target. Red squares indicate planned integration time and planned completeness based on ε maximizing summed completeness. Blue dots indicate observation integration time and observation completeness of the simulated observation. White dots represent completeness at $\Delta\mathrm{mag}_{\mathrm{lim}}$ and is plotted for the 10 highest, median, and lowest completeness planned targets. Blue diamonds show the completeness and integration time of the maximum c_i/t_i point for the 10 highest, median, and lowest completeness targets. This plot references data generated using C0vsT0andCvsTDATA_WFIRSTcycle6core-_CKL2_PPKL2_2019_10_07_11_58_.txt with specific target stars, integration times, and completeness included in Table B.1.

$c_i(t)$ lines have a lower ultimate completeness, but more targets have this limit. Additionally, each of these targets are observed for shorter integration times. which mostly have a higher theoretical maximum completeness and general shift towards higher completeness at lower integration times. There is addition-

ally a larger separation of lower completeness targets in Figure 3.10 compared to Figure 3.9. In general, completeness calculated using the SAG13 population is larger than completeness calculated using the Kepler Like population.

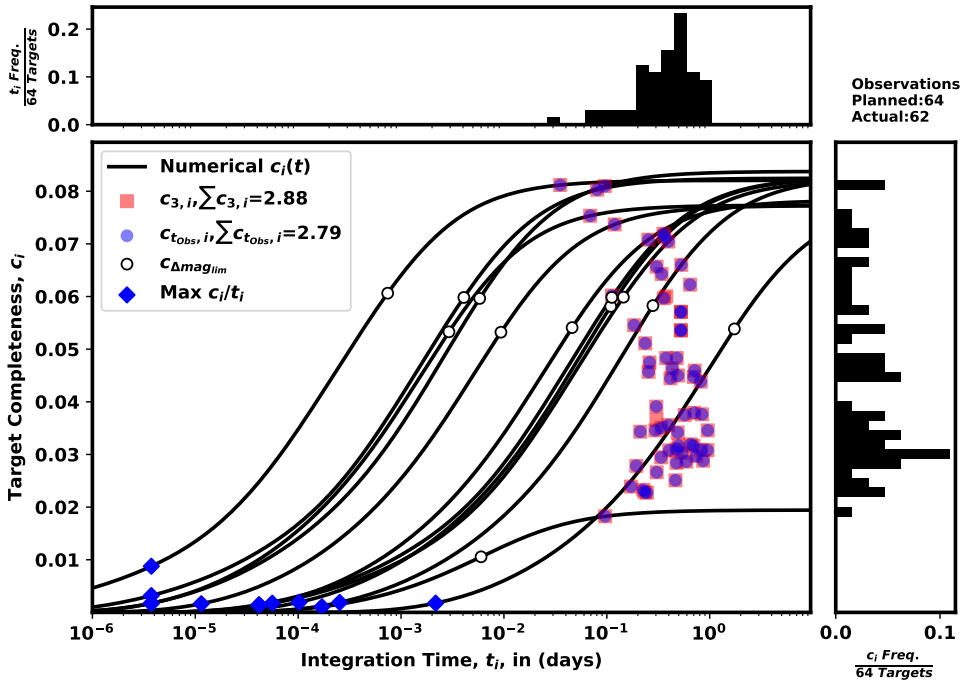

Figure 3.10: Completeness as a function of integration times calculated using the SAG13 distribution, EXOCAT-1 star catalog, Nemati SNR model[69], and Leinert Table Zodiacal Light[56]. Black lines show completeness vs integration time for the 10 highest planned completeness targets, the median completeness target, and the lowest completeness target. Red squares indicate planned integration time and planned completeness based on ε maximizing summed completeness. Blue dots indicate observation integration time and observation completeness of the simulated observations. White dots represent completeness at $\Delta\mathrm{mag}_{\mathrm{lim}}$ and is plotted for the 10 highest, median, and lowest completeness planned targets. Blue diamonds show the completeness and integration time of the maximum c_i/t_i point for the 10 highest, median, and lowest completeness targets. This plot references data generated using C0vsT0andCvsTDATA_WFIRSTcycle6core_CSAG13_PPSAG13_2019_10_07_14_29_.txt.

3.3.2 Sky Distribution of Completeness, Integration Times, and Targets

We are able to take the optimized target list included in Table B.1 and bin the heliocentric ecliptic coordinates (l,b) of each target, into triangular regions of approximately equivalent size and approximately isotropic distribution on the sky. When we sum integration time for all targets in each bin and normalize by bin area we get the skymap distribution shown in Figure 3.11. Since Figure 3.9 shows all integration times are between 0.1 and 2 days, we can conclude the $(l, b) = (-140°, 0°)$ and $(l, b) = (20°, 50°)$ bins have the highest concentrations of observing time. By summing the bins over heliocentric ecliptic latitudes (b), we see a large disparity in $\sum t_i$ vs l, target count vs l, and $\sum c_i$ vs l. Since Roman is planned to be on an L2 halo orbit and has a sun-orbital period of approximately 365.25 days, the Leinert local zodiacal light[56] is fixed in this rotating frame, and the time-distribution of stars is uneven, the optimally scheduled mission will have preferential observing times consistent with the distribution in Figure 3.11. This result is important for optimally distributing limited CGI time under the constraints of a 5 yr mission shared with multiple other instruments. Using this distribution, we can create preferentially distributed observing blocks for the CGI.

3.3.3 Detected Planet Properties

From our ensembles of survey simulations, we can look at how a and R of the detected planets are distributed. The top row of Figure 3.12 are the average distribution of R and a for all generated planets in a universe. In each sub-plot of

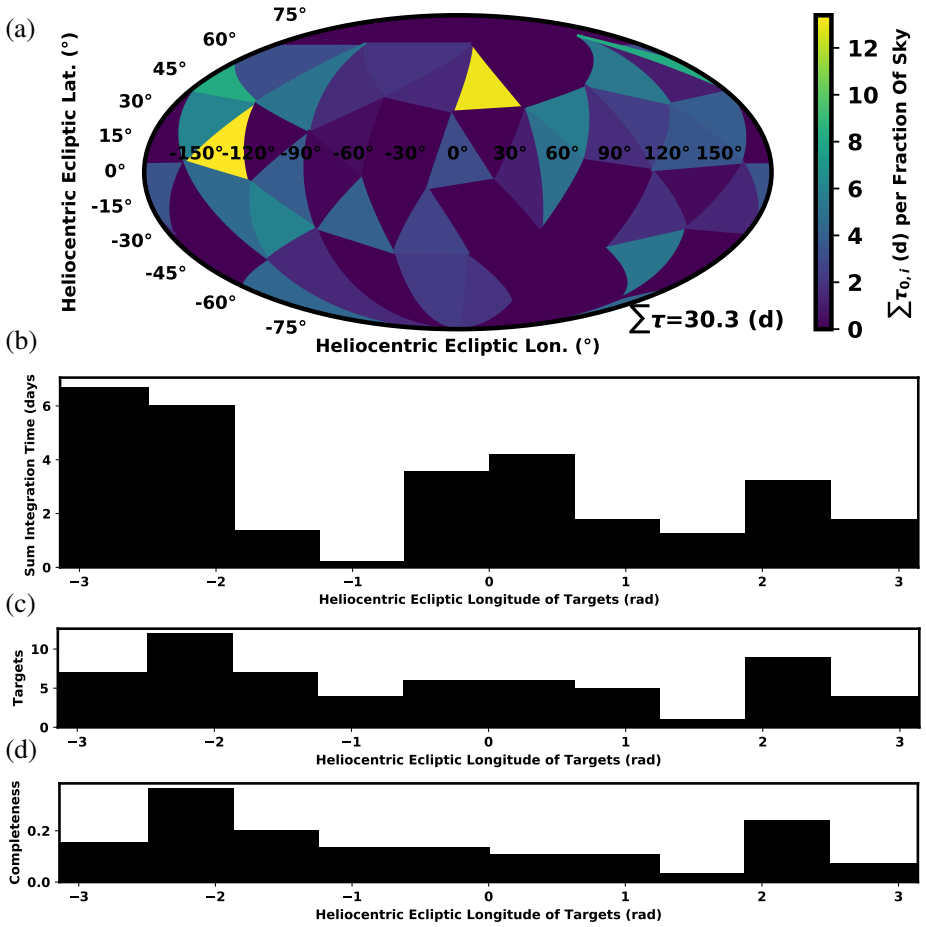

Figure 3.11: The distributions of a Kepler Like optimized target list including (a) a skymap divided into approximately evenly sized triangular bins with isotropic sky distribution showing the time/area density of observations, (b) a histogram of total sky time vs heliocentric ecliptic longitude (l), (c) a histogram of target counts vs l, (d) a histogram of summed completeness vs l

Figure 3.12, the top left and bottom right show the number of simulations used to generate the resulting distribution. Each 2D contour plot is normalized such that the integral over the area is 1 for the individual ensemble so the color scale can be shared. The white number in each gridded region shows the average number of planets generated or detected per simulation in that bin over the

ensemble of simulations. The number in the top right of (a) and (b) of Figure 3.12 are the sum total of all planets generated in the ensemble of universes. Sub-plots (c)-(f) of Figure 3.12 show the average distribution of detected planets over an ensemble. The number in the top right of (c)-(f) of Figure 3.12 are the sum total of all planets detected in the ensemble. These summations have been tabulated as average yields in Table 3.4. Sub-plots (c) and (d) of Figure 3.12 use a target list optimized for the Kepler Like planet population to observe universes of Kepler Like and SAG13 simulated planets. Similarly, sub-plots (e) and (f) of Figure 3.12 use a target list optimized for the SAG13 planet population to observe universes of Kepler Like and SAG13 simulated planets.

We can do an analysis on the kinds of planets Roman is expected to detect in a blind search survey. Since our universe is randomly generated, we show the distribution of generated R vs a planets for all stars for the Kepler Like and SAG13 planet populations in Figure 3.12. The implemented planet generation rate for the universe of Kepler Like planets is $\eta_{KL} \approx 2.377$, consistent to 2 decimal places with the planet population model in section 3.2.1. Here, η is simply calculated by dividing the sum total of planets in the ensemble of universes by the number of simulations in the ensemble (1000 from section 3.2.5) and number of target stars (651 from section 3.2.2). The $\eta_{\mathrm{SAG13}} \approx 5.618$ for SAG13 is also consistent to within 2 decimal places with the model in section 3.2.1. The generated planet populations are consistent with the limits presented in section 3.2.1. In section 3.2.1 we showed the smallest observable planet-star separation observable to be 0.292 AU and each of the four detected planets plots show all planets detected have $a > 0.292$ AU. A distinctive feature of the planet a generation is the "knee" applied at 10 AU which can be seen by the sharp drop-off in both populations.

There is a marginal difference in the y-axis of the contour plots between Kepler Like and SAG13 populations, as SAG13 generates smaller planet radii than Kepler like, so direct comparisons cannot be made between individual gridspace averages across universes. We also note the SAG13 universe generates an order of magnitude more large R and large a planets as indicated by the 24.29 and 221.19 grids from Kepler Like and SAG13 respectively (Figure 3.12 (a) and (b) gridspace (4,4)). Comparisons between planet populations used to calculate completeness observing the same planet population universe indicates that optimizing with the Kepler Like population results in marginally more smaller planet R detections. Specifically for the Kepler Like universe's largest average detection bin, we see that optimizing with the Kepler Like planet population results in 1.35 detected exoplanets on average and optimizing with the SAG13 planet population results in 1.11 detected exoplanets on average, which is significant, given our convergence results above. For the SAG13 universe's largest averaged detection bin, we see optimizing with the Kepler Like planet population results in the 3.51 detections and optimizing with SAG13 yields 3.55 detections but scaling by the number of detected planets gives $3.54 = 3.51 \times 16.266/16.101$ which is nearly identical. From these observations, we can conclude observing a universe of SAG13 planets with integration times optimized using completeness from a Kepler Like planet population results in more detections of small R planets. Each gridspace in the bottom two rows of Figure 3.12 (d) are greater than or equal to each gridspace in the bottom two rows of Figure 3.12 (f). We can specifically point to the 0.81 and 0.69 grid spaces that most evidently confirms this observation.

We can draw several conclusions by inspecting the average population of planets detected. Our simulations show Roman will not detect planets with

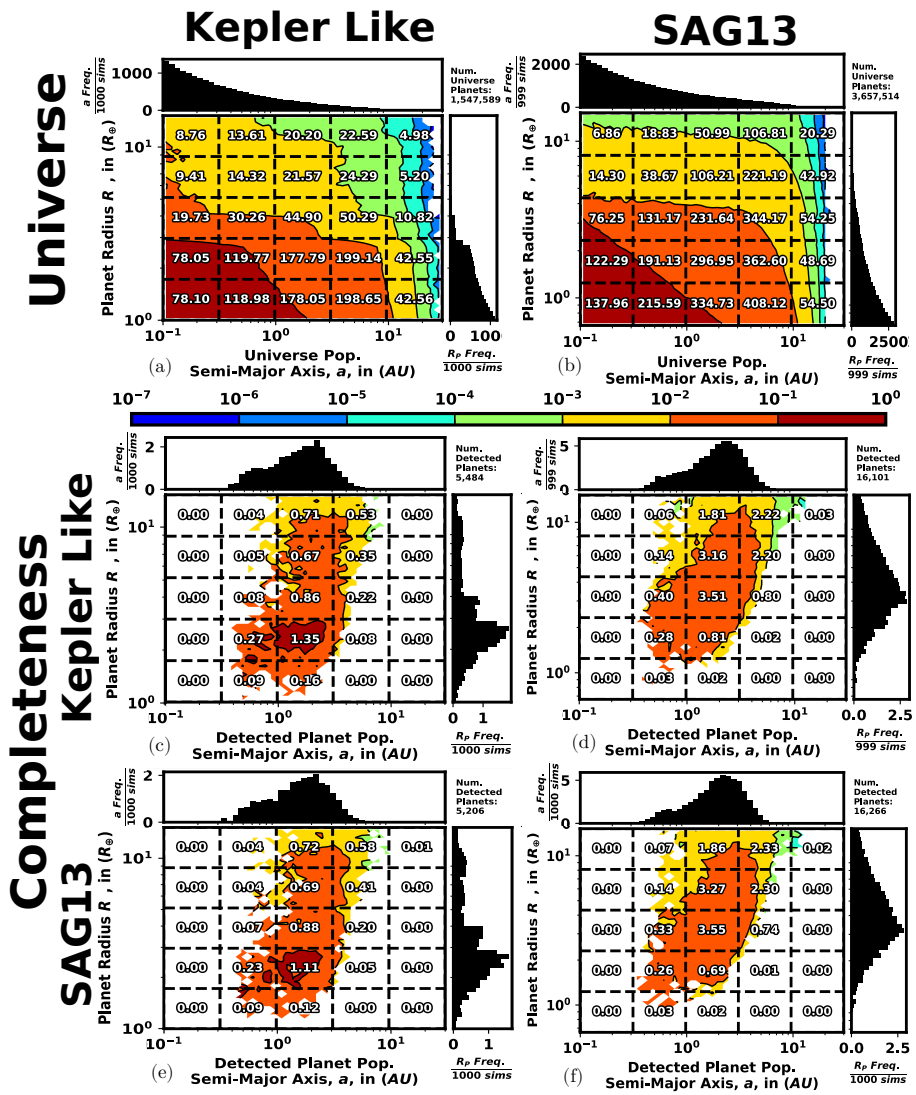

Figure 3.12: The universe of planets generated over all simulations for Kepler Like (a) and SAG13 (b) planet populations. (c) and (d) show the populations of detected planets for simulations run with completeness calculated using the Kepler Like planet population observing a universe of Kepler Like planets (a) and SAG13 universe of planets (b). (e) and (f) show the populations of detected planets for simulations run with completeness calculated using the SAG13 planet population observing a universe of Kepler Like planets (a) and SAG13 universe of planets (b). Overlay text on (a) and (b) shows average occurrences per grid-space averaged over the Monte Carlo of simulations. Overlay text on (e-f) shows average detections per grid-space averaged over the Monte Carlo of simulations. These plots reference RpvsSMAdetectionsDATA_WFIRSTcycle6core _CKL2_PPKL2_2019_04_05_19_34_.txt.

$a < a_{\mathrm{mercury}}$. We also see Roman is not capable of detecting planets with $R < R_{\oplus}$. We also note that Roman is not sensitive to planets beyond a_{saturn}. The majority of planets detectable by Roman are cold-Jovians and Super Earths. Based on Figure 3.12, we can conclude that optimizing integration times with the more pessimistic Kepler Like planet population universally biases detections towards smaller planets.

3.3.4 Overfitting

We have chosen to use the Kepler Like and SAG13 planet populations to optimize target lists in this paper, both of which are created based on the known population of exoplanets. Since a motivation for the Roman CGI is to observe new exoplanets in an unexplored region of space, we must investigate how yield for a target list of integration times optimized for one planet population changes when observing a universe full of planets based off another planet population.

In Table 3.4, optimizing a target list using completeness based off a planet population and observing that same planet population results in the highest yield. However, observing a universe of Kepler Like planets with a target list optimized for SAG13 planets results in a 5.06% decrease in exoplanets detected, a greater decrease than observing SAG13 planets with a target list optimized using Kepler Like planets (a 1.01% decrease). A possible explanation for this difference is our inclusion of the rare characterization. The characterization part of Table 3.4 does not indicate this is the case and shows more planets are characterized on average when optimized with the wrong planet population range. A characterization observation is triggered whenever a planet is detected with sufficiently small $\Delta\mathrm{mag}$ and separation such that the immediate re-observation could achieve a $SNR > 10$ with a newly calculated $t_i < 30$ d and all other detection observation filters in Section 3.2.5.

The conclusion we can draw from this exercise in overfitting is that optimizing with the more pessimistic Kepler Like planet population yields more robust detections and more characterizations if the planet population is actually SAG13. This warrants re-investigation with varying margins placed on $t_{\mathrm{obs},i}$.

Table 3.4: Summary of overfitting average unique detection yield and average characterizations from four Monte Carlo ensembles with optimized target list integration times calculated for different planet populations observing universes of different planets WFIRSTCompSpecPriors_WFIRSTcycle6core_3mo_405_19

		Planet Population	
	Completeness	Kepler Like	SAG 13
Average Yield	Kepler Like	5.484	16.117
	SAG13	5.206	16.266
Average Characterizations	Kepler Like	0.214	1.003
	SAG13	0.217	0.718

3.3.5 Varying Mission Length and Overhead Time

We investigate how the telescope's yield changes for varying time related aspects of the mission. The Roman telescope time is shared between 6 instruments, so we ran Monte Carlos of various surveys with different total telescope times dedicated to the CGI. This resulted in the yield distributions in Figure 3.13. From 0 to 3 months of telescope time, we see yield increase to 5 exoplanets. While from 3 months to 13 months, we only see a gain of 4 exoplanets. This is indicative of the diminishing returns from observing fainter stars further away.

The telescope overhead time is not precisely known (generally due to the uncertainty in time necessary to dig the CGI high contrast region). We took the time to investigate how changes in the telescope overhead time per observation effects the overall exoplanet yield that can be attained. The results are shown in Figure 3.14 are for a nominal 1 year mission. They indicate a very weak relationship where increasing overhead for all observations in the mission marginally reduces the mission yield. It is likely that this curve is quite similar to the slope of the curve in Figure 3.13 at 12 months of observing time and that shorter missions will be more sensitive to variations in overhead time.

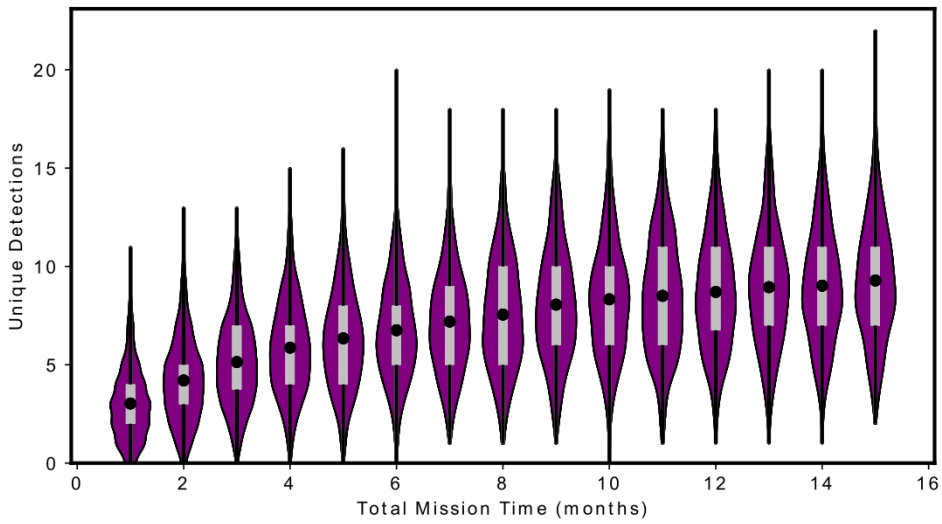

Figure 3.13: Number of unique detections vs mission length for the Roman Space Telescope

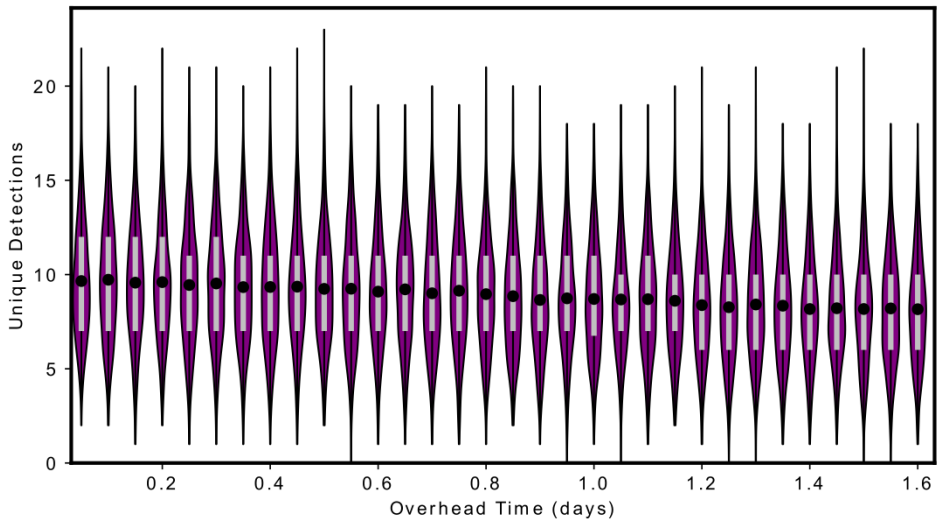

Figure 3.14: Number of unique detections vs total overhead time for the Roman Space Telescope

3.3.6 Selecting when to make observations in a single visit survey

We created a method for optimizing the distribution of integration time among select targets and selecting which targets to observe. Throughout each simulated survey in the Monte Carlo, we chose which target to observe based on when the next local zodiacal light minimum occurs for a target in the target list. We investigated several other metrics for selecting which target to observe next. In each case, our goal is the select the next target that minimizes the metric. These metrics and the associated yield from a Monte Carlo of simulated missions using this static selection metric is included in Table 3.5. The results in this table are the indicator of how the mission should be conducted and how we arrived at the selection metric used in this chapter. The single visit yield is maximized when we observe where the local zodiacal light of the target is furthest from its maximum zodiacal light intensity.

EXOSIMS is capable of dynamically scheduling a mission based on the current target star availability. This study is not particularly interesting because we will generally know when the CGI instrument can be used and when the target stars are available, but is demonstrative of EXOSIMS' capability to dynamically schedule missions. To implement a dynamically scheduled mission, we implement the optimization algorithm developed here and apply it to the set of targets currently available and the total amount of instrument time remaining. We can them select which target to observe at this particular moment. We tested a variety of different selection metrics to determine which one would maximize yield in a dynamically schedule mission. We found that the selection metric for a telescope forced to dynamically schedule itself is the $\frac{t_{fZ}}{C_{fZ}}$ selection

metric as noted in Table 3.5. We would also point out that a single-visit blind search which is implemented dynamically will find strictly less planets than the statically scheduled counterpart.

Metric	Static Yield	Dynamic Yield
$\frac{1}{C}$	8.70	8.28
$fZ(t) - fZ_{min}$	8.75	6.50
$fZ(t) - fZ_{max}$	8.83	6.22
$\frac{fZ(t)-fZ_{min}}{fZ_{max}-fZ_{min}}$	8.76	6.19
$\frac{fZ(t)-fZ_{min}}{fZ_{max}-fZ_{min}}$	8.78	6.21
$\frac{fZ(t)-fZ_{min}}{fZ_{max}-fZ_{min}}$	8.72	6.32
$\frac{t_{fZ}}{C_{fZ}}$	8.74	8.32
$\frac{t_{fZ_{min}}}{C_{fZ_{min}}}$	8.76	8.27

Table 3.5: Various selection metrics for choosing the next star in the target list to observe for the static and dynamic missions as well as the yield associated with a Monte Carlo of survey simulations using this selection metric.

3.3.7 Theoretical Single-Visit Yield of the Habitable Exoplanet Observatory

The optimized Target list has C_0 vs T_0 of Figures 3.9 and 3.10 show a scatter plot of the completeness vs integration times for the Roman 90 day technology demonstration mission. We similarly produced the scattering of completeness vs integration time for the target list resulting from optimizing the HabEx telescope with 6 years of observing time spread over a 12 year mission in Figure 3.15. This reflects the 50% of telescope time HabEx plans to dedicate to exoplanet direct imaging. The time represents an upper limit to the number of exoplanets discoverable since all time was dedicated to a single-visit survey. Most assuredly, the actual mission implemented will have a large portion of time dedicated to follow-ups and spectral characterizations. In Figure 3.15, the points near the top left are sparse, caused by the volume of space expanding with distance cubed (and the local star density remaining relatively constant) and the distribution of stellar luminosities resulting in some brighter stars. These top performers are almost certainly near their ultimate completeness. Moving clockwise around the arc we see an increasing density of targets as the distance-brightness begins to overlap and more targets become available that are lower performing. Some of these are at ultimate completeness and some of these have just reached the $\delta C/\delta t$ peak.

After optimizing the observation schedule for the HabEx telescope on the SAG13 planet population with 6 years of observing time, we ran a Monte Carlo of mission simulations and arrived at the yield histogram in Figure 3.16. The violin plots in Figure 3.17 show the distributions of various planets broken down by Kopparapu classification and Earth-like classification.

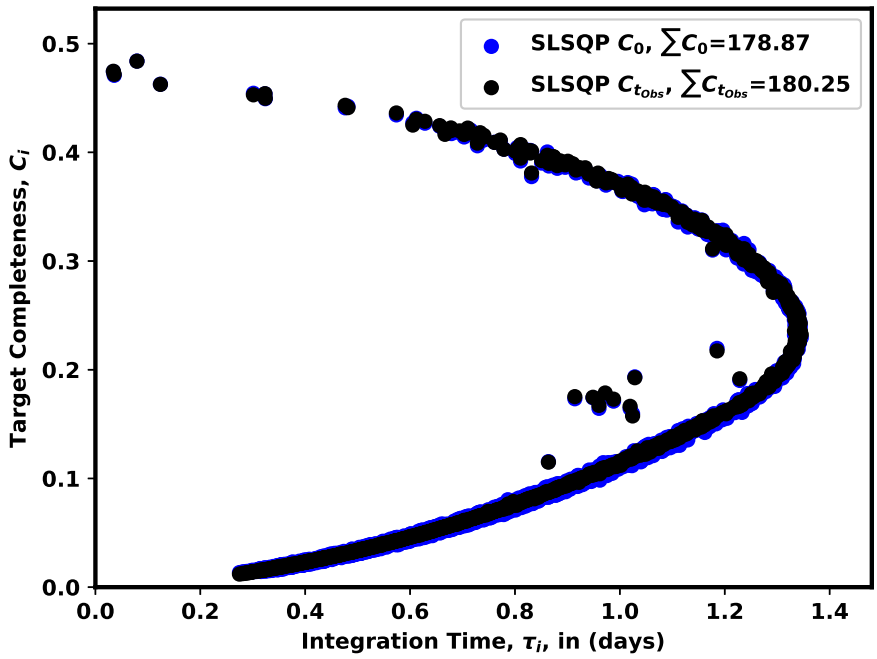

Figure 3.15: Completeness vs integration time of the target list optimized over the SAG13 planet population and HabEx telescope for the planned targets and implemented targets.

The complete R_p vs a distribution of the underlying population and the expected yields from the Monte Carlo of simulations are included in Figure 3.18. We are most interested in the two gridspaces at the bottom of the plot on either side of the $a = 1AU$ line. They are interesting because it is where most of the Earth-like exoplanets come from in the SAG13 planet population. We can note that despite 777 planets being simulated in that region, only 93 of them were detected at a ratio of 0.11. In contrast, near the top right, 191 planets were input and 67 of them were detected at a ratio of 0.35.

We adopted the same policy for scheduling this mission as in the Roman space telescope case, observing at the optimal conditions of local zodiacal light minimum. The timeline for one of these missions is plotted in Figure 3.19

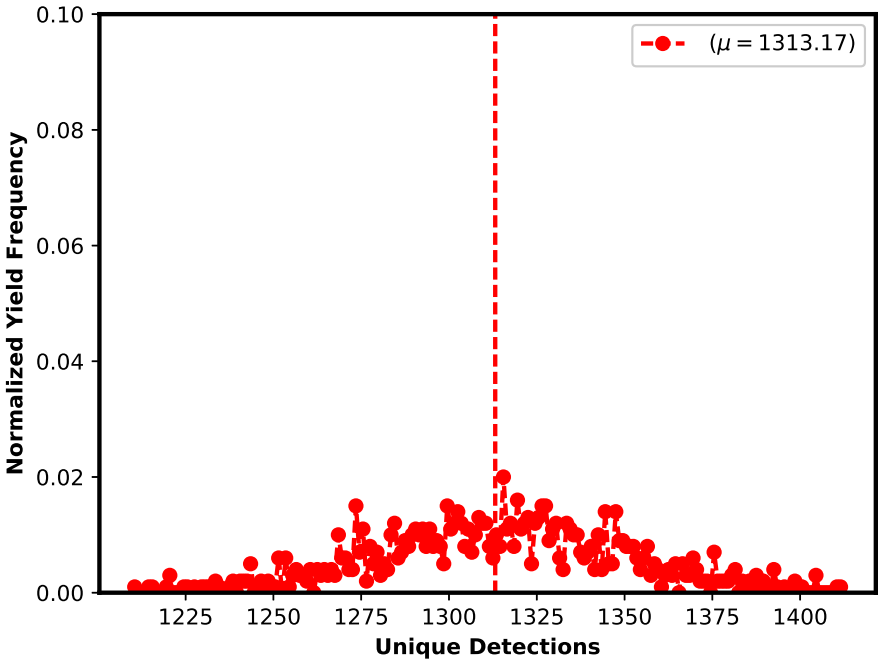

Figure 3.16: The yield histogram for an ensemble of HabEx blind search surveys optimized on and observing a universe of SAG13 planets.

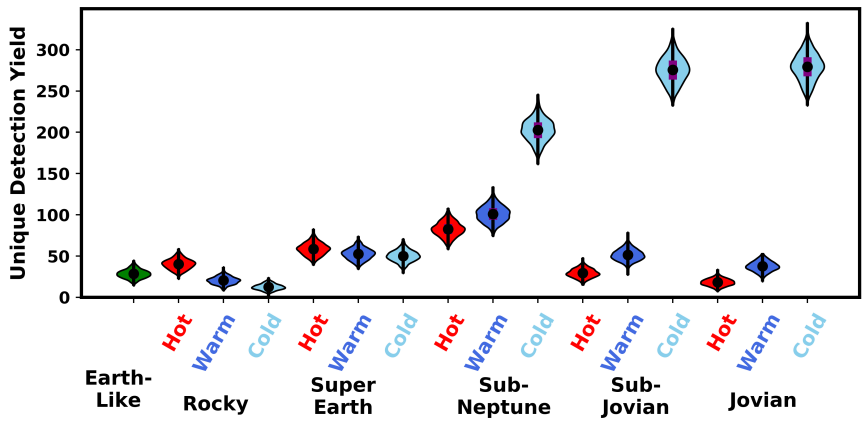

Figure 3.17: The yield distributions of planets detected during an exoplanet direct imaging blind search of the HabEx telescope optimized on and observing the SAG13 universe of planets broken down by Kopparapu classification and Earth-like classification.

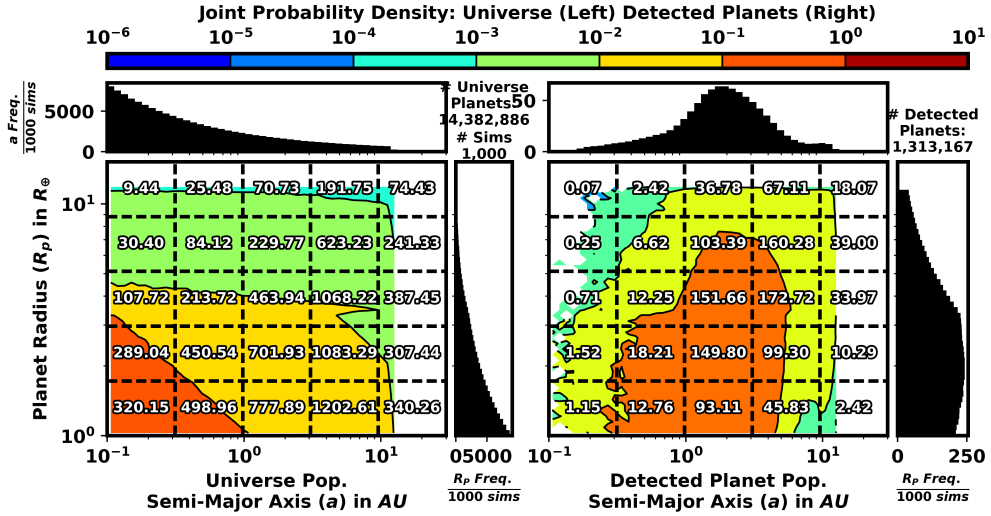

Figure 3.18: Universe population R_p vs a input distribution and output distribution.

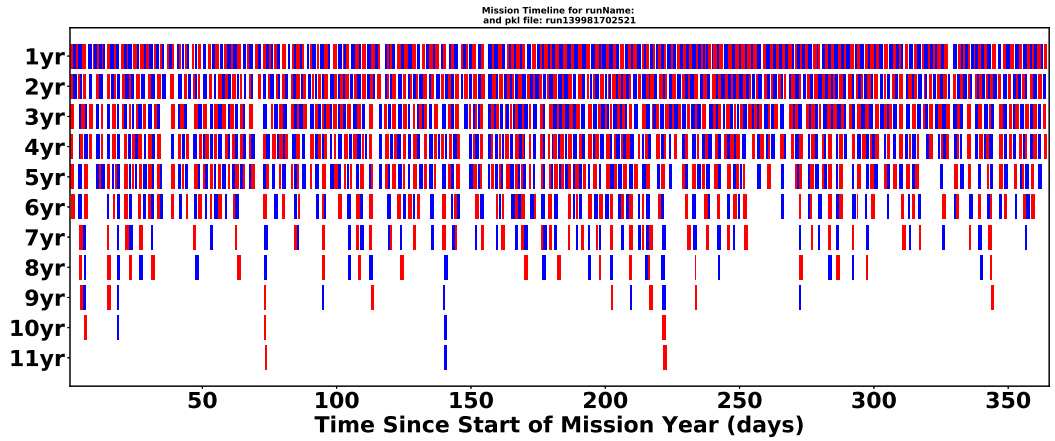

Figure 3.19: Example HabEx survey mission timeline. Observations alternate between blue and red colors to make observations more visibly obvious.

3.4 Conclusions

In this chapter, we presented our method of optimizing integration times and validating the optimized target list in a Monte Carlo of survey simulations using the EXOSIMS code base. We presented our implementation of a Kepler Like and SAG13 based planet populations and our associated methods for calculat-

ing completeness and simulating universes of planets. We presented our generalized target list integration time optimization process accommodating per observation overhead time constraints for a blind search single-visit survey and showed how the inclusion of overhead times is necessary when optimizing surveys. We discussed how EXOSIMS book-keeps all time varying aspects of a survey mission including keep-out regions of the sun and major planets using ephemeridis, the observatory's position on a L2 halo orbit, local zodiacal light for each target, positions of the target stars, positions of simulated planets around target stars, and our strict enforcement of total observing time. Under Roman's constraints, we show the optimal heliocentric ecliptic longitudes for target observation based on local zodiacal light intensity as well as more realistic local zodiacal light average minimum and average maximum magnitudes of 22.79 mag arcsec^{-2} and 21.59 mag arcsec^{-2}, respectively. The strictness of Roman's keep-out regions causes the visibility of some targets to drop below 28% which severely constrains both single visits and would constrain revisits. Making telescopes less sensitive to solar panel based and planet based keep-out regions keep-out regions enable observing at more ideal local zodiacal light conditions, increase the total target visibility, and will prevent aliasing of similar period planets when considering revisits. By making only optimal observations in our Monte Carlo survey simulations, we see the Roman optimized target list's preferential observing times are unevenly distributed on the sky and across heliocentric ecliptic longitudes,- but these longitudes do not necessarily line up with the completeness longitude distribution. The observed mismatch between the observing time distribution across the sky and the completeness distribution across the sky means observation at specific times of year will be more valuable than others throughout the mission. Most importantly, it means that in

the case where a mission is designed with pre-allocated observing blocks, blocks reserved for exoplanet imaging must take into account both the integration time and completeness distributions over ecliptic longitudes.

We validated our Roman optimized target list's summed completeness of 2.35 by performing a Monte Carlo of survey simulations on the Kepler Like planet population, achieving an observed summed completeness of 2.33 using our model of Roman. We have also demonstrated the convergence of the mean number of detected exoplanets from Monte Carlo of 1000 simulations to have 3.19% error at 3σ, giving additional confidence in the Monte Carlo results. Our Monte Carlo simulations also indicate that the Roman CGI detects 5.48 exoplanets, on average, when observing the Kepler Like planet population and 16.26 exoplanets on average when observing the SAG13 distribution. The vast majority of the Roman detectedable planets range in size from Super-Earths to Jovians at semi-major axes from 0.4 AU to 6 AU. Observing a population of Kepler Like planets with a target list optimized for a SAG13 population of planets results in a yield decrease in detections of $> 5\%$ whereas the inverse indicates a yield decrease $< 1\%$ indicating the Kepler Like planet population optimized target list is less sensitive to variations in the underlying planet populations and should be used to optimize CGI target lists. We also see that optimizing with a more pessimistic planet population universally results in more detections of small radius planets. The simulation inputs and results included in this paper are publicly available via Cornell's eCommons service at: `https://doi.org/10.7298/90n2-5j40`.

CHAPTER 4

PHASE FUNCTION YIELD COMPARISONS

All yield modeling results in this dissertation and every other publication (including Morgan et al. [65] and decadal telescope concept studies) are *substantially* effected by the underlying phase curves assumed; as we will show in this chapter. Since we only know the phase curves (and not even the entire phase curve in many cases) of a few planets, we are forced to assume what the phase function of the planet we are observing looks like. This is part of the reason orbit fitting with photometric measurements has not been attempted. In this chapter, we investigate the yield sensitivity of a single-visit exoplanet direct imaging mission to the actual planet phase function assumed and the actual planet phase function observed.

We ran 12 separate Monte Carlos of simulations testing the sensitivity of the overall exoplanet detection yield when optimizing over a planet population with different underlying phase curves. We are interested in knowing whether there are substantial differences between optimizing an observation schedule on a population with Φ_L, Earth's phase function, or quasi-Lambert phase function, and observing a universe of planets with a different phase function. These phase functions can be seen in Figure 2.2. The Lambert phase function is defined as

$$\Phi_L(\beta) = \left(\sin(\beta) + (\pi - \beta)\cos(\beta)\right)/\pi. \tag{4.1}$$

The quasi-Lambert phase function (Φ_{QL}) is defined in Eqn. 5.58 in chapter 5.

This study is relevant because the Φ_L (described in chapter 2) has been predominantly used in exoplanet direct-imaging mission modeling up until this point. At $\beta \approx 20°$, the Φ_L and Earth's phase function differ by approximately

5%. We wanted to know whether the use of this phase curve had a substantial impact on the overall yield. We additionally wanted to whether the assumption of Φ_{QL} for the work in chapters 5, 7, and 8 would have a substantive impact on overall mission yield.

4.1 Φ_L vs Φ_{QL} Comparison

We started with a comparison of the Φ_L vs Φ_{QL} yield results in Table 4.1. Across the board, observing a planet population with Φ_L resulted in higher overall yields which is to be expected since Φ_L is strictly higher over the entire range of phase angles. We also see the characteristic decrease in yield associated with optimizing over a planet population assumed to have the Φ_{QL} but observing a universe of planets with Φ_L. This also holds true when observing a universe of planets with Φ_{QL}. Effectively, **optimizing over a planet population with a different phase function from the underlying phase function had a minimal impact on the overall yield.**

We note here that the Lambert phase function, Earth's phase function, and quasi-Lambert phase function are all relatively similar and that other phase functions exist with a substantial impact on yield; like Mercury or Mars.

Figure 4.2 and Figure 4.1 show that a population of planets which have Φ_{QL} has a small bias towards detecting planets at smaller phase angles than planets with the Lambert phase function. Generally, Φ_{QL} is a better model of the Earth's phase function than the Lambert phase function concluded by observation of Figure 2.2.

Table 4.1: Number of unique detections from running a Monte Carlo of 1000 simulations optimized over the SAG13 planet population from chapter 2 assuming the Lambert phase function Φ_L, and Quasi-Lambert phase function Φ_{QL} and observing a population of planets with combinations of Φ_L and Φ_{QL}. The total observing time was set to 213.67125 days out of a 3 year mission using a HabEx-like telescope.

		Planet Population	
	Completeness	Φ_L	Φ_{QL}
Average	Φ_L	647.94	585.23
Yield	Φ_{QL}	647.73	585.41

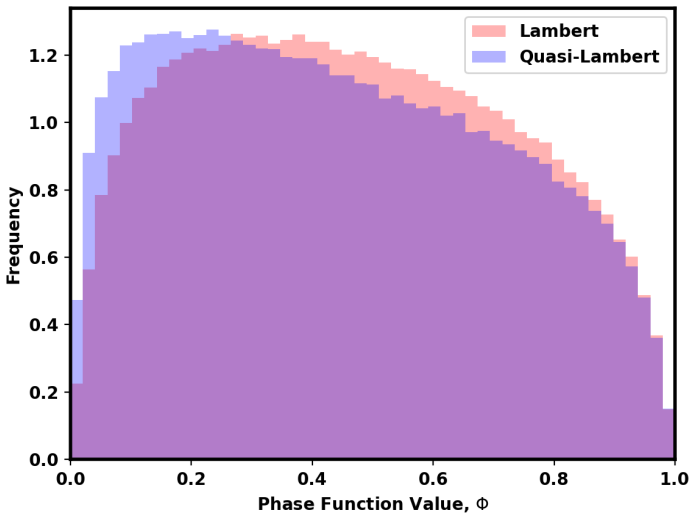

Figure 4.1: A histogram of planet phase function values at the time of detection from a Monte Carlo of 1000 mission simulations. In both cases, we optimize over and observe a universe of the SAG13 planet population. In the red histogram, we assume the Lambert phase function. In the blue histogram, we assume the quasi-Lambert phase function. (When the optimization was performed over a population with the opposite phase function, the histogram of phase function values was effectively identical to the underlying planet population.)

We additionally created histograms of the phase function values and phase angles of the planets detected when we optimized our target list on a population with one type of phase function and observed a population with another type of phase function. When optimizing over a population with the Lambert phase

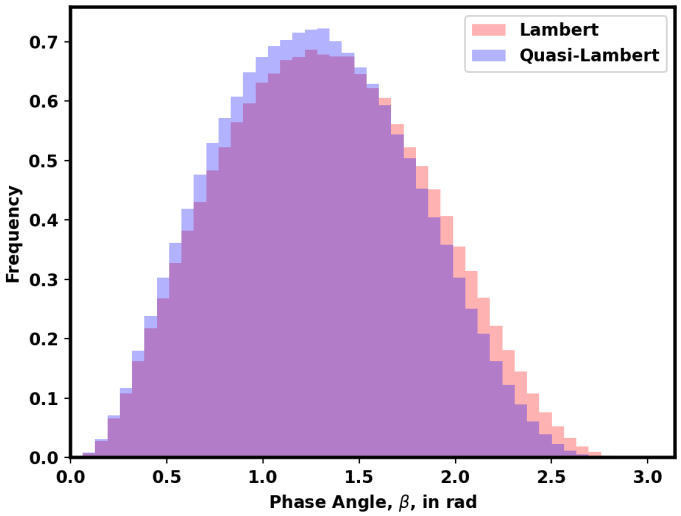

Figure 4.2: A histogram of phase angles of planets when they are detected for two separate simulations assuming the Lambert(red) and quasi-Lambert phase(blue) functions in planet models and when optimizing over the assumed SAG13 planet population. When the optimization was performed over a population with the opposite phase function, the histogram of phase angle values was effectively identical to the underlying planet population.

function but observing a population with Φ_{QL}, the histogram of phase function values looked identical to the blue histogram in Figure 4.1. The same can be said for the phase angles in Figure 4.2. When optimizing over a population of planets with Φ_{QL} but observing a population of planets with Φ_L, the underlying histograms of phase function values and phase angles of detected planets were nearly identical to when we optimized with Φ_{QL} and observed a universe of planets with Φ_{QL}.

4.2 Φ_L versus $\Phi_\oplus$ Comparison

We also took the time to test the sensitivity of the yield for different assumed phase curves on Earth-like populations of planets. In Morgan et al. [65] and

Table 4.2: Number of unique detections from running a Monte Carlo of 1000 simulations optimized over the Dulz Plavchan Earth Only planet population with the Lambert phase function Φ_L, and Earth's phase function $\Phi_\oplus$ and observing a population of planets with combinations of Φ_L and $\Phi_\oplus$. The total observing time was set to 213.67125 days out of a 3 year mission using a HabEx-like telescope.

		Planet Population	
	Completeness	Φ_L	$\Phi_\oplus$
Average	Φ_L	21.91	18.73
Yield	$\Phi_\oplus$	21.71	18.76

Table 4.3: Number of unique detections from running a Monte Carlo of 1000 simulations optimized over the "EarthTwinHabZone2" planet population with the Lambert phase function Φ_L, and Earth's phase function $\Phi_\oplus$ and observing a population of planets with combinations of Φ_L and $\Phi_\oplus$. The total observing time was set to 213.67125 days out of a 3 year mission using a HabEx-like telescope.

		Planet Population	
	Completeness	Φ_L	$\Phi_\oplus$
Average	Φ_L	6.92	5.72
Yield	$\Phi_\oplus$	6.82	5.69

Team [100], a population of "Earth-like" planets is used to optimize over and evaluate yield for the telescopes. In both cases, they evaluate these future telescopes by observing a population of "Earth-like" planets with Φ_L and optimize their DRM using Φ_L. We wanted to test the kind of differences in yield we could expect to see should the actual underlying planet population have different phase curves; Earth-like phase curves from chapter 2 to be precise. Table 4.3 **shows 20.9% overestimation of Earth-like exoplanet yield when observing exoplanets with Earth-like phase curves.** Table 4.2 shows 16.9% overestimation of Earth-like exoplanet yield when observing exoplanets with Earth-like phase curves. **These results indicate that the Earth-like exoplanet yields presented in** Morgan et al. [65] **and** Team [100] **are substantially overestimating their exoplanet yield.**

For a moment, let us inspect Table 4.3 from a different perspective. The Earth is constantly changing. The phase curve of Earth varies with time of year due to the tilt of its spin axis, throughout a day due to its surface variations, and by the hour due to cloud cover[59]. The broader statement is that institutions like **the Goddard Space Flight Center**[96, 97] **and Jet Propulsion Laboratory**[100]**are evaluating yield of telescopes using a phase curve that is substantially overoptimistic for the average Earth-like exoplanet phase curve, which itself could be optimistic considering the variability in Earth's own phase curve.**

4.3 Conclusions

Despite the Earth's average phase curve and Lambert phase function varying by only $\approx 5\%$ in amplitude, the results in this chapter indicate the Earth-like exoplanet yields presented in works like Morgan et al. [65] and Team [100] overestimate their Earth-like exoplanet yield by upwards of $\approx 20.9\%$.

We did not test the differences in yield between Φ_{QL} and $\Phi_{\oplus}$ due to the subjective similarity of Φ_{QL} and $\Phi_{\oplus}$ in Figure 2.2. The combination of mathematical simplicity in the quasi-Lambert phase function and apparent similarity to Earth's average phase function is justification enough for its prolific use in chapters 5, 7, and 8. It may be useful to confirm their similarity with simulation in the future. It may also be fruitful to investigate the effects of variability in Earth's phase function on yield.

CHAPTER 5

INTEGRATION TIME ADJUSTED COMPLETENESS

The original formulation of completeness uses instrument visibility limits, and ignores additional integration time and planetary motion constraints. Some of the sampled planets used to calculate completeness may transit in and out of an instrument's geometric and photometric visibility limits while they are being observed, thereby causing the integration time agnostic calculation to overestimate completeness. In this paper, we present a new method for calculating completeness, which accounts for the fraction of planets that leave the visibility limits of the telescope during the integration time period. We define completeness using the aggregate fraction of an orbital period during which planets are detectable, calculated using the specific times planets enter and leave an instrument's visibility limits and the integration time. To perform this calculation, we derive new analytical methods for finding the planet-star projected separation extrema, times past periastron these extrema occur, and times past periastron the planet-star projected separation intersects a specific separation circle. We also provide efficient numerical methods for calculating the planet-star difference in magnitude extrema and times past periastron corresponding to specific Δmag values. Our integration time adjusted completeness shows that, for a planned star observation at 25 pc with 1 day and 5 day integration times, integration time adjusted completeness of Earth-like planets is respectively reduced by 1% and 5% from the integration time agnostic completeness. By taking a mission optimized with Brown Completeness and calculating integration time adjusted completeness, we see the Brown Completeness optimized mission overpredicts yield by $\approx 9\%$. Integration time adjusted completeness calculated in this manner also provides a computationally inexpensive method for finding

dynamic completeness—the completeness change on subsequent observations.

Direct imaging blind search mission schedules can be optimized[47] by maximizing completeness[13]—the fraction of exoplanets from an assumed planet population that are detectable by a particular instrument at an arbitrary observation time. Completeness is typically parameterized by a limiting planet-star brightness difference ($\Delta\mathrm{mag}_{\mathrm{lim}}$), the inner working angle of the instrument (IWA), and outer working angle of the instrument (OWA). The original Monte Carlo approach developed by Brown in Ref. [13] involved creating a cloud of synthetic planets by sampling the underlying Keplerian orbital elements (KOE) and physical parameters of a planet population and determining the fraction of those individually simulated planets within the visible limits of the instrument. Multiplying completeness by the exoplanet occurrence rate gives the expected exoplanet yield for observing a given star. While completeness is a good metric for predicting instrument performance, the calculation described above only captures an instant in time and does not include whether the time that a planet is within the visible region of the telescope is sufficient to actually make a detection.

The original method of calculating completeness was developed by Robert Brown in Ref [13]. Our adaptation of this method in EXOSIMS[83] is extensively outlined in Ref [47] and involves randomly generating planet KOE, planet geometric albedo (p), and planetary radius (R) sampled from NASA's Exoplanet Program Analysis Group (ExoPAG) Study Analysis Group 13 (SAG13)[47, 50, 26] probability density functions, generating a finely binned 2D histogram of Δmag vs s (planet-star separation), and fitting a 2D spline to the histogram bins. In all current methods, completeness is calculated as the double integral of s and

Δmag over the joint probability density function as in Eqn. 17 of Ref [47] and Eqn. 7 in Ref [27]. The limits of integration define a detectable planet as one where $\Delta\mathrm{mag} < \Delta\mathrm{mag}_{\mathrm{lim}}$, and $d_i\mathrm{IWA} < s < d_i\mathrm{OWA}$, where d_i is the distance of the host star from the spacecraft. While the $\Delta\mathrm{mag}_{\mathrm{lim}}$ in this paper is used to describe a general upper limit of integration for calculating completeness, this $\Delta\mathrm{mag}_{\mathrm{lim}}$ can be formulated as a function of integration time as in Eqn. 12 of Ref. [47] by making assumptions about a multitude of instrument parameters and external noise sources. This approach, as conventionally implemented, is a good estimator for completeness[47], but does not take planet motion in time into account.

Searches like the Gemini Planet Imager and Nancy Grace Roman Space Telescope (Roman) Coronagraphic Instrument (CGI)[40] are sensitive to larger planets with larger planet-star separations and longer orbital periods[47]. They make use of Brown completeness to plan blind searches. However, future telescope concepts like the Habitable Exoplanet Observatory (HabEx)[100] and the Large UV/Optical/IR Surveyor (LUVOIR)[87] seek to find smaller Earth-like exoplanets, with shorter orbital periods, around stars further away. Their search criteria will result in Brown completeness based yield over-estimations due to planet motion out of instrument visibility limits. Figure 5.1 shows a schematic of a direct imaging observation, and demonstrates how a planet can be within the photometric and geometric visibility limits of the instrument and still not be detected. The red regions of the planet's orbit indicate where the planet is within the visible limits but not detectable because the planet will move out of the region in less time than it takes to detect the planet (case (b) in the figure). Since there will be some Earth-like exoplanets that are counted towards the completeness score but are not actually within the visibility constraints of

the instrument long enough to be directly imaged, we need a new method that only counts targets within the instrument visibility long enough to be observed or characterized.

Figure 5.2 demonstrates this phenomena in the separation vs. Δmag phase space commonly used to define instrument contrast curves and completeness. Figure 5.2(b), shows a short-period, fast-moving, Mars-like planet, which transitions into and out of the assumed instrument's visible limits before it can be detected. Figure 5.2(c) show the effect for a Uranus-like planet which crosses through and exits the visible region in less time than it takes for it to be detected. In these cases, Brown's completeness calculation would include simulated planets in these regions, thus overestimating the overall detection yield. Additionally, Figure 5.2(d) shows the last possible moment a Neptune-like planet could be imaged before it leaves the visible limits of the telescope. This demonstrates a portion of the orbit where the planet is within the visible limits of the telescope but is not detectable.

This paper presents a new method, implemented in the EXOSIMS modeling software[83], for calculating integration time adjusted completeness, which allows us to investigate exactly how much the original completeness definition overestimates planet yields. EXOSIMS is an exoplanet direct imaging mission modeling software used to simulate the Roman CGI[40] and future mission concepts such as HabEx[100] and LUVOIR[87]. EXOSIMS simulates populations of planets, observatories, instruments, and underlying dynamics to create full, end-to-end mission simulations. We derive distributions of potential mission yield from ensembles of these mission simulations. EXOSIMS utilizes completeness as a heuristic for target selection and observation scheduling[47],

implementing both Brown's Monte Carlo approach to completeness[13] as well as the analytical completeness formulation from Ref. [27]. However, EXOSIMS determines whether actual detections occur by evaluating the effective signal to noise ratio (SNR) of individual simulated observations on simulated planets. Ref. [47] discusses the full optimization process for a single-visit blind search, and showed that ideal yield from an EXOSIMS simulation ensemble (when mission constraints are discounted) for a limited blind search mission of Roman is equivalent to yield calculated via Brown Completeness.

Comparisons between Brown completeness based exoplanet yield estimations and Monte Carlo of full mission simulations have been done in Ref. [64] and the Standards Definitions and Evaluation Team Final Report[65]. The yields calculated by completeness are higher than the average yield from a Monte Carlo of full missions simulated in EXOSIMS as noted in Table 6 of Ref. [65]. These works attribute difference in yields to the additional mission constraints captured by the full mission simulation approach, inefficiencies in the optimization algorithms, and inefficiencies in the scheduling algorithms implemented in EXOSIMS.[39] The unmentioned assumption is that Brown completeness based yield estimates are accurate, but this paper demonstrates how the omission of planet motion and integration time reduces the resulting completeness yield estimates.

In order to know the amount of time an individual planet spends within the observable limits of an instrument, we need to calculate the times in a planet's orbit when a planet enters or exits these limits. This means that we need methods for calculating when a planet has a given planet-star separation and Δmag. Once we know all of the times when a planet enters or exits an instrument's

visibility limits, we know the fraction of time the planet is able to be detected with that instrument. Averaging over these visibility fractions for a large number of samples evaluates completeness in a fundamentally different way from its original formulation. These same methods also allow for the evaluation of integration time adjusted completeness, as well as a new method of calculating dynamic completeness[14].

Section 5.2 presents the derivation of this chain of calculations and discusses practical aspects of their implementation. Section 5.3 provides detailed validation of the methods, and presents results of the various calculations enabled by them. Finally, in Section 5.4, we discuss various aspects of the algorithms and results, as well as lay out future applications for this methodology.

5.1 Quartic Solution

The methods in this paper make use of the known analytical solutions to the quartic function[1]. We explicitly write them out here. We start with a set of

useful simplifying terms

$$
\begin{aligned}
p_0 =& \left(-\frac{3A^2}{8} + B\right)^3, \\
p_1 =& \left(A\left(\frac{A^2}{8} - \frac{B}{2}\right) + C\right)^2, \\
p_2 =& -A\left(A\left(\frac{3A^2}{256} - \frac{B}{16}\right) + \frac{C}{4}\right) + D, \\
p_3 =& -\frac{3A^2}{8} + B, \\
p_4 =& 2A\left(\frac{A^2}{8} - \frac{B}{2}\right), \\
p_5 =& -\frac{p_0}{108} - \frac{p_1}{8} + \frac{p_2 p_3}{3}, \\
p_6 =& \sqrt[3]{\frac{p_0}{216} + \frac{p_1}{16} - \frac{p_2 p_3}{6} + \sqrt{\frac{p_5^2}{4} + \frac{\left(-p_2 - \frac{p_3^2}{12}\right)^3}{27}}}, \\
p_7 =& \frac{A^2}{4} - \frac{2B}{3}, \\
p_8 =& \frac{2p_2 + \frac{p_3^2}{6}}{3p_6}, \\
p_9 =& \sqrt{-2\sqrt[3]{p_5} + p_7}, \\
p_{10} =& \sqrt{2p_6 + p_7 + p_8}, \text{ and} \\
p_{11} =& \frac{A^2}{2} - \frac{4B}{3}.
\end{aligned}
\tag{5.1}
$$

The analytical solutions are four piecewise functions

$$
x_0 = \begin{cases} -\frac{A}{4} + \frac{p_9}{2} - \frac{\sqrt{p_{11} + 2\sqrt[3]{p_5} + \frac{-2C - p_4}{p_9}}}{2} & \text{for } p_2 + \frac{p_3^2}{12} = 0 \\ -\frac{A}{4} - \frac{p_{10}}{2} - \frac{\sqrt{p_{11} - 2p_6 + p_9 + \frac{2C + p_4}{p_{10}}}}{2} & \text{otherwise} \end{cases}, \tag{5.2}
$$

$$
x_1 = \begin{cases} -\frac{A}{4} + \frac{p_9}{2} + \frac{\sqrt{p_{11} + 2\sqrt[3]{p_5} - \frac{2C + p_4}{p_9}}}{2} & \text{for } p_2 + \frac{p_3^2}{12} = 0 \\ -\frac{A}{4} - \frac{p_{10}}{2} + \frac{\sqrt{p_{11} - 2p_6 + p_9 + \frac{2C + p_4}{p_{10}}}}{2} & \text{otherwise} \end{cases}, \tag{5.3}
$$

$$x_2 = \begin{cases} -\frac{A}{4} - \frac{p_9}{2} - \frac{\sqrt{p_{11}+2\sqrt[3]{p_5}-\frac{-2C-p_4}{p_9}}}{2} & \text{for } p_2 + \frac{p_3^2}{12} = 0 \\ -\frac{A}{4} + \frac{p_{10}}{2} - \frac{\sqrt{p_{11}-2p_6+p_9+\frac{-2C-p_4}{p_{10}}}}{2} & \text{otherwise} \end{cases}, \text{ and} \tag{5.4}$$

$$x_3 = \begin{cases} -\frac{A}{4} - \frac{p_9}{2} + \frac{\sqrt{p_{11}+2\sqrt[3]{p_5}-\frac{-2C-p_4}{p_9}}}{2} & \text{for } p_2 + \frac{p_3^2}{12} = 0 \\ -\frac{A}{4} + \frac{p_{10}}{2} + \frac{\sqrt{p_{11}-2p_6+p_9+\frac{-2C-p_4}{p_{10}}}}{2} & \text{otherwise} \end{cases}. \tag{5.5}$$

Theoretically, we always have four solutions. Theoretically, we can use equations of coefficients to determine how many roots are real, complex, and double roots. The general form of the quartic defines the expressions Δ, P, D_2, R, and Δ_0 which are

$$\begin{aligned} \Delta =& 256D^3 - 192ACD^2 - 128B^2D^2 + 144BC^2D - 27C^4 + 144A^2BD^2 \\ & - 6A^2C^2D - 80AB^2CD + 18ABC^3 + 16B^4D - 4B^3C^2 \\ & - 27A^4D^2 + 18A^3BCD - 4A^3C^3 - 4A^2B^3D + A^2B^2C^2, \\ P =& 8B - 3A^2, \\ D_2 =& 64D - 16B^2 + 16A^2B - 16AC - 3A^4, \\ R =& A^3 + 8C - 4AB, \text{ and} \\ \Delta_0 =& B^2 - 3AC + 12D. \end{aligned} \tag{5.6}$$

After evaluation of these constants, we can determine

$$\text{Solution Types} = \begin{cases} \text{2 distinct } \Re \text{ roots \& 2 complex conjugate roots} & \Delta < 0 \\ \text{4 } \Re\text{distinct roots} & \Delta > 0 \ \& \ P < 0 \ \& \ D < 0 \\ \text{2 pair complex conjugate roots} & \Delta > 0 \ \& \ (P > 0 \mid D > 0) \end{cases} \tag{5.7}$$

However, the use of this theoretical classification does not work when numerical errors are introduced. The accumulation of numerical errors causes to solutions

to be improperly classified for a sufficiently large number of cases to prohibit the use of these classifications. The Δ expression rarely evaluates to $\Delta = 0$ when it should do so quite frequently. Numerical rounding errors can also frequently result in the evaluation $\Delta < 0$ when in reality $\Delta > 0$ and visa versa. To accommodate these differences between theoretical and practical implementation, we laboriously describe our implementation method for practically determining how many solutions exist and what they are in section 5.2

5.2 Methods

In this section, we present our detailed process for calculating integration time adjusted completeness. The methods detailed in this section are publicly available in the exodetbox Python repository[42]. We do this by finding the time windows where a planet is within the separation and Δmag visibility limits of an instrument, discounting each time window by the integration time. The general overview of this process is as follows:

1. Calculate locations of apparent intersections between the projection of the 3D orbit into the plane of the sky and the s_{WA} circle about the star
   (a) Parameterize the 3D orbit as an ellipse in the plane of the sky
   (b) Formulate the planet-star separation equation and its derivative
   (c) Solve for the magnitude and locations of planet-star separation extrema
   (d) Identify and assign the subset of algebraic solutions that are separation extrema

(e) Classify the expected number of intersections between the projected ellipse and the s_{WA} circle

(f) Solve for intersections between the projection of the orbital ellipse and the s_{WA} circle

(g) Identify and assign the subset of algebraic solutions that form intersections

2. Calculate locations and magnitudes of Δmag intersections

(a) Formulate an expression isolating the Δmag and ν terms and its' derivative

(b) Express this formulation as a polynomial and solve for the algebraic solutions

(c) Identify and assign the subset of algebraic solutions that are Δmag extrema

(d) Classify the expected number of Δmag and $\Delta\mathrm{mag}_{\mathrm{lim}}$ intersections

(e) Solve for Δmag and $\Delta\mathrm{mag}_{\mathrm{lim}}$ intersections

(f) Identify and assign the subset of algebraic solutions that form intersections

3. Calculate ν from X and Y for each intersection and extrema
4. Calculate t from ν of each intersection and extrema
5. Combine times of s_{WA} and $\Delta\mathrm{mag}_{\mathrm{lim}}$ intersections to create time-windows between intersections
6. Identify time-windows where the planet is visible or not visible
7. Calculate integration time adjusted completeness averaging the orbital fraction of time a planet is visible discounted by the integration time

The general equations for Δmag and s used in these derivations are

$$\Delta\text{mag} = -2.5\log_{10}\left(p\left(\frac{R}{|\underline{r}_{k/i}|}\right)^2\Phi(\beta)\right) \tag{5.8}$$

and

$$s = \|\underline{r}_{k/i} - (\underline{r}_{k/i}\cdot\hat{\underline{r}}_{i/SC})\hat{\underline{r}}_{i/SC}\|. \tag{5.9}$$

Here, R is the planet radius, p is the geometric albedo of the planet, and $\Phi(\beta)$ is the planet phase function. The other variables are defined in Figure 5.3, where β is the star-planet-observer angle (also called the phase angle) $\underline{r}_{k/i}$ is the vector from star i to planet k, and $\hat{\underline{r}}_{i/SC}$ is the unit vector from the spacecraft (SC) to the star ($\hat{\underline{r}}$ is the unit vector of $\underline{r}$). The plane of the sky for a given observation lies in the $\hat{\underline{x}}$ and $\hat{\underline{y}}$ plane where $\hat{\underline{r}}_{i/SC}$ defines $\hat{\underline{z}}$ of the target system. For our purposes, the direction of $\hat{\underline{x}}$ is arbitrary, but is typically taken to be a well-defined, inertially fixed direction, such as the ICRS mean equinox or pole direction. Here, and throughout the paper, i in a subscript refers to the i^{th} target star and i (not subscripted) refers to the orbit inclination.

5.2.1 Projected orbit and separation intersection

In this section we derive an analytical expression for the true anomaly (ν) of s-orbit intersection points between a circle in the plane of the sky and the projection of a 3D Keplerian orbit on the plane of the sky. A practical example of a circle in the plane of the sky is the projected inner or outer working angle of the instrument, equal to IWAd_i (or OWAd_i) for target star distance d_i. An orbit defined by Keplerian orbital elements (KOE) takes the shape of an ellipse in the orbital plane. The perpendicular projection of a 3D elliptical orbit onto the plane

of the sky is given by the $\underline{\hat{x}}$ and $\underline{\hat{y}}$ components of the 3D orbit. However, the resulting expression is not easily solvable for the true anomalies at intersection points. Instead, we can express the orbit projection in the plane of the sky as another ellipse. This simplifies the difficult intersection problem into analytically solvable sub-problems and yields a relatively simple solution to the intersection between a circle in the plane of the sky and the projected orbit in the plane of the sky. The full procedure is:

1. Define KOE
2. $\underline{r}_{k/i}$ from KOE
3. Orbiting Foci F from KOE
4. Calculate 3D Orbit Ellipse Center
5. Projecting 3D Ellipse to 2D Ellipse
   (a) Proof that 3D Ellipses Project to 2D Ellipses
   (b) Project 3D Ellipse Center to 2D Ellipse Center
   (c) Project Ellipse Orbiting Foci into plane of the sky
   (d) Project Semi-minor axis line of 3D Ellipse to 2D Ellipse
   (e) Project Semi-major axis line of 3D Ellipse to 2D Ellipse
   (f) Calculate $\overline{QQ'}$ construction line from Semi-minor and semi-minor axis
   (g) Calculate projected ellipse semi-major axis and semi-minor axis from $\overline{O'Q'}$ and $\overline{O'Q}$
   (h) Calculate projected semi-major axis angular offset from X-axis of plane of the sky

6. Derotate the projected ellipse
7. Center the projected ellipse
8. Find minimum, maximum, local minimum, and local maximum of projected planet-star separation
    (a) Formulate projected planet-star separation equation
    (b) Re-format and set $\delta s^2/\delta x_e$ equal to 0
    (c) Combine coefficients into standard Quartic form
    (d) Use standard general quartic solutions
    (e) Take the absolute value and only real component of x_e solutions
    (f) Calculate y_e associated with each solution
    (g) Assign solutions to minimum, maximum, local minimum, and local maximum planet-star separations
        i. For all solutions (All real and Only 2 Real)
            A. Calculate $s_{\min}$ from x_1 and assign $(x_{\min}, y_{\min})$ of quadrant 1
            B. Calculate $s_{\max}$ from x_0 and assign $(x_{\max}, y_{\max})$ of quadrant 1
        ii. All real solutions (where all solutions have $\Im(y) < 10^{-5}$, additionally assign)
            A. The larger of $s_{(x_2)}$ and $s_{(x_3)}$ becomes s_{lmax} and assign $(x_{\text{lmax}}, y_{\text{lmax}})$ of quadrant 1
            B. The smaller of $s_{(x_2)}$ and $s_{(x_3)}$ becomes s_{lmin} and assign $(x_{\text{lmin}}, y_{\text{lmin}})$ of quadrant 1
        iii. Assign solution signs to proper quadrants
9. Find circle and projected derotated centered ellipse intersection points

(a) Formulate circle-ellipse intersection equation

(b) Re-format into standard Quartic Form

(c) Use standard general quartic solutions

(d) Classify intersection solutions

i. Inside outer separation bounds, $s_{\text{min}} < s < s_{\text{max}}$

ii. Inside local min/max separation bounds, $s_{\text{lmin}} < s < s_{\text{lmax}}$

iii. Outside outer separation bounds (no intersections)

(e) Calculate intersection solutions for planets with s_{min}, s_{max}, s_{lmin}, and s_{lmax}

i. Two intersections on same y side of ellipse as the star, $s_{\text{min}} < s < s_{\text{lmin}}$

$$x = \begin{cases} x_3, \Im(x_1) > 10^{-10} \\ x_1, \Im(x_1) < 10^{-10} \\ x_0 \end{cases}$$

ii. Four intersections where, $s_{\text{lmin}} < s < s_{\text{lmax}}$

- calculate $\Delta x = x_k - |x|$, ($k \in \{0, 1, 2, 3\}$)
- sort Δx_k from min to max and rearrange the associated x_k to match that order
- Same XY points is x_3
- Same X opposite Y is x_2
- Opposite X Same Y is x_0
- Opposite X opposite Y is x_1

iii. Two intersections on opposite x side of ellipse as the star, $s_{\text{lmax}} < s < s_{\text{max}}$

- x_0 and x_1

- y_1 is opposite sign of $|y|$

(f) Calculate intersection solutions for planets with only $s_{\min}$ and $s_{\max}$

i. Calculate projected ellipse quadrant separation bounds $s_{x,b+y}$, $s_{x,b-y}$, $s_{a+x,y}$, and $s_{a-x,y}$

ii. Identify star location type and quadrant order

- Type 0 occurs where $s_{x+a,y} < s_{x,y+b}$. Smallest to largest order: $s_{x,b-y}$, $s_{a-x,y}$, $s_{x+a,y}$, $s_{x,y+b}$
- Type 1 occurs where $s_{x,y+b} < s_{a-x,y}$. Smallest to largest order: $s_{x,b-y}$, $s_{x,y+b}$, $s_{a-x,y}$, $s_{x+a,y}$
- Type 2 occurs where $s_{a-x,y} < s_{x,y+b}$ and $s_{x,y+b} < s_{x+a,y}$ and $s_{x,b-y} < s_{a-x,y}$. Smallest to largest order: $s_{x,b-y}$, $s_{a-x,y}$, $s_{x,y+b}$, $s_{x+a,y}$
- Type 3 occurs where $s_{a-x,y} < s_{x,b-y}$. Smallest to largest order: $s_{a-x,y}$, $s_{x,b-y}$, $s_{x,y+b}$, $s_{x+a,y}$

Projection of the elliptical orbit

Given the KOE of a 3D orbit and a plane to project it on, we can calculate the semi-major and semi-minor axes of the projected orbit (a_p and b_p, respectively), as well as the angle between the projected semi-major axis and $\hat{\underline{x}}$ which we call (θ). We first convert the KOE into orbital radius components in the Cartesian XYZ coordinate system as in Figure 5.3

$$\begin{aligned} X &= r(\cos(\Omega)\cos(\omega+\nu) - \sin(\Omega)\sin(\omega+\nu)\cos(i)) \\ Y &= r(\sin(\Omega)\cos(\omega+\nu) + \cos(\Omega)\sin(\omega+\nu)\cos(i)) \\ Z &= r\sin(i)\sin(\omega+\nu). \end{aligned} \tag{5.10}$$

Where r is the orbital radius (magnitude of $\underline{r}_{k/i}$), given by

$$r = \frac{a(1-e^2)}{1+e\cos(\nu)}\,, \tag{5.11}$$

Ω is the longitude of the ascending node, ω is the argument of periapsis, ν is the true anomaly, and e is the eccentricity of the planet's orbit.

Figure 5.4 shows a schematic view of the projection of the orbit onto the plane of the sky. There are two particularly important points associated with the projected orbit ellipse: F is the filled focus (star location) of the orbit and retains the same coordinates in the plane of the sky. When observing a star, F is the center of all working angle circles, and the origin of the XYZ coordinate system. Note that in Figure 5.4 the projected ellipse is located well below the original 3D ellipse for clarity, but the points F indicated by the orange circle and F indicated by the orange $\times$ are in fact coincident.

Second, O is the geometric center of the 3D orbit and is found most efficiently by averaging the XYZ locations of the planet at apoapsis and periapsis

$$\overline{FO} = \frac{1}{2}(\underline{r}_{k/i}(\nu=0) + \underline{r}_{k/i}(\nu=\pi))\,, \tag{5.12}$$

where $\overline{FO}$ is the line segment (equivalently Euclidean vector) from F to O and $\underline{r}_{k/i}(\nu)$ is the evaluation of Eqn. 5.10 for the given value of ν. As $\underline{\hat{x}}$ and $\underline{\hat{y}}$ define the plane of the sky, the XYZ coordinates of the geometric center of the projected ellipse (O') are given by

$$O' = < \overline{FO}\cdot\underline{\hat{x}}, \overline{FO}\cdot\underline{\hat{y}}, 0 > \ . \tag{5.13}$$

We can use a construction proof to show any generic 3D ellipse projects to a 2D ellipse, as shown graphically in Figure 5.4. Let us suppose we have some ellipse on an arbitrary plane indicated by the black ellipse in Figure 5.4. We

will say $\overline{AB}$ and $\overline{CD}$ are the principal axes of some this 3D ellipse. $\overline{AB}$ and $\overline{CD}$ intersect at point O, the geometric center of this 3D ellipse. We will say point P is any point on the ellipse with H being the projection of point P onto axis $\overline{AB}$ and K being the projection of point P onto axis $\overline{CD}$. By the definition of an ellipse, we have

$$\frac{\overline{OH}^2}{\overline{OB}^2} + \frac{\overline{OK}^2}{\overline{OD}^2} = 1. \tag{5.14}$$

Now we let A', B', C', D', O', K', H', and P' be the perpendicular projections of points A, B, C, D, O, K, H, and P onto any given plane. Since perpendicular projections preserve the ratios of segments on a line, we can now say

$$\frac{\overline{O'H'}^2}{\overline{O'B'}^2} + \frac{\overline{O'K'}^2}{\overline{O'D'}^2} = 1. \tag{5.15}$$

This equation means point P' belongs to the ellipse having $A'B'$ and $C'D'$ as conjugate diameters. For an ellipse, two diameters are conjugate if and only if the tangent line to the ellipse at an endpoint of one diameter is parallel to the other diameter.

The projection of the semi-major axis and semi-minor axis from the 3D orbit onto the 2D plane of the sky form conjugate diameters of the projected ellipse. Any two diameters of an ellipse are conjugate diameters if and only if the tangent line to the ellipse at an endpoint of one diameter is parallel to the other diameter[95]. Each pair of conjugate diameters of an ellipse has a corresponding tangent parallelogram, sometimes called a bounding parallelogram. In Figure 5.4, the pair of blue lines ($\overline{A'B'}$ and $\overline{C'D'}$) are specific examples of conjugate diameters. The pair of purple lines ($\overline{IR}$ and $\overline{ST}$) are also examples of conjugate diameters, and form the semi-major and semi-minor axes of the projected ellipse.

The semi-major and semi-minor axes of the projected ellipse may be found

from any conjugate diameters. We take the conjugate diameters $\overline{A'B'}$ and $\overline{D'C'}$ and draw line $\overline{QQ'}$ through B', perpendicular to $\overline{D'C'}$ as shown by the grey line in Figure 5.5. Points Q and Q' are chosen such that $\overline{B'Q} = \overline{B'Q'} = \overline{O'D'}$. The principal axes $\overline{IR}$ and $\overline{ST}$ lie on the bisectors of the angles formed by lines $\overline{O'Q}$ and $\overline{O'Q'}$. From this construction we can calculate the projected ellipse semi-major axis, semi-minor axis, and angular offset of the semi-major axis from $\underline{\hat{x}}$[12]. $\overline{IR}$ and $\overline{ST}$ are given by

$$\overline{IR} = \overline{O'Q'} + \overline{O'Q} \tag{5.16}$$

$$\overline{TS} = \overline{O'Q'} - \overline{O'Q}\,. \tag{5.17}$$

Defining the angle between $\overline{O'B'}$ and $\overline{O'D'}$ as ϕ, the cosine rule applied to triangles $O'B'Q$ and $O'B'Q'$ yielding

$$|\overline{O'Q}|^2 = |\overline{O'B'}|^2 + |\overline{O'D'}|^2 - 2|\overline{O'B'}||\overline{O'D'}|\sin\phi \tag{5.18}$$

$$|\overline{O'Q'}|^2 = |\overline{O'B'}|^2 + |\overline{O'D'}|^2 + 2|\overline{O'B'}||\overline{O'D'}|\sin\phi\,, \tag{5.19}$$

where $|\overline{O'B'}|$ denotes the length of $\overline{O'B'}$. Inserting these into Eqn. 5.16, we obtain

$$\overline{O'R}\cdot\overline{O'S} = |\overline{O'B'}||\overline{O'D'}|\sin\phi \tag{5.20}$$

$$|\overline{O'R}|^2 + |\overline{O'S}|^2 = |\overline{O'B'}|^2 + |\overline{O'D'}|^2. \tag{5.21}$$

$|\overline{IR}|$ must be twice the semi-major axis of the projected ellipse (a_p) so

$$a_p = \frac{|\overline{IR}|}{2} = |\overline{O'R}| \tag{5.22}$$

and $|\overline{TS}|$ must be twice the semi-minor axis of the projected ellipse so

$$b_p = \frac{|\overline{TS}|}{2} = |\overline{O'S}|\,. \tag{5.23}$$

The angle of the semi-major axis of the projected ellipse from $\underline{\hat{x}}$ can be calculated using the average of the angles between $\overline{O'Q}$ and $\underline{\hat{x}}$ and $\overline{O'Q'}$ and $\underline{\hat{x}}$

$$\theta = \frac{1}{2}\left(\tan^{-1}\left(\frac{\overline{O'Q}\cdot\underline{\hat{y}}}{\overline{O'Q}\cdot\underline{\hat{x}}}\right) + \tan^{-1}\left(\frac{\overline{O'Q'}\cdot\underline{\hat{y}}}{\overline{O'Q'}\cdot\underline{\hat{x}}}\right)\right). \tag{5.24}$$

We can write the analytical expressions for a_p, b_p, and θ using full expansions of Eqn. 5.22, Eqn. 5.23, and Eqn. 5.24. These expressions are far to long to be practically conveyed so we use the following intermediary parameters here and only here, to simplify these expressions.

$$
\begin{aligned}
K_0 &= e\left(1-e^2\right) \\
K_1 &= \sin\left(\Omega\right)\cos\left(\omega\right) + \sin\left(\omega\right)\cos\left(\Omega\right)\cos\left(i\right) \\
K_2 &= \sqrt{\tfrac{e+1}{1-e}} \\
K_3 &= a\left(1-e^2\right) \\
K_4 &= -\sin\left(\Omega\right)\sin\left(\omega\right)\cos\left(i\right) + \cos\left(\Omega\right)\cos\left(\omega\right) \\
K_5 &= \sqrt{K_1^2K_3^2 + K_4^2K_3^2 + K_3^2\sin^2\left(i\right)\sin^2\left(\omega\right)} \\
K_6 &= K_3\big(-\sin(\Omega)\cos(\omega) - \sin(\omega)\cos(\Omega)\cos(i)\big)/(1-e) \\
K_7 &= K_3\big(\sin(\Omega)\sin(\omega)\cos(i) - \cos(\Omega)\cos(\omega)\big)/(1-e) \\
K_8 &= \tfrac{K_3\left(\sin(\Omega)\cos(\omega+2\tan^{-1}(K_2))+\sin(\omega+2\tan^{-1}(K_2))\cos(\Omega)\cos(i)\right)}{(e\cos(2\tan^{-1}(K_2))+1)} \\
K_9 &= \tfrac{K_3\left(-\sin(\Omega)\sin(\omega+2\tan^{-1}(K_2))\cos(i)+\cos(\Omega)\cos(\omega+2\tan^{-1}(K_2))\right)}{(e\cos(2\tan^{-1}(K_2))+1)}
\end{aligned}
\tag{5.25}
$$

The simplified expression for the semi-major axis of the projected ellipse is

$$
a_p = \frac{1}{2}\sqrt{\left(\frac{K_0a^2K_1}{K_5} - \frac{K_0a^2K_4}{K_5} + K_6 - K_9\right)^2 + \left(\frac{K_0a^2K_1}{K_5} + \frac{K_0a^2K_4}{K_5} + K_7 + K_8\right)^2} + \frac{1}{2}\sqrt{\left(\frac{K_0a^2K_1}{K_5} - \frac{K_0a^2K_4}{K_5} - K_7 + K_8\right)^2 + \left(\frac{K_0a^2K_1}{K_5} + \frac{K_0a^2K_4}{K_5} + K_6 + K_9\right)^2}. \tag{5.26}
$$

The simplified expression for the projected ellipse semi-minor axis is

$$
b_p = -\frac{1}{2}\sqrt{\left|\frac{K_0a^2K_1}{K_5} - \frac{K_0a^2K_4}{K_5} + K_6 - K_9\right|^2 + \left|\frac{K_0a^2K_1}{K_5} + \frac{K_0a^2K_4}{K_5} + K_7 + K_8\right|^2} + \frac{1}{2}\sqrt{\left|\frac{K_0a^2K_1}{K_5} - \frac{K_0a^2K_4}{K_5} - K_7 + K_8\right|^2 + \left|\frac{K_0a^2K_1}{K_5} + \frac{K_0a^2K_4}{K_5} + K_6 + K_9\right|^2}. \tag{5.27}
$$

The simplified expression for the angle between the projected ellipse semi-major

axis and X-axis is

$$\theta = \frac{1}{2}\left[\tan^{-1}\left(\frac{\frac{K_0a^2K_1}{K_5} - \frac{K_0a^2K_4}{K_5} + K_6 - K_9}{\frac{K_0a^2K_1}{K_5} + \frac{K_0a^2K_4}{K_5} + K_7 + K_8}\right) + \tan^{-1}\left(\frac{\frac{K_0a^2K_1}{K_5} + \frac{K_0a^2K_4}{K_5} + K_6 + K_9}{-\frac{K_0a^2K_1}{K_5} + \frac{K_0a^2K_4}{K_5} + K_7 - K_8}\right)\right]. \quad (5.28)$$

Now that we know all the parameters necessary to describe the projected ellipse, we can standardize this ellipse into a simpler form in order to simplify subsequent calculations. We define a new frame (dr, as in Figure 5.4) as the derotation and geometric centering of the projected orbit such that the semi-major axis of the projected ellipse ($\overline{O'I}$) is aligned with $\underline{\hat{x}}_{dr}$, the semi-minor axis of the projected ellipse ($\overline{O'S}$) is aligned with $\underline{\hat{y}}_{dr}$, and O' is the origin of the dr coordinate system. The dr coordinates of the star location F (x_*,y_*) are given by a simple rotation of the projection of $\overline{O'F}$ onto the $\underline{\hat{x}}, \underline{\hat{y}}$ plane by angle θ

$$\begin{bmatrix} x_* \\ y_* \end{bmatrix}_{dr} = - \begin{bmatrix} \cos(\theta) & \sin(\theta) \\ -\sin(\theta) & \cos(\theta) \end{bmatrix} \begin{bmatrix} \overline{O'F} \cdot \underline{\hat{x}} \\ \overline{O'F} \cdot \underline{\hat{y}} \end{bmatrix}_{XYZ}. \quad (5.29)$$

Global and Local Extrema of Planet-Star Separation

Before solving for the true anomalies where the orbit's projected separation s is equal to s_{WA} (general working angle separation, WAd_i), we first need to know how many of these s_{WA}-orbit intersections we are looking for. We can find the expected number of solutions by finding the s extrema throughout the orbit. We do so by solving for the roots of the derivative of the projected planet-star separation.

We start with the general equation for an ellipse

$$\left(\frac{x_e}{a_p}\right)^2 + \left(\frac{y_e}{b_p}\right)^2 = 1, \quad (5.30)$$

where x_e and y_e are the coordinates of any point on the ellipse, and a_p, b_p are the semi-major and semi-minor axes respectively. We rewrite this in terms of x_e, giving

$$y_e = b_p \sqrt{1 - \frac{x_e^2}{a_p^2}} \,. \tag{5.31}$$

The projected separation is given by

$$s^2 = \left(-x_* + x_e\right)^2 + \left(-y_* + y_e\right)^2 \,. \tag{5.32}$$

Taking the derivative of Eqn. 5.32 with respect to x_e, substituting Eqn. 5.31 (and its derivative), and setting it equal to zero, we have

$$0 = \frac{\delta s^2}{\delta x_e} = -2x_* + 2x_e + \frac{2b_p x_e y_*}{a_p \sqrt{a_p^2 - x_e^2}} - \frac{2b_p^2 x_e}{a_p^2}. \tag{5.33}$$

Isolating the square root term to one side and squaring both sides of the equation gives

$$\left(-2x_* + 2x_e - \frac{2b_p^2 x_e}{a_p^2}\right)^2 = \left(\frac{2b_p x_e y_*}{a_p \sqrt{a_p^2 - x_e^2}}\right)^2 , \tag{5.34}$$

which can be expanded with coefficients of x_e, to get the polynomial expression

$$0 = x_e^4 + \frac{-8a_p^2 x_* + 8b_p^2 x_*}{(4a_p^4 - 8a_p^2 b_p^2 + 4b_p^4)/a_p^2} x_e^3 + \frac{-4a_p^4 + 8a_p^2 b_p^2 + 4a_p^2 x_*^2 - 4b_p^4 + 4b^2 y_*^2}{(4a_p^4 - 8a_p^2 b_p^2 + 4b_p^4)/a_p^2} x_e^2 + \frac{8a_p^4 x_* - 8a_p^2 b_p^2 x_*}{(4a_p^4 - 8a_p^2 b_p^2 + 4b_p^4)/a_p^2} x_e + \frac{-4a_p^4 x_*^2}{(4a_p^4 - 8a_p^2 b_p^2 + 4b_p^4)/a_p^2}. \tag{5.35}$$

This expression is a 4^{th} order polynomial. We can reduce this into the standard reduced form of a quartic expression

$$0 = x_e^4 + \frac{-2a_p^2 x_* + 2b_p^2 x_*}{(a_p^4 - 2a_p^2 b_p^2 + b_p^4)/a_p^2} x_e^3 + \frac{-a_p^4 + 2a_p^2 b_p^2 + a_p^2 x_*^2 - b_p^4 + b_p^2 y_*^2}{(a_p^4 - 2a_p^2 b_p^2 + b_p^4)/a_p^2} x_e^2 + \frac{2a_p^4 x_* - 2a_p^2 b_p^2 x_*}{(a_p^4 - 2a_p^2 b_p^2 + b_p^4)/a_p^2} x_e + \frac{-a_p^4 x_*^2}{(a_p^4 - 2a_p^2 b_p^2 + b_p^4)/a_p^2}. \tag{5.36}$$

The standard form of this quartic expression is

$$0 = x_e^4 + A_0 x_e^3 + B_0 x_e^2 + C_0 x_e + D_0 \,, \tag{5.37}$$

where A_0, B_0, C_0, and D_0 are constants and functions of a_p, b_p, x_*, and y_*. The coefficients of the quartic expression are

$$A_0 = \frac{-2a_p^2 x_* + 2b_p^2 x_*}{(a_p^4 - 2a_p^2 b_p^2 + b_p^4)/a_p^2}, \tag{5.38}$$

$$B_0 = \frac{-a_p^4 + 2a_p^2 b_p^2 + a_p^2 x_*^2 - b_p^4 + b_p^2 y_*^2}{(a_p^4 - 2a_p^2 b_p^2 + b_p^4)/a_p^2}, \tag{5.39}$$

$$C_0 = \frac{2a_p^4 x_* - 2a_p^2 b_p^2 x_*}{(a_p^4 - 2a_p^2 b_p^2 + b_p^4)/a_p^2}, \text{ and} \tag{5.40}$$

$$D_0 = \frac{-a_p^4 x_*^2}{(a_p^4 - 2a_p^2 b_p^2 + b_p^4)/a_p^2}. \tag{5.41}$$

We can now apply the analytical solutions of the general quartic expression in standard form, given in 5.1.

Solving this quartic gives us a set of four x_e solutions ($\mathbf{x}_e$) corresponding to two global extrema and two local extrema (if the latter exist for a particular orbit). Figure 5.6 shows a schematic representation of an orbit with four extrema. We can use the imaginary components of the solutions, geometry of the ellipse, and magnitude of the higher order terms in the quartic solutions to identify which solutions belong to which extrema. We first use the magnitude of the imaginary components of solutions to determine how many extrema there are and filter out solutions that are not extrema. The algebraic solutions of the quartic polynomial all give values in the first quadrant (quadrants 1 through 4 are numbered counter-clockwise such that quadrant 1 has strictly positive coordinates, see the four quadrants of Figure 5.6), so we must use geometry of the problem to determine the proper sign of each extremum's true coordinates $\mathbf{x}_{e,g}$ and $\mathbf{y}_{e,g}$ (g references solutions 0 through 3 Eqn. 5.2 through Eqn. 5.5).

All numerical solutions to the quartic have some degree of imaginary component due to accumulation of numerical errors. Quartic solution sets with only two extrema will have two real solutions (solutions with small imaginary com-

ponents only due to numerical error) and two solutions with large imaginary components (algebraic solutions that are artifacts to be thrown away). The majority of KOE have only two s extrema. The only case where no extrema exist is in a circular face on orbit. In this specific case, all solutions to the quartic will be nearly identical, have large imaginary components, and the resulting s extrema will be identical ($s_{\min} = s_{\max}$). We assume that all solutions are real if $|\Im(\mathbf{x}_{e,g})| < 10^{-5} \quad \forall g \in \{0,1,2,3\}$. We assume only two solutions are real if $|\Im(\mathbf{x}_e)| < 10^{-5}$ for only two solutions. We define a new ordered set containing either two or four elements depending on magnitude of the imaginary components as

$$\mathbf{x}_{\Re} = \{|\Re(\mathbf{x}_{e,g})| : |\Im(\mathbf{x}_{e,g})| < 10^{-5} \quad \forall g \in 0..3\}, \tag{5.42}$$

where the absolute value is due to the algebraic solutions of the quartic being only defined in the first quadrant.

We now know the number of expected solutions from the dimension of $\mathbf{x}_{\Re}$ but need to leverage the quartic algebraic solution and geometry to determine which components belong to which quadrant. For orbits with $\mathbf{x}_{\Re}$ containing only two solutions, the first two solutions to the quartic ($\mathbf{x}_{\Re,0}$ and $\mathbf{x}_{\Re,1}$) produce the largest and smallest $\mathbf{x}_{\Re,g} - x_*$, respectively. Due to the shape of an ellipse, these must necessarily produce $s_{\min}$ and $s_{\max}$. We define the set $\mathbf{y}_{\Re}$ as the application of Eqn. 5.31 to each element of $\mathbf{x}_{\Re}$. We define four separation quantities from the possible sign combinations of the coordinate magnitudes in $\mathbf{x}_{\Re}$ and $\mathbf{y}_{\Re}$

as

$$
\begin{aligned}
s_{-\pm 0} &= \sqrt{(\mathbf{x}_{\Re,0} - x_*)^2 + (\mathbf{y}_{\Re,0} \pm y_*)^2}, \\
s_{+\pm 0} &= \sqrt{(\mathbf{x}_{\Re,0} + x_*)^2 + (\mathbf{y}_{\Re,0} \pm y_*)^2}, \\
s_{-\pm 1} &= \sqrt{(\mathbf{x}_{\Re,1} - x_*)^2 + (\mathbf{y}_{\Re,1} \pm y_*)^2}, \text{and} \\
s_{+\pm 1} &= \sqrt{(\mathbf{x}_{\Re,1} + x_*)^2 + (\mathbf{y}_{\Re,1} \pm y_*)^2}.
\end{aligned} \tag{5.43}
$$

Typically, s_{--1} is smaller than s_{--0}, but in $\ll 0.01\%$ of cases s_{--0} can be the smallest separation due to numerical error (in this case we ensure $|s_{--1} - s_{--0}| < 10^{-8}$ and swap values). In addition to $s_{--1} < s_{--0}$, we also know $s_{-+0} < s_{-+1}$, $s_{+-1} < s_{+-0}$, and $s_{++1} < s_{++0}$ for all cases. Using this knowledge, we can reduce the number of comparisons we need to find the minimum planet-star separation to

$$
s_{\min} = \begin{cases}
s_{--1} \text{ where } (s_{--1} < s_{-+0}) \text{ and } (s_{--1} < s_{+-1}) \text{ and } (s_{--1} < s_{++1}), \\
s_{-+0} \text{ where } (s_{-+0} < s_{--1}) \text{ and } (s_{-+0} < s_{+-1}) \text{ and } (s_{-+0} < s_{++1}), \\
s_{+-1} \text{ where } (s_{+-1} < s_{-+0}) \text{ and } (s_{+-1} < s_{--1}) \text{ and } (s_{+-1} < s_{++1}), \\
s_{++1} \text{ where } (s_{++1} < s_{-+0}) \text{ and } (s_{++1} < s_{+-1}) \text{ and } (s_{++1} < s_{--1}).
\end{cases} \tag{5.44}
$$

The maximum separation similarly can be found as

$$
s_{\max} = \begin{cases}
s_{--0} \text{ where } (s_{--0} > s_{-+0}) \text{ and } (s_{--0} > s_{+-1}) \text{ and } (s_{--0} > s_{++0}), \\
s_{-+0} \text{ where } (s_{-+0} > s_{--0}) \text{ and } (s_{-+0} > s_{+-1}) \text{ and } (s_{-+0} > s_{++0}), \\
s_{+-1} \text{ where } (s_{+-1} > s_{-+0}) \text{ and } (s_{+-1} > s_{--0}) \text{ and } (s_{+-1} > s_{++0}), \\
s_{++0} \text{ where } (s_{++0} > s_{-+0}) \text{ and } (s_{++0} > s_{+-1}) \text{ and } (s_{++0} > s_{--0}).
\end{cases} \tag{5.45}
$$

We are able to find x_e and y_e of the minimum and maximum separation diamonds drawn in Figure 5.6 using the same logic for finding $s_{\min}$ and $s_{\max}$.

For the orbits with 4 solutions in $\mathbf{x}_{\Re}$, the first two elements will always be the global extrema, and the last two elements will be the local extrema, which are given by

$$s_{\min} = s_{--1}, \tag{5.46}$$

$$s_{\max} = s_{++0}, \tag{5.47}$$

$$s_{\mathrm{lmin}} = \begin{cases} s_{-+3}, & s_{-+2} > s_{-+3} \\ s_{-+2}, & \text{else} \end{cases} \tag{5.48}$$

$$s_{\mathrm{lmax}} = \begin{cases} s_{-+2}, & s_{-+2} > s_{-+3} \\ s_{-+3}, & \text{else} \end{cases} \tag{5.49}$$

where s_{-+2} and s_{-+3} are calculated in the same manner as s_{-+0} and s_{-+0}. We are able to find the coordinates of all four using the same logic as for finding $s_{\min}$, $s_{\max}$, s_{lmin}, and s_{lmax}. This procedure yields the coordinates of all existing extrema in the dr frame. To find their locations on the projection of orbit in the plane of the sky, we apply the inverse of Eqn. 5.29.

Intersections between a circle and an ellipse

We find s_{WA}-orbit intersections by formulating the circle-ellipse intersections as another quartic, solving this, and assigning the algebraic solutions to intersections. We assign solutions using the number of s extrema, the size of the s_{WA} intersecting circle relative to these s extrema, and the ellipse geometry. To formulate the s_{WA}-orbit intersections as a quartic, we start with Eqn. 5.32 and substitute in Eqn. 5.31. This gives us a separation equation solely as a function of x_e and star location. We expand and transform this into a general polynomial

of x_e with a general s,

$$\begin{aligned}0 = &\left(\frac{a_p^4 - 2a_p^2b_p^2 + b_p^4}{a_p^4}\right)x_e^4 + \left(\frac{-4a_p^2x + 4b_p^2x_*}{a_p^2}\right)x_e^3 + \\ &\left(\frac{2a_p^2b_p^2 - 2a_p^2s^2 + 6a_p^2x_*^2 + 2a_p^2y_*^2 - 2b_p^4 + 2b_p^2s^2 - 2b_p^2x_*^2 + 2b_p^2y_*^2}{a_p^2}\right)x_e^2 + \\ &\left(-4b_p^2x + 4s^2x - 4x_*^3 - 4x_*y_*^2\right)x_e \\ &+ \left(b_p^4 - 2b_p^2s^2 + 2b_p^2x_*^2 - 2b_p^2y_*^2 + s^4 - 2s^2x_*^2 - 2s^2y_*^2 + x_*^4 + 2x_*^2y_*^2 + y_*^4\right). \quad (5.50)\end{aligned}$$

As in Section 5.2.1, we divide by the leading coefficient to convert this to the general quartic form

$$0 = x_e^4 + A_1x_e^3 + B_1x_e^2 + C_1x_e + D_1, \quad (5.51)$$

where A_1, B_1, C_1, and D_1 are

$$\begin{aligned}A_1 =& -\frac{4a_p^2x_*}{a_p^2 - b_p^2},\\ B_1 =& \frac{2a_p^2\left(a_p^2b_p^2 - a_p^2s^2 + 3a_p^2x_*^2 + a_p^2y_*^2 - b_p^4 + b_p^2s^2 - b_p^2x_*^2 + b_p^2y_*^2\right)}{a_p^4 - 2a_p^2b_p^2 + b_p^4},\\ C_1 =& \frac{4a_p^4x_*\left(-b_p^2 + s^2 - x_*^2 - y_*^2\right)}{a_p^4 - 2a_p^2b_p^2 + b_p^4}, \text{ and}\\ D_1 =& \frac{a_p^4\left(b_p^4 - 2b_p^2s^2 + 2b_p^2x_*^2 - 2b_p^2y_*^2 + s^4 - 2s^2x_*^2 - 2s^2y_*^2 + x_*^4 + 2x_*^2y_*^2 + y_*^4\right)}{a_p^4 - 2a_p^2b_p^2 + b_p^4}.\end{aligned} \quad (5.52)$$

We solve this using the general quartic solution as given in 5.1. This results in a solutions for the x_e of intersections in the first quadrant of the dr frame.

We always have four algebraic x_e solutions which may or may not correspond to actual s_{WA}-orbit intersections. The number of s extrema (either two or four) and projected separation relative to these extrema determine how many intersections will occur (if we expect two intersections, then two of the four algebraic solutions must be real solutions and the other two are some combination

of repeated roots or non-physical imaginary solutions). In each of these cases, we must handle the assignment of x_e and y_e solutions to the correct quadrants. Figure 5.7 shows a schematic representation of two cases corresponding to four total intersection.

For KOE with four extrema and $s_{\min} < s_{\text{WA}} < s_{\text{lmin}}$, we know there will be two intersections on the same y side of the ellipse as the star (quadrants 1 or 2 in the dr frame). Of the four quartic solutions to Eqn. 5.51 we have to chose from, we know x_0 is one of them. The other solution could either be x_1 if $\Im(x_1) < 10^{-9}$ or x_3 if $\Im(x_1) > 10^{-9}$.

For KOE with four extrema and $s_{\text{lmax}} < s_{\text{WA}} < s_{\max}$, we know there will be two intersections on opposite x side of the ellipse as the star (quadrants 2 and 3 in the dr frame). In all cases x_0 and x_1 are the intersection solutions. This is because the first two solutions have the largest term in the quartic solution (Eqn. 5.2 and Eqn. 5.3). x_1 is slightly smaller than x_0 because it subtracts the second largest term. The relative magnitudes of x_0 and x_1 determine y_0 occurs in the same side of the ellipse as the star and y_1 must occur on the opposite side of the ellipse as the star. Therefore (x_0,y_0) occurs in quadrant 2 and (x_1,y_1) occurs in quadrant 3.

For KOE with four extrema and $s_{\text{lmin}} < s_{\text{WA}} < s_{\text{lmax}}$, we know there will be four intersections. Unlike in Section 5.2.1 and the rest of this paper where x_0 through x_3 are ordered as in 5.1, we order x_h based off $\Delta x_h = |x_h - x_*|$. We order the quartic solutions from x_0 to x_3 such that x_0 is where $\min(\{\Delta x_h \quad \forall h \in \{0,1,2,3\}\})$ and x_3 is where $\max(\{\Delta x_h \quad \forall h \in \{0,1,2,3\}\})$. These newly ordered Δx_h correspond to those shown in Figure 5.7. The (x_2, y_2) intersection occurs in either quadrant 1 or 2 but is always above and to the left of the star

in the dr frame and has the second largest Δx_h component. The (x_3,y_3) intersection occurs in either quadrant 1 or 4 but always has the largest Δx_h component. We resolve the sign of y_3 by testing it in both quadrants. In $> 99.992\%$ of cases, we can assign y_3 to quadrant 1 as in Figure 5.7(a), but for a minority of cases its correct assignment is quadrant 4 as in Figure 5.7(b). The (x_1, y_1) intersection always occurs in quadrant 4. The (x_0, y_0) intersection occurs in either quadrant 3 or quadrant 4, but is always below and to the left of the star in the dr frame and has the smallest Δx_h component.

For KOE with two extrema and $s_{\min} < s_{\text{WA}} < s_{\max}$, we know there will be two circle-ellipse intersections. The KOE determine where the star is located in the dr frame. The location of the star in the dr frame relative to the vertices of the projected ellipse ($(0, b_p)$, $(0, -b_p)$, $(-a_p, 0)$, and $(a_p, 0)$) determines the star-vertex separation ordering and subsequently which quadrants the two intersection solutions belong to. Instead of calculating the star-vertex separation for each orbit, we divide the first quadrant into four regions that specify the star location type (Type 0 through 3 as indicated in Figure 5.8(a)). This means that any KOE with star in location Type 2 has the associated star-vertex separation ordering.

Using the equidistant lines between ellipse vertices, we can divide the first quadrant into 4 regions (Type 0 through 3) as shown in Figure 5.8(a). The regions 0 and 2 are divided by the line defined by

$$y_{a_p-x,b_p-y} = \frac{a_p}{b_p}x + \frac{a_p^2}{2b_p} - \frac{b_p}{2}, \tag{5.53}$$

where a projected ellipse and star is of Type 0 if $y_* > y_{a_p-x,b_p-y}(x_*)$ and one of Types 1, 2, or 3 otherwise depending on the other equidistant lines. Similarly, the regions 1 and 2 are divided by the line defined by

$$y_{a_p+x,b_p-y} = -\frac{a_p}{b_p}x + \frac{a_p^2}{2b_p} - \frac{b_p}{2}, \tag{5.54}$$

the regions 2 and 3 are divided by the line defined by

$$y_{a_p+x,b_p+y} = \frac{a_p}{b_p}x - \frac{a_p^2}{2b_p} + \frac{b_p}{2}, \tag{5.55}$$

and the star-ellipse classification Type is calculated similar to Type 0.

An example star is shown in Figure 5.8(a). This star location is Type 2 because it is in the region bounded by the 3 dashed lines (grey, pink, and teal). This Type 2 star has the separation ordering indicated in Figure 5.8(a) and Table 5.1. Let us consider a s_{WA} separation circle such that $s_{a_p-x_*,y_*} < s_{\text{WA}} < s_{x_*,b_p+y_*}$. We therefore know the two intersections must occur in quadrant 2 and quadrant 4 of the dr frame.

The distances s_{x_*,b_p+y_*}, s_{x_*,b_p-y_*}, $s_{a_p+x_*,y_*}$, and $s_{a_p-x_*,y_*}$ in Figure 5.8(a) are the distances of the star to each of the ellipse vertices and are calculated by

$$s_{x_*,b_p\pm y_*} = \sqrt{x_*^2 + (b_p \pm y_*)^2} \tag{5.56}$$

$$s_{a_p\pm x_*,y_*} = \sqrt{(a_p \pm x_*)^2 + y_*^2}. \tag{5.57}$$

Figure 5.8(a) and Table 5.1 define orbit types sorted by vertex distances from smallest to largest based on star location type in the first quadrant of the dr frame.

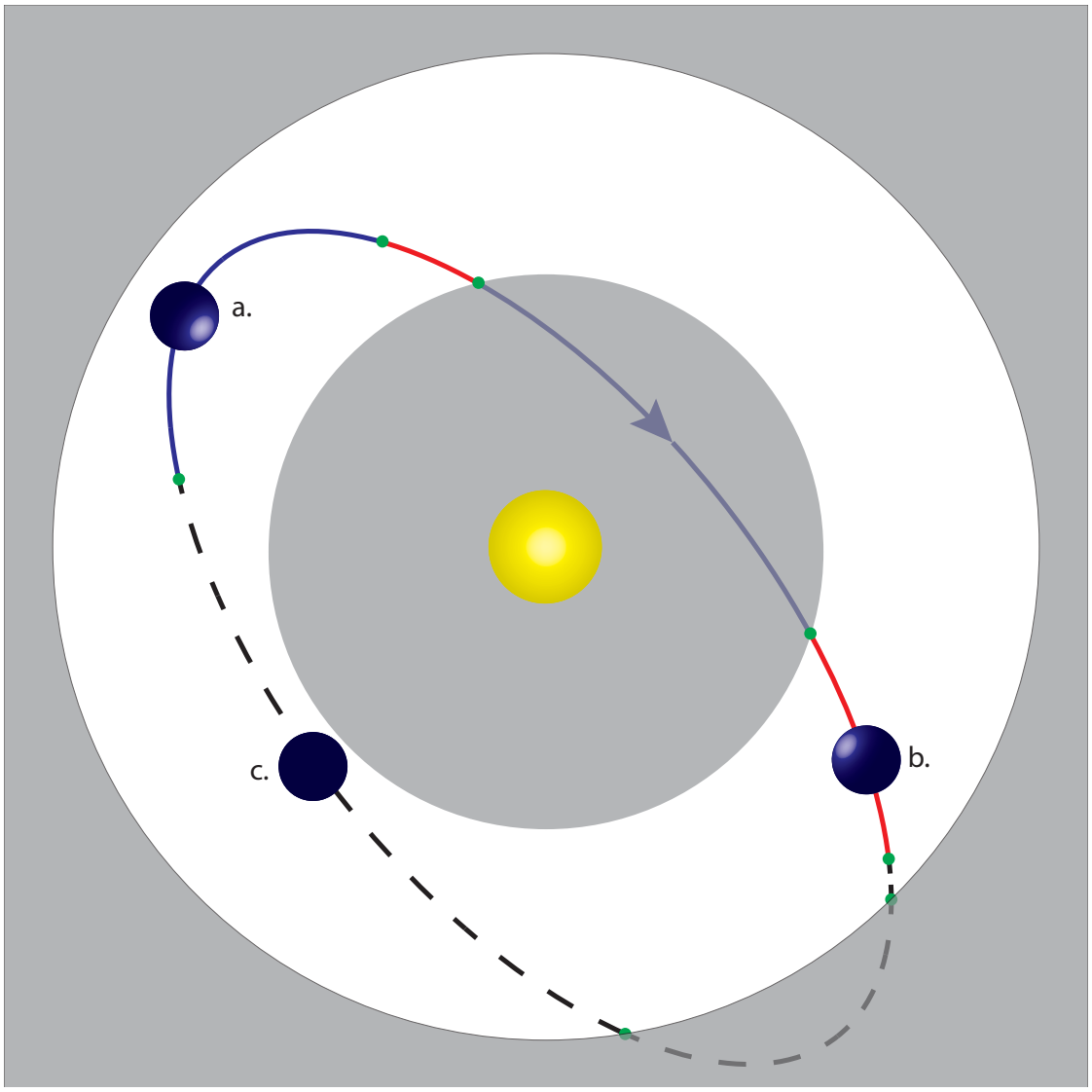

Figure 5.1: Schematic of a direct imaging observation. The line represents the projection of a planet's orbit about its parent star (yellow) into the plane of the sky as seen by a distant observer. The arrow indicates the planet's direction of motion. Blue portions of the orbit (a) indicate times when the planet is detectable. Red portions of the orbit (b) indicate times when the planet is within the visibility limits of the instrument, but not detectable due to integration time constraints. The dashed portions of the orbit (c) indicate times when the planet is too faint to be observed. The shaded grey regions represent the projected inner and outer working angles of the instrument. The planet is unobservable on portions of the orbit intersecting these grey regions. Green dots indicate transitions in and out of instrument visibility limits.

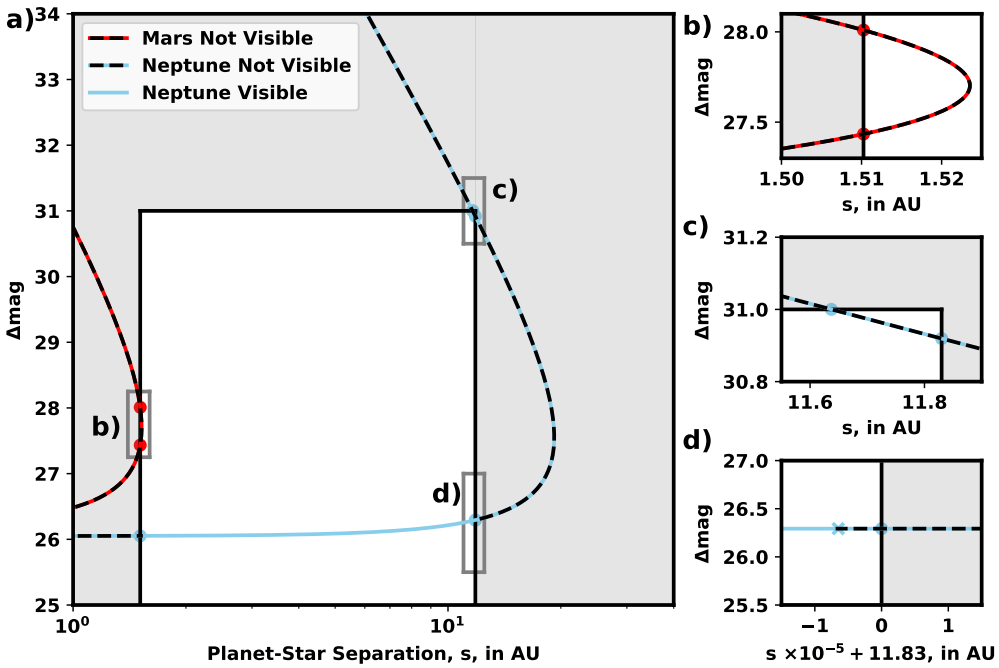

Figure 5.2: The Δmag vs s curve for Neptune (blue) and Mars (red). The instrument's visible region (white) is bounded by 0.066 arcsec, 0.517 arcsec, and Δmag =31 at $d_i = 22.87$ pc (we selected instrument parameters to make a demonstration on solar system planets about a Sun-like star, but any instrument will have planets with similar effects). Any planet in the greyed region is not visible by the instrument. Dots indicate calculated intersection points between the planet and the visible region bounds. The black dashed portions of planet orbits indicate portions of the orbit where the planet is not detectable. b) shows a portion of Mars's orbit where the planet enters and exits the visible limits of the instrument in less time than the required integration time[47]. c) shows a portion of Neptune's orbit where the planet enters and exits the visible region of the instrument in less time than the required integration time. d) shows Neptune's detectable region adjusted for integration time. If the observation of Neptune in d) is started when it is left of the blue $\times$ and in the visible region, then it will be detected; if it is started right of the blue $\times$, the planet will not be detected because the required integration time is larger than the time the planet will be in the visible region of the instrument.

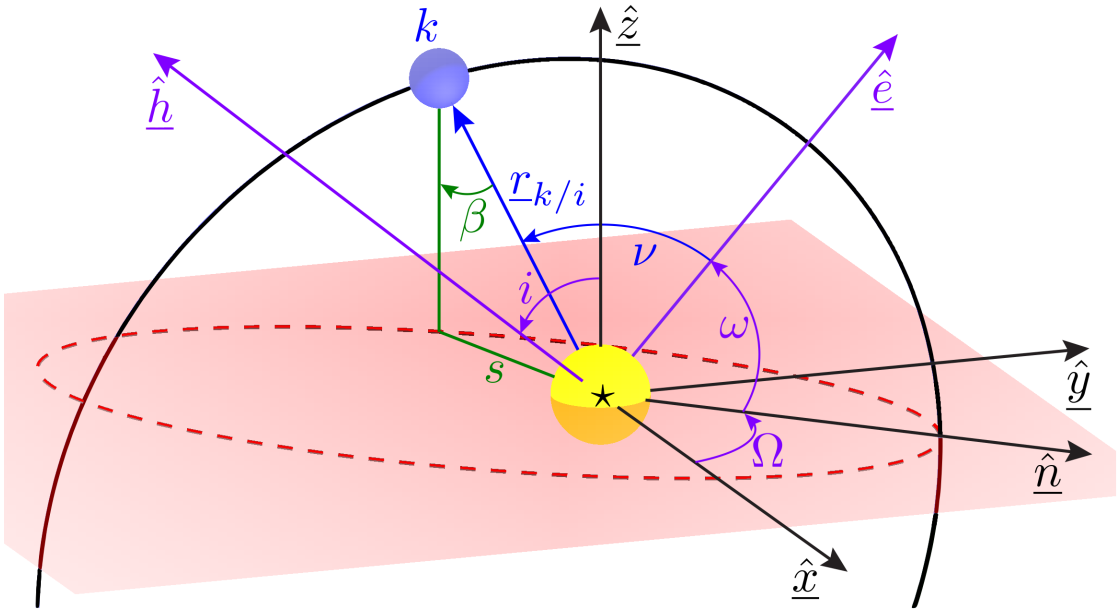

Figure 5.3: The orbital path of planet k (black) in a general XYZ Cartesian coordinate system. $\underline{r}_{k/i}$ (straight blue arrow) describes the location of the planet k (blue circle) relative to star i (yellow circle). The plane of the sky is noted by the translucent red parallelogram entirely in the $\underline{\hat{x}}$ and $\underline{\hat{y}}$ plane. The dashed ellipse (red) is the projection of the planet orbit (black) onto the plane of the sky. $\underline{\hat{h}}$ is the orbit angular momentum vector. $\underline{\hat{e}}$ is the orbit eccentricity vector. $\underline{\hat{n}}$ is the line of nodes. The star $*$ is generally referred to in subscripts as $*$ and often referred to in subscripts as the i^{th} star. This is not to be confused with the variable i which is the inclination of the planet orbit. ν is the true anomaly of the planet. ω is the argument of periapsis of the planet. Ω is the longitude of the ascending node of the planet.

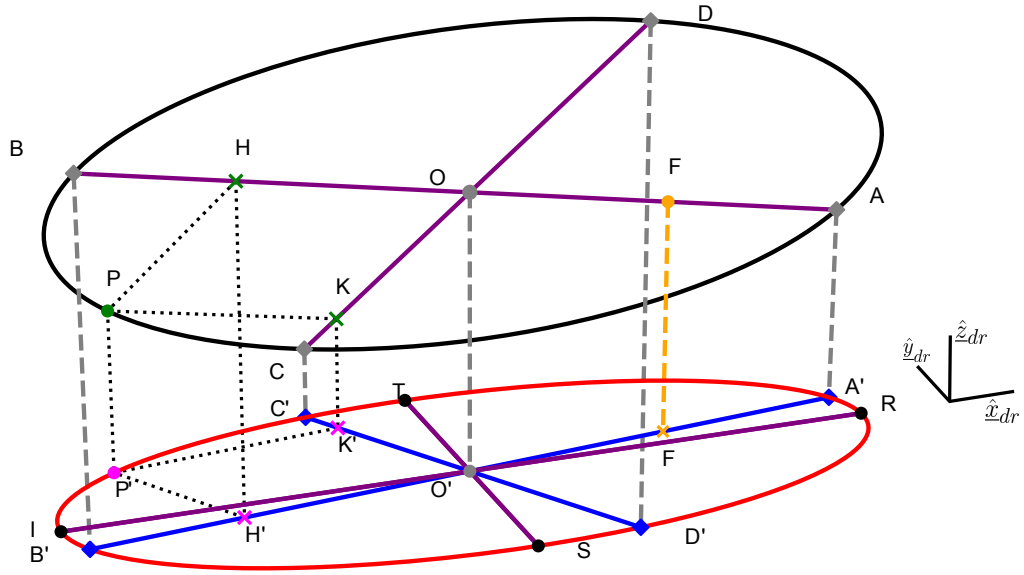

Figure 5.4: The original 3D elliptical orbit of a planet (black line) containing points A, B, C, and D; the grey endpoints of the purple semi-major axis, $\overline{AB}$, and semi-minor axis, $\overline{CD}$. The planet orbits about the star, which is located at focus F (orange circle). The orange dot and orange $\times$ denoted as F are the same point in space, but the red projection is shown as offset from the original orbit for clarity. The projection of the original 3D elliptical orbit onto the XY plane is given by the red ellipse containing points A', B', C', and D' (blue diamonds; perpendicular projections of A, B, C, and D). Point O is the geometric center of the 3D elliptical orbit and projects to O' in the plane of the sky. Point P (green circle) is any arbitrary point along the original 3D ellipse and maps to the semi-major axis and semi-minor axis components H and K respectively (green $\times$). P' (pink circle) is the perpendicular projection of P and H' and K' (pink $\times$) are projections of H and K, respectively. The components of these perpendicular projections preserve the ratios of their values to the semi-major and semi-minor axis which, given the equation for an ellipse, can be used to prove the projection of an ellipse is itself an ellipse. The blue lines $\overline{A'B'}$ and $\overline{C'D'}$ form conjugate diameters of the red ellipse and are the projection of the semi-major axis and semi-minor axis of the original 3D ellipse onto the plane of the sky. These conjugate diameters can then be used to find the semi-major axis and semi-minor axis of the red projected ellipse $\overline{IR}$ and $\overline{ST}$ respectively. $\hat{\underline{x}}_{dr}, \hat{\underline{y}}_{dr}, \hat{\underline{z}}_{dr}$ are the components of the derotated reference frame (dr) as defined in the text.

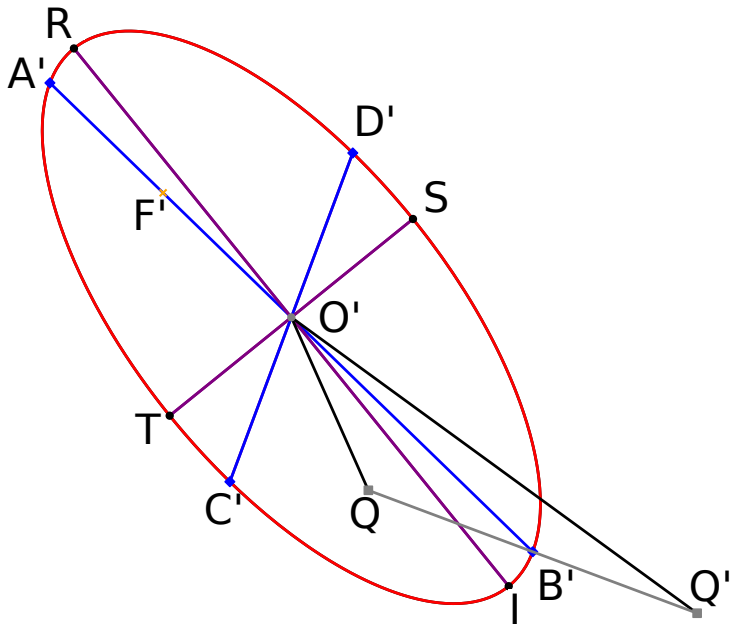

Figure 5.5: The projected ellipse (red) has semi-major axis $\overline{IR}$ and semi-minor axis $\overline{TS}$ (purple). Both are calculable from the conjugate diameters that are the projections of the semi-major and semi-minor axes of the original 3D ellipse ($\overline{A'B'}$, $\overline{C'D'}$, blue). The line $\overline{QQ'}$ is drawn such that it is perpendicular to the smaller conjugate diameter ($\overline{C'D'}$), and is bisected by B': $|\overline{B'Q}| = |\overline{B'Q'}| = |\overline{O'C'}|$. The semi-major axis of the projected ellipse is the angular bisector of $\overline{O'Q}$ and $\overline{O'Q'}$[9]. Finally, the semi-minor axis $\overline{TS}$ of the projected ellipse is perpendicular to the semi-major axis.

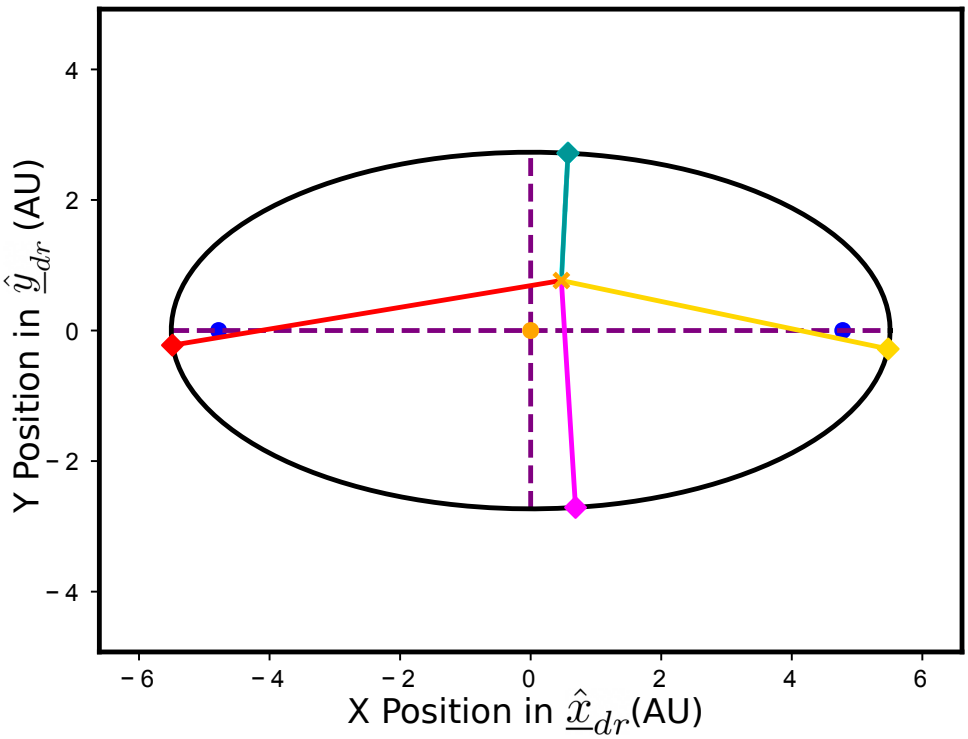

Figure 5.6: Planet orbit (black) in the dr frame and planet-star separation extrema. The minimum separation (cyan) always occurs in the same quadrant as the star in the dr frame (orange $\times$). The maximum separation (red) always occurs in the quadrants opposite the star. The local minimum separation (magenta) and local maximum separation (gold) occur in the same half-plane about the y axis as the star, but in opposite half-planes about the x axis as the star (4^{th} quadrant). This configuration applies to the vast majority of orbits. A small number of edge cases exist, including circular orbits and some edge on orbits. The blue dots represent the foci of the projected ellipse in the dr frame, the orange dot is the ellipse center, and the purple dashed lines are the semi-major and semi-minor axis.

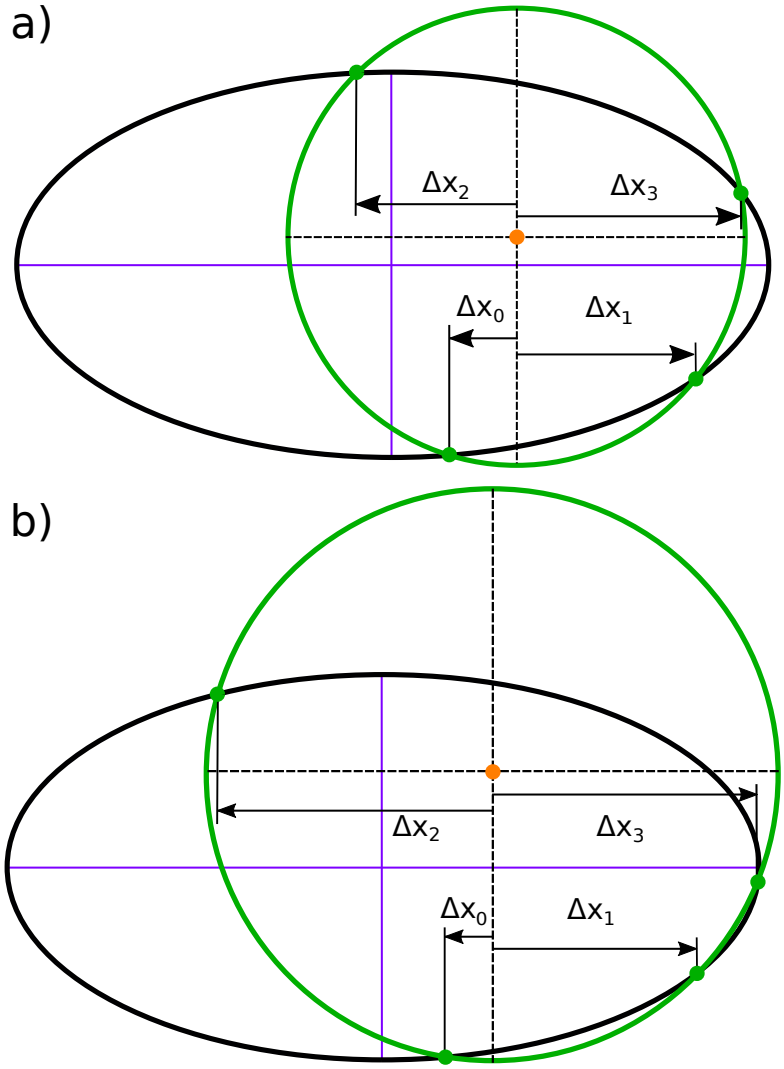

Figure 5.7: Diagrams of orbits where the projected ellipse in the dr frame produces four intersections (green dots) with the $s_{\rm WA}$ separation circle (green circle). The general orbit's projected ellipse (black) is centered at the origin and projected ellipse axes (purple) define the $\overline{\hat{x}}_{dr}$ and $\overline{\hat{y}}_{dr}$ axes (note that the projected ellipse semi-major axis has been derotated such that the star is always located in the first quadrant). The separation circle center (orange dot) is the star's location relative to the orbit's projected ellipse. The x_h points are the quartic solutions where subscripts are re-ordered in ascending distance from the star's x-position. This ordering means x_2 must always occur in the $4^{\rm th}$ quadrant, x_0 may occur in either the first or second quadrants and x_1 may occur in either the third or fourth quadrants. For 99.992% of KOE sampled from the SAG13 population that produce 4 intersections result in a), where the x_3 intersection occurs in the first quadrant. The other 0.008% of KOE result in the x_3 intersection occurring in the fourth quadrant b).

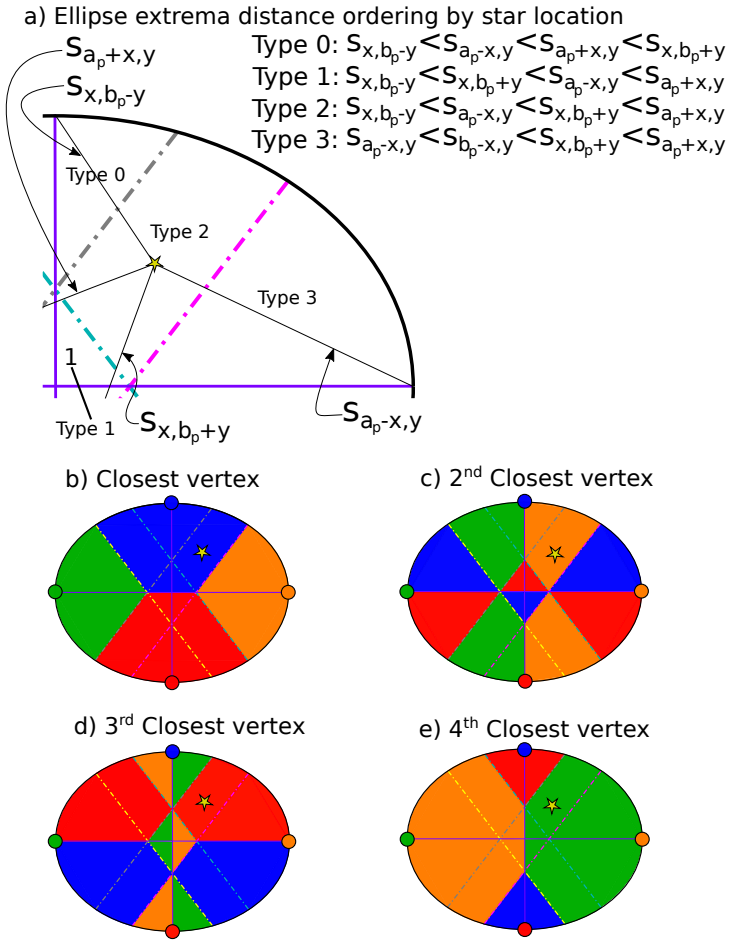

Figure 5.8: Here we show the regions identifying the star type and which vertices are closest to the host star. a) is a plot of the first quadrant of a projected ellipse (black curve) with the semi-major and semi-minor axis (purple) and 3 dashed lines dividing the quadrant into four regions defining the separation ordering. The pink dashed line represents the line of points equidistant from $(0, b_p)$ and $(a_p, 0)$. The grey dashed line represents the line of points equidistant from $(-a_p, 0)$ and $(0, -b_p)$. The turquoise dashed line represents the line of points equidistant from $(0, -b_p)$ and $(a_p, 0)$. The yellow dashed line represents the line of points equidistant from $(-a_p, 0)$ and $(0, b_p)$. We say the star in a) is a Type 2 star and has the associated separation ordering. Plots b) through e) color each region of the ellipse, identifying which vertex is closest, 2^{nd} closest, 3^{rd} closest, and 4^{th} closest. The star in a) is Type 2 and has the top vertex as the closest as seen in b). These plots are based off the projected ellipse of a planet with $a = 0.40$ AU, $e = 0.23$, $i = 0.69$ rad, $\Omega = 3.49$ rad, and $\omega = 5.64$ rad.

Table 5.1: Separation order from smallest to largest by star location type.

Type	Condition	Separation Order From Smallest to Largest 1^{st}	2^{nd}	3^{rd}	4^{th}
0	$s_{a_p+x_*,y_*} < s_{x_*,b_p+y_*}$	s_{x_*,b_p-y_*}	$s_{a_p-x_*,y_*}$	$s_{a_p+x_*,b_p}$	s_{x_*,b_p+y_*}
1	$s_{x_*,b_p+y_*} < s_{a_p-x_*,y_*}$ $s_{a_p-x_*,y_*} < s_{x_*,b_p+y_*}$ $s_{x_*,b_p+y_*} < s_{a_p+x_*,y_*}$	s_{x_*,b_p-y_*}	s_{x_*,b_p+y_*}	$s_{a_p-x_*,y_*}$	$s_{a_p+x_*,y_*}$
2	$s_{x_*,b_p-y_*} < s_{a_p-x_*,y_*}$	s_{x_*,b_p-y_*}	$s_{a_p-x_*,y_*}$	s_{x_*,b_p+y_*}	$s_{a_p+x_*,y_*}$
3	$s_{a_p-x_*,y_*} < s_{x_*,b_p-y_*}$	$s_{a_p-x_*,y_*}$	s_{x_*,b_p-y_*}	s_{x_*,b_p+y_*}	$s_{a_p+x_*,y_*}$

Finally, after determining the correct number of intersection solutions and the proper quadrants these solutions belong to, we re-rotate and translate the intersection solution locations back into the 2D projection of the 3D orbit.

5.2.2 Δmag intersections

In this section, we present our method for calculating the values of ν on a planet's orbit where the planet has a specific value of $\Delta\text{mag}_{\text{lim}}$, called Δmag intersections. As in Section 5.2.1, in order to compute these solutions, we first need to calculate all Δmag extrema ($\Delta\text{mag}_{\text{min}}$, $\Delta\text{mag}_{\text{max}}$, $\Delta\text{mag}_{\text{lmin}}$, and $\Delta\text{mag}_{\text{lmax}}$). The brief process for calculating Δmag extrema is:

1. Express Δmag as a polynomial in $\cos(\nu)$
2. Find the values of ν and Δmag for all polynomial roots
3. Remove invalid and duplicate solutions.

The general process for calculating the true anomalies where a planet has $\Delta\text{mag}_{\text{lim}}$ is similar to the extrema-finding process, but with some minor modifications. After calculating the Δmag extrema, we determine how many Δmag

intersections a given orbit should have with a particular $\Delta\text{mag}_{\text{lim}}$ value. If $\Delta\text{mag}_{\text{lim}} < \Delta\text{mag}_{\text{min}}$ or $\Delta\text{mag}_{\text{lim}} > \Delta\text{mag}_{\text{max}}$, there are no intersections. If $\Delta\text{mag}_{\text{min}} < \Delta\text{mag}_{\text{lim}} < \Delta\text{mag}_{\text{lmin}}$ or $\Delta\text{mag}_{\text{lmax}} < \Delta\text{mag}_{\text{lim}} < \Delta\text{mag}_{\text{max}}$, then there are exactly two intersections. If $\Delta\text{mag}_{\text{lmin}} < \Delta\text{mag}_{\text{lim}} < \Delta\text{mag}_{\text{lmax}}$, then there are exactly four intersections. When the orbit does not contain local Δmag extrema, there are just two Δmag intersections if $\Delta\text{mag}_{\text{min}} < \Delta\text{mag}_{\text{lim}} < \Delta\text{mag}_{\text{max}}$.

Knowing the number of solutions to expect, we can follow the same steps as above: finding a governing polynomial equation, solving for its roots (represented by the ordered set x), and filtering out the relevant solutions. We additionally throw out any solutions with large error from the input $\Delta\text{mag}_{\text{lim}}$. Here we present the full outline of our process for calculating true anomalies where the planet's orbit has a specified Δmag, which we call an intersection.

1. Find Δmag extrema
2. Find planets where $\Delta\text{mag} < \Delta\text{mag}_{\text{max}}$, $\Delta\text{mag} > \Delta\text{mag}_{\text{min}}$, and $\Delta\text{mag} > \Delta\text{mag}_{\text{lmax}}$ or $\Delta\text{mag} < \Delta\text{mag}_{\text{lmin}}$ (these planets have only 2 intersections)
3. Substitute into Δmag equation components and expand until all terms are functions of KOE
4. Manipulate the equation until all ν terms are isolated on the right hand side
5. Expand
6. Replace $\sin(\nu)$ with $\sqrt{1-\cos(\nu)^2}$
7. Replace all $\cos(\nu)$ with x
8. Isolate all square root terms to general form $A^2\sqrt{1-x^2} = B^2$
9. Square both sides

10. Expand
11. Find polynomial coefficients of x
12. Solve with root solver
13. Filter out solutions with imaginary components ($> 10^{-7}$)
14. Filter out solutions $1 < x_k$ or $-1 > x_k$
15. Take arrays $\nu_0 = \cos^{-1}(x)$ and $\nu_1 = 2\pi - \nu_0$
16. Solve for associated arrays Δmag_0 and Δmag_1
17. Remove solutions where $|\Delta\text{mag}_0 - \Delta\text{mag}| > 0.01$ and $|\Delta\text{mag}_1 - \Delta\text{mag}| > 0.01$ (Note: 0.01 is $< \pm 0.08\%$ error on dmag)
18. Remove duplicate solutions
19. Verify there are only 2 viable solutions
20. Assign solutions to ν.

We start with the definition of Δmag, given in Eqn 5.8. While this expression contains multiple terms that are fully defined by an orbit's KOE, it is also a function of other planet properties, including the planet's radius, geometric albedo, and phase function. In order to make the mathematical development presented below tractable, we assume that the quasi-Lambert phase function[4] is a sufficient approximation of any planet's phase function. In general, the quasi-Lambert phase function is a better representation of the Earth's phase function than the Lambert phase function.

This quasi-Lambert phase function is given by

$$\Phi_{QL}(\beta) = \cos^4\left(\frac{\beta}{2}\right). \tag{5.58}$$

We take advantage of this function's form by substituting the half-angle formula

$$\cos\left(\frac{\beta}{2}\right) = \sqrt{\frac{1+\cos(\beta)}{2}}. \tag{5.59}$$

At the same time, from the orbital geometry defined in Figure 5.3 and Eqn. 5.10, we can write

$$\beta = \cos^{-1}\left(\sin(i)\sin(\nu+\omega)\right), \tag{5.60}$$

where the final term can be expanded by the angle addition formula as

$$\sin(\nu+\omega) = \sin(\nu)\cos(\omega) + \cos(\nu)\sin(\omega). \tag{5.61}$$

Substituting in β from Eqn. 5.60 expanded with Eqn. 5.61 into Eqn. 5.59 allows us to reduce the order of the fully substituted Eqn. 5.58. Note that this expression for β depends on making the approximation that the observer-star and observer-planet vectors are parallel, which introduces minor error given the large distances to even the nearest stars[82].

After making these substitutions, as well as taking Eqn. 5.11 for the planet-star distance term $|\underline{r}_{k/i}|$, simplifying, and collecting all of the non-orbital planet parameters on the left hand side, we find

$$\frac{a^2(1-e^2)^2}{pR^2}10^{-2.5\Delta\text{mag}} = \frac{1}{4}\big(e\cos(\nu)+1\big)^2\big(1+\sin(i)\cos(\omega)\sin(\nu)+\sin(i)\sin(\omega)\cos(\nu)\big)^2. \tag{5.62}$$

We now have an expression which isolates terms containing ν and can be decomposed into a numerically-solvable polynomial. In order to improve solving efficiency and determine which subset of planets should have ν solutions for a given Δmag, we need to first calculate the Δmag extrema over the full orbit. Here we present the full outline of our process for calculating true anomalies where the planet's orbit has a Δmag extrema.

1. Substitute into Eqn. 5.8 components and expand until all terms are functions of KOE
2. Manipulate the Δmag equation until all ν terms are isolated on the right hand side
3. Take the derivative
4. Replace $\sin(\nu)$ with $\sqrt{1-\cos(\nu)^2}$
5. Replace all $\cos(\nu)$ with x
6. Isolate all square root terms to general form $\mathbb{A}^2\sqrt{1-x^2} = \mathbb{B}^2$
7. Square both sides
8. Find polynomial coefficients of x
9. Solve with root solver
10. Filter out $\mathbf{x}$ solutions with imaginary components ($> 10^{-7}$) (10^{-8} is approximately $\sqrt{10^{-16}}$, machine precision)
11. Filter out invalid solutions, $1 < \mathbf{x}$ or $-1 > \mathbf{x}$
12. Compute $\boldsymbol{\nu}_0 = \cos^{-1}(\mathbf{x})$ and $\boldsymbol{\nu}_1 = 2\pi - \boldsymbol{\nu}_0$
13. Compute associated $\boldsymbol{\Delta\mathbf{mag}}_0$ and $\boldsymbol{\Delta\mathbf{mag}}_1$
14. Remove solutions that are not extrema
15. Assign solutions $\Delta\mathrm{mag}_{\mathrm{max}} = \min(\boldsymbol{\Delta\mathbf{mag}}_0, \boldsymbol{\Delta\mathbf{mag}}_1)$
16. Assign solutions $\Delta\mathrm{mag}_{\mathrm{min}} = \max(\boldsymbol{\Delta\mathbf{mag}}_0, \boldsymbol{\Delta\mathbf{mag}}_1)$
17. Remove duplicate solutions
18. Remove assigned solutions
19. Check if solution is extrema
20. Assign $\Delta\mathrm{mag}_{\mathrm{lmin}}$ and $\Delta\mathrm{mag}_{\mathrm{lmax}}$.

To calculate these Δmag extrema, we first find the derivative of Eqn. 5.62 and multiply by two (for simplification purposes) to get

$$\begin{aligned}
0 = &-e^2 \sin^2(i) \sin^3(\nu) \cos(\nu) \cos^2(\omega) - 3e^2 \sin^2(i) \sin^2(\nu) \sin(\omega) \cos^2(\nu) \cos(\omega) \\
&- 2e^2 \sin^2(i) \sin(\nu) \sin^2(\omega) \cos^3(\nu) + e^2 \sin^2(i) \sin(\nu) \cos^3(\nu) \cos^2(\omega) \\
&+ e^2 \sin^2(i) \sin(\omega) \cos^4(\nu) \cos(\omega) - 2e^2 \sin(i) \sin^2(\nu) \cos(\nu) \cos(\omega) \\
&- 3e^2 \sin(i) \sin(\nu) \sin(\omega) \cos^2(\nu) \\
&+ e^2 \sin(i) \cos^3(\nu) \cos(\omega) - e^2 \sin(\nu) \cos(\nu) - e \sin^2(i) \sin^3(\nu) \cos^2(\omega) \\
&- 4e \sin^2(i) \sin^2(\nu) \sin(\omega) \cos(\nu) \cos(\omega) - 3e \sin^2(i) \sin(\nu) \sin^2(\omega) \cos^2(\nu) \\
&+ 2e \sin^2(i) \sin(\nu) \cos^2(\nu) \cos^2(\omega) + 2e \sin^2(i) \sin(\omega) \cos^3(\nu) \cos(\omega) \\
&- 2e \sin(i) \sin^2(\nu) \cos(\omega) - 4e \sin(i) \sin(\nu) \sin(\omega) \cos(\nu) \\
&+ 2e \sin(i) \cos^2(\nu) \cos(\omega) - e \sin(\nu) - \sin^2(i) \sin^2(\nu) \sin(\omega) \cos(\omega) \\
&- \sin^2(i) \sin(\nu) \sin^2(\omega) \cos(\nu) + \sin^2(i) \sin(\nu) \cos(\nu) \cos^2(\omega) \\
&+ \sin^2(i) \sin(\omega) \cos^2(\nu) \cos(\omega) - \sin(i) \sin(\nu) \sin(\omega) + \sin(i) \cos(\nu) \cos(\omega),
\end{aligned} \tag{5.63}$$

which is a function of $\sin(\nu)$ and $\cos(\nu)$ terms. We can now fully expand this expression and substitute in

$$\sin(\nu) = \sqrt{1 - \cos^2(\nu)} \tag{5.64}$$

to get an expression in $\cos(\nu)$ only. We define $x = \cos(\nu)$, isolate the $\sqrt{1-x^2}$ term, square both sides, and expand to get an 8^{th} degree polynomial in x of the form

$$0 = A_2 x^8 + B_2 x^7 + C_2 x^6 + D_2 x^5 + E_2 x^4 + F_2 x^3 + G_2 x^2 + H_2 x + I_2. \tag{5.65}$$

The coefficients of this expression are

$$A_2 = e^4 \sin^4(i),$$

$$
\begin{aligned}
B_2 =& 3e^3 \left(e \sin\left(\omega\right) + \sin\left(i\right)\right) \sin^3\left(i\right), \\
C_2 =& \frac{1}{4} e^2 \left[4e^2 \sin^2\left(i\right) \sin^2\left(\omega\right) - 8e^2 \sin^2\left(i\right) + 8e^2 \sin^2\left(\omega\right) + 5e^2 \right. \\
& \left. + 34e \sin\left(i\right) \sin\left(\omega\right) + 13 \sin^2\left(i\right)\right] \sin^2\left(i\right), \\
D_2 =& \frac{1}{2} e \left[2e^3 \sin^2\left(i\right) \sin^3\left(\omega\right) - 8e^3 \sin^2\left(i\right) \sin\left(\omega\right) + 3e^3 \sin\left(\omega\right) \right. \\
& + 5e^2 \sin^3\left(i\right) \sin^2\left(\omega\right) - 11e^2 \sin^3\left(i\right) + 10e^2 \sin\left(i\right) \sin^2\left(\omega\right) + 7e^2 \sin\left(i\right) \\
& \left. + 17e \sin^2\left(i\right) \sin\left(\omega\right) + 3 \sin^3\left(i\right)\right] \sin\left(i\right), \\
E_2 =& -\frac{5e^4 \sin^4\left(i\right) \sin^2\left(\omega\right)}{4} + \frac{5e^4 \sin^4\left(i\right)}{4} - \frac{7e^4 \sin^2\left(i\right) \sin^2\left(\omega\right)}{4} - \frac{3e^4 \sin^2\left(i\right)}{2} \\
& + \frac{e^4}{4} + \frac{3e^3 \sin^3\left(i\right) \sin^3\left(\omega\right)}{2} - 10e^3 \sin^3\left(i\right) \sin\left(\omega\right) + \frac{7e^3 \sin\left(i\right) \sin\left(\omega\right)}{2} \\
& + 2e^2 \sin^4\left(i\right) \sin^2\left(\omega\right) - \frac{21e^2 \sin^4\left(i\right)}{4} + 4e^2 \sin^2\left(i\right) \sin^2\left(\omega\right) \\
& + \frac{7e^2 \sin^2\left(i\right)}{2} + \frac{7e \sin^3\left(i\right) \sin\left(\omega\right)}{2} + \frac{\sin^4\left(i\right)}{4}, \\
F_2 =& -\frac{3e^4 \sin^3\left(i\right) \sin^3\left(\omega\right)}{2} + \frac{3e^4 \sin^3\left(i\right) \sin\left(\omega\right)}{2} - \frac{3e^4 \sin\left(i\right) \sin\left(\omega\right)}{2} \\
& - \frac{e^3 \sin^4\left(i\right) \sin^4\left(\omega\right)}{2} - \frac{5e^3 \sin^4\left(i\right) \sin^2\left(\omega\right)}{2} + 3e^3 \sin^4\left(i\right) \\
& - 5e^3 \sin^2\left(i\right) \sin^2\left(\omega\right) - \frac{7e^3 \sin^2\left(i\right)}{2} + \frac{e^3}{2} - \frac{e^2 \sin^3\left(i\right) \sin^3\left(\omega\right)}{2} \\
& - 8e^2 \sin^3\left(i\right) \sin\left(\omega\right) + \frac{5e^2 \sin\left(i\right) \sin\left(\omega\right)}{2} + \frac{e \sin^4\left(i\right) \sin^2\left(\omega\right)}{2} - 2e \sin^4\left(i\right) \\
& + e \sin^2\left(i\right) \sin^2\left(\omega\right) + \frac{3e \sin^2\left(i\right)}{2} + \frac{\sin^3\left(i\right) \sin\left(\omega\right)}{2}, \\
G_2 =& -\frac{e^4 \sin^4\left(i\right) \sin^4\left(\omega\right)}{4} + \frac{e^4 \sin^4\left(i\right) \sin^2\left(\omega\right)}{2} - \frac{e^4 \sin^4\left(i\right)}{4} - \frac{e^4 \sin^2\left(i\right) \sin^2\left(\omega\right)}{2} \\
& + \frac{e^4 \sin^2\left(i\right)}{2} - \frac{e^4}{4} - \frac{7e^3 \sin^3\left(i\right) \sin^3\left(\omega\right)}{2} + \frac{7e^3 \sin^3\left(i\right) \sin\left(\omega\right)}{2} \\
& - \frac{7e^3 \sin\left(i\right) \sin\left(\omega\right)}{2} - \frac{5e^2 \sin^4\left(i\right) \sin^4\left(\omega\right)}{4} - e^2 \sin^4\left(i\right) \sin^2\left(\omega\right) \\
& + \frac{9e^2 \sin^4\left(i\right)}{4} - 5e^2 \sin^2\left(i\right) \sin^2\left(\omega\right) - \frac{5e^2 \sin^2\left(i\right)}{2} + \frac{e^2}{4} \\
& - \frac{3e \sin^3\left(i\right) \sin^3\left(\omega\right)}{2} - 2e \sin^3\left(i\right) \sin\left(\omega\right) + \frac{e \sin\left(i\right) \sin\left(\omega\right)}{2} \\
& - \frac{\sin^4\left(i\right)}{4} + \frac{\sin^2\left(i\right)}{4},
\end{aligned}
$$

$$
\begin{aligned}
H_2 = &-\frac{e^3\sin^4(i)\cos^4(\omega)}{2} + e^3\sin^2(i)\cos^2(\omega) - \frac{e^3}{2} + \frac{5e^2\sin^3(i)\sin(\omega)\cos^2(\omega)}{2} \\
&- \frac{5e^2\sin(i)\sin(\omega)}{2} - \frac{3e\left(\cos(2i)-1\right)^2\left(\cos(4w)-1\right)}{64} + \frac{e\sin^4(i)\cos^4(\omega)}{2} \\
&- \frac{5e\sin^2(i)\sin^2(\omega)}{2} - \frac{e\sin^2(i)\cos^2(\omega)}{2} - \frac{\sin^3(i)\sin^3(\omega)}{2}, \text{ and} \\
I_2 = &-\frac{e^2\sin^4(i)\cos^4(\omega)}{4} + \frac{e^2\sin^2(i)\cos^2(\omega)}{2} - \frac{e^2}{4} + \frac{e\sin^3(i)\sin(\omega)\cos^2(\omega)}{2} \\
&- \frac{e\sin(i)\sin(\omega)}{2} \\
&- \frac{\left(\cos(2i)-1\right)^2\left(\cos(4w)-1\right)}{128} - \frac{\sin^2(i)\sin^2(\omega)}{4}.
\end{aligned} \tag{5.66}
$$

While 8^{th} degree polynomials do not have analytical solutions, a numerical root solver can determine the eight roots of this function denoted as the ordered set $\mathbf{x}$. We discard any $\mathbf{x}_p > 1 \quad \forall p \in \{0..8\}$, $\mathbf{x}_p < -1 \quad \forall p \in \{0..8\}$, or solutions with large imaginary components. We then calculate the remaining true anomaly solutions by $\boldsymbol{\nu}_0 = \cos^{-1}(\mathbf{x})$ and $\boldsymbol{\nu}_1 = 2\pi - \boldsymbol{\nu}_0$. Of the remaining valid solutions, we identify whether each solution is an extremum by evaluating whether $\Delta\text{mag}(\boldsymbol{\nu}_0 \pm \delta\nu)$ are both larger or both smaller than $\Delta\text{mag}(\boldsymbol{\nu}_0)$. If identified as a potential extremum, the smallest and largest extremas are assigned to $\Delta\text{mag}_{\text{min}}$ and $\Delta\text{mag}_{\text{max}}$. The remaining extrema are checked for duplicates, identified by solutions with (ν,Δmag) values close to existing extrema. If any solutions are remaining, an additional check and assignment is them made for the local extrema. Through this process, a solution identified in $\boldsymbol{\nu}_0$ has the associated solution in $\boldsymbol{\nu}_1$ removed.

In order to calculate the Δmag intersections, we apply the same process for turning Eqn. 5.62 into a polynomial as in the Δmag extrema calculation. By following the process in section 5.2.2, we arrive at

$$
\xi = A_3x^8 + B_3x^7 + C_3x^6 + D_3x^5 + E_3x^4 + F_3x^3 + G_3x^2 + H_3x + I_3\,, \tag{5.67}
$$

where ξ is the collection of constants on the left hand side of Eqn. 5.62. The coefficients of this polynomial are

$$
\begin{aligned}
A_3 =& \frac{e^4 \sin^4(i)}{16}, \\
B_3 =& \frac{1}{4} e^3 \left(e \sin(\omega) + \sin(i)\right) \sin^3(i), \\
C_3 =& \frac{1}{8} e^2 \Big(e^2 \cos^2(i) \cos^2(\omega) - 3e^2 \cos^2(\omega) + 3e^2 + 8e \sin(i) \sin(\omega) \\
& -3 \cos^2(i) + 3\Big) \sin^2(i), \\
D_3 =& \frac{1}{4} e \left[-e^3 \sin^3(\omega) \cos^2(i) + e^3 \sin^3(\omega) + e^3 \sin(\omega) \cos^2(i) \right. \\
& - 2e^2 \sin^3(i) \cos^2(\omega) - 4e^2 \sin(i) \cos^2(\omega) + 6e^2 \sin(i) \\
& \left. -6e \sin(\omega) \cos^2(i) + 6e \sin(\omega) + \sin^3(i)\right] \sin(i), \\
E_3 =& \frac{e^4 \sin^4(i) \sin^4(\omega)}{16} - \frac{e^4 \sin^4(i) \sin^2(\omega)}{8} + \frac{e^4 \sin^4(i)}{16} + \frac{e^4 \sin^2(i) \sin^2(\omega)}{8} \\
& - \frac{e^4 \sin^2(i)}{8} + \frac{e^4}{16} + e^3 \sin^3(i) \sin^3(\omega) - e^3 \sin^3(i) \sin(\omega) + e^3 \sin(i) \sin(\omega) \\
& - e^2 \xi \sin^2(i) \sin^2(\omega) + \frac{e^2 \xi \sin^2(i)}{2} + \frac{3e^2 \sin^4(i) \sin^2(\omega)}{4} - \frac{3e^2 \sin^4(i)}{4} \\
& + \frac{3e^2 \sin^2(i) \sin^2(\omega)}{2} + \frac{3e^2 \sin^2(i)}{4} + e \sin^3(i) \sin(\omega) + \frac{\sin^4(i)}{16}, \\
F_3 =& \frac{e^3 \sin^4(i) \sin^4(\omega)}{4} - \frac{e^3 \sin^4(i) \sin^2(\omega)}{2} + \frac{e^3 \sin^4(i)}{4} + \frac{e^3 \sin^2(i) \sin^2(\omega)}{2} \\
& - \frac{e^3 \sin^2(i)}{2} + \frac{e^3}{4} - e^2 \xi \sin(i) \sin(\omega) + \frac{3e^2 \sin^3(i) \sin^3(\omega)}{2} \\
& - \frac{3e^2 \sin^3(i) \sin(\omega)}{2} + \frac{3e^2 \sin(i) \sin(\omega)}{2} - 2e \xi \sin^2(i) \sin^2(\omega) \\
& + e \xi \sin^2(i) + \frac{e \sin^4(i) \sin^2(\omega)}{2} - \frac{e \sin^4(i)}{2} + e \sin^2(i) \sin^2(\omega) \\
& + \frac{e \sin^2(i)}{2} + \frac{\sin^3(i) \sin(\omega)}{4}, \\
G_3 =& - \frac{e^2 \xi \sin^2(i) \cos^2(\omega)}{2} - \frac{e^2 \xi}{2} + \frac{3e^2 \sin^4(i) \cos^4(\omega)}{8} - \frac{3e^2 \sin^2(i) \cos^2(\omega)}{4} \\
& + \frac{3e^2}{8} - 2e \xi \sin(i) \sin(\omega) - e \sin^3(i) \sin(\omega) \cos^2(\omega) + e \sin(i) \sin(\omega) \\
& - \frac{\xi \sin^2(i) \sin^2(\omega)}{2} + \frac{\xi \sin^2(i) \cos^2(\omega)}{2} + \frac{\left(\cos(2i) - 1\right)^2 \left(\cos(4w) - 1\right)}{256} \\
& - \frac{\sin^4(i) \cos^4(\omega)}{8} + \frac{3 \sin^2(i) \sin^2(\omega)}{8} + \frac{\sin^2(i) \cos^2(\omega)}{8},
\end{aligned}
$$

$$
\begin{aligned}
H_3 =& -e\xi\sin^2(i)\cos^2(\omega) - e\xi + \frac{e\sin^4(i)\cos^4(\omega)}{4} - \frac{e\sin^2(i)\cos^2(\omega)}{2} \\
&+ \frac{e}{4} - \xi\sin(i)\sin(\omega) - \frac{\sin^3(i)\sin(\omega)\cos^2(\omega)}{4} + \frac{\sin(i)\sin(\omega)}{4}, \text{ and} \\
I_3 =& \xi^2 - \frac{\xi\sin^2(i)\cos^2(\omega)}{2} - \frac{\xi}{2} + \frac{\sin^4(i)\cos^4(\omega)}{16} - \frac{\sin^2(i)\cos^2(\omega)}{8} + \frac{1}{16}. \quad (5.68)
\end{aligned}
$$

We again use a numerical root solver to find the roots of this function, $\mathbf{x}$, and again discard all $\mathbf{x}_p > 1 \quad \forall p \in \{0..8\}$, $\mathbf{x}_p < -1 \quad \forall p \in \{0..8\}$, and solutions with large imaginary components. We then calculate the true anomalies of all remaining solutions by $\boldsymbol{\nu}_0 = \cos^{-1}(\mathbf{x})$ and $\boldsymbol{\nu}_1 = 2\pi - \boldsymbol{\nu}_0$. We then evaluate $\boldsymbol{\Delta\mathbf{mag}}_0 = \Delta\mathrm{mag}(\boldsymbol{\nu}_0)$ and $\boldsymbol{\Delta\mathbf{mag}}_1 = \Delta\mathrm{mag}(\boldsymbol{\nu}_1)$ and remove solutions where $|\boldsymbol{\Delta\mathbf{mag}}_0 - \Delta\mathrm{mag}_{\mathrm{lim}}| > 0.01$ and $|\boldsymbol{\Delta\mathbf{mag}}_1 - \Delta\mathrm{mag}_{\mathrm{lim}}| > 0.01$ (Note that 0.01 is $< \pm 0.08\%$ error on Δmag). We do an iterative process of selecting (ν,Δmag) which are unique (not duplicate solutions) and are closest to the expected $\Delta\mathrm{mag}_{\mathrm{lim}}$ until we have the expected number of solutions. In the majority of cases where solutions exist, there are generally only two viable solutions, the assignment of which is simple. In some cases the solution selection is more ambiguous as double roots are possible.

5.2.3 ν from X and Y

Section 5.2.1, 5.2.1, and 5.2.2 give locations of extrema at intersections in the plane of the sky of the form (x, y), but we need to know the true anomalies of the orbit where these intersections occur.

We start with X and Y in Eqn. 5.10 and solve for $(1 + e\cos(\nu))/(a(1 - e^2))$ resulting in

$$
\frac{1 + e\cos(\nu)}{a(1 - e^2)} = \frac{1}{Y}\left[\sin\Omega\cos(\omega + \nu) + \cos\Omega\sin(\omega + \nu)\cos i\right] \quad (5.69)
$$

and

$$\frac{1+e\cos(\nu)}{a(1-e^2)} = \frac{1}{X}\left[\cos(\Omega)\cos(\omega+\nu) - \sin(\Omega)\sin(\omega+\nu)\cos(i)\right]. \tag{5.70}$$

In both of these expressions, we substitute angle addition formulas of $\sin(\omega+\nu)$ and $\cos(\omega+\nu)$ and subsequently set the two equations equal to each other.

We can set Eqn. 5.69 and Eqn. 5.70 equal to each other, expand, isolate a $\cos(\nu)$ term and $\sin(\nu)$ term, solve for ν, and rearrange to get

$$\nu = \tan^{-1}\left[\frac{-\frac{X}{Y}\sin\Omega\cos\omega - \frac{X}{Y}\cos\Omega\cos i\sin\omega + \cos\Omega\cos\omega - \sin\Omega\cos i\cos\omega}{-\frac{X}{Y}\sin\Omega\sin\omega + \frac{X}{Y}\cos\Omega\cos i\cos\omega + \cos\Omega\sin\omega + \sin\Omega\cos i\cos\omega}\right]. \tag{5.71}$$

We now have an analytical expression for ν solely as a function of the KOE, X, and Y of a particular point on the orbital ellipse.

By combining the original X and Y equations to solve for ν analytically, we have created two potential solutions at ν and $\nu \pm \pi$. One of these is the correct ν value and the other is not. To calculate the correct intersection point, we calculate the separations at both ν and $\nu \pm \pi$ to find absolute error in s and use the smaller error of the two.

5.2.4 Calculate t from ν

We have ν for the locations where s extrema, Δmag extrema, s_{WA}-orbit intersections, and Δmag intersections occur but we need them in terms of time. We can calculate eccentric anomaly E of these events directly from ν as

$$E = \tan^{-1}\left(\frac{\sqrt{1-e^2}\sin\nu}{e+\cos\nu}\right), \tag{5.72}$$

which gives the corresponding time

$$t = \frac{E - e\sin(E)T}{2\pi}, \tag{5.73}$$

where T is the orbital period of a general planet.

5.2.5 Converting From Star to Star

The planet-star intersection points and visibility ranges can be saved as either true anomalies or as specific times for a reference star. It makes the most sense to store the values as times and use $1M_\odot$ as the reference time. The times can be scaled to any star mass M by

$$T = T_\odot \sqrt{\frac{M_\odot}{M}}. \tag{5.74}$$

5.2.6 Calculating Completeness

We calculate integration time adjusted completeness using the aggregated fraction of time planets are detectable. Using the methods described in Section 5.2 on the instrument's photometric visibility limit ($\Delta\mathrm{mag}_{\mathrm{lim}}$) and astrometric visibility limits (IWA and OWA), we can calculate the specific times the planet enters or exists the instruments visibility limits. By collecting these times and inspecting intermediate test points, we identify the time windows any planet is detectable by the instrument. Given an integration time (t_{max}) required to reach some SNR consistent with a clear detection (typically a value > 5), we can throw out all visibility time windows less than t_{max} and discount all other visibility windows by t_{max}. Dividing the sum of all integration time discounted visibility windows for a planet by it's orbital period gives us the fraction of time a planet is detectable by the instrument. Aggregating the fractions of time planets are detectable by the instrument gives us integration time adjusted completeness.

In mathematical form this looks like

$$C_{t_{\max}} = \frac{1}{N}\left(\sum_{\forall k}\frac{\sum_{\forall j}(\delta t_{j,k} - t_{\max}U_k)}{T_k}\right). \tag{5.75}$$

Here, $\delta t_{j,k}$ is the j^{th} time window larger than $t_{\max}$ that the k^{th} planet is visible, U_k is a boolean indicating the planet is always visible 0 or at least sometimes visible 1, N is the total number of planets, and T_k is the orbital period for the k^{th} planet.

We can also calculate the completeness for an Earth-Like exoplanet of the Earth-Like exoplanets sub-population

$$C_{\oplus,t_{\max}} = \frac{1}{N_\oplus}\left(\sum_{\forall k\in\oplus}\frac{\sum_{\forall j}(\delta t_{j,k} - t_{\max}U_k)}{T_k}\right), \tag{5.76}$$

where $N_\oplus$ is the total number of Earth-like planets simulated.

Similarly, this capability can be extended to the entirety of the Kopparapu classification scheme. [50] Our new method uses orders of magnitude fewer exoplanets and an equivalent memory but fills in the Δmag space using an order of magnitude better accounting with strategically calculated true anomalies.

5.2.7 Calculating Dynamic Completeness

The methods presented in this paper can also be used to calculate dynamic completeness[14]. Dynamic completeness extends the original concept of completeness by considering the fraction of planets observable on subsequent observations of the same target. For the original formulation of completeness, which relies on simulating a cloud of planets, this requires propagating every simulated planet along its orbits. Dynamic completeness is frequently used to com-

pute the fraction of planets in a population that are initially undetectable, but become detectable upon a second observation some time later.

We define $\mathbf{P}$ as the unordered set of all planets, $\mathbf{P}_{\mathrm{detected,1}}$ as the set of planets detected at observation time one, $\mathbf{P}_{\mathrm{undetected,1}}$ as the set of planets not detected at observation time one. To find the sets of detected planets at the first observation, we start by generating an random observation time for the k^{th} planet ($t_{\mathrm{start},k}$) between 0 and T_k. We can then determine which planets are within the instrument's visibility limits at $t_{\mathrm{start},k}$ to create $\mathbf{P}_{\mathrm{detected,1}}$ and its' complement $\mathbf{P}_{\mathrm{undetected,1}}$.

For a subsequent observation sometime later (t_{wait}), we find the time past periastron the observation occurs at by ($mod(t_{\mathrm{start}} + t_{\mathrm{wait}}, T_k)$), determine which planets are within the instrument's visibility limits at that time. This defines the unordered set of planets detected at observation time two as $\mathbf{P}_{\mathrm{detected,2}}$. Its' complement is $\mathbf{P}_{\mathrm{undetected,2}}$, the set of planets not detected at observation time two.

Dynamic completeness for the second observation of a target star is given by the fraction of planets undetected in the initial observation but detected on the second one

$$C_2 = \frac{1}{N} n\left(\mathbf{P}_{\mathrm{undetected,1}} \cap \mathbf{P}_{\mathrm{detected,2}}\right), \tag{5.77}$$

where $n(\mathbf{P})$ is a function giving the number of elements in set $\mathbf{P}$ and N is the total number of planets.

Dynamic completeness of the m^{th} visit is similarly given by the fraction of previously undetected planets that are detected on that visit

$$C_m = \frac{1}{N} n\left(\left(\bigcap_{j=0}^{m-1} \mathbf{P}_{\mathrm{undetected,j}}\right) \cap \mathbf{P}_{\mathrm{detected,m}}\right). \tag{5.78}$$

5.3 Results

5.3.1 ν from s

We apply the methods developed Section 5.2 to calculate the planet-star separation extrema, the true anomalies they occur at, the times past periastron the extrema occur at, the true anomalies where the separation circle intersects with the projected orbital ellipse, and the times these intersections occur at for a planet orbit. Figure 5.9 shows the projected separation of a sample orbit with global and local extrema calculated via Section 5.2 methods. This figure also demonstrates the ability of our methods to find all true anomalies (and times) when the projected separation takes a specific value (in this case $s_{\mathrm{WA}} = 1$ AU).

We now want to determine the accuracy of the methods implemented. To do this, we calculate the true anomalies of s_{WA}-orbit intersections for 10^5 orbits using the method in Section 5.2.1 and $s_{\mathrm{WA}} = 1$ AU. We then calculate the planet-star separation by substituting these true anomalies back into Eqn. 5.9 and plot the error between these separations and the input s_{WA} in Figure 5.10. Of the 10^5 planets orbits simulated, $\sim$25,000 orbits produced two or more intersections. The largest intersection error observed is less than 10^{-6}. Since machine precision error is $\sim 10^{-16}$ and the square root of this is 10^{-8}, this indicates we have approached machine precision in our method.

5.3.2 ν from $\Delta\mathrm{mag}$

We apply the methods developed Section 5.2 to calculate the Δmag extrema, the true anomalies they occur at, the times past periastron the extrema occur at, the true anomalies where the Δmag intersections occur, and the times these Δmag intersections occur at for a planet orbit. Figure 5.11 shows the Δmag of a sample orbit with global and local extrema calculated via Section 5.2 methods. This figure also demonstrates the ability to find all true anomalies (and times) when the Δmag takes a specific value (in this case $\Delta\mathrm{mag}_{\mathrm{lim}} = 25.0$).

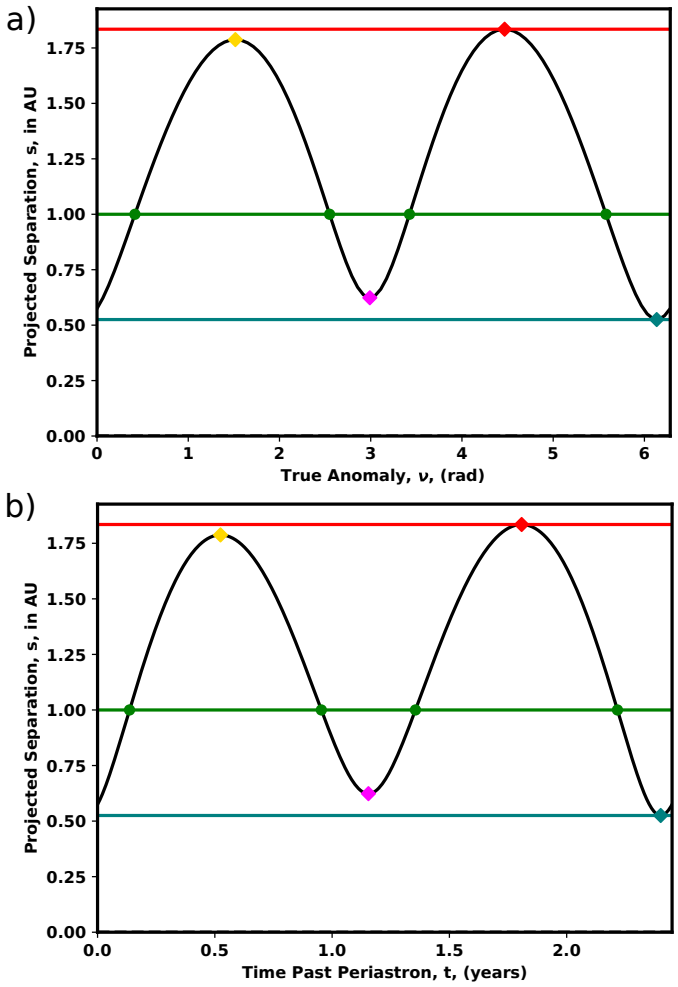

Figure 5.9: Planet-star separation of the planet is plotted in black. The separation extrema are indicated by diamonds where the maximum is red, local maximum is yellow, local minimum is magenta, and minimum is teal. Lines are drawn at the minimum and maximum separations. For the input separation of s =1 AU, the green dots are the analytically calculated orbit intersections. a) is the separation vs true anomaly and b) is the separation vs time past periastron for a planet orbit with a = 1.82 AU, e = 0.09, Ω = 3.37 rad, ω = 4.86 rad, i = 1.25 rad.

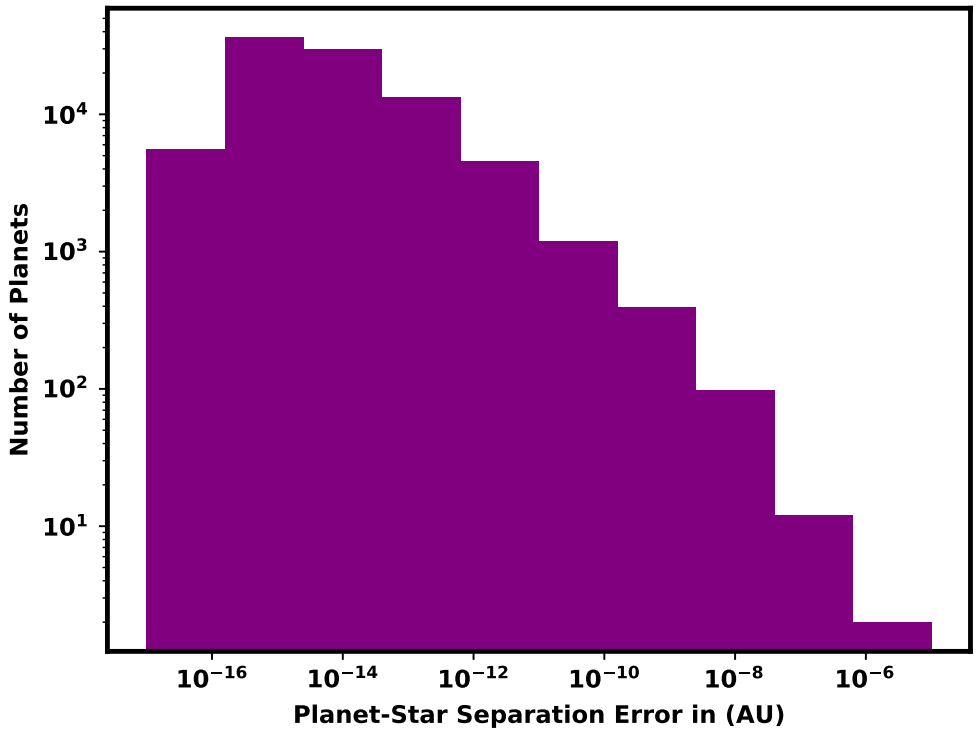

Figure 5.10: s_{WA}-orbit intersection error histogram calculated for a separation of $s_{\mathrm{WA}} = 1$ AU for 10^5 planet orbits generated from the SAG13 planet population. Of these 10^5 planet orbits, 6201 orbits have two intersections with the s_{WA} circle and 17952 have four intersections with the s_{WA} circle. This results in a total of 84210 planet-star intersections. After calculating and identifying true anomalies of intersections using the methods described in this paper, we evaluated the planet-star separation of each orbit at the true anomalies and calculated error from the input s_{WA}.

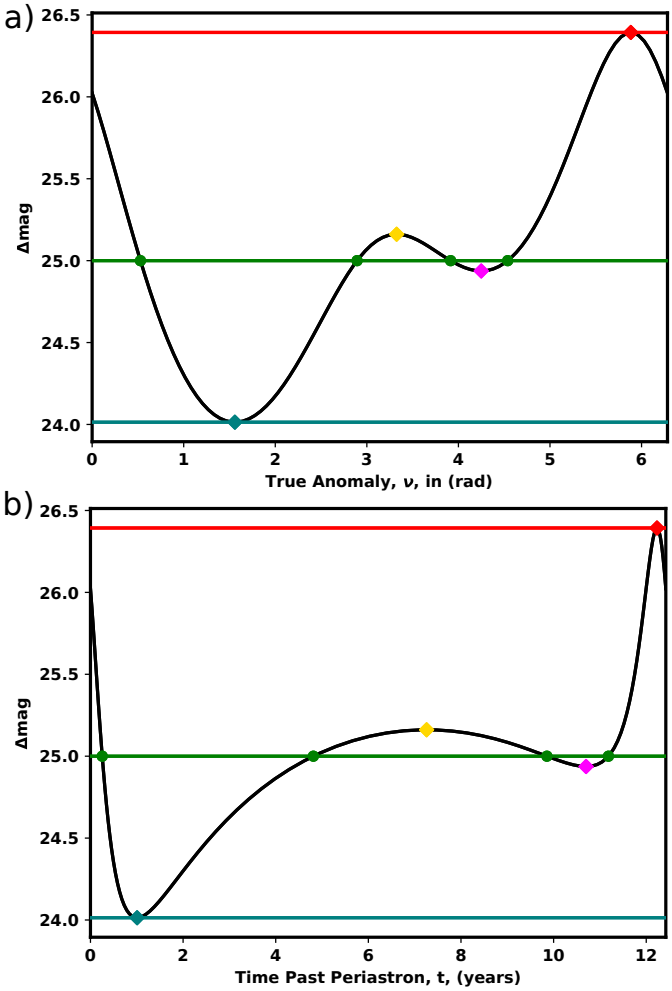

Figure 5.11: The Δmag of a planet (black line) plotted against ν (a) and time past periastron (b). Δmag extrema are indicated by diamonds where the maximum is red, local maximum is yellow, local minimum is magenta, and minimum is teal. Separation minimum and maximum are indicated by horizontal lines. For an input $\Delta\mathrm{mag}_{\mathrm{lim}} = 25$ (green line), we calculated the specific true anomalies (green dots) where the planet's Δmag intersects this line. The specific planet KOE are a = 5.36 AU, e = 0.56, ω = 5.06 rad, Ω = 0.69 rad, i = 0.81 rad), p =0.3, and $R = 4\,R_{\oplus}$.

In order to check the error in true anomaly produced by the Δmag intersection method in this paper, we compare the ν of Δmag intersections calculated with alternative numerical solving methods. The method presented in this paper can find Δmag intersections of 10^6 planets within ~ 6.3 seconds. The first error checking method uses a cubic spline fit to 300 (ν,Δmag) points along each planet's orbit.We then subtract $\Delta\mathrm{mag}_{\mathrm{lim}} = 29$ (our test-point) from the spline and find the roots. This univariate spline root solving method is capable of executing in 419 seconds on the 510120 planets in the population that produced two intersections, a rate of 8.1×10^{-4} seconds per planet. The univariate spline root solving method is 100$\times$ slower than the Δmag intersection method in Section 5.2.2. The separation error between the univariate spline method and the Δmag intersection method is $< 6 \times 10^{-5}$ for $> 99.98\%$ of planets and $< 10^{-4}$ for the other 0.02%. These high error targets are planets with low variation in $\Delta\mathrm{mag}(\nu)$ orbits. The second error checking method solves for the (ν,$\Delta\mathrm{mag}$) intersections using a numerical minimization method on a random subset of 10^4 planets. This method is far more inefficient taking 1646 seconds on 10^4 planets with two intersections time at a rate of 0.1646 seconds per planet. Using a minimization function allows us to determine the error in Δmag of an intersection point to within 10^{-8}. This numerical minimization method independently confirms the accuracy of solutions to the univariate spline roots method on the limited number of targets tested. We plotted the normalized frequency of true anomaly error of both the numerical minimization method and univariate spline root solving method compared against the Δmag intersection method in Figure 5.12. Note that the total number of incidences of a given error is normalized by the bin width and total number of targets so the non-normalized frequency of the 3×10^{-11} bin is incredibly large compared to the 5×10^{-4} bin.

Both methods indicate the resulting true anomalies of the Δmag intersections are within 10^{-4} rad of each other.

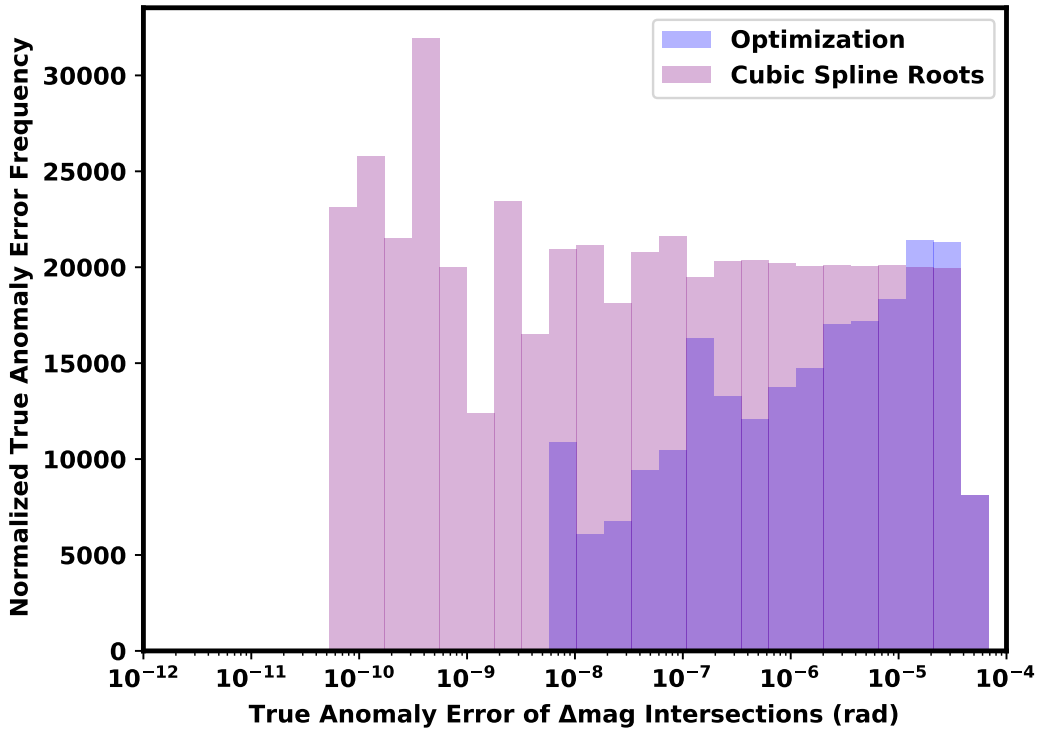

Figure 5.12: A histogram of $\nu(\Delta\text{mag})$ error between the root solving method described in this paper and a root solver of a cubic spline fit method (purple) for 510120 planet orbits that produce two intersections (totalling 1020240 datapoints). We also compare the error between the root solving method described in this paper and an optimization method (blue) for 10^4 planet subset of the planet orbits that produce intersections. The optimization method investigates fewer planets because it is orders of magnitude more computationally expensive, but is a fundamentally different approach to validating our method than a root solver.

While the Δmag intersection method featured in this paper is orders of magnitude faster than the univariate-spline-roots method and just as accurate, the quasi-lambert phase function required for its use is not the best phase function for all planets but does fit Earth-Like planet phase function quite well. At a substantial time cost, the univariate-spline-roots method can be used for planets with any phase function.

5.3.3 Convergence and Validation

We test convergence of our method for calculating completeness by repeatedly calculating completeness on 10^5 planets. We test convergence of Brown's method by repeatedly calculating completeness over a set of logarithmically increasing number of planets. We use the same SAG13 planet population parameters from Keithly et al. [47] but make the substitution of a quasi-Lambert phase function to define the underlying planet population. Since this technique will be most relevant to future highly capable telescopes, we are using the HabEx IWA of 0.045 arcsec, OWA of 6 arcsec, and upper Δmag limit of 25 on a star that is 10 pc away.[100] This resulting instrument visibility limits and planet population cover a well populated region of the Δmag vs s joint probability density function (see Figure 1 in Keithly et al. [47] for a comparable example of the joint probability density function). Convergence of the two completeness methods is demonstrated in Figure 5.13.

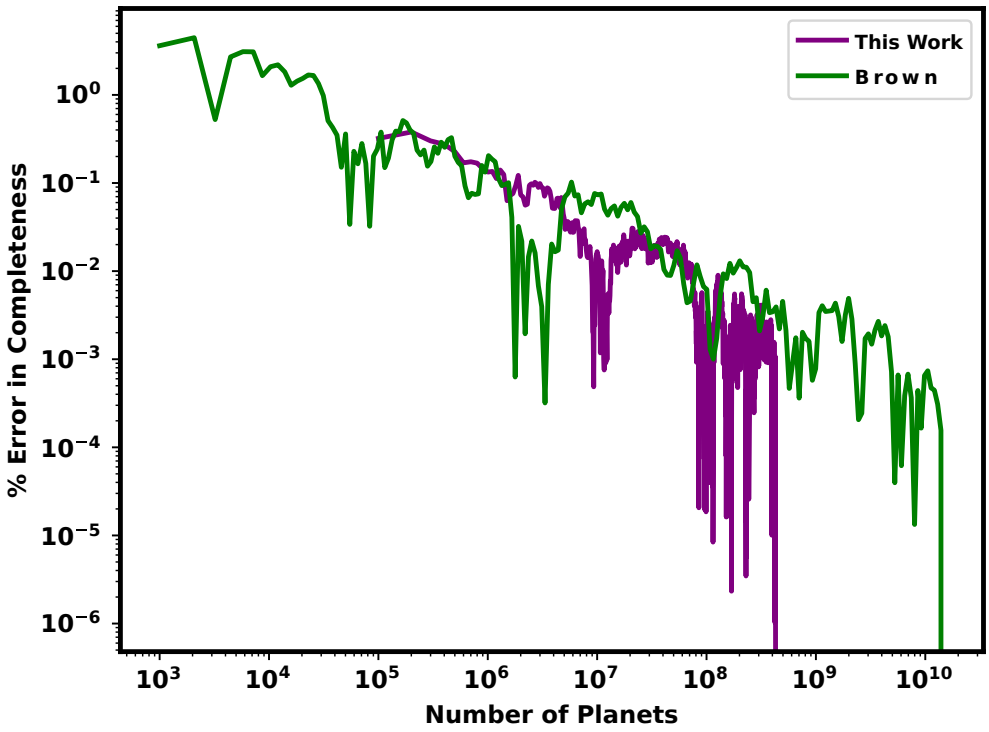

Figure 5.13: Convergence of % error in completeness for varying numbers of planets used in its computation for Brown's method (green) and the method presented in this work with $t_{\max} = 0$ d (purple). Completeness at the maximum number of planets is assumed to be the converged value of completeness of the respective methods. The converged mean of Brown's method is 0.25783 compared to the converged mean of the method in this paper of 0.25785. The standard deviation of the method in this paper is 0.0010.

Both methods presented in Figure 5.13 demonstrate similar percent convergence to their own converged means. Completeness repeatedly calculated using the method in Section 5.2.6 with 10^5 planets has a mean of 0.25785 with a standard deviation of 0.0010 for 4.28×10^8 planets. In comparison, the Brown Completeness method converges to 0.25783. This error in the converged mean of the two methods is consistent with the completeness error identified in Figure 5.14. We expect completeness calculated using the method in this paper will have comparatively better convergence in sparsely populated regions of the Δmag vs s joint probability density function (see Figure 1 in Keithly et al. [47]).

Since completeness for an individual planet is the fraction of time a planet is visible to the instrument, we can validate individual planet visibility windows using test points. To calculate a ground truth fraction of time a planet is visible, we create 10^5 test points, evenly spaced in time, and calculate both the planet-star separation and planet-star Δmag at each of those test points. We then determine whether each point is within the visibility limits of the instrument. The fraction of visible points is the fraction of time that a planet is visible. We repeated this for 25000 planets due to computational cost of the test point method. The histogram of error in completeness for individual planets calculated using the test point method and method in this paper is shown in Figure 5.14. The maximum error in completeness is observed to be near 5×10^{-5} which is consistent with the converged error between Brown completeness and integration time adjusted completeness.

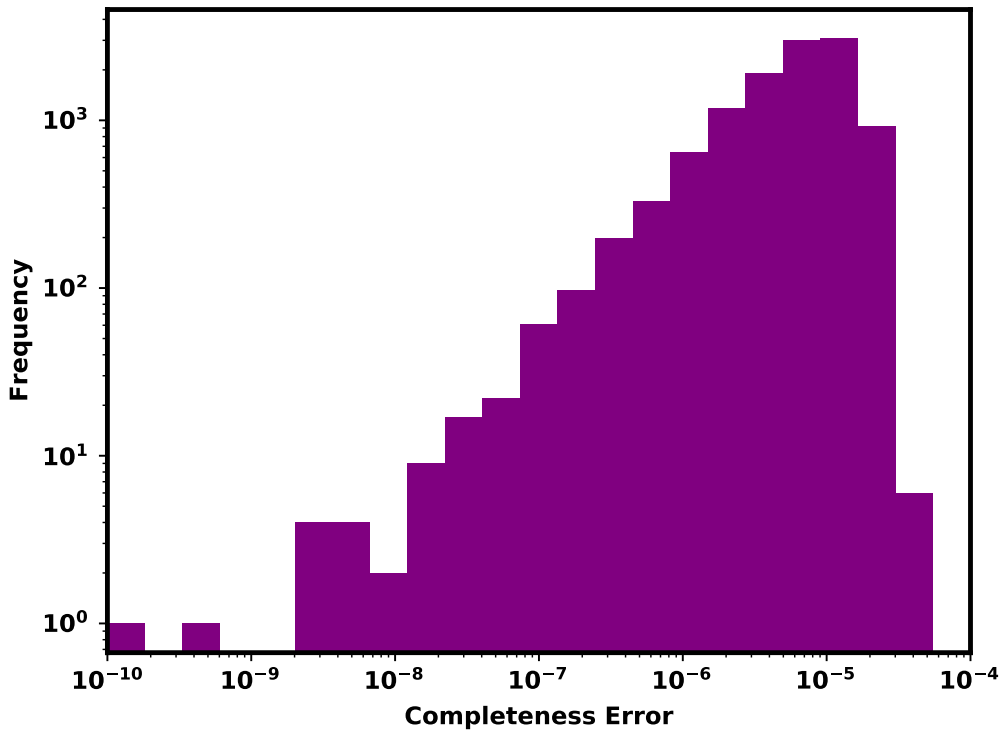

Figure 5.14: Per planet completeness error histogram between the integration time adjusted completeness method with $t_{\max} = 0$ d and the test point method for 25000 planets.

The test point method we used to validate integration time adjusted completeness calculations took over 52 hours on only 25000 planets (less than a quarter of the planets needed to compute completeness using integration time adjusted completeness). The computation time for the integration time adjusted completeness calculation on 10^5 planets is 21.34 seconds with a standard deviation of 0.4 seconds over 1000 calculations. Brown Completeness, including the joint probability density function generation, has a mean execution time of 3.19 seconds and standard deviation of 0.13 sec over 1000 calculations. This execution time of all these methods scales linearly with number of planets. Some room for optimization exists in integration time adjusted completeness.

5.3.4 Completeness vs Integration Time

To evaluate the effects of integration time on completeness, we calculate integration time adjusted completeness for various integration times, star distances, and planet populations (SAG13 and Earth-like planet population). Figure 5.15 shows the integration time adjusted completeness for the modified SAG13 planet population[47] and the Earth-like planet sub-population defined in 2.5. The decrease in completeness for longer integration times is most prominent for nearby stars for both populations. As expected, longer integration times decrease completeness.

For the assumed observatory parameters, the Brown completeness of an Earth-like population for a target 5 pc away is 0.583. As we increase integration time to 1, 2, and 5 days, the associated integration time adjusted completeness decreases by 0.63%, 1.27%, and 3.15% respectively. Recalculating Brown com-

pleteness for a target at 25 pc in Figure 5.15(b) is 0.583. As we increase integration time to 1, 2, and 5 days on this 25 pc target, the associated integration time adjusted completeness decreases by 0.989%, 1.97%, and 4.92% respectively. Our integration time adjustment of completeness shows Brown completeness overestimates exoplanet yields for any observation. Brown completeness applied to stars further away results in a substantial overestimation of exoplanet yield.

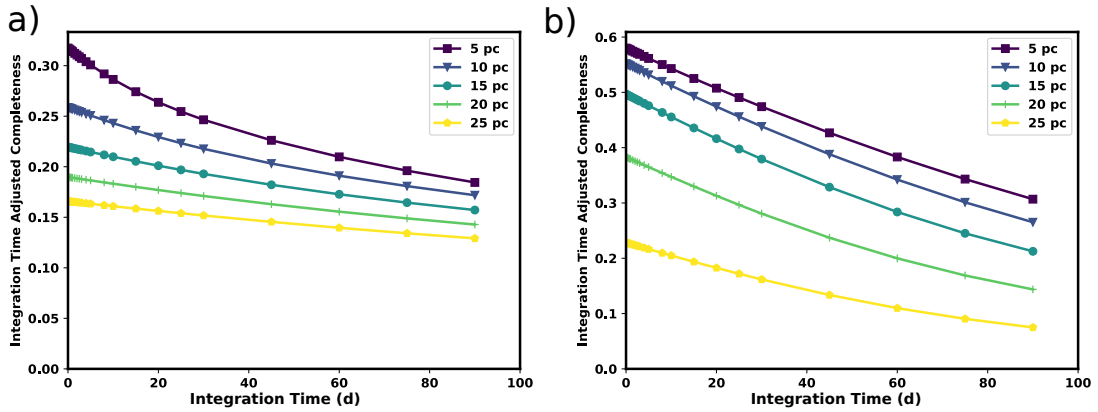

Figure 5.15: Integration time adjusted completeness values of (a) SAG13 planet population and (b) Earth-like planet population with IWA=0.045 arcsec, OWA=6 arcsec, and $\Delta\mathrm{mag} = 25$ for varying integration times and star distances.

Technically, the $\Delta\mathrm{mag}_{\mathrm{lim}}$ used as the upper limit for calculating completeness is a function of integration time and will approach a theoretical upper limit as the noise floor is reached. By calculating $\Delta\mathrm{mag}_{\mathrm{lim}}$ using Eqn. 12 of Ref. [47], we can calculate completeness at each integration time to get the completeness vs integration time curve. We created a 4 m telescope as in B.2 and evaluated completeness at each integration time to create an example demonstrating how Brown completeness and integration time adjusted completeness vary with integration time in Figure 5.16. We can see the completeness of both methods track very closely until they diverge. Brown completeness approaches its asymptotic limit as expected while integration time adjusted completeness approaches a

maximum and begins decreasing past ∼0.2 d.

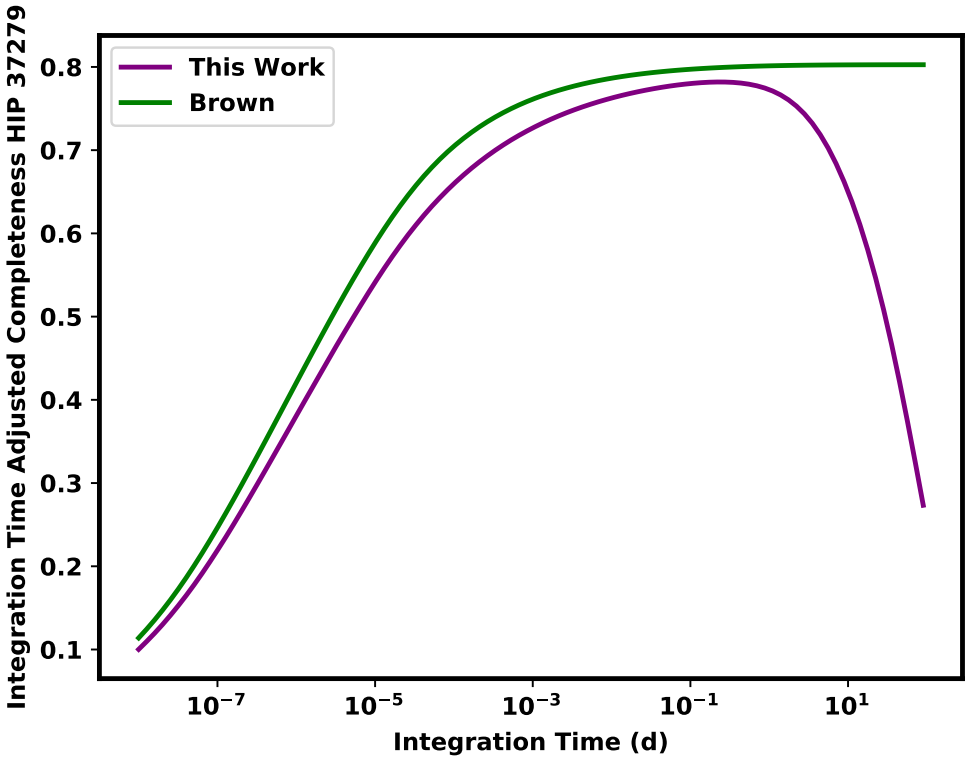

Figure 5.16: Brown completeness and integration time adjusted completeness vs integration time for HIP 32279 assuming a mass of 1.564 $M_{\odot}$, luminosity of 7.12 $L_{\odot}$, and distance of $d_i = 3.51$ pc. The assumed telescope is a 4 m monolith with IWA=0.045 arcsec and OWA=6 arcsec and $\Delta\mathrm{mag}_{\mathrm{lim}}$ computed using the instrument noise model as in Ref. [47].

5.3.5 Dynamic Completeness

We compute dynamic completeness for the example test case in Figure 1 of Ref. [14] using the method described in this paper and replicating the approach of the original work. This computation is only for a second epoch. We replicated the original work by sampling a large number of planets, finding the planets initially visible, propagating these planets to some time past initial observation,

and determining what fraction of these planets were not detected the first time but were detected the second time. We replicated Brown's work using both the Lambert phase function (orange line in Figure 5.17) to match the original work as well as the quasi-Lambert phase function (red line in Figure 5.17).

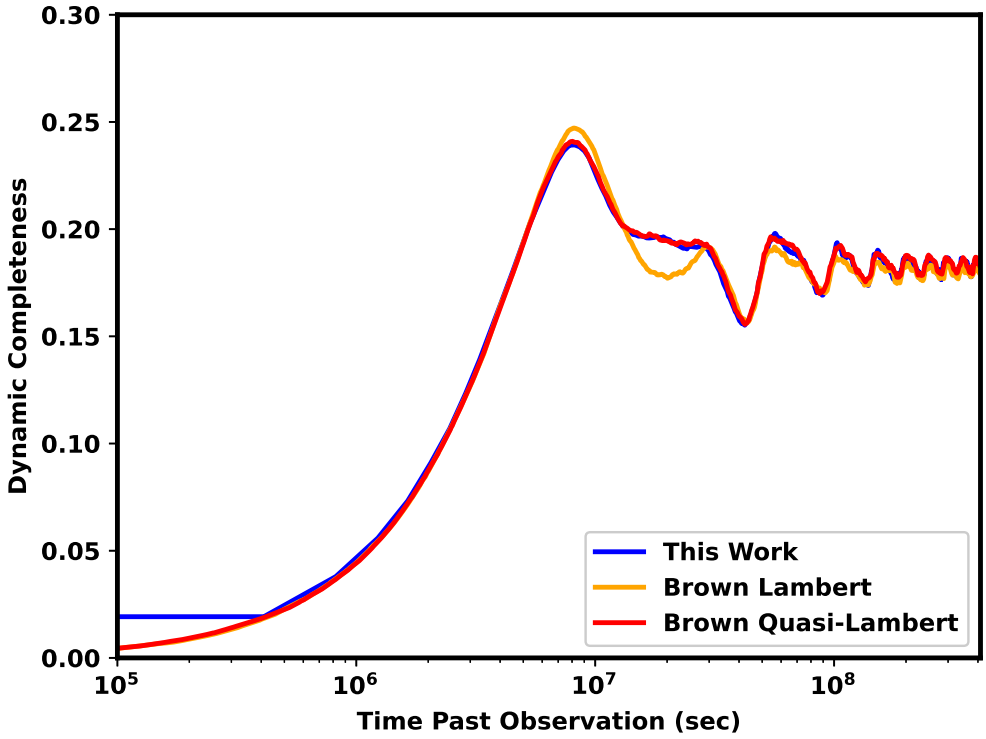

Figure 5.17: Dynamic completeness assuming the same parameters as in Ref. [14] ($\Delta\text{mag} = 26$, $M_{\text{HIP29271}} = 1.103\,M_\odot$, $d_i = 10.215$ pc, OWA = 600 arcsec, IWA = 0.075 arcsec, $0.7\sqrt{L} \leq a \leq 1.5\sqrt{L}$, $0 \leq e \leq 0.35$, $p = 0.26$, $R = 1\,R_\oplus$, and $L = 0.83\,L_\odot$). In this work (blue), we assume a quasi-lambert phase function, but in Ref. [14], a lambert phase function is assumed. Work was done to replicate Brown's original work (Brown Lambert, orange line) and replicate Brown's work using the quasi-lambert phase function (Brown Quasi-Lambert, red line).

We compared the dynamic completeness computation time for 1000 dynamic completeness calculations testing 1000 individual points in time past initial observation. Brown's dynamic completeness had an average execution time of 34.62 seconds with standard deviation of 0.99 seconds. Calculating dynamic

completeness using the method presented in this work resulted in an average execution time was 4.757 seconds with a standard deviation of 0.036 seconds. The dynamic completeness calculation presented in this paper is $\approx 7\times$ faster than the traditional Brown Completeness method enabling its' use in optimization.

5.4 Discussion

5.4.1 Convergence

Both methods of calculating completeness suffer from sparse sampling of the exoplanet population parameter space. Brown completeness is most affected as it needs planets sampled over Ω, ω, a, e, i, ν, p, and R. The current implementation of our method needs the same parameters except for ν. We are therefore surprised that Brown's method and our method share such similar completeness convergence. We hypothesize that the similar convergence results are because the integration bounds used for calculating completeness are over a dense region of the joint probability density function. If we examined a more sparse region of the joint probability density function such as high Δmag or larger separation (where the larger, lower occurrence rate planets occur), we expect our completeness methods to have marginally better convergence for low numbers of planets. Regardless, integration time adjusted completeness easily reaches completeness errors below 10^{-3} (translates to $\approx 0.8\%$ where $C = 0.12$, the largest completeness of an observation in Ref. [47]); sufficient error for use in optimization.

5.4.2 Reducing Parameter Spaces

The integration time adjusted completeness method implemented in EXOSIMS is not cached for computational efficiency like the Brown completeness is. While we are able to store the joint probability density function of Δmag vs s with Brown's method, integration time completeness requires the KOE of each simulated planet to be stored. The curse of dimensionality prohibits us from finely sampling the entire subspace of exoplanets making the caching of integration time adjusted completeness prohibitive, but not all our methods require all 6 KOE, p, and R. So, in the future, it may be possible to create a representative sub-sampling of planets weighted by occurrence rate based on the parameters needed for different calculations. For example, s extrema, S_{WA}-orbit intersections, and Δmag extrema calculations only require ω, a, e, and i (Note: the ν locations of the Δmag extrema are independent of p and R, but the magnitude of Δmag extrema are dependent upon them). The photometric property $p \times R$ could then be sampled and independently combined with individual (ω,a,e,i) combinations. The primary benefit is that given some instrument parameters and star properties, we could determine the subset of parameters that can physically be observed prior to calculating completeness, thus making the per-star completeness calculations more efficient.

5.4.3 Limitations

The approach we implemented in this paper did not vary the $\Delta\mathrm{mag}_{\mathrm{lim}}$ as we varied the integration time. If properly executed, $\Delta\mathrm{mag}_{\mathrm{lim}}$ should increase with increased integration time. However, calculating the planet true anomaly inter-

sections with a given $\Delta\mathrm{mag}_{\mathrm{lim}}$ is the most expensive calculation so repeatedly calculating this to convergence is not desirable.

The $\Delta\mathrm{mag}_{\mathrm{lim}}$ of coronagraph designs are working angle dependent and therefore separation dependent, but we assume this limit is a fixed quantity. If there is substantial variation in the limiting Δmag, it is better to use the conservative value with this method. If a higher level of predictive accuracy is desired, these methods could be used to ascertain if any intersection with the $\Delta\mathrm{mag}_{\mathrm{lim}}$ exist and subsequently use another method on the subset of planets with known intersections.

5.4.4 Impact of the Integration Time Adjusted Completeness

As we showed in this paper, integration time adjusted completeness and brown completeness converge to the same value to within 0.00002 when evaluated at $t_{\mathrm{max}} = 0$ d. The integration time adjusted completeness for an observation of an Earth-like planet population on a 1 $M_{\odot}$ star 5 pc away and integration time of ≈ 1 day is 0.64% lower than the comparable Brown Completeness. For reference, the Roman target list in Table 9 of Ref. [47] has a maximal integration time of 1.71 d but most are < 0.6 d. This means we could expect an average reduction in yield below 0.64% when observing a population of Earth-like planets around sun-like stars. This integration time completeness adjustment is within the 3.19%, 3σ, margin of error from 1000 Monte Carlo simulations of the Cycle 6 Roman in Ref. [47] and cannot be considered statistically significant. However, a ~ 4 day integration time on a sun-like star 25 pc away observing an Earth-like population has a decrease in completeness above the Ref. [47] 3σ margin

of error. However, the threshold of statistical significance should not deter the wide-spread use of integration time adjusted completeness as the adoption of this method can shore up the differences between completeness based yields and simulation based yields. We can also say that integration time has a muted effect when observing stars that are further away. This can most likely be attributed to the increase in $s_{\min}$ and resulting decrease in the total time-fraction that smaller period planets spend within the visible limits of the telescope. Big planets with the orbital radius of Jupiter will move more slowly and be less effected by integration times.

In B.2, we optimized an exoplanet direct imaging mission maximizing single-visit Brown completeness yield and included the resulting Design Reference Mission (DRM) in Table B.2. The resulting DRM has a Brown completeness yield of 387.16 exoplanet detections in a single-visit detection survey on average, but the integration time adjusted completeness yield expects only 354.67 exoplanets on average. This means Brown completeness for the particular instrument parameters optimized over the SAG13 planet population with the particular mission parameters overpredicts the actual exoplanet yield by 32.49 exoplanets on average; 9.16% more than the integration time adjusted completeness yield. When calculating completeness, we are careful to scale the completeness limits of integration by the star's luminosity. For the integration time adjusted completeness method, we additionally scale the planet's orbital periods based off the mass of the host star. The percentage difference above and beyond that expected from Figure 5.15 can be found by looking at these two adjustments applied to each star and the target list in Table B.2. The average star in the target list has a larger mass and has a brighter luminosity than that of the Sun. The brighter luminosity results in a smaller $s_{\min}$ and $s_{\max}$ which serves to incor-

porate more smaller semi-major-axis planets into the completeness calculations and the larger star masses result in shorter periods meaning the planet visibility windows all decrease in duration.

Integration time adjusted completeness is crucial for determining the ability of an Earth-like planet to be spectrally characterized. A spectral characterization with a coronagraph could take between a few days and 60 days. Because of the long integration time, the planners of a HabEx use the "characterization completeness" of 10% and maximum integration time of 60 days as a filter on stars to consider observing.[100] The calculation of this critical filter could be substantially improved by considering integration time adjusted completeness if the spectrum of the planet must be taken all at once (i.e. and observation spanning multiple weeks) and not spread across multiple epochs. just because a planet can be detected does not mean it can be spectrally characterized.

5.4.5 Dynamic Completeness and Computation Cost

The greatest benefit of using the methods in this paper to calculate completeness is the marginal additional cost of calculating dynamic completeness. Generally, dynamic completeness requires the computation of true anomalies from time, which is prohibitive for $> 10^5$ orbits at > 100 different times in the future. With our methods, calculating visibility windows allows us to use boolean operations to compute dynamic completeness about $7\times$ faster than Brown's dynamic completeness method. The computational cost of calculating completeness using the method described in this paper is an order of magnitude larger than Ref. [13] but can use orders of magnitude fewer planets to do so. Unlike Brown's

method, within the computation time of our method, we also get additional desirable information about the detectable planets such as such as their s extrema and Δmag extrema.

5.4.6 Revisiting the same exoplanet

Another limitation present in the planning of exoplanet direct-imaging missions is the telescope keep-out angles. Figure 3 of Ref. [47] contains a keep-out map for a subset of the design reference mission created in that paper. The smallest percent of time a target star is visible for the Roman is nominally 28%. Due to symmetry of the keep-out region, this translates into two separate time-windows of visibility of ~ 51 days. Instead of considering the integration time as a integration time input, it can also be considered as a revisit time input for determining the probability of being able to observe a planet twice in the same target-star visibility window.

5.4.7 Exoplanet Classification

The underlying methods in this paper are used to find locations along a planet's orbit where s and Δmag intersections occur. The methods in this paper, with some modification, can also be use to probabilistically classify an exoplanet subtype[50]. If an exoplanet is detected with a particular (s,Δmag) and an uncertainty region of $s \pm \sigma_s$ and $\Delta\mathrm{mag} \pm \sigma_{\Delta\mathrm{mag}}$, then the methods in this paper can be applied to each of these four bounding lines. By finding the average orbital time-fraction that exoplanets of each type spend in the bounding uncertainty

box, we can find the probability that the exoplanet belongs to a specific exoplanet sub-type. This requires additional work beyond the scope of this paper.

5.5 Conclusion

We have demonstrated an accurate method for calculating integration time adjusted completeness and its adaptation to calculating dynamic completeness. In the process, we also created fast and accurate methods for calculating the true anomalies where a planet's orbit has specific values of projected separation, Δmag, and their extrema. We demonstrated how to use these novel methods to calculate a more accurate integration time adjusted completeness using the fractions of time a planet is detectable by a instrument. We demonstrate that traditional methods of calculating completeness overestimates the number of observable planets because they do not subtract the integration time used in observing the target. For a Sun-like star at 25 pc with 1 day and 5 day integration times, integration time adjusted completeness of Earth-like planets is reduced by 1% and 5% respectively. We applied integration time adjusted completeness to a target list optimized using the Brown completeness method and found that Brown completeness overestimated yields by 9.61%. We also demonstrated that our methods can be used to quickly calculate dynamic completeness for determining when the optimal time to revisit a target star is.

CHAPTER 6

THE SOLAR SYSTEM AS AN EXOSYSTEM: PLANET CONFUSION

Previous chapters discuss the optimization of single-visit detection surveys with a coronagraph but do not handle what happens post-detection. Currently it is assumed between 2 and 3 additional detection observations are required to fit a single detected planet's semi-major axis, eccentricity, and inclination with sufficient certainty to identify the planet as within the Habitable Zone and justify a follow-up spectral characterization[35, 34]. Team [100] optimizes and plans observations of Earth-analogs in isolation, assuming no other planets exist in the system or that the Earth-like planet can be distinctly identified from the other planets when it is first detected. Considering other non-Earth-like planets like this introduces a planet classification confusion problem when other planets are included as exemplified by the Neptune-Earth false positive Monte Carlo study in Guimond and Cowan [33]. We know that planets even as extreme as Hot Jupiters can have the same Δmag as an Earth-like planet and any planet can have the same s as Earth (in some cases), but can planets as different as Earth and Neptune have the same (s,Δmag) in the same system?

This question takes on more significance as we consider large-scale exoplanet direct imaging missions capable of discovering and characterizing Earth-like exoplanets.[100] A telescope capable of detecting Earth-like exoplanets would also be sensitive to a myriad of non-Earth-like exoplanets in the broader population with the same instantaneous planet-star separation (s) and planet-star difference in magnitude (Δmag), even planets like those in our solar system. In this chapter, we consider the Solar System as a previously unexplored exosystem, viewed by an external direct-imaging observer for the first time.

We focus on the first direct-image of Solar System planets where only estimates of the planet-star separation (s) and planet-star difference in magnitude (Δmag) for detected planets are measured. We assume each of the exoplanets detected are spatially resolved. Even if the limited information collected indicates an exoplanet has a (s,Δmag) characteristic of an Earth-like exoplanet, it is not possible to discern with certitude that the exoplanet is Earth-like. While orbit fitting of multiple simultaneously detected and resolved exoplanets could preclude this, it is possible for multiple exoplanets to be detected and the Earth-like exoplanet be indiscernible from non-Earth-like exoplanets.

While the set of potential planets around a host star has a broad diversity and the habitability classification is broadly defined, we choose to study the classification confusion problem of our own Solar System treated as an exosystem. We are motivated to do this for multiple reasons. The decadal survey seeks insight and answers as to how our Solar System was formed and how it fits into the vast collection of other planetary systems[18]. The abundance or rarity of planetary systems similar to the Solar System is currently unknown [98, 68]. Future exoplanet direct-imaging missions will have the capability to discover Solar System-like star systems[100]. Engineers are motivated to design future telescopes to the most strict requirements stemming from the challenges of detecting Earth-like exoplanets, meaning many other types of exoplanets in the star system will also be detected[100]. Third, we know more about the Solar System planets than any other planets in the galaxy thanks to the multitude of missions and studies of these bodies.

Using the Solar System planet population described in 2.3, we will show that an external observer would find that many of our planetary bodies have multi-

ple points of (s,Δmag)-coincidence along their orbits. In Section 6.1 we present the underlying planet photometric and astrometric models and how we combine them to get continuous phase curves spanning the entire range of phase angles. 2.3 contains the melded planet phase curves derived from Mallama and Hilton [61]. In Section 6.2 we show our process for finding the locations of (s,Δmag)-coincidences and inclination deviations from edge on where intersections still occur. Finally, in Section 6.3, we calculate the fraction of Solar Systems where a given planet has (s,Δmag)-coincidence with Earth.

6.1 s-Δmag Curves

Our goal is to find the fraction of inclined Solar Systems which could have (s,Δmag)-coincidence between any two planets. To do this, we first need a method for finding the (s,Δmag)-coincidence points between any two Solar System planets.

We start with the general equation for Δmag given in Eqn. 3 of Brown [13]. By assuming the orbits are circular ($e = 0$), this simplifies to:

$$\Delta\text{mag} = -2.5 \log_{10} \left(p \left(\frac{R}{a} \right)^2 \Phi(\beta) \right). \tag{6.1}$$

The geometric albedo (p) and planetary volumetric mean radius (R) can be substituted in from Table 2.2 for each planet. This results in Δmag as a function of the planet phase function (Φ) and phase angle (β).

The phase angles are limited by the common system inclination (i). The global β extrema are in the edge-on ($i = 90°$) system, but the β extrema for any

given inclination are

$$\beta_{\text{extrema}} = 90^\circ \pm i. \tag{6.2}$$

We make use of the high order, parametric, polynomial fit phase functions from Mallama and Hilton [61] and detailed in chapter 2.3.

Brown [13] took the general planet-star separation equation and reduced it into a function of phase angle, by adding our circular orbit simplification we get

$$s = a \sin(\beta). \tag{6.3}$$

We plot the Δmag vs s curves for each Solar System planet in Figure 6.1 at varying inclinations with HabEx angular measurement uncertainty of $\sigma_{\text{WA}} = 0.05$ mas at 10 pc and Δmag uncertainty derived from Team [100] to be $\sigma_{\Delta\text{mag}} = 0.145$. This photometric uncertainty assumes a signal to noise ratio of 7 will be achieved on every planet and is achievable across the entire Δmag range of the planets. We plot the measurement uncertainty bounds by sampling Δmag and s over β and plotting the resulting 1σ bounds in Figure 6.1a and 3σ in Figure 6.1b-f. The Δmag vs s curves in Figure 6.1a show 21 different locations where planet-pairs have coincidence in the edge-on system. As the system inclination changes from edge-on to face on in Figure 6.1b-f, we see the number of intersections and visible range of the planets decrease. These Δmag vs s curves give us the core components required to find the (s,Δmag)-coincidence for any give planet pair.

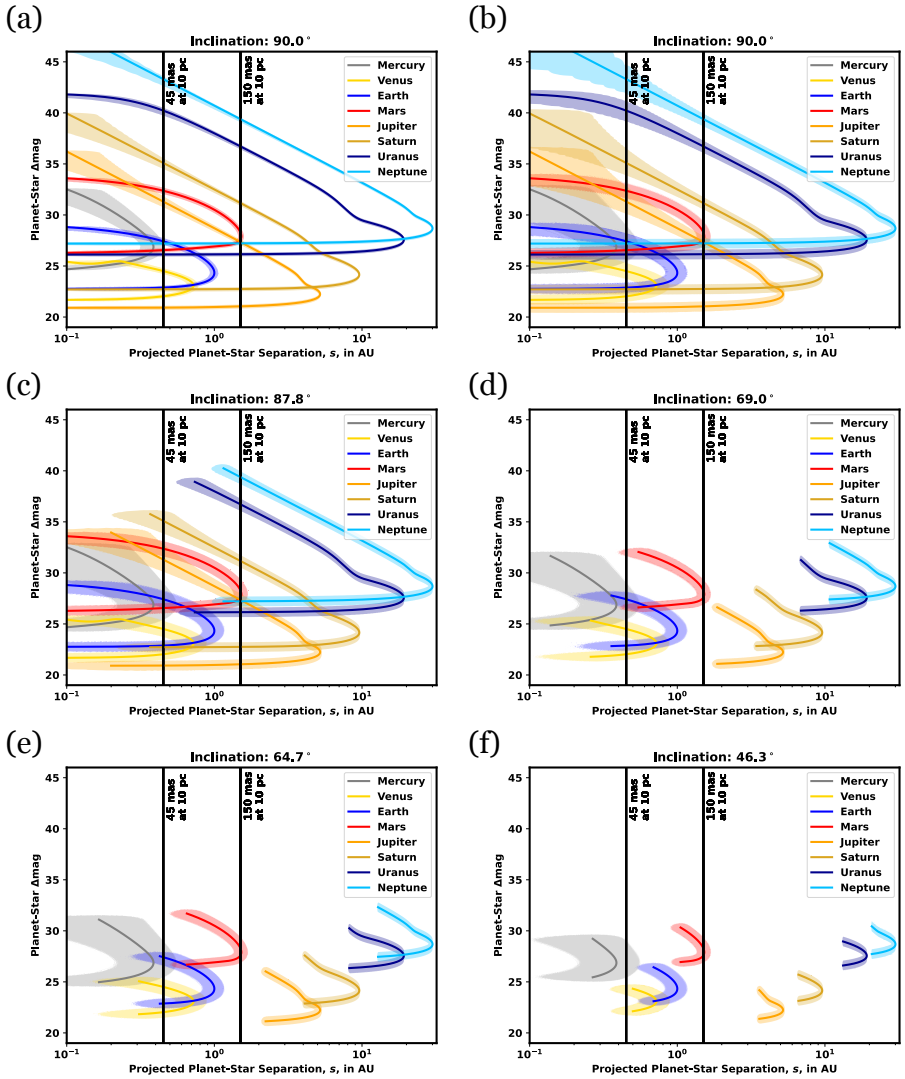

Figure 6.1: Δmag vs s plots of Solar System planets for varying star system inclinations with separation lines at working angles of 45 mas and 150 mas at 10 pc. The $1\sigma_{\Delta\text{mag}} = 0.01\%$ and $1\sigma_s = 5$ mas[100] are plotted in (a). The 3σ bounds are plotted in (b)-(f) for varying inclinations; (b) $i = 90°$, (c) the Earth-Saturn intersection where $i \geq 87.8°$ (d) the Earth-Mercury intersection where $i \geq 69.0°$, (e) the Earth-Mars intersection occurring where $i \geq 64.7°$ (f) the Earth-Venus intersection occurring at $i \geq 46.3°$. Additional Earth-Uranus and Earth-Neptune intersections occur at $i = 1.0°$ and $i = 1.7°$ respectively and can be seen in (a) and (b). The phase functions for these planets are included in 2.3. Planet radius, geometric albedo, and orbital radius are as in Table 2.2. Note that Saturn's Δmag calculation omits the light contribution from the rings which can quadruple the brightness [22].

6.2 (s,Δmag)-Coincidence Points

We cannot solve for (s,Δmag)-coincidence using conventional root finding techniques because the underlying equations are non-linear, their combination is under-constrained, and we do not know good initial guesses of the (s,Δmag)-coincidence points. This problem has three degrees of freedom: the phase angle of each planet (β_s and β_l for the interior and exterior planet, respectively) and the inclination of the common orbital plane. We only have the Δmag and s constraint equations making this problem under-constrained. To circumvent this issue, we formulate the problem as a constrained minimization problem and include i as a constraint on β_s and β_l.

In our optimization formulation, we minimize the absolute difference between the Δmag values of each planet, Δmag error. We additionally require both planets have same planet-star separation. For each planet-star separation, there are two associated Δmag values. The larger Δmag, and therefore dimmer side, occurs where $\beta > 90°$. The smaller Δmag, and therefore brighter side, occurs where $\beta < 90°$. When optimizing, it is not possible for β_s or β_l to cross the infinite slope point of the Δmag vs s curve. We therefore formulate four separate optimization initial conditions and phase angle constraints associated with the portions of the phase curve the interior and exterior planets could have coincidence on: where the interior-exterior planets are brighter-dimmer, brighter-brighter, dimmer-dimmer, and dimmer-brighter, which we label as $Q \in \{0, 1, 2, 3\}$. Therefore, there are four sets of initial guesses of ($\beta_{s,0}$,$\beta_{l,0}$)

to test the optimization process which we differentiate with $Q \in \{0, 1, 2, 3\}$:

$$(\beta_{s,0}, \beta_{l,0}) = \begin{cases} \left(\frac{90+i}{2}, \left(\sin^{-1}\left(\frac{a_s}{a_l}\right)\frac{180}{\pi} + 90\right) \times 0.3 + (180 - i) \times 0.7\right), & Q = 0 \\ \left(\frac{90+i}{2}, \frac{1}{2}\left(i + \sin^{-1}\left(\frac{a_s}{a_l}\right)\frac{180}{\pi}\right)\right), & Q = 1 \\ \left(90 \times 0.3 + (180 - i) \times 0.7, \right. \\ \left. \left(\sin^{-1}\left(\frac{a_s}{a_l}\right)\frac{180}{\pi} + 90\right) \times 0.3 + (180 - i) \times 0.7\right), & Q = 2 \\ \left(90 \times 0.3 + (180 - i) \times 0.7, \frac{1}{2}\left(i + \sin^{-1}\left(\frac{a_s}{a_l}\right)\frac{180}{\pi}\right)\right), & Q = 3 \end{cases} \tag{6.4}$$

The 0.3 and 0.7 values were selected to create a midpoint value between the minimum and maximum possible β for the interior and exterior planet.

Algorithm 4: Minimum Δmag error producing phase angles

Input: i, a_s, a_l, R_s, R_l, p_s, p_l, $\beta_{s,0}$, $\beta_{l,0}$, and Q

Output: β_s^* and β_l^*, the optimal planet phase angles of the small a_s and large a_l planet respectively

$$\beta_s^*, \beta_l^* = \underset{\beta_s, \beta_l}{\arg\min} \left| \begin{array}{l} 2.5 \log_{10}\left(p_s \left(\frac{R_s}{a_s}\right)^2 \Phi_s(\beta_s)\right) \\ -2.5 \log_{10}\left(p_l \left(\frac{R_l}{a_l}\right)^2 \Phi_l(\beta_l)\right) \end{array} \right|$$

s.t.

$$\begin{aligned} 0 = \quad & a_s \sin(\beta_s) - a_l \sin(\beta_l) && , \\ -\beta_s \leq & -i && \text{If } Q = 0, 1 \quad , \\ \beta_s \leq & 180 - i && \text{If } Q = 2, 3 \quad , \\ -\beta_l \leq & -\sin^{-1}\left(\frac{a_s}{a_l}\right)\frac{180}{\pi} - 90 && \text{If } Q = 0, 2 \quad , \\ \beta_l \leq & 180 - i && \text{If } Q = 0, 2 \quad , \\ -\beta_l \leq & -i && \text{If } Q = 1, 3 \quad , \\ \beta_l \leq & \sin^{-1}\left(\frac{a_s}{a_l}\right)\frac{180}{\pi} && \text{If } Q = 1, 3 \end{aligned}$$

We run Algorithm 4 over each unique pair of Solar System planets and each

constraint associated with $Q \in \{0, 1, 2, 3\}$. Some of these optimization processes do not successfully terminate. This occurs when the inclination constraints do not allow the separation constraint to be satisfied. While other optimization formulations may successfully terminate via convergence to a minimum error solution, not all minimum error solutions are locations of (s,Δmag)-coincidence. We apply a threshold, defining planet-pairs with $|\Delta\mathrm{mag}_s - \Delta\mathrm{mag}_l| < 10^{-5}$ as coincident. This selection forces the omission of the Mars-Uranus intersection despite the two planets having a substantial region of overlapping uncertainty, but still includes the Earth-Saturn intersection. Table 6.1 contains the s and Δmag of coincidence as well as the phase angles of the interior and exterior planet. Only the Mars-Jupiter pair has two (s,Δmag)-coincidence points. There are only 5 instances where (s,$\Delta\mathrm{mag}$)-coincidence occurs over a phase angle region using the Lambert phase function. They occur for Jupiter at Jupiter-Neptune, Jupiter-Uranus, Mars-Jupiter (1), and Mars-Jupiter (2) as well as Saturn-Neptune.

With these phase angles of coincidence, we can calculate the deviations from edge on inclinations where the Solar System no longer has (s,Δmag)-coincidence for any given planet pair. We define these critical inclination deviations as ($\delta i_{\mathrm{crit},\pm}$). They can be found by

$$\delta i_{\mathrm{crit},\pm} = 90^\circ \pm \min\left[\min\left(\beta_s, 180^\circ - \beta_s\right), \min\left(\beta_l, 180^\circ - \beta_l\right)\right]. \tag{6.5}$$

6.3 Fraction of Affected Solar Systems

We consider the Earth's Δmag vs s curve in Figure 6.1, which we take as representative of the highest scientific priority exoplanet type. The Earth's curve crosses those of Mercury, Neptune, Uranus, Mars, Venus, and Saturn (within

Table 6.1: Planet-planet coincidence locations. The planet-star difference in magnitude, Δmag, planet-star separation s in AU, phase angle of the interior planet (β_s) in deg, phase angle of the exterior planet (β_l) in deg, maximum system inclination where intersections occur (δi_{crit}) in deg of the planet-planet coincidence

	Δmag	s (AU)	β_s (deg)	β_l (deg)	δi_{crit} (deg)
Mercury-Venus	25.41	0.26	42.18	158.94	21.06
Mercury-Earth	27.72	0.36	111.84	158.94	21.06
Mercury-Mars	26.57	0.38	81.16	14.54	14.54
Mercury-Uranus	26.13	0.36	67.06	1.06	1.06
Mercury-Neptune	27.2	0.38	99.27	0.73	0.73
Venus-Earth	23.15	0.72	92.46	46.27	46.27
Venus-Saturn	22.72	0.69	73.37	4.15	4.15
Earth-Mars	26.6	0.65	139.34	25.32	25.32
Earth-Saturn	22.8	0.29	17.06	1.75	1.75
Earth-Uranus	26.13	0.76	130.77	2.26	2.26
Earth-Neptune	27.12	0.53	148.27	1.0	1.0
Mars-Jupiter (1)	27.48	1.48	76.61	163.45	16.55
Mars-Jupiter (2)	32.98	0.27	169.67	176.99	3.01
Mars-Uranus	26.2	0.0	0.0	0.0	0.0
Mars-Neptune	27.22	1.38	65.07	2.64	2.64
Jupiter-Saturn	22.83	4.58	118.24	28.58	28.58
Jupiter-Uranus	26.1	2.18	155.24	6.52	6.52
Jupiter-Neptune	27.19	1.58	162.36	3.01	3.01
Saturn-Uranus	26.19	5.47	145.21	16.55	16.55
Saturn-Neptune	27.27	4.35	153.02	8.32	8.32
Uranus-Neptune	27.66	19.16	93.89	39.61	39.61

the 3σ uncertainty region). Furthermore, the critical inclinations in Table 6.3 indicate (s,Δmag)-coincidence persists across a broad range of inclinations.

When simulating a multitude of inclined star systems, we randomly sample inclinations such that the probability density function is $f_{\bar{i}}(i) = \sin(i)/2$ following after Brown [13], Savransky, Kasdin, and Cady [79] and Keithly et al. [47]. Since we are assuming circular orbits, we can calculate the percentage of randomly generated Solar Systems where any Solar System planet will have (s,Δmag)-coincidence with the Earth by integrating over the inclination proba-

Table 6.2: Planet-planet coincidence locations and the probability a planet is within the $n\sigma$ uncertainty limits. The planet-star difference in magnitude, Δmag and planet-star separation s in AU. The probability the smaller semi-major axis planet is within $n\sigma$ of the intersection point ($P_{n\sigma s}$) in % and the same probability for the larger semi-major axis planet ($P_{n\sigma l}$). Rounding means probabilities of 0 are less than 0.05%.

	Δmag	s (AU)	$P_{1\sigma s}$	$P_{1\sigma l}$	$P_{2\sigma s}$	$P_{2\sigma l}$	$P_{3\sigma s}$	$P_{3\sigma l}$
Mercury-Venus	25.41	0.26	7.8	4.7	14.7	9.6	20.5	13.9
Mercury-Earth	27.72	0.36	4.8	3.7	9.6	7.8	14.5	11.4
Mercury-Mars	26.57	0.38	3.3	2.2	6.7	4.4	11.5	6.7
Mercury-Uranus	26.13	0.36	3.6	0.0	7.3	0.0	11.1	0.0
Mercury-Neptune	27.2	0.38	5.8	0.0	11.5	0.0	16.1	0.0
Venus-Earth	23.15	0.72	7.9	5.5	14.8	11.0	21.7	15.9
Venus-Saturn	22.72	0.69	5.1	0.1	10.2	0.2	16.6	0.3
Earth-Mars	26.6	0.65	4.7	3.9	9.5	7.6	14.2	11.0
Earth-Saturn	22.8	0.29	2.5	0.5	4.9	1.0	7.5	1.4
Earth-Uranus	26.13	0.76	5.1	0.0	10.2	0.1	15.0	0.1
Earth-Neptune	27.12	0.53	3.6	0.0	7.2	0.0	10.8	0.0
Mars-Jupiter (1)	27.48	1.48	4.1	0.9	7.9	2.2	11.2	3.3
Mars-Jupiter (2)	32.98	0.27	0.8	0.3	1.6	0.5	2.4	0.7
Mars-Uranus	26.2	0.0	0.0	0.1	0.2	0.2	0.4	0.3
Mars-Neptune	27.22	1.38	3.5	0.2	7.5	0.4	11.0	0.5
Jupiter-Saturn	22.83	4.58	1.8	0.7	3.6	1.4	5.5	2.0
Jupiter-Uranus	26.1	2.18	0.7	0.3	1.4	0.6	2.1	0.9
Jupiter-Neptune	27.19	1.58	0.5	0.2	1.0	0.4	1.5	0.5
Saturn-Uranus	26.19	5.47	0.6	0.3	1.2	0.6	1.8	0.9
Saturn-Neptune	27.27	4.35	0.4	0.2	0.9	0.4	1.3	0.6
Uranus-Neptune	27.66	19.16	4.9	0.2	7.8	0.4	9.1	0.6

bility density function,

$$P(\delta i_{\text{crit},-} \leq i \leq \delta i_{\text{crit},+}) = \frac{1}{2}\int_{\delta i_{\text{crit},-}}^{\delta i_{\text{crit},+}} \sin(i)\delta i. \tag{6.6}$$

This distribution of inclinations peaks at $i = 90^\circ$ (edge on) and has minimums at $i = 0^\circ$ and $i = 180^\circ$. We compute these probabilities and compile them in Table 6.3.

Table 6.3 shows the fraction of Solar Systems with (s,Δmag)-coincidence independent of instrument capabilities. We can determine which intersecting

Table 6.3: The percent of Solar Systems where each respective planet having any (s,Δmag)-coincidence with Earth. Assumes circular orbits and co-planar planet orbits.

	Neptune	Saturn	Uranus	Mercury	Mars	Venus
% of Solar Systems	1.7%	3.0%	3.8%	36.0%	42.7%	72.2%

planet pairs are visible to an instrument by comparing the Δmag and s of intersection with the instrument limited Δmag ($\Delta\mathrm{mag}_{\mathrm{lim}}$) and working angle limits at a star distance. For the Earth's (s,Δmag)-coincidence referenced in Table 6.3, an instrument with a contrast of 10^{-10} and inner working angle of 45 mas at 10 pc would only be able to see Earth's coincidence with Venus. As we can see from Table 6.1, increasing the limiting Δmag of a telescope exacerbates the potential for planet-type confusion by including more instances of (s,Δmag)-coincidence. Assuming the same instrument as in Table 6.3, only the Earth-Venus, Venus-Saturn, and Jupiter-Saturn coincidences are detectable. If, at some point in the future, a contrast of 10^{-11} with inner working angle of 30 mas were achievable; then 15 intersections could be observable in Solar System analogs.

Assuming a system produces (s,Δmag)-coincidence between two planets, we can compute the probability a planet randomly located along its orbit is within $n\sigma$ of the coincidence point. We randomly sample inclinations from $f_{\bar{i}}(i)$ between the critical inclination limits and randomly distribute these planets uniformly in time along their orbit. s and Δmag of each randomly sampled planet can be computed and we can find the fraction of these planets within the $n\sigma$ uncertainty region of the (s,Δmag)-coincidence point. This fraction is the fraction of an orbit the planet spends within this uncertainty region and is converted into the percentages in Table 6.2. In all cases, the probability of the larger semi-major axis planet being within the uncertainty bounds is less than the probability of the smaller semi-major axis planet being within the mea-

surement uncertainty bounds ($P_{n\sigma l} < P_{n\sigma s}$). The maximum probability of coincidence is between Venus-Earthbibdata followed by Mercury-Venus, Mercury-Earth, and Earth-Mars. If a planet from a Solar System-like star system at the (s,Δmag)-coincidence of Earth with either Uranus or Neptune is detected, it is $\sim 150\times$ more likely that the planet is an Earth than a Uranus or Neptune. In general, the probabilities of either planet being within the instrument uncertainty bounds are within an order of magnitude of one another. Only the instances of Mercury-Uranus, Mercury-Neptune, Venus-Saturn, Earth-Uranus, and Earth-Neptune have occurrence disparities greater than an order of magnitude.

6.4 Conclusion

Future exoplanet direct-imaging missions must make multiple observations to differentiate between Earth-like exoplanets and the myriad of other planets in the population. We took phase functions derived from a variety of deep space missions to create melded phase functions of Solar System planets. We showed that up to 21 cases of (s,Δmag)-coincidence between planet pairs exist in the Solar System. We additionally showed how an Earth can have the same (s,Δmag)-coincidence with up to 6 other Solar System planets. We found the inclination range where each Solar System planet could still have coincidence with another planet. We found 36% to 69% of inner Solar System planets and 1% to 4% of outer Solar System planets share (s,Δmag)-coincidence with Earth. While the Nancy Grace Roman Space Telescope would only be capable of seeing coincidences between Earth and Venus, further improvement in instrument contrast and inner working angles will exacerbate the planet confusion problem.

CHAPTER 7

MINIMUM REVISIT TIME

Telescope time is wasted if the exoplanet is missed on the second detection or it is detected in the same region of (s,Δmag,θ) phase space (nothing *new* is learned). There are no tools or capabilities to reliably plan a revisit of an exoplanet, only some baseline heuristics developed by JPL for a specific planet population.

In this chapter, I present my method to determine the earliest time the detected exoplanet could be revisited and be in a unique region of (s,Δmag,θ) phase space. I also suggest an ideal time to revisit an exoplanet such as when the fraction of planets that are distinctly distinguishable and still detectable is maximized. Another option I present is when the fraction of distinctly distinguishable and still detectable Earth-like planets is maximized relative to the fraction of distinctly distinguishable and still detectable SAG13 planets.

7.1 Introduction

The second detection provides an opportunity to gain more information about the target planet, but also comes with the risk of wasting telescope time.

It is of the utmost importance that the second detection is not missed or made in the same region of (s,Δmag,θ) space; either scenario means valuable telescope time was wasted.

Problem 1:

If the exoplanet is revisited too quickly it will be too close in (s,Δmag,θ) space to the previous detection to extract any sort of useful data out of the detection (although some probabilistic statement about common proper motion might be able to be made).

Problem 2:
If the time between discovery and revisit is too long, the exoplanet could leave the visibility limits of the telescope and become undetectable.

I am therefore interested in finding the minimum revisit time of an Earth-like exoplanet for the execution of a rapid revisit. A **rapid revisit** is an observation made as quickly as possible with the caveat that the observed exoplanet appears in a *distinctly distinguishable* region of the (s,Δmag,θ) phase space and still within the detectable region of the instrument.

At one point in time, the Jet Propulsion Lab conducted a private study of the optimal revisit time for Earth Twin exoplanets. Their primary conclusion was that Earth Twin exoplanets could be revisited at 14 days after a detection at quadrature, this was then adopted as a default value in EXOSIMS. The SDET[65] says "The wait period for each star is a third of the period of an earth twin around that star." Meaning the suggested revisit time for an Earth Twin around a sun-like star will be 121 days. Additional studies in the SDET considers revisit times between 2 months and 6 months to be reasonable to image a planet over a large portion of its orbit. These suggestions are reasonable and are sometimes consistent with the results shown, but they do not go into sufficient analysis in depth to substantiate their policy decision. However, no additional studies of substance have been conducted which investigate what the minimum revisit time is, so I have done so here.

In my study, there are two parameters of importance. The first is the number of σ to consider the uncertainty limits of the detection. The second is the fraction of planets that have left the σ uncertainty region. In this work, I feel 3σ and 99.7% should be sufficient. In reality, an additional study should be done which determines which $n\sigma$ limits and $X\%$ of planets maximizes yield of a Monte Carlo of simulations.

In section 7.1.1, I give my definition of *distinctly distinguishable* (and suggest a secondary definition) that combines the detection parameter deltas into a single parameter. In section 7.2.1, I describe my procedure for calculating the minimum revisit time for a detection at a particular (s,Δmag). I create a grid of (s,Δmag) points in section 7.2.2 to calculate the minimum revisit times for. In section 7.2.3, I present a method for calculating the time to revisit which maximizes the probability the detected planet is Earth-like. In section 7.3.1, I show the changes in measurables of a particular detected sub-population, found using exodetbox, as a function of time as well as the combined metric. In section 7.2.1, I find the time when $X\%$ of planets have left the $n\sigma$ detection box for each (s,Δmag) point for different planet populations. In section 7.3.3, I combine the combined metric used to determine the minimum revisit time with the fraction of planets still within the planet visibility limits and find the time where this peaks. In section 7.1.3, I show a histogram of the star visibility windows caused by the telescope keep-out regions, which can provide an upper bound on revisit time if I want to observe the same target within a keepout window.

7.1.1 Distinctly Distinguishable

I want a way to find the minimum revisit time for an exoplanet detected with a given (s_0,Δmag_0,θ_0) such that the exoplanet is detected at a different location in space.

Up until this point, I have not concerned myself with the angular position of the detected exoplanet relative to $\hat{\underline{x}}$ axis in Figure 5.3 about the $\hat{\underline{z}}$ axis (θ). This is because it is largely irrelevant for single-visit detections (with some exceptions). Considering the second detection requires us to consider this angle (θ) or change in angle $\Delta\theta$. I calculate the θ angle of an individual detection by

$$\theta = \tan^{-1}\left(\frac{Y}{X}\right), \tag{7.1}$$

where X and Y are given Eqn. 5.10.

The second detection must not be the same as the first detection an exoplanet in the same region of phase space as (s_0,Δmag_0,θ_0). That is to say, I want the second detection to be in a distinctly distinguishable region of (s,Δmag,θ) phase space. More formally, (s_1,Δmag_1) such that $|s_0 - s_1| > n\sigma_s$ and/or $|\Delta\text{mag}_0 - \Delta\text{mag}_1| > n\sigma_{\Delta\text{mag}}$) and/or $\Delta\theta > n\sigma_\theta$.

It is distinctly possible for exoplanets to appear stationary in s and Δmag space but move in θ space. To account for this, I calculate the combined metric, ξ. ξ is the root mean square summation of the deltas normalized by their respective σ. I calculate this as

$$\xi = \sqrt{\left(\frac{\Delta s}{\sigma_s}\right)^2 + \left(\frac{\Delta\Delta\text{mag}}{\sigma_{\Delta\text{mag}}}\right)^2 + \left(\frac{\Delta\theta}{\sigma_\theta}\right)^2}. \tag{7.2}$$

It may also be possible to use $\max(s/\sigma_s, \Delta\text{mag}/\sigma_{\Delta\text{mag}}, \theta/\sigma_\theta)$ to achieve good results, but this needs to be tested in future work.

7.1.2 Probability and the treatment of $n\sigma$

There is difficulty in defining the probability a particular planet belongs to a specific (s_0,Δmag_0,θ_0) detection because the probability a particular planet has a specific (s_0,Δmag_0,θ_0) at an instant in time is 0, the probability this point is even along the particular planet's orbit is 0, and the (s,Δmag,θ) of a particular planet changes in time. What I would ideally like to see is the computation of the combined time-fraction and distance probability a particular planet belongs to the detection with something like

$$P(a_k, e_k, i_k, \omega_k, \Omega_k, p_k, R_k | s_0, \Delta\text{mag}_0, \sigma_s, \sigma_{\Delta\text{mag}}, \sigma_\theta) =$$
$$\frac{1}{T}\int_0^T \int_{s_0}^{s(t)} \int_{\Delta\text{mag}_0}^{\Delta\text{mag}(t)} \int_0^{\Delta\theta(t)} f_{\text{meas}}(s_0, \Delta\text{mag}_0, \sigma_s, \sigma_{\Delta\text{mag}}, \sigma_\theta)\delta\Delta\theta\delta\Delta\text{mag}\delta s\delta t. \quad (7.3)$$

Which is then iterated for a population of planets. However, this is a quadruple integral and it would still requires us to average this operation over a population of planets meaning this is computationally intractable.

Instead, I define the exoplanet detection box (exodetbox) as the region of phase space bounded by $n\sigma$ of (s,Δmag). I then use the exodetbox methods[42] discussed in chapter 5 to quickly find the time(s) planets in the population are within the exodetbox. What this means is that I will know the time(s) along each particular planet's orbit when the planet crosses $s \pm n\sigma_s$ or $\Delta\text{mag} \pm n\sigma_{\Delta\text{mag}}$. This also gives us the total time-fraction of an orbit the planet spends within the particular exodetbox. I can then say the particular planet spends $X\%$ of its orbit within the $n\sigma$ uncertainty box. Here, I have made the implicit assumption that the probability of this planet being drawn is equal to all other exoplanets in the distribution. In future work, an amendment must be made that weights each planet by the time fraction of an orbit the planet spends within the $n\sigma$ visibility

limits.

For a single variable randomly sampled from a gaussian distribution, 68.27% of the samples drawn will be within $\pm 1\sigma$ of the mean, 95.45% of samples will be within $\pm 2\sigma$ of the mean, and 99.73% of samples will be within $\pm 3\sigma$ of the mean. When I increase dimensionality to two parameters (as is the case for the exodetbox), there is only a $46.61\% = 68.27\% \times 68.27\%$ chance a randomly drawn sample is within the 1σ detection box (1σ for both parameters). For the 2σ exodetbox applied to two parameters, the probability a randomly sampled (s,Δmag) is within 2σ is $91.11\% = 95.45\% \times 95.45\%$. For the 3, 4, and 5 σ boxes this is 99.46%, 99.98%, and 99.99%. While the astrophysics community will use up to 5σ for some applications, I suggest the use of 3σ since it encompasses the vast majority of exoplanets (all but $\approx 0.54\%$ of planets that could belong to the (s,Δmag) detection) and mitigates some of the flat probability assumption used by the exodetbox in Δparameter vs time calculations. In the future, it may be desirable to perform multiple exodetbox calculations for a discretization and weighting of $n\sigma$ levels.

7.1.3 Star Observing Limitations

In chapter 3, I state that the optimal time to make a single-visit detection of a target star is when the local zodiacal light is minimized. While true for a single-visit blind search, planning multiple visits of a target star induces new constraints on the times to make the first detection. These constraints are imposed by logistical limitations imposed by the telescope or starshade, namely the keep-out zones.

For Roman at L2, there are up to two keep-out zones which limit when the star is able to be observed. The first is the Sun, Earth, and Moon keep-out which are too bright in in the night sky to look at, they would saturate or damage the detector if an observation was made within 24° of them. The second is the solar panel keep-out, where the telescope cannot sustainably look more than $124\circ$ away from the sun or it will not be able to power the deformable mirrors required to make the observation. The distribution of stars in the sky result in a distribution of maximum per-year target availability in Figure 7.1. The shortest of these are around 50 d and the largest are visible year-round. As seen in Figure 7.5, the detection of exoplanets at some (s,Δmag) with 3σ and 99% have approach 40 d, only a 10 d margin for some stars when looking at Figure 7.1.

7.2 Methods

In section 7.2.1, I present my process for calculating the minimum revisit times following the detection of an exoplanet. In section 7.2.2, I create a set of (s,Δmag) points space 1σ apart so I may apply the minimum revisit time method and others over the Earth-like planet population phase space to see how minimum revisit times vary over the detection space.

7.2.1 Minimum Revisit Time

The general process for calculating the minimum revisit times for an exoplanet detected at (s_0,Δmag_0,θ_0) is outlined here and discussed below.

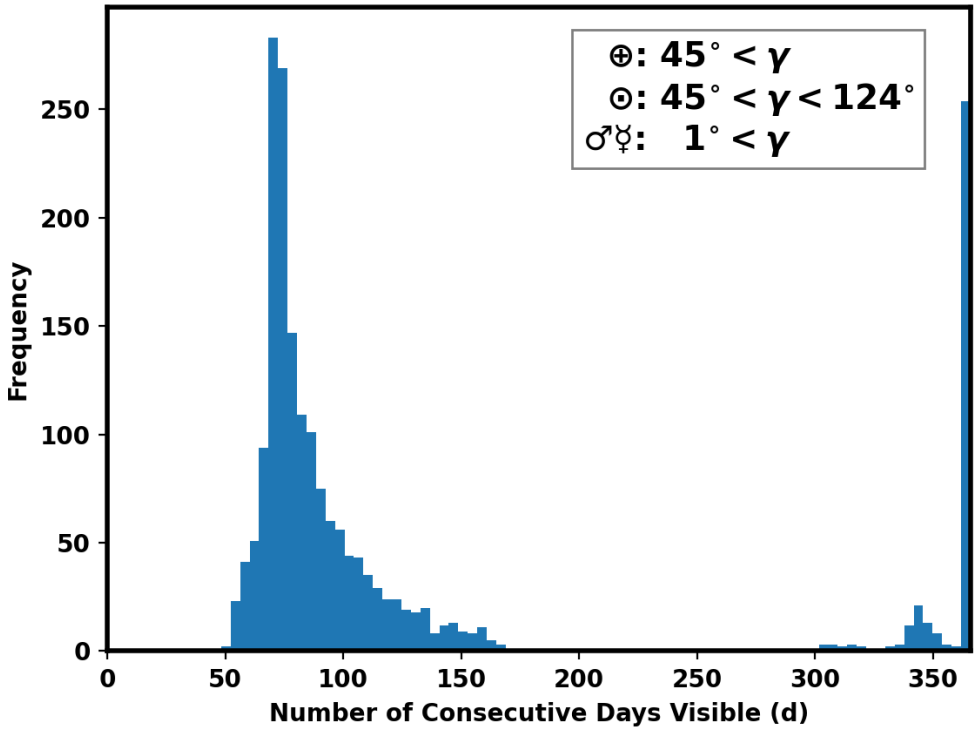

Figure 7.1: A histogram of the maximum time target stars have continuous, uninterrupted, visibility.

1. Randomly sample KOE from a planet population
2. apply the exodetbox method described in section 5.2 of chapter 5 to $s \pm \sigma_s$ and $\Delta\text{mag} \pm \sigma_{\Delta\text{mag}}$
3. calculate times of intersection from true anomalies of intersections
4. calculate the average time of each visibility window t_0
5. for each planet with multiple visibility windows, select a specific time window of detection weighted by the time spent within the $n\sigma$ of that particular visibility window
6. propagate each planet $\Delta t + t_0$
7. establish common proper motion based on $sign(\cos(i))$

8. calculate the fraction of exoplanets that are detectable from t_0 to $t_0 + \Delta t$
9. calculate
10. calculate the fraction of exoplanets within $n\sigma$ of (s_0,Δmag_0,θ_0)
11. calculate ξ
12. find where $\xi(\Delta t) > n\sigma$

I create a random sampling of planets from a planet population using the sampling techniques described in chapter 2. The size of the exodetbox determines the number of planets that need to be simulated. For the HabEx telescope detection σ described in chapter A applied to the SAG13 planet population, around 10^5 to 10^6 exoplanets are required to create a sufficiently large detected sub-population ($> 10^3$ is sufficiently large). I then apply the exodetbox method from chapter 5, using the $n\sigma$ box around the (s,Δmag) detection point as inputs to exodetbox. This narrows down the planet population into only those that spend some portion of their orbit within the $n\sigma$ detection box. For each planet with more than one visibility window within the exodetbox, I randomly select a visibility window weighted by the time spent within the exodetbox. I treat the selected visibility window as the times past periastron where that planet was detected. For the selected window of time the planet is within the exodetbox, I calculate the average time past periastron ($t_{avg,0}$) that the planet is within the exodetbox. I take this average time past periastron of the planet and compute the (s,Δmag) of the planet at that time and assume this was the (s_0,Δmag_0) that the particular planet was detected at.

I must make an aside to discuss this particular assumption mentioned. Without directly modifying the underlying planet population, it is not possible to find a collection of planets at an exact (s,Δmag) point since the probability

of a singular event occurring is exactly 0. This is why I must use the $n\sigma$ exodetbox to find the sub-population of planets in the original population that come within $n\sigma$ of the detected planet. If it were possible, it would behoove a successor/inheritor of this work to find a mechanism to "weight" each particular planet and somehow use the likelihood of a planet having the (s,Δmag) measured. This task is extraordinarily difficult for a multitude of reasons, but mainly because the planet is moving in (s,Δmag) space during the detection so any kind of specific probability the planet belongs to the detection is difficult to specify without substantial computational cost. This is also relevant because there are some planets which can broach the edge of the exodetbox and not come substantially closer to the (s,Δmag) point than $n\sigma$.

I may now take each planet in the sub-population within $n\sigma$ of (s,Δmag) at their (s_0,$\Delta\mathrm{mag}_0$) at $t_{avg,0}$ and calculate (s_1,$\Delta\mathrm{mag}_1$,$\Delta\theta$) of each planet at $t_{avg,0} + \Delta t$ in the future. By sampling enough times in the future, I can determine the Δt where the ξ metric crosses the $n\sigma$ threshold. This Δt becomes the minimum revisit time.

7.2.2 Creating the s vs Δmag grid

Using Daniel Garrett's analytical[27] planet population (s,Δmag) limits applied to the Earth Twin planet population, I can create an even spacing of points spread across this phase space. I create an even spacing of separations, each $2\sigma_s$ from the other, sample each separation at the analytical lower s,Δmag limit and create a grid of points $2\sigma_{\Delta\mathrm{mag}}$ apart from the lower s,Δmag limit to the upper s,Δmag limit shown in Figure 7.2.

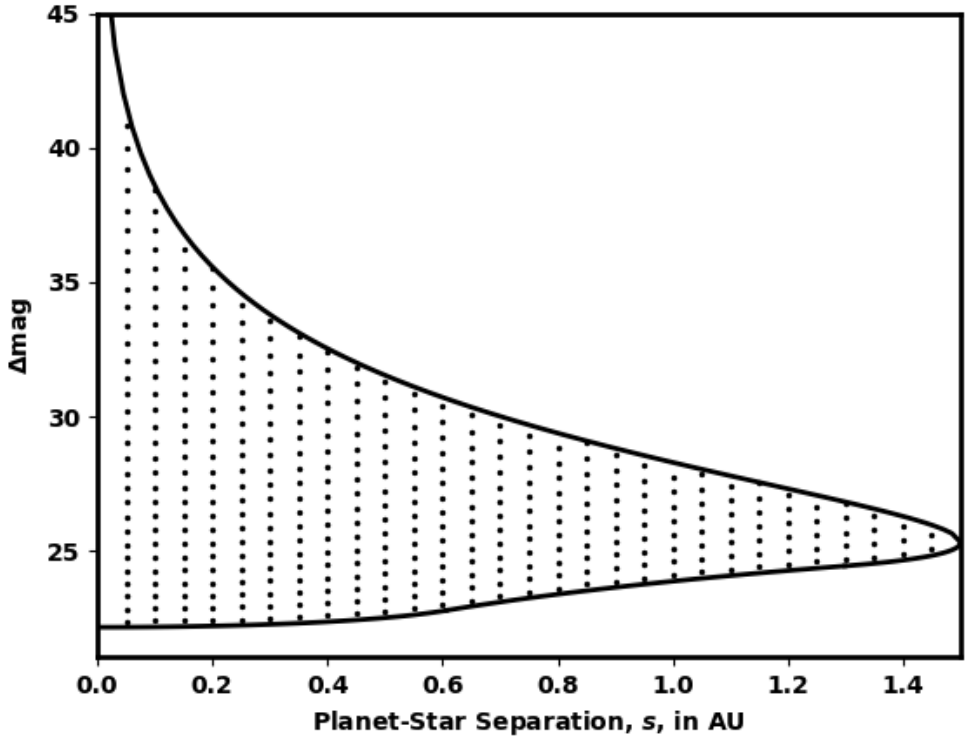

Figure 7.2: s vs Δmag points spaced 2σ apart within the analytical s,Δmag bounds of the Earth Twin planet population.

7.2.3 Fraction of Planets Distinctly Distinguishable and Still Detectable

While the minimum revisit time represents the soonest I should consider revisiting the target star, I do not want to waste telescope time observing nothing. To this end; I also want to revisit before the detected exoplanet leaves the telescope visibility limits. A missed detection is effectively a detection with very large error bars with little utility for orbit fitting. This incentivizes us to create a combined metric that describes the fraction of planets that are **distinctly distinguishable and still detectable**.

Using ξ, I can find the fraction of planets that have left the $n\sigma$ box; noted here as $f_{n\sigma}$ and calculated as

$$f_{n\sigma}(t) = \frac{\text{Number of planets still inside } n\sigma \text{ box at time } \Delta t}{\text{Total number of planets initially detected}}. \tag{7.4}$$

I can also find the fraction of the sub-population that is still within the detection limits of the instrument; noted here as f_{det} and calculated as

$$f_{\text{det}}(t) = \frac{\text{Fraction of planets within telescope detection limits at time } \Delta t}{\text{Total number of planets initially detected}} \tag{7.5}$$

I now combine these by multiplying, $f_{n\sigma} \times f_{\text{det}}$.

Assuming the instrument detection limits do not encompass the entire (s,Δmag) space of the planet population, then $f_{n\sigma} \times f_{\text{det}}$, where it exists, has some maximum value. The time this maximum value occurs at an optimal time to re-observe the star system since it maximized the probability the planet is in a unique region of (s,Δmag) phase space and still within the detection limits of the telescope. These times will be unique for each $n\sigma$ and for each (s,Δmag) point.

There is one final consideration relating to the discernment of Earth-like exoplanets. In the first few detections of exoplanets with direct-imaging, I want to differentiate between Earth-like exoplanets and other non-habitable exoplanets that are not particularly interesting to follow up on. I may want to observe when the ratio of the fraction of Earth-like exoplanets distinctly distinguishable and still detectable to the fraction of SAG13 exoplanets distinctly distinguishable and still detectable is maximized, t^*. This occurs when

$$\Delta t^* = \text{argmax}\left(\frac{f_{n\sigma,\oplus}(\Delta t) \times f_{det,\oplus}(\Delta t)}{f_{n\sigma,SAG13w/o\oplus}(\Delta t) \times f_{det,SAG13w/o\oplus}(\Delta t)}\right). \tag{7.6}$$

7.3 Results

I assume a telescope has an upper limiting Δmag of 25, IWA of 0.045″ (the smallest separation detectable around a star at 10 pc is 0.45 AU, s_{IWA}), OWA of 6″, a σ_s of 0.05 AU (the largest separation detectable around a star at 10 pc is 60 AU, s_{OWA}), a $\sigma_{\Delta\text{mag}}$ of 0.145, and uncertainty in θ calculated by

$$\sigma_\theta = \tan^{-1}\left(\frac{\sigma_s}{s_{IWA}}\right), \tag{7.7}$$

of about 0.111 rad.

7.3.1 Δ Parameter vs Time Results

I take a particular (s,Δmag) detection occurring within the s and Δmag space that is known to have Earth Twin exoplanets and apply the methods in this section ($s = 0.464$ AU,$\Delta\text{mag} = 23.471$). I plot the change in parameters as a function of time in Figure 7.3 for both the Earth Twin planet population and

SAG13 w/o Earths-like planet populations. The location of this particular detection is approximately $1\sigma_s$ from the inner working angle of the telescope and at the maximum phase of the Earth Twin planets. This means many of the planets in the Earth Twin planet population will tend to have large $\Delta s(t)/t$ and small $\Delta\Delta\mathrm{mag}(t)/t$ which is substantiated by the figure. Particularly note the closeness of the $n\sigma$ points in the $\Delta s(t)$ of the Earth Twin planet population for small Δt as compared to the SAG13 w/0 $\oplus$. This is indicative of the bifurcation in planet motion towards or away from the host star. The SAG13 w/o $\oplus$ has a larger spread in all parameters than the narrowly defined Earth Twin planet population.

The bottom row of plots in Figure 7.3 shows the change in each parameter normalized by its uncertainty as a function of time as well as ξ. These are different for each individual (s,Δmag).

The $\Delta\Delta\mathrm{mag}(t)$ in the second row of plots in Figure 7.3, is particularly useful for determining the second observation's integration time. Since I already know $\Delta\mathrm{mag}_0$, I can easily compute the integration time required to detect an Earth-like exoplanet using $\Delta\mathrm{mag}_0 + \max(\Delta\Delta\mathrm{mag})$ (or $\Delta\mathrm{mag}_0 + \Delta\Delta\mathrm{mag}_{n\sigma}$) by reworking Eqn. 3.3 in chapter 3.

I am not just concerned with the mean change in planet parameters vs time shown in the bottom row plots of Figure 7.3, but also the fraction of planets that exceed a given σ threshold. I plot the fraction of planets in the detected sub-population that exceed the $n\sigma$ level in each parameter and the combined parameter in Figure 7.4. Most importantly, the fraction of planets within the detection zone is drastically different between the two planets. Note the apparent plateau from $\sim$ 5 d to $\sim$ 90 d of the Earth Twin planet population's

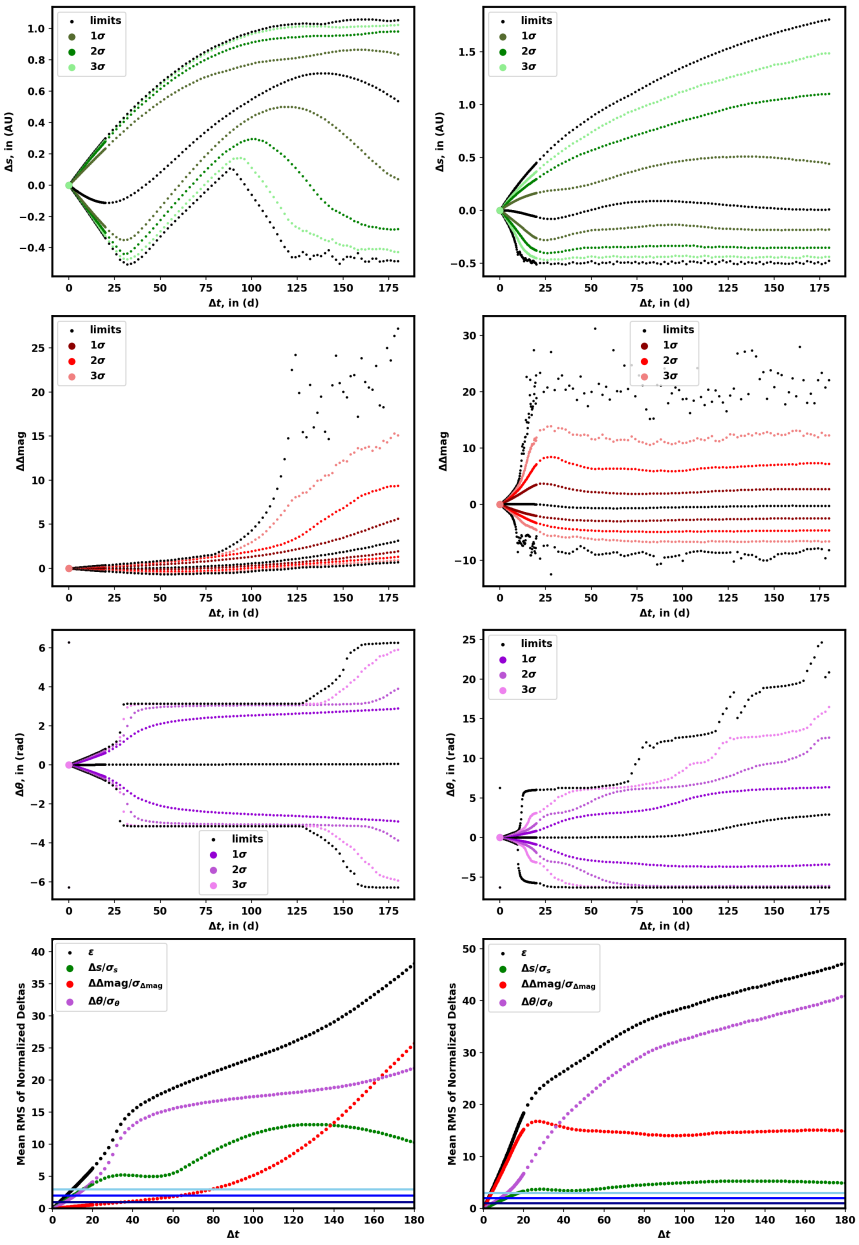

Figure 7.3: Rows are the change in s, Δmag, θ, and ξ as a function of time and columns are for the Earth Twin (left) and SAG13 w/o $\oplus$ planet population. The exoplanet is detected at $s = 0.464$ AU and $\Delta\text{mag} = 23.471$. The telescope used here has $\Delta\text{mag}_{\text{lim}}$=25, $s_{IWA} = 0.5$ AU, and $s_{OWA} = 60$ AU with uncertainties of $\sigma_s = 0.05$ AU, $\sigma_{\Delta\text{mag}} = 0.145$, and $\sigma_\theta = 0.111$ rad.

fraction of planets still detectable as compared to the SAG13 w/o $\oplus$ noticeably declining fraction of planets still detectable. This means past ~ 10 d, the Earth Twin planet population incentivizes us to wait longer to maximize the fraction of Earth Twins within the telescope's detection limits relative the SAG13 w/o $\oplus$ fraction of planets within the telescope's detection limits (missions should implement this provided waiting longer also maximizes orbit fit uncertainty reduction).

In all cases, I account for planets that leave the visible region of the telescope and re-enter the visible region of the telescope.

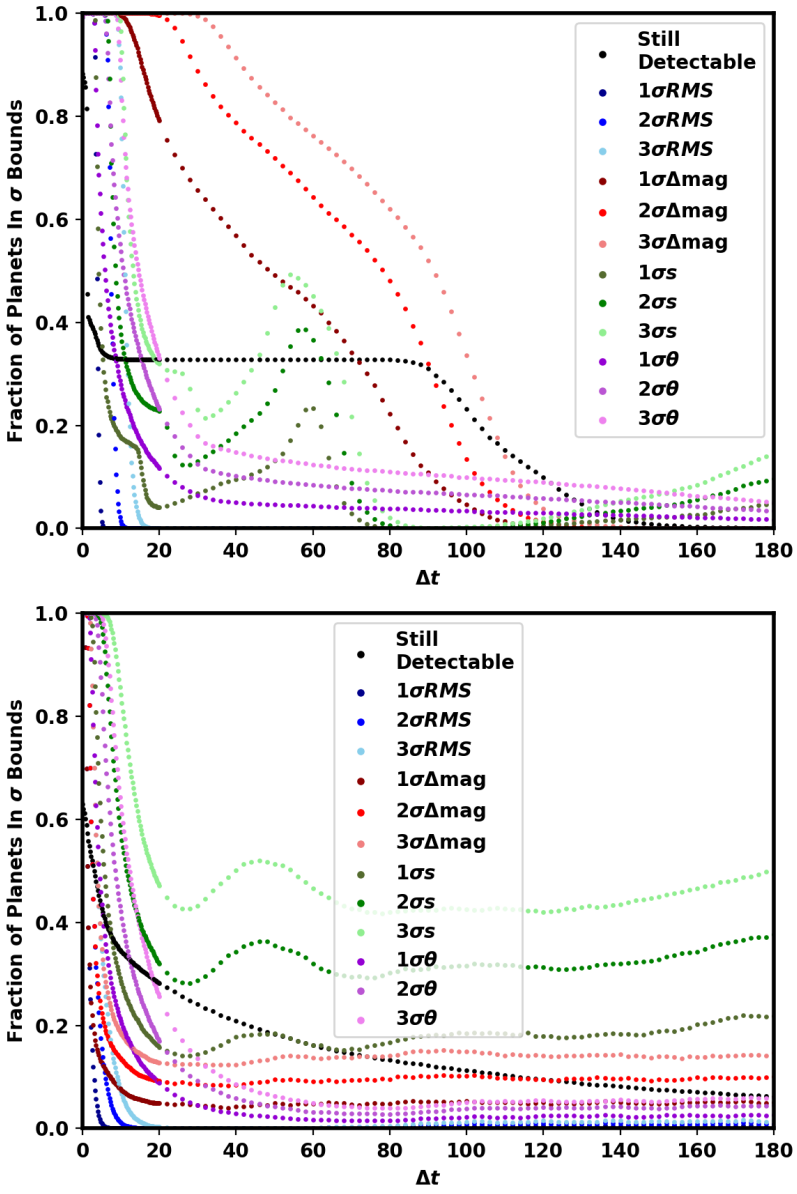

Figure 7.4: The fraction of planets still within $n\sigma$ of the original value are plotted vs time for the detection of an exoplanet at $s = 0.464$ AU and $\Delta\text{mag} = 23.471$. The top plot is for the Earth Twin planet population and the bottom plot is of the SAG13 planet population. I additionally plot the fraction of planets still detectable vs time.

7.3.2 Minimum Revisit Time

I find the minimum revisit time for each (s,Δmag) point for 68%, 95%, and 99% of planets where $\xi > n\sigma$ for $n = 1, 2, 3$. I do this for the Earth Twin planet population in Figure 7.5. While the original 14 day minimum revisit time originally assumed by JPL is *reasonable*, this figure demonstrates the variability in minimum revisit time based on the s and Δmag of the initial detection from 10 d to 40 d. The strongest correlation is that the larger the separation a planet is detected at, the longer the minimum revisit time should be. Over the region where planets are generally detectable (i.e. $\Delta\mathrm{mag}_{\mathrm{lim}} < 27.5$), there is a secondary (smaller) effect where detections at brighter (smaller) Δmag require a longer minimum revisit time.

Applying the same process to the SAG13 planet population without the Earth-like exoplanets, I see different portrait of minimum revisit times for this planet population shown in Figure 7.6. The same observations apply for this population as the Earth Twin population, but the recommend revisit times are more extreme. At smaller separations, the minimum revisit time is noticeably smaller than in the Earth Twin. At larger separations, the minimum revisit time is noticeably larger than in the Earth Twin case.

I additionally looked at the minimum revisit time for the SAG13 planet population (I just kept the Earth-like planets in this case). The minimum revisit times are shown in Figure 7.7 There is no substantial difference in minimum revisit times between the SAG13 planet population and the SAG13 planet population without Earth-like exoplanets

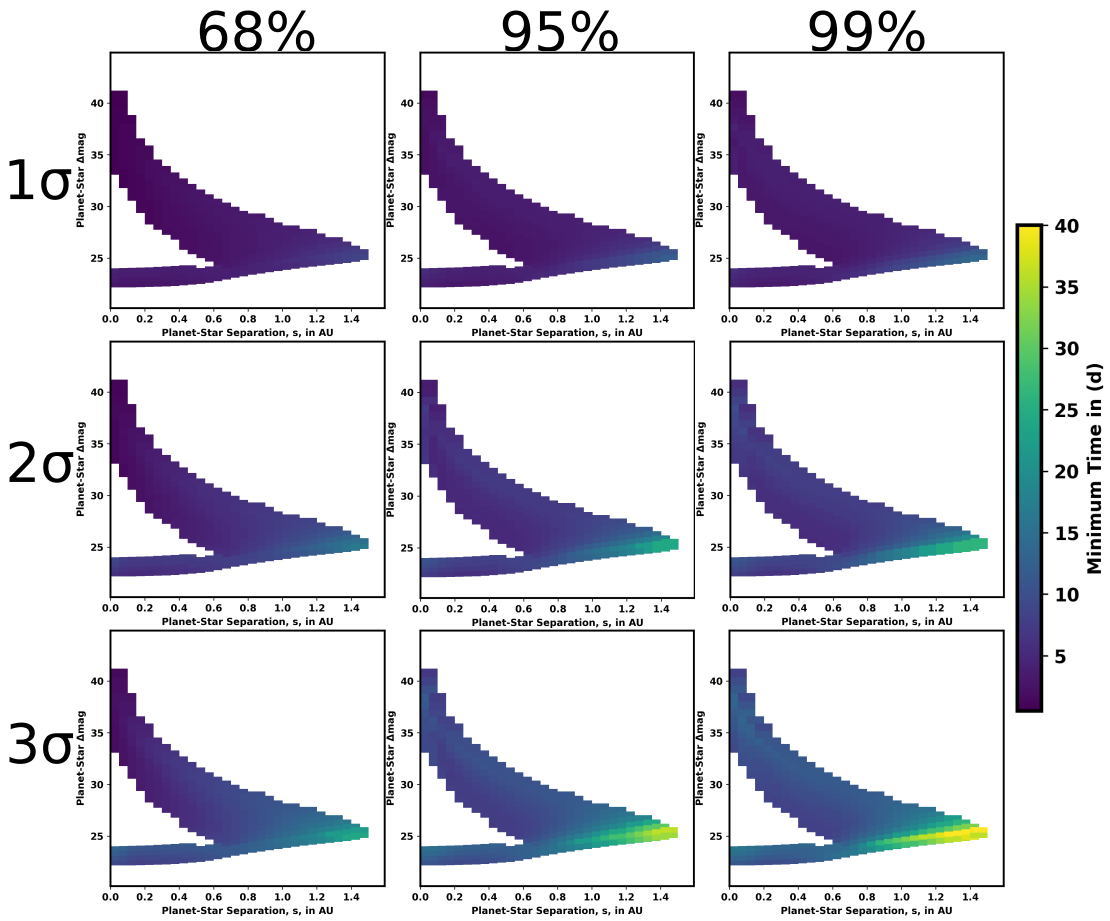

Figure 7.5: Minimum revisit times for the Earth Twin planet population for the population's (s,Δmag) points with $\sigma_s = 0.05$ AU and $\sigma_{\Delta\text{mag}} = 0.145$.

7.3.3 Incentives to Wait Longer

I calculated $f_{n\sigma,\text{population}}(t) \times f_{det,\text{population}}(t)$ for both the Earth Twin and SAG13 w/o $\oplus$ planet populations and multiple different (s,Δmag) points. In each case, the fraction of planets that have left the $n\sigma$ exodetbox (1σ, 2σ, and 3σ in blue dots in Figure 7.8) will constantly increase and the fraction of planets that are still detectable should decrease over time (black dots in Figure 7.8). These conflicting trends and their multiplication results in peak "combined" values. The time location of the $n\sigma$ peaks is notated by the blue X (for some reason the y-axis value of the X is not being properly plotted).

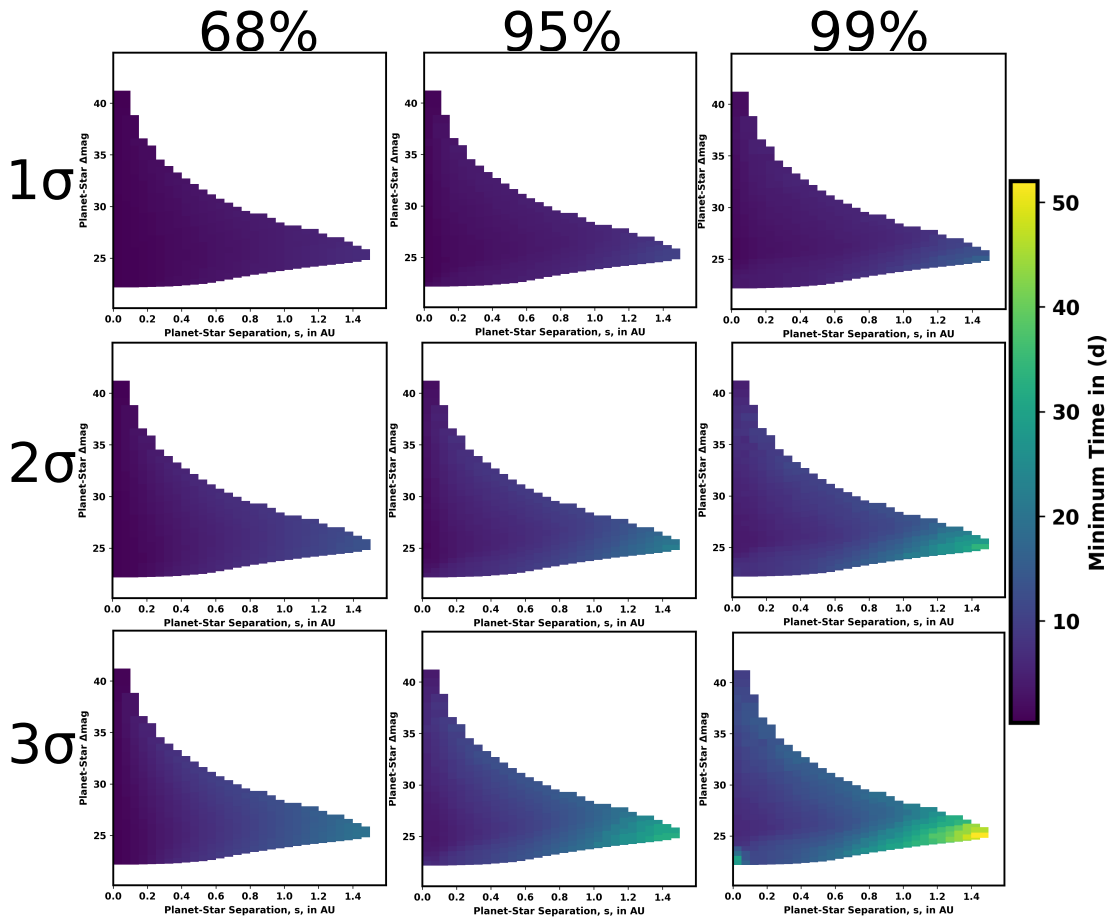

Figure 7.6: Minimum revisit times for the SAG13 planet population without Earth-like planets for the population's (s,Δmag) points with $\sigma_s = 0.05$ AU and $\sigma_{\Delta\text{mag}} = 0.145$.

For all detections, I see a sharp drop off in fraction of planets still detectable and a sharp increase in fraction of planets outside the exodetbox in the first few days. As detections occur at a larger separation, the fraction of planets outside the $n\sigma$ box increases at a slower rate. This means the time where $\max(f_{n\sigma,\text{population}}(t) \times f_{det,\text{population}}(t))$ occurs later for larger separation detections.

In all cases for the Earth Twin planet population, past the early drop off in fraction detectable, there is a plateau in $f_{n\sigma,\text{Earth Twin}}(t) \times f_{det,\text{Earth Twin}}(t)$. This plateau appears to have variable length depending on the location of the detection. It is possible there is structure here that is specifically related to the

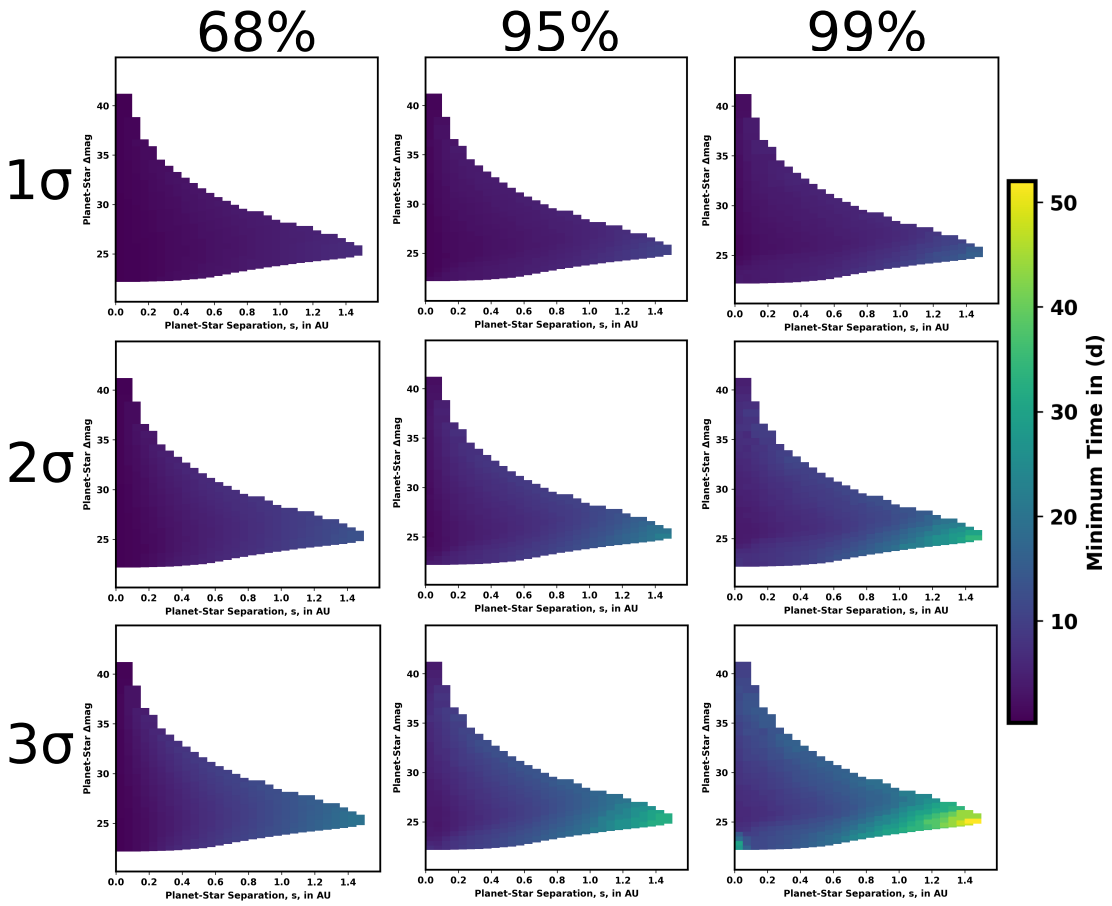

Figure 7.7: Minimum revisit times for the SAG13 planet population for the population's (s,Δmag) points with $\sigma_s = 0.05$ AU and $\sigma_{\Delta\text{mag}} = 0.145$.

average behavior of the Earth Twin planet population detected, but this needs to be studied further.

When I compare the time range of the apparent plateaus in the left hand plots of Figure 7.8 with that on the right, I do not see the same plateau occurring. Instead, I mainly see a continual decrease in the fraction of planets in the SAG13 w/o $\oplus$ population that are still visible. This incentivizes us not to observe at the peak combined σ, but where the Earth Twin combined σ relative to SAG13 w/o $\oplus$ combined is maximized. For these specific populations and the (s,Δmag), this will occur around the apparent "drop-off" from the plateau.

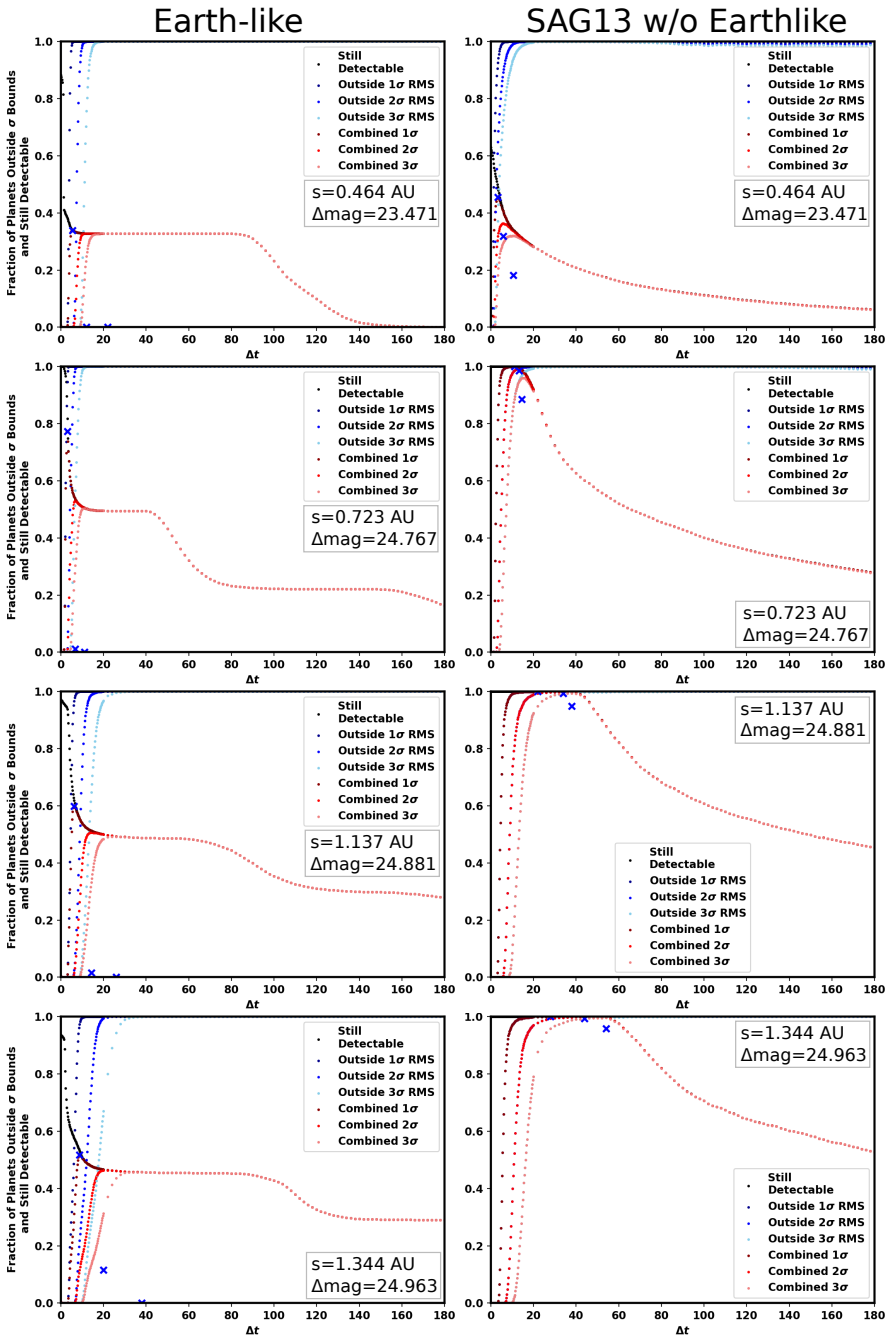

Figure 7.8: Fraction of planets still detectable, outside of the $n\sigma$ exodetbox and the multiplication of these two for the Earth Twin population (left) and SAG13 w/o $\oplus$ planet population. Rows are for individual (s,Δmag) points (0.464 AU, 23.471), (0.723 AU, 24.767), (1.137 AU, 24.881), and (1.344 AU, 24.963) from top to bottom.

7.4 Conclusions

I leverage the power of exodetbox method to narrow the vast range of planets in a planet population into the sub-population possibly produced by a detection. I took a detection grid of the Earth-like planet population and found the minimum revisit time for multiple planet populations for 1, 2, and 3σ and 68%, 95%, and 99%. I found the static 14 d wait time used by the JPL is far from the 10-40 d minimum revisit times seen and that **the minimum revisit times vary substantially based on where the planet was detected**. I showed that the $\Delta\Delta\mathrm{mag}(t)$ for some (s,Δmag) is narrowly bounded meaning it can be used to plan the integration time of the second observation. For the particular ($s = 0.464$ AU, $\Delta\mathrm{mag} = 23.471$) detection, the minimum revisit times are relatively similar between the Earth Twin and SAG13 w/o $\oplus$ planet population, but the fraction of planets within the visible region of the telescope remains relatively constant from 10-90 d for the Earth Twin planet population while the SAG13 w/o $\oplus$ planet population's fraction of planet's still detectable continually declines. **This presents an incentive to wait until 90 d past the initial detection to maximize the probability our revisit confirms the planet is Earth-like**. Additional work must be conducted which finds the reduction in orbit fit uncertainty as a function of wait time for a particular detection.

CHAPTER 8

TWO DETECTION ORBIT FITTING: EXO-DET-BOX

In order to complete the work in chapter 7 it is necessary to understand how waiting between first and second observation effects the orbit fit of a planet in the population. To plan beyond the second visit, it is important to have an orbit fit incorporating the additional astrometric and photometric data collected to determine timing of subsequent revisits or spectral characterizations of the planet.

Currently, Morgan et al. [65] plans to revisit planets with a fixed 120 d cadence which agrees with the minimum revisit times in chapter 7, but, for some (s,Δmag) detections, is not consistent with the still detectable criteria. The motivation in Morgan et al. [65] stems from Horning, Morgan, and Nielson [35] which focuses on a specific Earth with a $i = 45^\circ$ around a star at 10 pc which is a very narrow planet population space. This heuristic is valid for a specific planet orbit type which is favorable conditions and doesn't account for a broader population of Earth-like planets or even Earths. **I am therefore motivated to develop a method that can orbit fit a planet from two detections to determine another ideal time to make the second visit.**

In chapter 5, I presented the exodetbox method which is capable of **quickly** identifying the sub-population that transits a given (s,Δmag) within $n\sigma$, as well as the times these crossings occur at. In this chapter, I apply exodetbox to orbit fitting from two detections and out-perform current orbit fitting techniques, both in accuracy and execution time, with the inclusion of photometric data. **This enables improved orbit fitting of planets from just two detections within computational times necessary to run full mission simulations. This also en-**

ables another measurable (the uncertainty in orbit fit reduction) to determine the minimum revisit time.

8.1 Introduction

In order to implement a full mission simulation that plans the first visit through 6^{th} visit of a target star, I need machinery that can *quickly and accurately* orbit fit the planet's KOE using the information obtained from previous direct images.

8.1.1 Degrees of Freedom and Including Photometry

The first detection of an exoplanet slightly constrains the KOE phase space of the detected planet; their distributions are largely uniform. The most utility extractable from the first detection is the minimum revisit times calculated in chapter 7 and the probability the planet belongs to a particular sub-population calculated in chapter 2 (i.e. the probability the detected exoplanet is Earth-like). This is because we really only get 3 measured parameters from the first image (s_0,Δmag_0,θ_0) and have 7 unknowns ($a, e, i, \omega, \Omega, \nu, pR$) so orbit fitting problem is severely underconstrained.

After scheduling and planning the duration of the revisit using the methods in chapter 7, I might get a second detection which brings the number of measured parameters up to 7 (s_0,Δmag_0,θ_0,s_1,Δmag_1,θ_1,Δt). Conventional orbit fitting methods like Orbits For The Impatient (OFTI)[10] use only the 4 astrometric measurements and time (s_0,θ_0,s_1,θ_1,Δt) to fit the planet's orbit. This means that after two detections, OFTI will continue to have difficulty in reducing uncer-

tainty in the KOE of detected exoplanets. However, if I make an assumption about the underlying planet phase function, I can create an orbit fitting method around the exodetbox methods to orbit fit the planets with the 7 measured parameters from two detections that substantially constrains the KOE of the detected exoplanet.

OFTI is likely to produce better orbit fits when more than 3 detections are made, so **the purpose of this work is to quickly reduce the uncertainty in KOE of the detection as much as possible with only two images**. The KOE and associated uncertainty can then be used in future works to optimize the third detection observation.

8.1.2 Computation Speed Differences in OFTI and exodetbox

In order to implement orbit fitting in full scale mission simulations, I need the orbit fitting computation time to be reduced by several orders of magnitude over existing methods. Traditional MCMC orbit fitting techniques take far too long to implement in a full mission simulation context. Already, running a MC of 1000 Roman 1 year, single-visit, missions takes about ~ 8 hours on 24 cores and makes ~ 10 detections. Running a MC of 1000 HabEx 6 year, single-visit, missions takes about ~ 72 hours on 24 cores and makes ~ 1300 detections. In a simulation with orbit fits, I will need to perform an orbit fit after each detection observation. This means the mission simulation time with orbit fitting can be estimated by taking the 72 hours and adding 120,000 hours spent orbit fitting (1300 detections $\times$ 1000 simulations $\div$ 24 cores $\times$ 2.23 hr orbit fit time from Blunt et al. [10]).

The test-case MCMC implemented to fit KOE distributions for ROXs 42B b in Figure 4 of Blunt et al. [10] took > 30 hrs on 10 cores to fit and was still not converged. In comparison, the OFTI method presented in Blunt et al. [10] produces 10^6 permissible orbits in 134 minutes.

The exodetbox method in Keithly, Savransky, and Spohn [43] is quite fast, and may be capable of comparable performance to OFTI if not better. In the IAC paper, we tested the IAC speed and found it can execute on 10^5 simulated exoplanets in nominally 21.34 seconds. This speed only accounts for 2 qty Δmag related calculations, the Δmag extrema and the $\Delta\mathrm{mag}_{\mathrm{lim}}$ intersections. For exodetbox applied to exoplanet detections, we would need an additional Δmag intersection calculations which adds nominally 50% to this execution time (making it ~ 32 seconds). The executing time will now scale linearly with the number of exoplanet direct imaging detections. Out of 10^5 exoplanets, only ~ 3000 are typically within a reasonable detection box. This means we would need to simulate and run this program ~ 300 times, a total executing time of 160 minutes (32 sec $\times 10^6 \div 3000$), to get the 10^6 planets OFTI achieved. These extrapolated timings are in the same order of magnitude, but would need to be run to make a direct comparison. However, exodetbox has a cunning advantage. I am able to weight each planet simulated by the fraction of the orbit it spends within the detection uncertainty limits. I do not yet know how great of an impact this will have on convergence. I will be necessary to apply exodetbox to ROXs 42B b and the underlying data in Kraus et al. [52], Currie et al. [20], and Bryan et al. [15] to get a sufficient computation time and orbit fit accuracy between the two.

Objective: The purpose and problem tackled in this chapter is to present and demonstrate a method for quickly and accurately orbit fitting exoplanets

from two detections using their photometric data.

8.2 Methods

In section 8.2.1 I outline the orbit fitting methods implemented in this work.

8.2.1 Two Detection Orbit Fitting with exodetbox

The two detection Monte Carlo method I present uses exodetbox from chapter 5 for its underlying computational substructure. Since the angular component is important in the second detection, I need to introduce additional machinery to handle this.

1. Randomly generate a planet population KOE ($a_p, e_p, i_p, \omega_p, \Omega_p, M_{p,0}, pR_p$)
2. Correct the generated system inclinations to have the same common proper motion as the target planet (this step doubles the effectiveness of the number of planets sampled by moving the inclinations to the proper range)
3. Estimate KOE
    - Weighted Distribution or Rejection Sampling
        (a) calculate $\nu_{p,0}$ from $M_{p,0}$
        (b) calculate ($s_{p,0}$,$\Delta\mathrm{mag}_{p,0}$, $\theta_{p,0}$)
        (c) calculate $f_{\mathrm{meas}}(s_{p,0}, \Delta\mathrm{mag}_{p,0}|s_0, \Delta\mathrm{mag}_0, \sigma_s, \sigma_{\Delta\mathrm{mag}})$
        (d) calculate $M_{p,1}$ from $t_{p,1} = t_{p,0} + \Delta t$

(e) calculate $\nu_{p,1}$ from $M_{p,1}$

(f) calculate ($s_{p,1}$,$\Delta\text{mag}_{p,1}$, $\theta_{p,1}$)

(g) calculate $f_{\text{meas}}(s_{p,1}, \Delta\text{mag}_{p,1}|s_1, \Delta\text{mag}_1, \sigma_s, \sigma_{\Delta\text{mag}})$

(h) calculate $f_{\text{meas}}(\theta_{p,1} - \theta_{p,0}|\theta_1 - \theta_0, \sigma_\theta)$

(i) calculate weight w_k for each planet

(j) calculate weighted KOE estimate, $\hat{a} = \sum w_k a_p / \sum w_k$

(k) calculate rejection sampling KOE estimate,

- generate 3 random uniform numbers for each planet ($q_{p,1}$, $q_{p,2}$, and $q_{p,3}$)
- multiply them together $Q_p = q_{p,1}q_{p,2}q_{p,3}$
- calculate the average $\hat{a}$ for planets with the normalized $\frac{w_k}{\sum w_k} > Q_p$

- Unweighted/weighted Exodetbox

(a) calculate $\nu_{p,0}$ intersections with $s_0 \pm \sigma_s$ and $\Delta\text{mag}_0 \pm \sigma_{\Delta\text{mag}}$ with exodetbox

(b) calculate $t_{p,0}$ from $\nu_{p,0}$

(c) calculate $\theta_{p,0}$ from $\nu_{p,0}$

(d) stitch the first and last visibility window together

(e) calculate $\nu_{p,1}$ intersections with $s_1 \pm \sigma_s$ and $\Delta\text{mag}_1 \pm \sigma_{\Delta\text{mag}}$ with exodetbox

(f) calculate $t_{p,1}$ from $\nu_{p,1}$

(g) calculate $\theta_{p,1}$ from $\nu_{p,1}$

(h) calculate angular motion direction

(i) calculate $\Delta\theta_p$ accounting for "wrapping"

(j) identify the set of all planets with intersections with $s_0 \pm \sigma_s$ and/or $\Delta\mathrm{mag}_0 \pm \sigma_{\Delta\mathrm{mag}}$

(k) identify the set of all planets with intersections with $s_1 \pm \sigma_s$ and/or $\Delta\mathrm{mag}_1 \pm \sigma_{\Delta\mathrm{mag}}$

(l) find the subset of planets with both intersections

(m) of this subset, find the number of visibility windows each planet has with the first and second detection

(n) for each visibility window combination

i. calculate θ_i and θ_j at the enter and exit time of each visibility window respectively

ii. calculate number of periods that have passed for the Δt waited between visits

iii. calculate the $\Delta t_{i,j}$ between the enter and exit time of each visibility window accounting for "wrapping"

iv. calculate the $\Delta\theta_{i,j}$ between the enter and exit angles of each visibility windows accounting for "wrapping"

v. apply a time tolerance (t_{tol}) the duration of the observation and overhead time (in this case we used 5 d)

vi. determine if one or more pairs of visibility windows exist for the first and second detection that have $\Delta t_{i,j} - t_{\mathrm{tol}} < \Delta t < \Delta t_{i,j} + t_{\mathrm{tol}}$ and $\Delta\theta_{i,j} - \sigma_\theta < \Delta\theta < \Delta\theta_{i,j} + \sigma_\theta$

(o) for each visibility window detectable, compute the time-fraction of an orbit the planet can be detected within the 1σ limits the first detection and still be within the visibility limits of the second detection Δt later, w_k

(p) calculate $\hat{a} = \sum w_k a_p / \sum w_k$ using w_k calculated in the last step

(weighted)

(q) calculate $\hat{a}$ by averaging the planets within the uncertainty limits of the two detections (unweighted)

For the weighted and rejection sampling methods, I orbit fit using an underlying planet population of 10^8 planets. Since I randomly simulate the start time of planets in this population, it is rare for a planet to be within 1σ of the first s_0 and Δmag_0 ($< 1\%$). This means I need to use substantially more planets than the exodetbox approach.

For the exodetbox orbit fitting methods, I orbit fit using an underlying planet population with 10^6 planets. In general, the exodetbox method applied to a *normal* detection ($< 99^{\text{th}}$ percentile) reduces a planet population of 10^5 planets down to about 10^3 planets. While 10^3 planets is sufficient to do statistics on, a second exodetbox applied to the 10^3 sub-population further reduces the planet population; typically 1-2 orders of magnitude. Because of this reduction, I start with 10^6 planets which can pair down to somewhere between 10^3 and 10^2 planets which is *reasonable* for statistics. exodetbox run on a single core on 10^6 planets takes less than ~ 5 minutes in its un-optimized form.

I elaborate on the details of the baseline comparison weighted and rejection sampling approaches in section 8.2.1. The weighted and unweighted exodetbox approach is outlined in

Weighted Distribution and Rejection Sampling

I present the process for estimating KOE using weights based off the probability distribution. Since the rejection sampling method is, for the most part, the same

as the weighted approach, I provide an additional explanation at the end to explain how and where the rejection sampling method differs.

I start with 10^8 randomly sampled planet KOE and pR from one of the planet populations in chapter 2 ($a_p, e_p, i_p, \omega_p, \Omega_p, M_{p,0}, pR_p$). Of these planets, I modify the i_p such that it is in the same inclination range as the planet being observed. This operation is acceptable under the assumption that the second observation is a *rapid revisit*. If two observations of a target are made sufficiently close to one another, common proper motion should be established and the inclination of the system can be deciphered based on the location of the second detection (whether the second detection occurs at a larger or smaller separation and whether the second detection occurs on the same projected separation hemisphere or the opposite one).

The mean anomalies ($M_{p,0}$) are sampled uniformly to create an even distribution of the planets in time. While the p and R are independently sampled, I combine them into a single parameters pR since that is the only parameter discernible from direct images.

Since I am orbit fitting to measurements that have already been made, I know the input $s_0, \Delta\mathrm{mag}_0, \theta_0, s_1, \Delta\mathrm{mag}_1, \theta_1, \Delta t, \sigma_s, \sigma_{\Delta\mathrm{mag}}$. From these inputs, I can define measured probability density functions. While there is likely *some* covariance between the 3 measurables in an observation, it is unlikely for anyone to know what they are. So I assume the uncertainty in the measurables to

be independent gaussian distributions to get

$$f_{\text{meas},s_0}(s) = \frac{1}{\sigma_s\sqrt{2\pi}} \exp -\frac{1}{2}\left(\frac{s - s_0}{\sigma_s}\right)^2, \tag{8.1}$$

$$f_{\text{meas},\Delta\text{mag}_0}(\Delta\text{mag}) = \frac{1}{\sigma_{\Delta\text{mag}}\sqrt{2\pi}} \exp -\frac{1}{2}\left(\frac{\Delta\text{mag} - \Delta\text{mag}_0}{\sigma_{\Delta\text{mag}}}\right)^2, \text{ and} \tag{8.2}$$

$$f_{\text{meas},\Delta\theta_0}(\Delta\theta) = \frac{1}{\sigma_{\Delta\theta}\sqrt{2\pi}} \exp -\frac{1}{2}\left(\frac{\Delta\theta - \Delta\theta_0}{\sigma_{\Delta\theta}}\right)^2. \tag{8.3}$$

For each planet simulated, I calculate their measurable parameter at time zero (the randomly generated $M_{p,0}$) to get ($s_{p,0}$,$\Delta\text{mag}_{p,0}$, $\theta_{p,0}$). I also calculate $M_{p,1}$ from $t_{p,1} = t_{p,0} + \Delta t$. This gives me $\nu_{p,1}$ from $M_{p,1}$ and ($s_{p,1}$,$\Delta\text{mag}_{p,1}$, $\theta_{p,1}$).

I can now evaluate the probability density function of each simulated planet for each measurable at the two times of detection. Note that the uncertainty $\sigma_{\Delta\theta}$ is the combined uncertainty from adding two variables with σ_θ and will be $\sigma_{\Delta\theta} = \sqrt{2}\sigma_\theta$. I arrive at a "weight" w_k for each planet by multiplying the individual evaluations of the probability density functions together such that

$$w_k = f_{\text{meas},s_0}(s_{p,0,k}) f_{\text{meas},\Delta\text{mag}_0}(\Delta\text{mag}_{p,0,k}) f_{\text{meas},s_1}(s_{p,1,k}) \\ f_{\text{meas},\Delta\text{mag}_1}(\Delta\text{mag}_{p,1,k}) f_{\text{meas},\Delta\theta}(\theta_{p,1,k} - \theta_{p,0,k}). \tag{8.4}$$

Using the weighted approach, I arrive at the weighted KOE estimate for semi-major axis ($\hat{a}$) by

$$\hat{a} = \frac{\sum_{\forall k \in p} w_k a_k}{\sum_{\forall k \in p} w_k}. \tag{8.5}$$

This process can be applied for each planet KOE and pR, but semi-major axis is most important as the habitable zone constraint is largely dictated by the semi-major axis of the planet.

There is an additional caveat, to this weighted calculation. I presented the exact method implemented for a single set of 10^8 planets. In order to get con-

vergence of the mean and prevent memory overflows, I need to run multiple batches. I present my unweighted and weighted incremental batch mean and variance estimation in section 8.2.2.

Rejection Sampling

For the rejection sampling approach, an identical set of steps are followed for the weighted distribution up until the estimation of the KOE. I randomly sample 5 numbers from a uniform distribution for each planet ($q_{p,1}$, $q_{p,2}$, $q_{p,3}$, $q_{p,4}$, and $q_{p,5}$). I multiply them together to get $Q_p = q_{p,1}q_{p,2}q_{p,3}q_{p,4}q_{p,5}$. I find the subset of planets where $w_p > Q_p$ and use a uniform weighting of this subset to arrive at the average semi-major axis by

$$\hat{a} = \sum_{k \in \{w_p > Q_p\}} a_k. \tag{8.6}$$

Weighted and Unweighted exodetbox

I start with 10^6 randomly sampled planet KOE and pR from one of the planet populations in chapter 2 excluding $M_{p,0}$ ($a_p, e_p, i_p, \omega_p, \Omega_p, pR_p$). I can exclude the $M_{p,0}$ parameter because it is what I will solve for using exodetbox.

In the first step, I calculate $\nu_{p,0}$ intersections with $s_0 \pm \sigma_s$ and $\Delta\text{mag}_0 \pm \sigma_{\Delta\text{mag}}$ using exodetbox presented in chapter 5. From here I can calculate $t_{p,0}$ from $\nu_{p,0}$. I can also calculate $\theta_{p,0}$ from $\nu_{p,0}$. A nuance in exodetbox where I add the start and end of a visibility window at $\nu = 0, 2\pi$ in order to account for planets that are within $s_0 \pm \sigma_s$ and $\Delta\text{mag}_0 \pm \sigma_{\Delta\text{mag}}$ for the entire duration of the planet's orbit require me to merge these kinds of visibility windows when planets do leave the exodetbox. I stitch the first and last visibility window together to preserve $\Delta\theta$ ranges. I then calculate $\nu_{p,1}$ intersections with $s_1 \pm \sigma_s$ and $\Delta\text{mag}_1 \pm \sigma_{\Delta\text{mag}}$ using

exodetbox and find the times past periastron of these intersections $t_{p,1}$ from $\nu_{p,1}$.

Since the exodetbox only gives times past periastron of intersections, I need to calculate the number of full orbital periods that have lapsed between the first detection and subsequent detections. This is

$$n_T = \lceil \frac{\Delta t}{T} \rceil. \tag{8.7}$$

I then calculate the angular motion direction of the planet using

$$\text{sign}(\Delta\theta) = \text{sign}(\Delta\theta). \tag{8.8}$$

This is important when accounting for motion of the planet that "wraps" from $< 2\pi$ to $> 2\pi$ or from > 0 to < 0 over multiple periods. I now calculate $\Delta\theta_p$ between accounting for this "wrapping". This allows me to calculate $\theta_{p,1}$ from $\nu_{p,1}$ and add the number of subsequent orbital periods that have lapsed.

Since each planet can have multiple visibility windows, I identify the set of all planets with intersections with $s_0 \pm \sigma_s$ and/or $\Delta\text{mag}_0 \pm \sigma_{\Delta\text{mag}}$ and identify the set of all planets with intersections with $s_1 \pm \sigma_s$ and/or $\Delta\text{mag}_1 \pm \sigma_{\Delta\text{mag}}$. I can then find the subset of planets with both intersections. With this subset, I can find the number of visibility windows each planet has with the first and second detection (sets **I** and **J** respectively). I then iterate over each planet's visibility window combinations (i, j) for the first detection and second detection. For each (i, j) combination, I calculate the times between each combination of starts and ends of the two target visibility windows. I also calculate the changes in θ between the starts and stops of the two visibility windows. In both cases, I account for "wrapping" by adding the time or 2π multiplied by the number of periods that have passed.

Of all four differences in angles between the limits of the two visibility windows, I find the minimum and maximum angular change between the two, $\theta_{i,j,\min}$ and $\theta_{i,j,\min}$. Of all four time differences between the limits of the two visibility windows, I find the minimum and maximum time changes between the two, $\Delta t_{i,j,\min}$ and $\Delta t_{i,j,\min}$.

I now check whether the times and angles of the entrances and exits of the two visibility limits are within the range and tolerance dictated by the observation. I first check if $\Delta t > \Delta t_{i,j,\min} - t_{\text{tol}}$ and $\Delta t < \Delta t_{i,j,\max} + t_{\text{tol}}$. If this is true, then, depending on $mathrmsign(\Delta\theta)$, I check if $\Delta\theta < \Delta t_{i,j,\max} + \sqrt{\sigma_{\theta_0}^2 + \sigma_{\theta_1}^2}$ and $\Delta\theta > \Delta t_{i,j,\min} - \sqrt{\sigma_{\theta_0}^2 + \sigma_{\theta_1}^2}$ I create two sets of planets from this; those that satisfy **only** the time criteria and those that satisfy **both** the time criteria and the angular criteria. I do this because the angular criteria can be too restrictive and limit the planet population that is detected twice. The average KOE of the planets satisfying both the time criteria and angular criteria is the unweighted orbit fit of the planet.

In order to calculate a weighted orbit fit, I need to apply a weighting to each of the individual planets being averaged to get the KOE estimate. The weighting is important to apply so that Neptune-like exoplanets, which spend a small fraction of their orbit within an Earth-like exodetbox relative to Earth, are not over-represented in the KOE estimation. The weights I apply are the fraction of the orbital period a planet can be detected in the first exodetbox and be detected in the second exodetbox.

To calculate w_k of each planet for the weighted exodetbox approach, I iterate over each visibility window for the first exodetbox (indexed by j) and iterate over each visibility window of the second exodetbox (indexed by k). For each

(j, k) combination, I check if Δt is between the start and stop times of the two different visibility windows ($t_{k,1} < t_{j,0} + \Delta t$ and $t_{k+1,1} < t_{j,0} - \Delta t$) When this is true, I calculate the range of time in the first visibility window the planet can be observed in the second exodetbox visibility windows ($t_{k,1} - \Delta t, t_{j,0}$) and index this particular pairing as l. The weighting applied to exodetbox is

$$w_k = \frac{1}{T} \sum_{\forall l} t_{j,0} - (t_{k,1} - \Delta t). \tag{8.9}$$

I now estimate the KOE using Eqn. 8.5.

8.2.2 Incremental Statistics

I state that I calculate the mean using Eqn. 8.5 and 8.6, but this is only true for a single batch. The large volume of data required to calculate the MC makes it prohibitive for me to instantly calculate statistical parameters of the planet population. Things like the mean and standard deviation must therefore be calculated incrementally or in batches. I note here that this is purely for validation of the exodetbox-powered orbit fitting method by generating a sufficiently large number of planets to get the orbit fit.

Methods for calculating the weighted batch means already exist but are included here to be thorough, but methods for estimating the incremental weighted batch variance do not exist.

Incremental Weights

The average weight for the collection of data at $j+1$ is

$$\overline{w}_{j+1} = \frac{j\overline{w}_j + \overline{w}_m}{(j+1)}. \tag{8.10}$$

Where $\overline{w}_j$ is the weight of the j^{th} batch of data.

Weighted Averages

For a collection of data with size N_m and individual weights in this dataset w_i, the average weight for this dataset is

$$\overline{w}_m = \frac{1}{N_m} \sum w_i. \tag{8.11}$$

Incremental Average Weight

The average weight of the data set after adding two equal size sets of data together, $\overline{w}_j$, is

$$\overline{w}_j = \frac{j\overline{w}_j + \overline{w}_m}{j+1}. \tag{8.12}$$

Weighted Batch Mean

For data which is weighted, the weighted mean of the m^{th} batch of data, $\overline{x}_m$, is

$$\overline{x}_m = \frac{1}{\overline{w}_m N_m} \sum w_i x_i. \tag{8.13}$$

Incremental Mean of Different Size Batches

Given different size batches, the mean of these batches can be incrementally calculated using

$$\overline{x}_{j+1} = \frac{N_j \overline{x}_j + N_m \overline{x}_m}{N_j + N_m}. \tag{8.14}$$

Incremental Weighted Mean

Suppose we have accounted the weighted mean of the previous j batches of

data, $\overline{x}_j$ and wish to calculate the weighted mean after adding some small set of new data added to this weighted mean, $\overline{x}_{j+1}$. This would be

$$\overline{x}_{j+1} = \frac{1}{j\overline{w}_j + \overline{w}_m}(j\overline{x}_j\overline{w}_j + \overline{x}_m\overline{w}_m). \tag{8.15}$$

Variances

Weighted Standard Deviation

The standard deviation for a set of weighted batch of data, σ_m, is given by

$$\sigma_m = \sqrt{\frac{1}{\sum w_i}\sum(w_i(x_i - \overline{x}_m)^2)}. \tag{8.16}$$

Incremental Variance of Batch Data We need a method of calculating the variance of two combined sets of data. In our specific scenario, we are calculating the variance of batch j of data with size N_m and combine this to the converged variance of all previous batches, σ_j. In Eqn. 8.17, the first two terms are the weighting of the individual variances of the new batch and converged variance of all previous batches. The second term has w_i which is the weighting applied to the i^{th} piece of data. x_i is the i^{th} piece of data. $\overline{x}_j$ is the converged mean of batches 0 to j. $\overline{x}_m$ is the mean of batch $j+1$. The final term is a correction for the differences between the mean of the two sets of data.

$$\sigma^2_{j+1} = \frac{jN_m}{jN_m + N_m}\sigma^2_j + \frac{N_m}{jN_m + N_m}\frac{\sum(w_i(x_i - \overline{x}_m)^2)}{\sum(w_i)} + \frac{jN^2_m}{(jN_m + N_m)^2}(\overline{x}_{j+1} - \overline{x}_m)^2 \tag{8.17}$$

Incremental Variance of Incremental Data With Different Batch Sizes An estimate of the variance can be produced when combining batches of data of

different sizes. Where the first batch of data has number of data points N_j and the new additional batch of data has number of datapoints N_m, the mean of the j^{th} batch of data is $\overline{x}_j$, then the standard deviation of the $j+1$ batch is

$$\sigma_{j+1}^2 = \frac{N_j}{N_j+N_m}\sigma_j^2 + \frac{N_m}{N_m+N_j}\sigma_m^2 + \frac{N_m N_j}{(N_j+N_m)^2}(\overline{x}_j - \overline{x}_m)^2. \tag{8.18}$$

8.2.3 Testing Orbit Fitting

In order to test the exodetbox orbit fitting method, I need take care in how I select the planets I orbit fit with. It would be inappropriate to randomly select a planet because I may select an *unreasonable* planet that would never be detectable by one of the instruments in chapter A. Similarly, if I randomly select an initial observation time of a detectable planet, it may not be within the instrument's visibility limits or even within the instrument's visibility limits Δt later.

The process I outline here uses exodetbox to randomly select a target planet weighted by the time-fraction of an orbit each planet spends within the telescope's visible limits and is detectable now and Δt later (either within the current visibility window or the future visibility window).

The process I use to randomly generate a single test planet is outlined here:

- randomly sample KOE
- use exodetbox to find the true anomalies of planet orbit intersections with s_{min}, s_{max}, $\Delta\text{mag}_{\text{max}}$
- calculate the time past periastron of these intersections

- calculate the number of periods in δt
- calculate $\delta t_{mod} = \delta t \bmod T$
- for each planet visibility time window, calculate the total fraction of an orbit in the j^{th} a planet can be observed now and some δt later, $w_{k,j}$
- randomly select one planet weighted by each planet's $\sum_{\forall j} w_{k,j}$
- randomly select the viable visibility window of the first observation of the planet weighted by the planets visibility windows time-fraction, $w_{k,j}$
- randomly select the time of first observation of the planet by uniformly sampling within the entrance and exit time of the visibility window (s_0, Δmag_0, θ_0)
- calculate the implicit second time of observation of the planet (s_1, Δmag_1, θ_1)

8.3 Results

I use the results from Guimond and Cowan [32] as a reference point to measure how good our exodetbox powered two detection orbit fitting process is. Figure 8.1 is the semi-major axis orbit fit results for varying epochs when applied to the Guimond and Cowen 2019 planet population included in chapter 2. Since I am targeting the two detection performance, I can pull out the mean error in semi-major axis for two detection orbit fitting from Figure 8.1 which is ~ 0.41 AU. I note here that the particular planet population selected to orbit fit is the most difficult, the uniform eccentricity distribution. This is because smaller or larger semi-major axis can appear in vastly different (s,Δmag) locations than their circular counterparts.

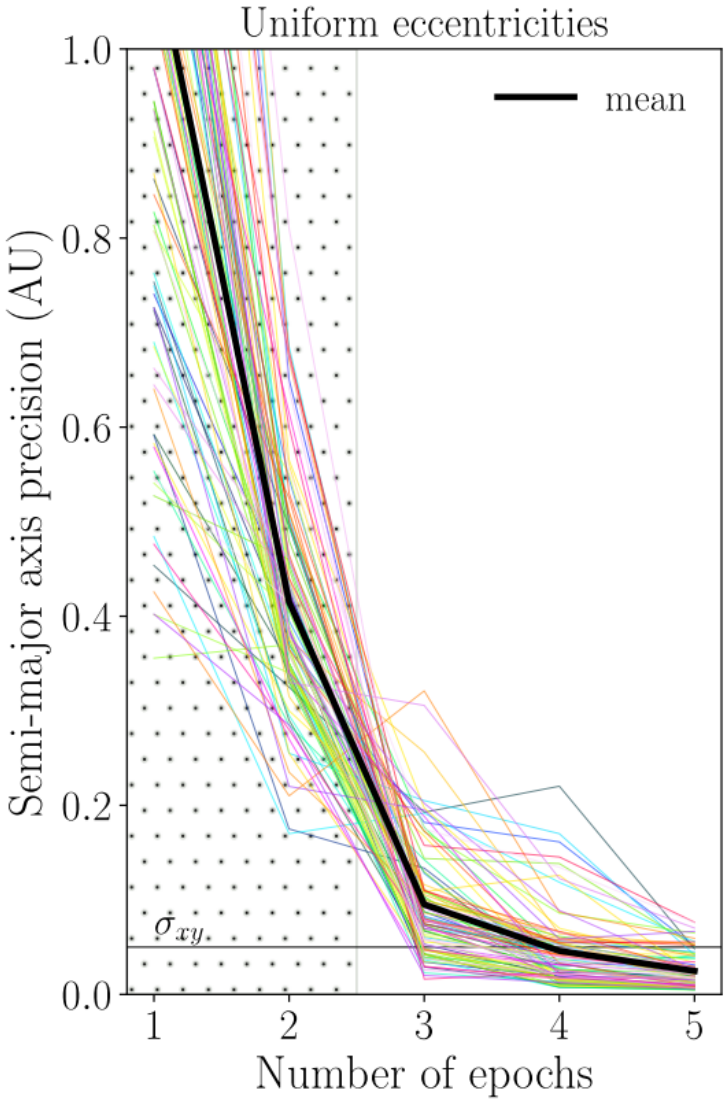

Figure 8.1: Figure 5(c) from Guimond and Cowan [32] for the orbit fit of 100 planets randomly sampled from the Guimond and Cowan [32] planet population with log-uniform distribution of eccentricities. The detections are made with $\sigma_s = 3.5$ mas at 10 pc with a 90 d cadence considering only astrometry.

I ran the exodetbox-powered two detection orbit fitting method (both the weighted and unweighted as well as the weighted averaging and rejection sampling methods) on the Guimond and Cowen 2019 planet population included in chapter 2. I plotted the orbit fitting results in Figure 8.2 for $\Delta t = 30, 60,$ and 90 d wait times for each of the four methods discussed in this work. The mean

absolute error in Figure 8.2 of the unweighted exodetbox approach achieved ~ 0.1 AU uncertainty. This means that in nominally 50% of cases the uncertainty in semi-major axis estimated was within 10% of the planets semi-major axis, the threshold for the planet's orbit being sufficiently constrained to warrant a spectral characterization[65]. This absolute error in semi-major axis orbit fit achieved by my unweighted exodetbox orbit fitting method substantially improves on the mean absolute error of ~ 0.4 from Figure 8.1 of Guimond and Cowan [32] and can do so in a shorter amount of time. The planet population being orbit fit to uses the least-favorable to orbit fitting eccentricity distribution, the uniform distribution. I expect that orbit fitting using other eccentricity distributions from Guimond and Cowan [32] or other planet populations in chapter 2 will produce even better orbit fits. The caveat to this work is that the Guimond and Cowan [32] planet population uses a narrow semi-major axis range. The confusion work in chapter 6 indicates that orbit fitting may be marginally more difficult when a broader planet population is considered. **This work shows that a planet's semi-major axis can be sufficiently constrained to within 10% of its value by 2 direct imaging observations.**

There is an additional, subjective, observation that can be made of Figure 8.2. The variance in absolute error appears to increase from 30 d to 60 d wait times and decrease from 60 d to 90 d. The smallest variances are observed on the 90 d wait times. **This observed trend is significant because it indicates that waiting longer between detections changes the orbit fit precision.** While the "rapid revisit" can make a *distinctly distinguishable* second detection of an exoplanet, it does not necessarily provide us with the maximum amount of orbit fit constraint. There is a trade study to be conducted between the risk of missing the second detection and the reward of waiting and constraining the planet's or-

bit to within 10%. It is likely there will also be a Δt point of diminishing returns where waiting longer increases the uncertainty in the semi-major axis.

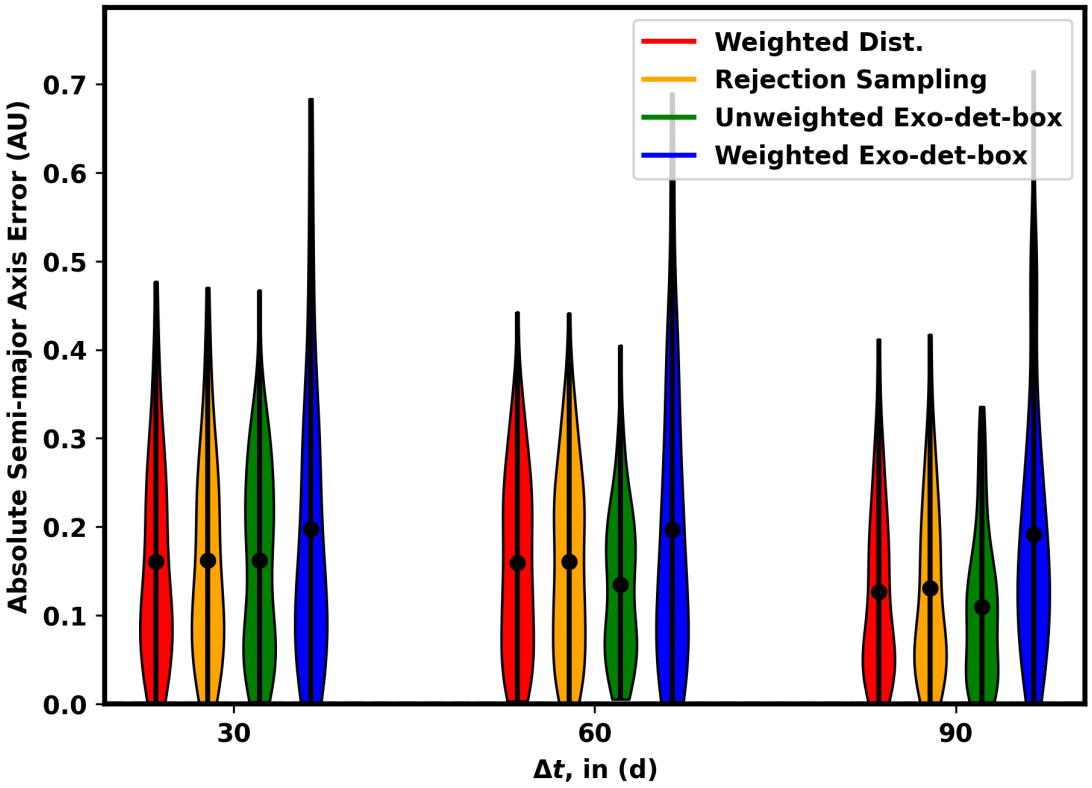

Figure 8.2: Histograms of absolute error in semi-major axis estimation from the weighted (red), rejection sampling (yellow), unweighted exodetbox (green), and weighted exodetbox (blue). Each histogram is of 100 different planets within the visible limits of the telescope at the first and second detection ($s_{\min} = 0.45$ AU, $s_{\max} = 60$ AU, $\Delta\text{mag}_{\text{lim}} = 27.5$) for Δt wait times of 30, 60, and 90 days. The detections are made with $\sigma_s = 3.5$ mas at 10 pc, $\sigma_{\Delta\text{mag}} = 0.145$, and $\sim \sigma_\theta = 0.077$ rad.

I additionally plotted the semi-major axis error in Figure 8.3 to look for bias in the orbit fit results. In general, I am surprised the unweighted exodetbox method produces a lower absolute error orbit fit than the weighted exodetbox approach. The weighted exodetbox approach has performed better when applied to a broader population because of the inherent bias in the originating planet population, but some of that work must be redone before it is suitable

for presentation.

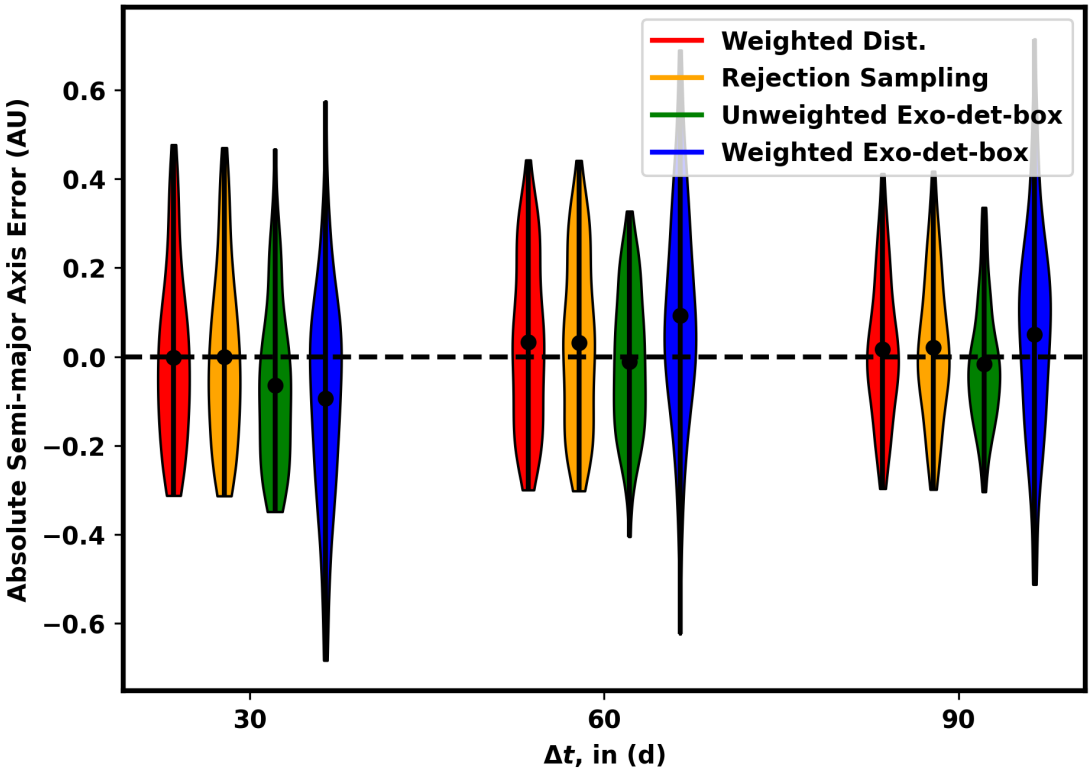

Figure 8.3: Histograms of error in semi-major axis estimation from the weighted (red), rejection sampling (yellow), unweighted exodetbox (green), and weighted exodetbox (blue). Each histogram is of 100 different planets within the visible limits of the telescope at the first and second detection ($s_{\min} = 0.45$ AU, $s_{\max} = 60$ AU, $\Delta\text{mag}_{\text{lim}} = 27.5$) for Δt wait times of 30, 60, and 90 days. The detections are made with $\sigma_s = 3.5$ mas at 10 pc, $\sigma_{\Delta\text{mag}} = 0.145$, and $\sim \sigma_\theta = 0.077$ rad.

8.4 Conclusions

In this work, I presented my *quick* exodetbox-powered two detection orbit fitting method. The exodetbox-powered two detection orbit fitting method demonstrated shows that the average planet's semi-major axis can be sufficiently constrained to within 10% of its value by 2 direct imaging observations. This 10% is the sufficient to qualify a detected exoplanet for spectral characterization threshold specified by the Standards Definition and Evaluation Team final report. Results in this work also indicate that the exodetbox method has a minimal bias for the particular planet population studied. The orbit fit trend shows differing variations in the variance for different wait times. From 30 d to 60 d the variance appeared to increase and from 60 d to 90 d the variance appeared to decrease warranting further in-depth investigation.

CHAPTER 9

CONCLUSIONS

In this dissertation, I presented a series of methods which can improve the yield of the general exoplanet direct imaging mission through more efficient operations and planning.

I formulated a method for optimizing integration times for a single-visit blind search using probabilistic estimates. I then validated this approach by running a Monte Carlo of mission simulations considering the full dynamics of the telescope, solar system, and exosystems. Both methods agreed to within 0.001 that the Roman CGI on a 9 month blind-search would detect, on average, 5.48 exoplanets.

The traditional probabilistic yield estimation method, which does not account for planet motion in time, results in an overestimation of yield. While ignoring planet motion is an acceptable assumption for Roman, which is sensitive to gas giants at larger separations that are likely to move slowly, the impact on yield can be large for future telescopes sensitive to Earth-like exoplanets. I therefore developed a series of underlying methods, called exodetbox, for calculating Integration Time Adjusted Completeness. I found that a design reference mission optimized with traditional completeness overestimates yield by 9.61% compared to Integration Time Adjusted Completeness.

Since many planets can share the same (s,Δmag) as an Earth-like one, I present two methods for computing the probability a detected exoplanet is Earth-like. I also quantified how common planet confusion is by treating out own solar system as an exosystem. I found that up to 6 other solar system

planets could be confused with Earth where 36% to 69% of inner Solar System planets and 1% to 4% of outer Solar System planets share (s,Δmag)-coincidence with Earth. I also found that 21 different solar system planets could be confused with each other, the worst of which exceeds a 21% probability.

I created methods to identify the minimum revisit time for a rapid revisit for detection at a particular (s,Δmag) such that the detected planet is distinctly distinguishable. These minimum revisit times can vary from 10d to 40d depending on where the detection was made. I also identify two ideal revisit times; one where the ratio of simulated planets still detectable to planets that are distinctly distinguishable is maximized, the other is when this ratio is maximized for the Earth-like planet population relative to the broader SAG13 planet population.

I also present an orbit fitting technique using both the photometry and the astrometry of the two detections that is faster and more accurate than any current orbit fitting. While the Standards Definition and Evaluation Team Final Report found three to four detections are necessary to orbit fit semi-major axis to within 10% accuracy, I found this accuracy can be achieved with as few as two detections.

BIBLIOGRAPHY

[1] M. Abramowitz and I. A Stegun. *Handbook of Mathemaical Functions with Formulas, Graphsm and Mathematical Tables*. 9th. Dover, 1972, pp. 17–18.

[2] Charles Acton et al. "A look towards the future in the handling of space science mission geometry". In: *Planetary and Space Science* 150 (Jan. 2018), pp. 9–12. ISSN: 0032-0633. DOI: 10.1016/J.PSS.2017.02.013. URL: https://www.sciencedirect.com/science/article/pii/S0032063316303129.

[3] Charles H. Acton. "Ancillary data services of NASA's Navigation and Ancillary Information Facility". In: *Planetary and Space Science* 44.1 (Jan. 1996), pp. 65–70. ISSN: 0032-0633. DOI: 10.1016/0032-0633(95)00107-7. URL: https://www.sciencedirect.com/science/article/pii/0032063395001077.

[4] Eric Agol. "Rounding up the wanderers: Optimizing coronagraphic searches for extrasolar planets". In: *Monthly Notices of the Royal Astronomical Society* 374.4 (2007), pp. 1271–1289. ISSN: 00358711. DOI: 10.1111/j.1365-2966.2006.11232.x. arXiv: 0610697 [astro-ph].

[5] B. A. Archinal et al. "Report of the IAU Working Group on Cartographic Coordinates and Rotational Elements: 2015". In: *Celestial Mechanics and Dynamical Astronomy* 130.3 (2018), pp. 1–46. ISSN: 15729478. DOI: 10.1007/s10569-017-9805-5. URL: https://doi.org/10.1007/s10569-017-9805-5.

[6] Isaac Asimiv. *Foundation*. Gnome Press, 1951.

[7] J. K. Barstow et al. “Transit spectroscopy with James Webb Space Telescope: Systematics, starspots and stitching”. In: *Monthly Notices of the Royal Astronomical Society* 448.3 (2015), pp. 2546–2561. ISSN: 13652966. DOI: 10.1093/mnras/stv186.

[8] Rus Belikov et al. *Exoplanet Occurrence Rates and Distributions*. Tech. rep. 2017. URL: https://exoplanets.nasa.gov/exep/exopag/sag/.

[9] W. H. Besant. *Conic sections, treated geometrically.* 9th ed., London, 1895. URL: http://hdl.handle.net/2027/coo.31924059322481.

[10] Sarah Blunt et al. “Orbits for the Impatient: a Bayesian Rejection Sampling Method for Quickly Fitting the Orbits of Long-Period Exoplanets”. In: *arXiv* 153.5 (2017), p. 229. ISSN: 23318422. DOI: 10.3847/1538-3881/aa6930. arXiv: 1703.10653. URL: http://dx.doi.org/10.3847/1538-3881/aa6930.

[11] Paul T. Boggs and Jon W. Tolle. “Sequential Quadratic Programming”. In: *Acta Numerica* 4 (1995), p. 1. ISSN: 14740508. DOI: 10.1017/S0962492900002518. arXiv: 10.1.1.40.1157. URL: http://www.journals.cambridge.org/abstract%7B%5C_%7DS0962492900002518.

[12] T. A. A. Broadbent, L. Kuipers, and R. Timman. *Handbook of Mathematics*. 5th. Vol. 54. 389. Berlin: Springer, 1970, p. 304. ISBN: 9783540721215. DOI: 10.2307/3613809.

[13] Robert A. Brown. “Single-Visit Photometric and Obscurational Completeness”. In: *The Astrophysical Journal* 624.2 (May 2005), pp. 1010–1024. ISSN: 0004-637X. DOI: 10.1086/429124. URL: http://stacks.iop.org/0004-637X/624/i=2/a=1010.

[14] Robert A. Brown and Rémi Soummer. "NEW COMPLETENESS METHODS FOR ESTIMATING EXOPLANET DISCOVERIES BY DIRECT DETECTION". In: *The Astrophysical Journal* 715.1 (May 2010), pp. 122–131. ISSN: 0004-637X. DOI: 10.1088/0004-637X/715/1/122. URL: http://stacks.iop.org/0004-637X/715/i=1/a=122?key=crossref.6ee7d8434f43e7a0b7eaa2af9dccd921.

[15] Marta L. Bryan et al. "Searching for Scatterers: High-Contrast Imaging of Young Stars Hosting Wide-Separation Planetary-Mass Companions". In: *The Astrophysical Journal* 827.2 (2016), p. 100. ISSN: 0004-637X. DOI: 10.3847/0004-637x/827/2/100. arXiv: 1606.06744. URL: http://dx.doi.org/10.3847/0004-637X/827/2/100.

[16] Kerri L Cahoy, Mark S Marley, and Jonathan J Fortney. "EXOPLANET ALBEDO SPECTRA AND COLORS AS A FUNCTION OF PLANET PHASE, SEPARATION, AND METALLICITY". In: *The Astrophysical Journal* 724 (2010), pp. 189–214. DOI: 10.1088/0004-637X/724/1/189. URL: https://iopscience.iop.org/article/10.1088/0004-637X/724/1/189/pdf.

[17] David C. Catling and James F. Kasting. *Escape of Atmospheres to Space*. 2017, pp. 129–168. ISBN: 9781139020558. DOI: 10.1017/9781139020558.006.

[18] Committee on the Planetary Science Decadal Survey and Space Studies Board. *Vision and Voyages for Planetary Sicence in the Decade 2013-2022*. National Academy of Sciences, 2011. ISBN: 9780309224642.

[19] Andrew Cumming et al. "The Keck Planet Search: Detectability and the Minimum Mass and Orbital Period Distribution of Extrasolar Planets". In: *Publications of the Astronomical Society of the Pacific* 120.867 (May 2008),

pp. 531–554. ISSN: 0004-6280. DOI: 10.1086/588487. URL: http://iopscience.iop.org/article/10.1086/588487.

[20] Thayne Currie et al. "Direct imaging and spectroscopy of a candidate companion below/near the deuterium-burning limit in the young binary star system, ROXs 42B". In: *Astrophysical Journal Letters* 780.2 (2014), pp. 1–8. ISSN: 20418205. DOI: 10.1088/2041-8205/780/2/L30. arXiv: 1310.4825.

[21] Ulyana Dyudina et al. "Reflected Light Curves, Spherical and Bond Albedos of Jupiter- and Saturn-Like Exoplanets". In: *The Astrophysical Journal* 822.2 (2016), p. 76. ISSN: 0004-637X. DOI: 10.3847/0004-637x/822/2/76. arXiv: 1511.04415. URL: http://dx.doi.org/10.3847/0004-637X/822/2/76.

[22] Ulyana A. Dyudina et al. "Phase Light Curves for Extrasolar Jupiters and Saturns". In: *The Astrophysical Journal* 618.2 (2005), pp. 973–986. ISSN: 0004-637X. DOI: 10.1086/426050.

[23] R. W. Farquhar. *The Utilization of Halo Orbits in Advanced Lunar Operations*. Tech. rep. 1971, pp. 1–99. URL: https://ntrs.nasa.gov/archive/nasa/casi.ntrs.nasa.gov/19710021579.pdf.

[24] Rachel B Fernandes et al. "Hints for a Turnover at the Snow Line in the Giant Planet Occurrence Rate". In: *The Astrophysical Journal* 874.1 (Mar. 2019), p. 81.

[25] François Fressin et al. "THE FALSE POSITIVE RATE OF KEPLER AND THE OCCURRENCE OF PLANETS". In: *The Astrophysical Journal* 766.2 (Mar. 2013), p. 81. DOI: 10.1088/0004-637X/766/2/81. URL:

http://stacks.iop.org/0004-637X/766/i=2/a=81?key=crossref.61220c7d574853ef276f8ffca21a3682.

[26] Daniel Garrett. "Dissertation: Exoplanet Direct Imaging Detection Metrics and Exoplanet Populations". In: December (2018).

[27] Daniel Garrett and Dmitry Savransky. "ANALYTICAL FORMULATION OF THE SINGLE-VISIT COMPLETENESS JOINT PROBABILITY DENSITY FUNCTION". In: *The Astrophysical Journal* 828.1 (Aug. 2016), p. 20. ISSN: 1538-4357. DOI: 10.3847/0004-637X/828/1/20. URL: http://stacks.iop.org/0004-637X/828/i=1/a=20?key=crossref.b2ae3f98f2997e6b3dee9331319a4f6a.

[28] Daniel Garrett and Dmitry Savransky. "Building Better Planet Populations for EXOSIMS". In: *American Astronomical Society, AAS Meeting #231, id.#246.04* 231 (2018). URL: http://adsabs.harvard.edu/abs/2018AAS...23124604G.

[29] Daniel Garrett and Dmitry Savransky. "Planet Occurrence Rate Density Models Including Stellar Effective Temperature". In: *Publications of the Astronomical Society of the Pacific* (2018).

[30] Daniel Garrett, Dmitry Savransky, and Bruce Macintosh. "A Simple Depth-of-Search Metric for Exoplanet Imaging Surveys". In: *The Astronomical Journal* (2017). URL: https://iopscience.iop.org/article/10.3847/1538-3881/aa78f6/pdf.

[31] Goddard Space Flight Center. *LUVOIR Interim Report*. Tech. rep. 2018. DOI: 10.1007/BF01867395.

[32] Claire Marie Guimond and Nicolas B Cowan. "Three Direct Imaging Epochs Could Constrain the Orbit of Earth 2.0 inside the Habitable

Zone". In: *The Astronomical Journal* 157 (2019), p. 188. DOI: 10.3847/1538-3881/ab0f2e. URL: https://doi.org/10.3847/1538-3881/ab0f2e.

[33] Claire Marie Guimond and Nicolas B. Cowan. "The direct imaging search for Earth 2.0: Quantifying biases and planetary false positives". In: *arXiv* (2018). ISSN: 23318422. DOI: 10.3847/1538-3881/aabb02. arXiv: 1804.00699.

[34] Claire Marie Guimond and Nicolas B. Cowan. "Three direct imaging epochs could constrain the orbit of Earth 2.0 inside the habitable zone". In: *arXiv* (2019), pp. 1–13. ISSN: 23318422. DOI: 10.3847/1538-3881/ab0f2e. arXiv: 1903.06184.

[35] Andrew Horning, Rhonda M. Morgan, and Eric Nielson. "Minimum number of observations for exoplanet orbit determination". In: September 2019. SPIE, 2019, pp. 427–437. ISBN: 9781510629271. DOI: 10.1117/12.2529741.

[36] A W Howard et al. "The occurrence and mass distribution of close-in super-Earths, Neptunes, and Jupiters". In: *Science* 330.6004 (2010), pp. 653–655.

[37] Sarah L. Hunyadi, Stuart B. Shaklan, and Robert A. Brown. "The lighter side of TPF-C: evaluating the scientific gain from a smaller mission concept". In: ed. by Daniel R. Coulter. International Society for Optics and Photonics, Sept. 2007. DOI: 10.1117/12.733454. URL: http://proceedings.spiedigitallibrary.org/proceeding.aspx?doi=10.1117/12.733454.

[38] NASA Exoplanet Science Institute. *NASA Exoplanet Archive*. 2021. URL: https://exoplanetarchive.ipac.caltech.edu/.

[39] Jet Propulsion Laboratory. *Habitable Exoplanet Observatory Final Report*. Tech. rep. 2019.

[40] N. Jeremy Kasdin et al. "The Nancy Grace Roman Space Telescope Coronagraph Instrument (CGI) technology demonstration". In: (2020), p. 194. ISSN: 1996756X. DOI: 10.1117/12.2562997. arXiv: 2103.01980.

[41] James F. Kasting, Daniel P. Whitmire, and Ray T. Reynolds. "Habitable Zones around Main Sequence Stars". In: *Icarus* 101 (1993), pp. 108–128. DOI: 0019-1035/93.

[42] Dean Keithly. *exodetbox*. 2021. URL: https://github.com/SIOSlab/exodetbox.

[43] Dean Keithly, Dmitry Savransky, and Corey Spohn. "Integration Time Adjusted Completeness". In: *Journal of Astronomical Telescopes, Instruments, and Systems* 7.3 (2021). DOI: 10.1117/1.JATIS.7.3.037002.

[44] Dean Keithly et al. "Blind Search Single-Visit Exoplanet Direct Imaging Yield for Space Based Telescopes". In: *American Astronomical Society, AAS Meeting #233, id.140.40*. Vol. 233. 2019. URL: http://adsabs.harvard.edu/abs/2019AAS...23314040K.

[45] Dean Keithly et al. "Scheduling and target selection optimization for exoplanet imaging spacecraft". In: *Space Telescopes and Instrumentation 2018: Optical, Infrared, and Millimeter Wave*. Ed. by Howard A. MacEwen et al. Vol. 10698. SPIE, July 2018, p. 191. ISBN: 9781510619494. DOI: 10.1117/12.2311717. URL: https://www.spiedigitallibrary.org/conference-proceedings-of-spie/10698/2311717/

Scheduling-and-target-selection-optimization-for-exoplanet-imaging-spacecraft/10.1117/12.2311717.full.

[46] Dean Keithly et al. "WFIRST: Exoplanet Target Selection and Scheduling with Greedy Optimization". In: *American Astronomical Society, AAS Meeting #231, id. 246.06*. Vol. 231. 2018. URL: http://adsabs.harvard.edu/abs/2018AAS...23124606K.

[47] Dean R. Keithly et al. "Optimal scheduling of exoplanet direct imaging single-visit observations of a blind search survey". In: *Journal of Astronomical Telescopes, Instruments, and Systems* (2020).

[48] Egemen Kolemen, N. Jeremy Kasdin, and Pini Gurfil. "Quasi-Periodic Orbits of the Restricted Three-Body Problem Made Easy". In: *AIP Conference Proceedings*. Vol. 886. AIP, 2007, pp. 68–77. DOI: 10.1063/1.2710044. URL: http://aip.scitation.org/doi/abs/10.1063/1.2710044.

[49] Ravi Kopparapu et al. "Exoplanet Diversity in the Era of Space-based Direct Imaging Missions. A white paper submitted in response to the NAS call on Exoplanet Science Strategy". In: (). arXiv: 1803.03812.

[50] Ravi Kumar Kopparapu et al. "Exoplanet Classification and Yield Estimates for Direct Imaging Missions". In: *The Astrophysical Journal* 856.2 (Mar. 2018), p. 122. ISSN: 1538-4357. DOI: 10.3847/1538-4357/aab205. URL: http://stacks.iop.org/0004-637X/856/i=2/a=122?key=crossref.df3dcdea83ce9cf80cca8f7132072c22.

[51] Ravi Kumar Kopparapu et al. "Habitable zones around main-sequence stars: New estimates". In: *Astrophysical Journal* 765.2 (2013). ISSN: 15384357. DOI: 10.1088/0004-637X/765/2/131. arXiv: 1301.6674.

[52] Adam L. Kraus et al. “Three wide planetary-mass companions to fw Tau, ROXs 12, and ROXs 42B”. In: *Astrophysical Journal* 781.1 (2014). ISSN: 15384357. DOI: 10.1088/0004-637X/781/1/20. arXiv: 1311.7664.

[53] John Krist, Bijan Nemati, and Bertrand Mennesson. “Numerical modeling of the proposed WFIRST-AFTA coronagraphs and their predicted performances”. In: *Journal of Astronomical Telescopes, Instruments, and Systems* 2.1 (2015), p. 011003. ISSN: 2329-4124. DOI: 10.1117/1.jatis.2.1.011003.

[54] John E. Krist. “End-to-end numerical modeling of AFTA coronagraphs”. In: *Space Telescopes and Instrumentation 2014: Optical, Infrared, and Millimeter Wave* 9143 (2014), p. 91430V. DOI: 10.1117/12.2056759.

[55] Glen A. Larson. *Battlestar Galactica*. 1978.

[56] Ch Leinert et al. “The 1997 reference of diffuse night sky brightness”. In: *PAGE 1 SUPPLEMENT SERIES Astron. Astrophys. Suppl. Ser* 127 (1998), pp. 1–99. URL: https://aas.aanda.org/articles/aas/pdf/1998/01/ds1449.pdf.

[57] Liming Li et al. “Less absorbed solar energy and more internal heat for Jupiter”. In: *Nature Communications* 9.1 (2018), pp. 1–10. ISSN: 20411723. DOI: 10.1038/s41467-018-06107-2. URL: http://dx.doi.org/10.1038/s41467-018-06107-2.

[58] R. Lougee-Heimer. “The Common Optimization INterface for Operations Research: Promoting open-source software in the operations research community”. In: *IBM Journal of Research and Development* 47.1 (Jan. 2003), pp. 57–66. ISSN: 0018-8646. DOI: 10.1147/rd.471.0057. URL: http://ieeexplore.ieee.org/document/5388980/.

[59] Rodrigo Luger et al. “Analytic Light Curves in Reflected Light: Phase Curves, Occultations, and Non-Lambertian Scattering for Spherical Planets and Moons”. In: (2021). arXiv: 2103.06275. URL: http://arxiv.org/abs/2103.06275.

[60] J. H. Madden and Lisa Kaltenegger. “A catalog of spectra, albedos, and colors of solar system bodies for exoplanet comparison”. In: *arXiv* (2018), pp. 1–20. ISSN: 23318422. DOI: 10.1089/ast.2017.1763.

[61] A. Mallama and J. L. Hilton. “Computing apparent planetary magnitudes for The Astronomical Almanac”. In: *Astronomy and Computing* 25 (2018), pp. 10–24. ISSN: 22131337. DOI: 10.1016/j.ascom.2018.08.002. arXiv: 1808.01973.

[62] Christian Marois et al. “GPI PSF subtraction with TLOCI: the next evolution in exoplanet/disk high-contrast imaging”. In: ed. by Enrico Marchetti, Laird M Close, and Jean-Pierre Véran. Vol. 9148. International Society for Optics and Photonics, July 2014, 91480U. DOI: 10.1117/12.2055245. URL: http://proceedings.spiedigitallibrary.org/proceeding.aspx?doi=10.1117/12.2055245.

[63] Althea V. Moorhead et al. “THE DISTRIBUTION OF TRANSIT DURATIONS FOR ¡i¿KEPLER¡/i¿ PLANET CANDIDATES AND IMPLICATIONS FOR THEIR ORBITAL ECCENTRICITIES”. In: *The Astrophysical Journal Supplement Series* 197.1 (Nov. 2011), p. 1. ISSN: 0067-0049. DOI: 10.1088/0067-0049/197/1/1. URL: http://stacks.iop.org/0067-0049/197/i=1/a=1?key=crossref.c2bec061e14588060385533d7df36f2a.

[64] Rhonda Morgan et al. “Exoplanet Yield Estimation for Decadal Study Concepts using EXOSIMS”. In: *227th Meeting of the American Astronomical Society*. 2020.

[65] Rhonda Morgan et al. *The Standard Definitions and Evaluation Team Final Report A common comparison of exoplanet yield*. Tech. rep. Pasadena: Jet Propulsion Laboratory, 2019.

[66] Nicole Mortillaro. *Astronomers estimate 29 potentially habitable exoplanets may have received signals from Earth*. June 2021. URL: https://www.cbc.ca/news/science/exolanets-signals-earth-1.6078841.

[67] National Aeronautics and Space Administration (NASA). *FY 2021 Budget Estimates*. Tech. rep. June. 2021.

[68] National Research Council. *Panel Reports–New Worlds, New Horizons in Astronomy and Astrophysics*. Washington, D.C.: National Academies Press, May 2011. ISBN: 978-0-309-15962-3. DOI: 10.17226/12982. URL: http://www.nap.edu/catalog/12982.

[69] Bijan Nemati. “Detector selection for the WFIRST-AFTA coronagraph integral field spectrograph”. In: ed. by Jacobus M. Oschmann et al. International Society for Optics and Photonics, Aug. 2014. DOI: 10.1117/12.2060321. URL: http://proceedings.spiedigitallibrary.org/proceeding.aspx?doi=10.1117/12.2060321.

[70] Bijan Nemati, John E. Krist, and Bertrand Mennesson. “Sensitivity of the WFIRST coronagraph performance to key instrument parameters”. In: *Techniques and Instrumentation for Detection of Exoplanets VIII*. Ed. by Stuart Shaklan. SPIE, Sept. 2017, p. 7. ISBN: 9781510612570. DOI: 10.1117/12.2274396. URL: https://www.spiedigitallibrary.

org/conference-proceedings-of-spie/10400/2274396/Sensitivity-of-the-WFIRST-coronagraph-performance-to-key-instrument-parameters/10.1117/12.2274396.full.

[71] Eric L. Nielsen et al. "The Gemini Planet Imager Exoplanet Survey: Giant Planet and Brown Dwarf Demographics from 10 to 100 au". In: *The Astronomical Journal* 158.1 (2019), p. 13. ISSN: 1538-3881. DOI: 10.3847/1538-3881/ab16e9. arXiv: 1904.05358.

[72] Christopher Nolan. *Interstellar*. 2014.

[73] Mark J Pecaut and Eric E Mamajek. "INTRINSIC COLORS, TEMPERATURES, AND BOLOMETRIC CORRECTIONS OF PRE-MAIN-SEQUENCE STARS". In: *The Astrophysical Journal Supplement Series* 208.22pp (2013), p. 9. DOI: 10.1088/0067-0049/208/1/9. URL: http://www.astro.sunysb.edu/fwalter/SMARTS/smarts%7B%5C_%7D15msched..

[74] Michael Perryman. *The Exoplanet Handbook Second Edition*. 2018, pp. 199–210, 283–287, 299–307. ISBN: 9781108419772. URL: http://weekly.cnbnews.com/news/article.html?no=124000.

[75] Panel Reports and New Worlds. *Panel reports-new worlds, new horizons in astronomy and astrophysics*. 2011, pp. 1–551. ISBN: 0309159628. DOI: 10.17226/12982.

[76] Paul Rincon. *'Earth 2.0' found in Nasa Kepler telescope haul*. July 2015. URL: https://www.bbc.com/news/science-environment-33641648.

[77] Gene Roddenberry. *Star Trek*. 1966.

[78] Joseph H. Saleh et al. “To reduce or to extend a spacecraft design lifetime?” In: *Journal of Spacecraft and Rockets* 43.1 (2006), pp. 207–217. ISSN: 15336794. DOI: 10.2514/1.10991.

[79] D. Savransky, N. J. Kasdin, and E. Cady. “Analyzing the designs of planet finding missions”. In: (Mar. 2009). DOI: 10.1086/652181. arXiv: 0903.4915. URL: http://arxiv.org/abs/0903.4915%20http://dx.doi.org/10.1086/652181.

[80] Dmitry Savransky. “SEQUENTIAL COVARIANCE CALCULATION FOR EXOPLANET IMAGE PROCESSING”. In: *The Astrophysical Journal* 800 (2015), pp. 100–9. DOI: 10.1088/0004-637X/800/2/100. URL: http://iopscience.iop.org/article/10.1088/0004-637X/800/2/100/pdf.

[81] Dmitry Savransky. “Space mission design for exoplanet imaging”. In: *Proc. SPIE*. Vol. 8864. 2013.

[82] Dmitry Savransky, Eric Cady, and N Jeremy Kasdin. “PARAMETER DISTRIBUTIONS OF KEPLERIAN ORBITS”. In: *The Astrophysical Journal* 728.7pp (2011), p. 66. DOI: 10.1088/0004-637X/728/1/66. URL: https://iopscience.iop.org/article/10.1088/0004-637X/728/1/66/pdf.

[83] Dmitry Savransky, Christian Delacroix, and Daniel Garrett. *EXOSIMS*. 2017. URL: http://ascl.net/1706.010.

[84] Dmitry Savransky, Christian Delacroix, and Daniel Garrett. “Multi-mission modeling for space-based exoplanet imagers”. In: *Techniques and Instrumentation for Detection of Exoplanets VIII*. Ed. by Stuart Shaklan. SPIE, Sept. 2017, p. 54. ISBN: 9781510612570. DOI: 10.1117/

12.2274098. URL: https://www.spiedigitallibrary.org/conference-proceedings-of-spie/10400/2274098/Multi-mission-modeling-for-space-based-exoplanet-imagers/10.1117/12.2274098.full.

[85] Dmitry Savransky and Daniel Garrett. "WFIRST-AFTA coronagraph science yield modeling with EXOSIMS". In: *Journal of Astronomical Telescopes, Instruments, and Systems* 2.1 (Dec. 2015), p. 011006. ISSN: 2329-4124. DOI: 10.1117/1.JATIS.2.1.011006. URL: http://astronomicaltelescopes.spiedigitallibrary.org/article.aspx?doi=10.1117/1.JATIS.2.1.011006.

[86] Dmitry Savransky et al. "Exploration of the dynamical phase space of stars with known planets". In: September 2019 (2019), p. 51. ISSN: 1996756X. DOI: 10.1117/12.2529521.

[87] Science and Technology Definition Team. *LUVOIR Final Report*. Tech. rep. NASA, 2019.

[88] Science Definition Team and WFIRST Study Office. *Wide-Field InfraRed Survey Telescope - Astrophysics Focused Telescope Assets WFIRST-AFTA 2015 Report*. Tech. rep. 2015.

[89] K. P. Seidelmann. *Explanatory Supplement to the Astronomical Almanac*. Mill Valley: University Science Books, 1992.

[90] Kenneth Seidelmann. *Explanatory Supplement to the Astronomical Almanac*. Mill Valley: University Science Books, 2006.

[91] Sobolev. *Light Scattering in Planetary Atmospheres*. Elsevier, 1975. ISBN: 978-0-08-017934-6. DOI: https://doi.org/10.1016/C2013-0-05661-7.

[92] Gabriel Soto et al. “Optimal starshade observation scheduling”. In: *Space Telescopes and Instrumentation 2018: Optical, Infrared, and Millimeter Wave*. Ed. by Howard A. MacEwen et al. Vol. 10698. SPIE, July 2018, p. 159. ISBN: 9781510619494. DOI: 10.1117/12.2311771. URL: https://www.spiedigitallibrary.org/conference-proceedings-of-spie/10698/2311771/Optimal-starshade-observation-scheduling/10.1117/12.2311771.full.

[93] Gabriel Soto et al. “Optimization of high-inclination orbits using planetary flybys for a zodiacal light-imaging mission”. In: *Techniques and Instrumentation for Detection of Exoplanets VIII*. Ed. by Stuart Shaklan. Vol. 10400. SPIE, Sept. 2017, p. 68. ISBN: 9781510612570. DOI: 10.1117/12.2274069. URL: https://www.spiedigitallibrary.org/conference-proceedings-of-spie/10400/2274069/Optimization-of-high-inclination-orbits-using-planetary-flybys-for-a/10.1117/12.2274069.full.

[94] Gabriel Soto et al. “Parameterizing the Search Space of Starshade Fuel Costs for Optimal Observation Schedules”. In: *Journal of Guidance, Control, and Dynamics* (submitted (2018).

[95] Barry Spain. *Analytical Conics*. London: Dover, 2007. ISBN: 978-0486457734.

[96] Christopher C Stark et al. “Maximizing the ExoEarth Candidate Yield from a Future Direct Imaging Mission”. In: *The Astrophysical Journal* 795.2 (2014), p. 122.

[97] Christopher C. Stark et al. “ExoEarth yield landscape for future direct imaging space telescopes”. In: *Journal of Astronomical Telescopes, Instruments, and Systems* 5.02 (May 2019), p. 1. ISSN: 2329-4124. DOI:

10.1117/1.JATIS.5.2.024009. URL: https://www.spiedigitallibrary.org/journals/Journal-of-Astronomical-Telescopes-Instruments-and-Systems/volume-5/issue-02/024009/ExoEarth-yield-landscape-for-future-direct-imaging-space-telescopes/10.1117/1.JATIS.5.2.024009.full.

[98] COMMITTEE ON EXOPLANET SCIENCE STRATEGY. *Exoplanet science strategy*. Washington DC: National Academy of Sciences, 2019, pp. 1–172. ISBN: 9780309479417. DOI: 10.17226/25187.

[99] Ashley Strickland. *These potentially habitable exoplanets can see Earth as it evolves*. June 2021. URL: https://www.cnn.com/2021/06/23/world/earth-sight-exoplanets-scn/index.html.

[100] Science adn Technology Definition Team. *HabEx Final Report*. Tech. rep. Jet Propulsion Laboratory, 2019.

[101] Wesley A Traub et al. "Science yield estimate with the Wide-Field Infrared Survey Telescope coronagraph". In: *Journal of Astronomical Telescopes, Instruments, and Systems* 2.1 (Mar. 2016), p. 11020. ISSN: 2329-4124. DOI: 10.1117/1.JATIS.2.1.011020. URL: http://astronomicaltelescopes.spiedigitallibrary.org/article.aspx?doi=10.1117/1.JATIS.2.1.011020.

[102] Margaret C Turnbull. "ExoCat-1: The Nearby Stellar Systems Catalog for Exoplanet Imaging Missions". In: *arXiv preprint arXiv:1510.01731* (2015).

[103] Margaret C Turnbull et al. "THE SEARCH FOR HABITABLE WORLDS: 1. THE VIABILITY OF A STARSHADE MISSION Short title: Searching

for Earths with a Starshade". In: (2012). URL: https://arxiv.org/pdf/1204.6063.pdf.

[104] Margaret C. Turnbull et al. "Spectrum of a Habitable World: Earthshine in the Near-Infrared". In: *The Astrophysical Journal* 644.1 (2006), pp. 551–559. ISSN: 0004-637X. DOI: 10.1086/503322.

[105] David A Vallado. *Fundamentals of Astrodynamics and Applications*. 4th. Hawthorne: Microcosm Press, 2013.

[106] Jules Verne. *From the Earth to the Moon: A Direct Route in 97 Hours, 20 Minutes*. Pierre-Jules Hetzel, 1865.

[107] H. G. Wells. *The War of the Worlds*. Harper & Bros, 1898.

[108] Joshua N. Winn. "Transits and Occultations". In: (2010). arXiv: 1001.2010. URL: http://arxiv.org/abs/1001.2010.

[109] A. Wolszczan and D. A. Frail. "A planetary system around the millisecond pulsar PSR1257+12". In: *Nature* 359 (1992), pp. 167–169.

[110] Gary L Wycoff, Brian D Mason, and Sean E Urban. "DATA MINING FOR DOUBLE STARS IN ASTROMETRIC CATALOGS". In: *The Astronomical Journal* (2006), pp. 50–60. URL: http://ad.usno.navy.mil.

[111] Kevin J. Zahnle and David C. Catling. "The Cosmic Shoreline: The Evidence that Escape Determines which Planets Have Atmospheres, and what this May Mean for Proxima Centauri B". In: *The Astrophysical Journal* 843.2 (2017), p. 122. ISSN: 1538-4357. DOI: 10.3847/1538-4357/aa7846. arXiv: 1702.03386.

APPENDIX A

EXOPLANET DIRECT IMAGING TELESCOPES

A.1 WFIRST Cycle 6

The NGRST/WFIRST cycle 6 parameters[53] in Table A.1 used to calculate completeness and integration times in [47]. It specifically lays out the subcomponents of the SNR-integration time equations in[47].

Table A.1: WFIRST Cycle 6 input parameters[53] as defined by the EXOSIMS[83] JSON input script.

Subgroup	Description	Value	EXOSIMS JSON Name
INST	Clock Induced Charge	0.01	CIC
INST	Excess Noise Factor	1.0	ENF
INST	Field Of View	9.5 arcsec	FoV
INST	Photon counting efficiency	0.8	PCeff
INST	Quantum Efficiency	Figure A.2	QE
INST	Spectral Resolving Power (specific to spectrometers)	1	Rs
INST	Detector f-number	60.977	fnumber
INST	focal length	144.515 m	focal
INST	Dark current per pixel	0.000114 s^{-1}	idark

Continued on next page

INST	Lenslet sampling, number of pixel per lenslet rows or cols (specific to spectrometers)	1.0	lenslSamp
INST	Attenuation due to optics specific to the science instrument	0.518018	optics
INST	Detector array format, # of pixels per detector	1024	pixelNumber
INST	Pixel Scale in arcsec per pixel	0.01855469″	pixelScale
INST	Pixel pitch	1.3e-5 m	pixelSize
INST	Detector effective read noise per frame per pixel	0	sread
INST	Exposure Time	100 s	texp
SYST	Bandwidth Fraction	0.1	BW
SYST	Inner Working Angle	0.15″	IWA
SYST	Outer Working Angle	0.428996″	OWA
SYST	Area of FWHM region of planet PSF, in arcsec^2	Figure A.1	core_area

Continued on next page

SYST	Mean starlight residual normalized intensity per pixel, required to calculate total core intensity as $\Psi \times N_{pix}$	Figure A.1	core_mean_intensity
SYST	Core platescale	0.3	core_platescale
SYST	System throughput in the FWHM region of the planet PSF core	Figure A.1	core_thruput
SYST	Bandwidth	56.5 nm	deltaLam
SYST	Central wavelength	565 nm	lam
SYST	Coronagraph name	HLC-565	name
SYST	Intensity transmission of extended background sources such as f_Z. Includes pupil mask, occulter, Lyot stop and polarizer.	Figure A.1	occ_trans
SYST	Overhead time	0.5 d	ohTime
SYST	Attenuation due to optics specific to the CGI e.g. polarizer, Lyot stop, extra flat mirror	0.983647	optics
SYST	Signal to noise ratio threshold	5	SNR

Continued on next page

Observatory	Anti-solar keep-out region	124°	koAngleMax
Observatory	Maximum time past mission start an observation can be made	6 yrs	missionLife
Observatory	Fraction of mission life spent observing	0.04166	missionPortion
Observatory	Settling time after repoint	0.5 d	settlingTime
-	Post processing efficiency	0.1	ppFact
Technical	$\Delta\mathrm{mag}$ used to calculate minimum integration times for inclusion in target list	22.5	dMag0
Technical	Maximum allowed integration time in units of day	30d	intCutoff

Many of the instrument parameters are multi-dimensional interpolants as a function of working angle. Here we include functions and interpolants used in the calculation of $\Delta\mathrm{mag}$ in Eq. 3.3, including expressions for the zero-magnitude flux, star apparent V magnitude, throughput, intensity transmission of extended background sources, core mean intensity, core area, and quantum efficiency.

A.1.1 Zero-Magnitude Flux

The zero-magnitude flux, $\mathcal{F}_0$, used in the calculation of spectral flux density, $C_{\mathcal{F}_0}$, in Eqs. 3.4, 3.18 and 3.3, is given by

$$\mathcal{F}_0(\lambda) = 10^4 \times 10^{(4.01 - \frac{\lambda - 550\text{nm}}{770\text{nm}})} ph/s/m^2/nm \tag{A.1}$$

from Traub et al. [101].

A.1.2 Star Apparent V Magnitude

The calculation of Δmag_i relies upon the star's color-adjusted visual magnitude, $\nu_i(\lambda)$, given by the parametric equation from Traub et al. [101]

$$\nu_i = \begin{cases} V_{\text{mag},i} + 2.20BV_i(1/\lambda - 1.818) & \lambda < 550\text{nm} \\ V_{\text{mag},i} + 1.54BV_i(1/\lambda - 1.818) & \lambda \geq 550\text{nm}\,. \end{cases} \tag{A.2}$$

$V_{\text{mag},i}$ is the V-band apparent magnitude of the i^{th} target star and is taken from EXOCAT star catalog used in Turnbull [102]. BV_i is the color of the star as measured by the difference between B and V bands (in magnitudes). The parameters for the target stars used in the final target list are included in Table B.1 in Appendix B.1.

A.1.3 Characterization Parameters

In this work, we include characterization observations, which slightly detract from executing the planned observation schedule in Table B.1 of Appendix B.1. These characterization observations immediately follow the detection of a planet so long as the star $\underline{r}_{i/SC}$ is not obstructed by a keep-out region,

is not filtered by integration time, and there is sufficient time to make the observation before the target enters a keep-out region. A detected planet is considered for characterization if $SNR > 10$. These characterization observations use slightly modified set of parameters.

Our characterization observation integration time is calculated using $SNR = 10$, at $\lambda = 660$ nm, $PPL = 4.0$, $\epsilon_{syst} = 0.46584$, $N_{pix} = 76$, $PS = 0.02631$, and $Rs = 50$. Rs, the spectral resolving power specifically changes the $\Delta\lambda$ to λ/Rs.

A.1.4 WFIRST Cycle 6 Derivative 2D Interpolants

The fits files used for 2D interpolants of core throughput $T(\lambda, WA)$, intensity transmission of extended background sources $\gamma(\lambda, WA)$, core mean intensity $\Psi(\lambda, WA)$, core area $\Gamma(\lambda, WA)$, and quantum efficiency ϵ_q are derivative of Nemati, Krist, and Mennesson [70], Krist [54], and Krist, Nemati, and Mennesson [53].

A.1.5 Electron Count Rates

This section lays out Nemati's SNR equation and all sub-components from Nemati [69]. The SNR equation used in this paper is

$$t_i = \frac{SNR^2 \times C_{b,i}}{C_{p,i}^2 - (SNR \times C_{sp,i})^2}. \tag{A.3}$$

This uses $C_{p,i}$, $C_{b,i}$, and $C_{sp,i}$ which are respectively the planet signal, background signal, and residual speckle spatial structure in electron count rates in

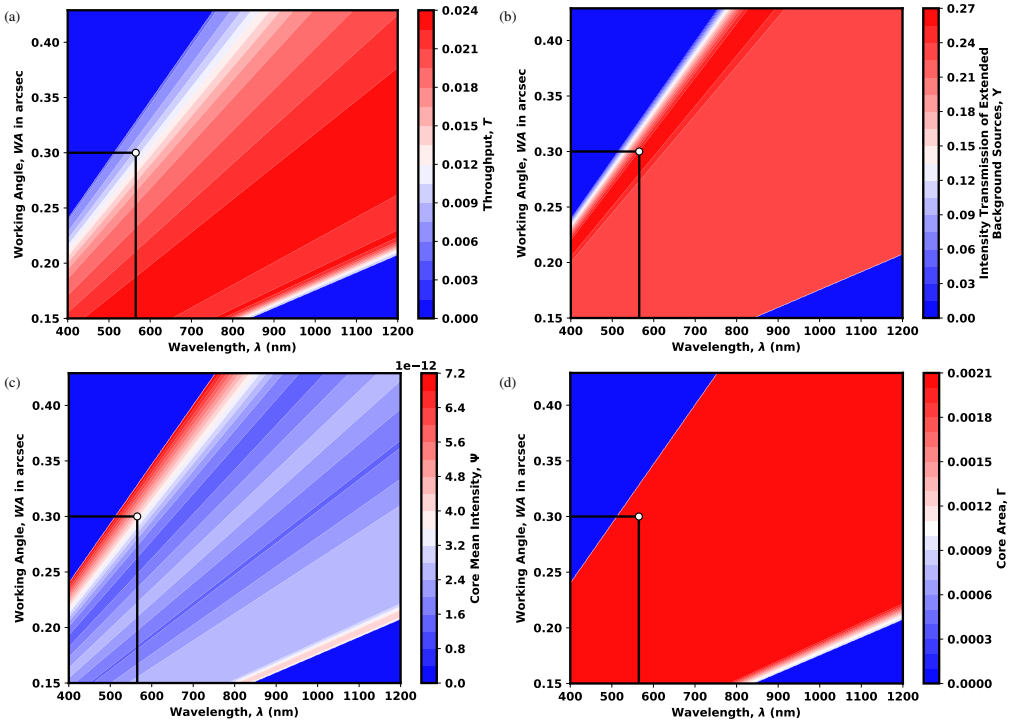

Figure A.1: System throughput in the FWHM region of the planet PSF core (a) from /WFIRST_cycle6/G22_FIT_565/G22_FIT_565_thruput.fits. Intensity transmission of extended background sources such as zodiacal light including the pupil mask, Lyot stop and polarizer (b) from /WFIRST_cycle6/G22_FIT_565/G22_FIT_565_occ_trans.fits. Core mean intensity as a function of wavelength and working angle. Black lines and dot represent detection mode wavelength (565 nm) and inner working angle (0.3 arcsec) for integration time calculation (c) from /WFIRST_cycle6/G22_FIT_565/G22_FIT_565_mean_intensity.fits. Area of the FWHM region of the planet PSF in arcsec^2 (d) from /WFIRST_cycle6/ G22_FIT_565/-G22_FIT_565_area.fits.

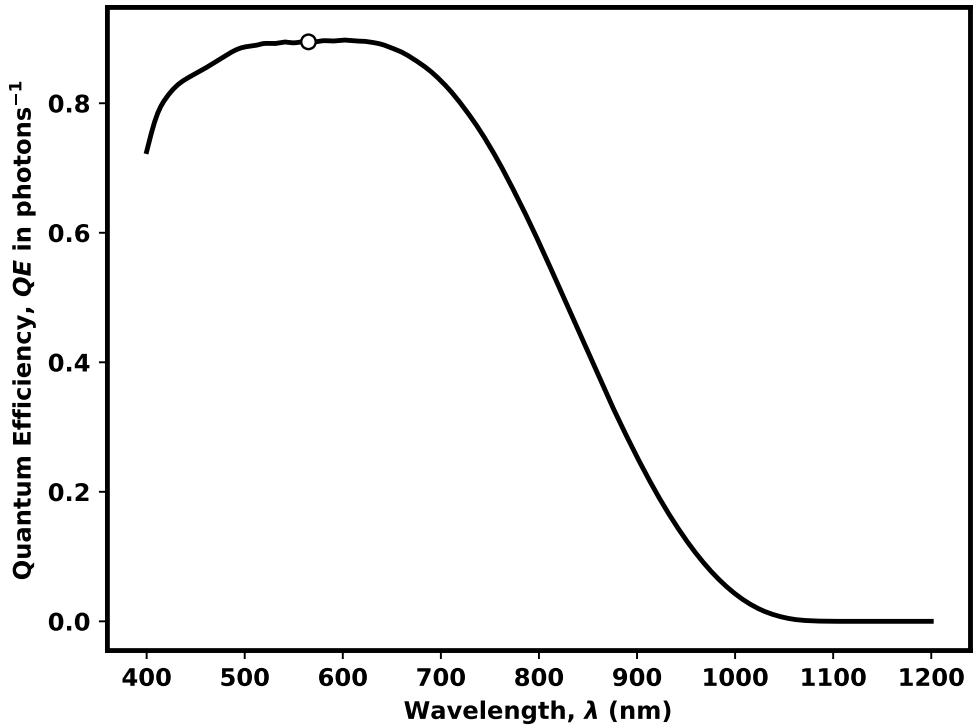

Figure A.2: Quantum Efficiency of the detector as a function of wavelength. White dot represents detection mode wavelength (565 nm). From /WFIRST_cycle6/QE/Basic_Multi2_std_Si.fits

s^{-1}.

We calculate $C_{p,i}$ using

$$C_{p,i} = C_{\mathcal{F}_0} \times 10^{-0.4(\nu_i + \Delta\mathrm{mag}_i)} \times T(\lambda, WA) \times \epsilon_{PC} \times NCTE. \tag{A.4}$$

$NCTE$ is the net charge transfer efficiency.

We calculate $C_{b,i}$ using

$$C_{b,i} = ENF^2 \times (C_{sr,i} + C_{z,i} + C_{ez}) + (ENF^2 \times (C_{dc} + C_{cc}) + C_{rn}). \tag{A.5}$$

$C_{sr,i}$, $C_{z,i}$, C_{ez}, C_{dc}, C_{cc}, and C_{rn} are electron count rates with units of s^{-1} for

starlight residual, zodiacal light, exozodiacal light, dark current, clock-induced-charge, and readout noise respectively. ENF is an excess noise factor.

We calculate the starlight residual count rate, $C_{sr,i}$, for each target star i by

$$C_{sr,i} = C_{\mathcal{F}_0} \times 10^{-0.4 \times \nu_i} \times \Psi(\lambda, WA) \times N_{pix}. \tag{A.6}$$

Where N_{pix} is the number of pixels in the photometric aperture ($\Gamma(\lambda, WA)/\theta^2$) calculated by

$$N_{pix} = PPL \times \frac{\Gamma(\lambda, WA)}{PS^2}. \tag{A.7}$$

Where PPL is the number of pixels per lenslet and is simply the lenslSamp^2, a parameter specified in Table A.1. Where PS is the detector pixel scale in arcsec per pixel. $\Psi(\lambda, WA)$ is the core mean intensity from Figure A.1. ν_i is given by the Eq. A.2.

We calculate the zodiacal light count rate, $C_{z,i}$, using

$$C_{z,i} = C_{\mathcal{F}_0} \times f_{Z,i} \times \Gamma(\lambda, WA) \times \gamma(\lambda, WA). \tag{A.8}$$

Where $\gamma(\lambda, WA)$ comes from Figure A.1.

We calculate the exozodiacal light attributed count rate, C_{ez}, as

$$C_{ez} = C_{\mathcal{F}_0} \times f_{EZ} \times \Gamma(\lambda, WA) \times T(\lambda, WA). \tag{A.9}$$

We calculate the dark current count rate, C_{dc}, as

$$C_{dc} = N_{pix} \times i_{dark}. \tag{A.10}$$

Where i_{dark} is the dark current per pixel.

We calculate clock induced charge count rate ,C_{cc}, as

$$C_{cc} = N_{pix} \times CIC/t_{exp}. \tag{A.11}$$

Where CIC is the clock induced charge per pixel and t_{exp} is the exposure time.

We calculate the readout noise count rate, C_{rn}, as

$$C_{rn} = N_{pix} \times s_{read}/t_{exp}. \tag{A.12}$$

Where s_{read} is the readout noise per pixel.

We calculate $C_{sp,i}$ using

$$C_{sp,i} = C_{sr,i} \times \epsilon_{pp}. \tag{A.13}$$

Where ϵ_{pp} is the post processing efficiency.

Using these photon count rate models in applied to HIP 25278, a 5^{th} magnitude star assuming $f_{Z,0}$, $f_{EZ,0}$, with a planet at $WA = 0.28$ arcsec and $\Delta\text{mag} = 22.5$, at $\lambda = 565$ nm, using the instrument parameters in Figure A.1, we get the photon count rates $C_p = 0.00174175\ s^{-1}$, $C_b = 0.00646741\ s^{-1}$, and $C_{sp} = 0.00016929\ s^{-1}$.

A.2 Analytical Δmag uncertainty derivation

Science Objective 1 of the Science Traceability Matrix of the Table 5.1-2 of [100] specifies the baseline level of performance which we derive here into an uncertainty in Δmag.

The planet star flux ratio difference for the science requirement is set at 10^{-10}

and we can calculate the planet-star difference in magnitude as

$$\Delta\text{mag} = -2.5 \log_{10}\left(10^{-10}\right) = 25. \tag{A.14}$$

The test-star given in the requirement is specified with $V_{\text{mag},*} = 4.6$ which means the planet visual magnitude is $V_{\text{mag,planet}} = \Delta\text{mag} + V_{\text{mag},*} = 29.6$. We can then calculate the test planet flux as

$$S = 10^{\left(\frac{V_{\text{mag,planet}}}{-2.5}\right)} = -1.4454 \times 10^{-12}. \tag{A.15}$$

The signal to noise ratio (SNR) specified as 7 allowing us to rearrange SNR into

$$N = \frac{S}{7}, \tag{A.16}$$

where S is the planet flux assuming no uncertainty, and N is the signal noise. We now know the noise flux from the sample scenario to be $N = 2.0649 \times 10^{-13}$.

In the plots included in this work, we assume the planet-star difference in magnitude is relative to a $V_{\text{mag}} = 0$ reference star. The combined term inside the log in Eqn. 6.1 is the planet flux. If we assume the noise flux is a constant, then we can get an expression for the error in Δmag as a function of the planet Δmag,

$$\Delta\text{mag}_{\text{error}} = 2.5 \log_{10}\left(1 + N10^{\left(\frac{\Delta\text{mag}}{2.5}\right)}\right). \tag{A.17}$$

APPENDIX B

DESIGN REFERENCE MISSIONS

B.1 Roman DRM from Keithly et al. [47]

Table B.1: Planned observation target list optimized using the Kepler Like planet population. sInd refers to the index of the planet in the filtered, initial target list of 651 targets. Name refers to the Hipparcos star catalog name of the target star. V_{mag} refers to the visual magnitude of the target star. d_i is the distance from the sun to the host star. BV is the color of the star as measured by the difference in B and V bands (in magnitudes). $t_{obs,i}$ is the observing time planned by the optimization algorithm. $c_i(t_{obs})$ is the expected completeness reward for making an observation of this star for the prescribed integration time. The "Known Planet" column in Table B.1 was generated by taking all target star names in the optimized target list derived from the EXOCAT-1 star catalog, and cross-referencing them using a list of aliases from SIMBAD and the NASA Exoplanet Archive. In total, 9 of the 60 planned targets already have known exoplanets. The final column contains each target star's spectral type. Data in this table is taken from C0vsT0andCvsTDATA_WFIRSTcycle6core_CKL2_PPKL2_2019_10_07_11_40_.txt

sInd	Name	V mag	B-V	d_i (pc)	$t_{obs,i}$ (d)	$c_i(t_{obs,i})$	Known Planet	Spectral Type
1	HIP 746	2.26	0.36	16.78	0.157	0.016	0	F2III-IV
9	HIP 1599	4.23	0.58	8.59	0.860	0.049	0	G0V
12	HIP 2021	2.82	0.62	7.46	0.483	0.067	0	G1IV
25	HIP 3765	5.74	0.89	7.45	0.806	0.025	0	K1V

Continued on next page

46	HIP 7513	4.09	0.54	13.49	0.459	0.021	1	F8V
51	HIP 7918	4.96	0.62	12.74	0.481	0.017	0	G2V
52	HIP 7981	5.24	0.84	7.53	1.232	0.039	0	K1V
53	HIP 8102	3.49	0.73	3.65	0.740	0.097	1	G8.5V
54	HIP 8362	5.63	0.8	10.07	0.576	0.019	0	K0V
70	HIP 10644	4.86	0.61	10.78	0.736	0.026	0	G0V
79	HIP 12777	4.1	0.49	11.13	0.640	0.032	0	F7V
80	HIP 12843	4.47	0.48	14.22	0.419	0.016	0	F5/6V
90	HIP 14632	4.05	0.6	10.54	0.672	0.036	0	G0V
97	HIP 15457	4.84	0.68	9.14	0.995	0.036	0	G5V
98	HIP 15510	4.26	0.71	6.04	1.059	0.072	1	G8.0V
100	HIP 16537	3.71	0.88	3.21	0.809	0.099	1	K2.0V
101	HIP 16852	4.29	0.58	13.96	0.432	0.018	0	F8V
104	HIP 17378	3.52	0.93	9.04	0.607	0.050	0	K0IV
136	HIP 22449	3.17	0.46	8.07	0.576	0.060	0	F6V
153	HIP 24813	4.69	0.61	12.63	0.525	0.019	0	G0V
165	HIP 27072	3.59	0.48	8.93	0.630	0.051	0	F7V
176	HIP 28103	3.71	0.34	14.88	0.334	0.018	0	F1V
199	HIP 32349	-1.44	0.01	2.63	0.066	0.113	0	A1.0V
229	HIP 37279	0.4	0.43	3.51	0.163	0.105	0	F5IV-V
233	HIP 37826	1.16	0.99	10.36	0.178	0.046	1	K0IIIvar
270	HIP 44127	3.1	0.21	14.51	0.295	0.021	0	A7IV
280	HIP 46853	3.16	0.47	13.48	0.338	0.025	0	F6IV
288	HIP 49908	6.6	1.34	4.87	0.663	0.020	0	K7.0V
295	HIP 51459	4.82	0.54	12.78	0.505	0.018	0	F8V

Continued on next page

311	HIP 54872	2.56	0.13	17.91	0.165	0.013	0	A4V
318	HIP 56997	5.31	0.72	9.61	0.798	0.026	0	G8Vvar
319	HIP 57443	4.89	0.66	9.22	0.978	0.036	1	G3/5V
321	HIP 57632	2.14	0.09	11	0.280	0.040	0	A3Vvar
322	HIP 57757	3.59	0.52	10.93	0.561	0.036	0	F9V
328	HIP 59199	4.02	0.33	14.94	0.362	0.016	0	F0IV/V
341	HIP 61317	4.24	0.59	8.44	0.892	0.050	0	G0V
353	HIP 64394	4.24	0.57	9.13	0.841	0.045	0	G0V
372	HIP 67927	2.68	0.58	11.4	0.340	0.037	0	G0IV
376	HIP 68933	2.06	1.01	18.03	0.131	0.013	0	K0IIIB
385	HIP 70497	4.04	0.5	14.53	0.377	0.018	0	F7V
398	HIP 71908	3.16	0.26	16.57	0.231	0.015	0	APSREU(CR)
429	HIP 77257	4.41	0.6	12.12	0.603	0.025	0	G0Vvar
433	HIP 77952	2.81	0.32	12.38	0.329	0.031	0	F0III/IV
434	HIP 78072	3.85	0.48	11.25	0.574	0.033	0	F6V
488	HIP 86974	3.41	0.75	8.31	0.599	0.057	0	G5IV
508	HIP 91262	0.03	0	7.68	0.122	0.069	0	A0Vvar
527	HIP 95501	3.36	0.32	15.53	0.279	0.017	0	F2IV
529	HIP 96100	4.67	0.79	5.75	1.295	0.070	0	G9.0V
540	HIP 97649	0.76	0.22	5.12	0.195	0.092	0	A7IV-V
543	HIP 98036	3.71	0.86	13.7	0.399	0.022	0	G8IVvar
557	HIP 99240	3.53	0.76	6.11	0.728	0.076	0	G8.0IV
561	HIP 99825	5.72	0.91	8.91	0.573	0.019	1	K3V
571	HIP 102422	3.41	0.91	14.27	0.324	0.021	0	K0IV
581	HIP 105199	2.43	0.24	15.04	0.209	0.021	0	A7IV-V

Continued on next page

585	HIP 105858	4.22	0.47	9.26	0.812	0.044	0	F7V
594	HIP 107556	2.85	0.3	11.87	0.370	0.034	0	A5mF2 (IV)
602	HIP 109176	3.77	0.44	11.73	0.527	0.031	0	F5V
623	HIP 113368	1.23	0.14	7.7	0.223	0.068	1	A3V
642	HIP 116727	3.21	1.03	14.1	0.309	0.023	1	K1IV
645	HIP 116771	4.13	0.51	13.71	0.453	0.019	0	F7V

B.2 4m Monolith Design Reference Mission from Keithly, Savransky, and Spohn [43]

We calculated the Brown Completeness and Integration Time Adjusted Completeness for a 4 meter monolith telescope with a contrast of 10^{-10} on the SAG13 planet population discussed in Keithly et al. [47]. The Δmag and separations of integration is scaled by the luminosity of each candidate target star. The orbital periods are similarly scaled by the mass of each target star in the case of integration time adjusted completeness. We optimized the mission schedule using the sequential least squares quadratic programming method discussed in Keithly et al. [47] with the Brown Completeness method. Our approach included the adoption of the use of the local zodiacal light minimum and filtering of target stars.

We assume a total telescope time of 213.67 d ($\sim$7 months) and that each observation requires 0.1 d of overhead time and 0.042 d settling time. The coronagraph parameters used are from a Vortex Charge 6 coronagraph at a wavelength of 500 nm with an inner working angle of 0.045 arcsec and outer working angle

of 2.127 arcsec and a working angle of integration consistent with that used in Keithly et al. [47].

The resulting Brown Completeness optimized integration times for a Design Reference Mission (DRM) are included in Table B.2. The summed Brown Completeness for this DRM is 68.89 whereas the same summed Integration Time Adjusted Completeness is 63.11, a difference of 5.78. We can multiply either of these numbers by the SAG13 exoplanet occurrence rate of 5.62 to get the expected number of exoplanets detected in a single-visit blind search. These are 387.16 and 354.67 on average respectively. This means 32.49 planets are lost in a mission by not taking into account integration times when optimizing the mission schedule.

Table B.2: 4m Monolith Design Reference Mission from Keithly, Savransky, and Spohn [43]

Name	Dist (pc)	Int. Time (d)	Δmag	C_{brown}	C_{IAC}
HIP 439	4.34	0.399	19.557	0.049	0.041
HIP 522	25.71	0.181	23.476	0.038	0.033
HIP 544	13.67	0.6	23.403	0.16	0.141
HIP 746	16.78	0.066	27.142	0.247	0.24
HIP 910	18.75	0.383	24.916	0.16	0.146
HIP 950	21.28	0.341	24.504	0.106	0.095
HIP 1292	17.5	0.338	22.181	0.054	0.047
HIP 1392 B	15.19	0.293	21.362	0.039	0.033
HIP 1475	3.57	0.625	20.237	0.105	0.089

Continued on next page

HIP 1499	23.25	0.139	21.736	0.018	0.016
HIP 1599	8.59	0.374	25.793	0.47	0.438
HIP 1803	20.86	0.241	22.209	0.036	0.031
HIP 2021	7.46	0.179	26.942	0.55	0.525
HIP 2072	23.81	0.129	25.773	0.103	0.097
HIP 2081	25.97	0.053	26.432	0.082	0.078
HIP 2711	25.48	0.193	23.752	0.045	0.039
HIP 3093	11.06	0.745	23.731	0.242	0.213
HIP 3170	24.96	0.192	23.257	0.038	0.033
HIP 3419	29.53	0.035	26.545	0.048	0.046
HIP 3497	22.06	0.184	21.928	0.025	0.022
HIP 3505	26.75	0.169	24.171	0.044	0.039
HIP 3583	15.16	0.567	23.919	0.17	0.151
HIP 3765	7.45	0.861	23.974	0.38	0.339
HIP 3810	23.45	0.27	24.446	0.078	0.07
HIP 3909	15.75	0.515	24.685	0.207	0.187
HIP 4148	14.17	0.293	21.192	0.039	0.033
HIP 4151	18.74	0.353	25.07	0.166	0.152
HIP 5336	7.55	0.66	24.859	0.459	0.418
HIP 5862	15.11	0.46	25.001	0.238	0.217
HIP 6379	16.81	0.217	21.188	0.028	0.024
HIP 6706	25.21	0.207	23.99	0.051	0.046
HIP 6813	28.62	0.13	24.535	0.037	0.033
HIP 7235	19.05	0.164	21.17	0.021	0.018

Continued on next page

HIP 7339	20.66	0.236	22.106	0.035	0.03
HIP 7513	13.49	0.296	25.765	0.309	0.288
HIP 7601	27.38	0.129	23.04	0.023	0.02
HIP 7734	21.37	0.17	21.643	0.022	0.019
HIP 7918	12.74	0.521	24.978	0.295	0.269
HIP 7978	17.43	0.483	24.302	0.153	0.137
HIP 7981	7.53	0.733	24.611	0.44	0.398
HIP 8102	3.65	0.323	26.364	0.745	0.704
HIP 8362	10.07	0.753	24.254	0.318	0.285
HIP 8433	27.86	0.119	23.024	0.021	0.019
HIP 8497	23.19	0.241	25.078	0.098	0.09
HIP 8796	19.42	0.141	26.116	0.18	0.17
HIP 8903	17.99	0.08	26.814	0.217	0.209
HIP 9007	17.85	0.199	25.89	0.207	0.194
HIP 9236	22.01	0.069	26.565	0.138	0.132
HIP 9884	20.18	0.069	26.753	0.172	0.165
HIP 10138	10.78	0.746	23.544	0.231	0.204
HIP 10306	28.87	0.115	23.779	0.026	0.023
HIP 10644	10.78	0.528	25.092	0.359	0.329
HIP 10723	24.35	0.218	23.513	0.047	0.041
HIP 10798	12.67	0.605	22.975	0.146	0.128
HIP 11029	29.66	0.097	23.551	0.02	0.018
HIP 11783	26.7	0.179	24.768	0.055	0.049
HIP 12114	7.18	0.88	23.866	0.379	0.337

Continued on next page

HIP 12186	25.78	0.173	23.307	0.034	0.03
HIP 12444	21.76	0.299	23.526	0.067	0.059
HIP 12623	24.19	0.249	24.661	0.076	0.068
HIP 12653	17.17	0.488	24.473	0.167	0.15
HIP 12777	11.13	0.324	25.829	0.381	0.356
HIP 12843	14.22	0.352	25.471	0.28	0.259
HIP 13402	10.35	0.771	23.572	0.245	0.216
HIP 13665	26.71	0.159	23.616	0.035	0.031
HIP 14146	27.17	0.112	25.539	0.062	0.058
HIP 14150	20.64	0.162	21.435	0.021	0.018
HIP 14632	10.54	0.328	25.855	0.402	0.375
HIP 14954	22.58	0.299	24.511	0.09	0.08
HIP 15330	12.01	0.669	24.437	0.278	0.25
HIP 15371	12.03	0.592	24.779	0.303	0.275
HIP 15457	9.14	0.567	25.073	0.413	0.378
HIP 15510	6.04	0.426	25.751	0.581	0.541
HIP 16245	21.68	0.264	25.16	0.121	0.111
HIP 16537	3.21	0.377	26.121	0.768	0.722
HIP 16852	13.96	0.339	25.542	0.289	0.268
HIP 17378	9.04	0.286	26.162	0.466	0.438
HIP 17420	13.95	0.326	21.324	0.044	0.038
HIP 17439	16.03	0.286	21.475	0.039	0.033
HIP 17651	17.63	0.25	25.64	0.206	0.192
HIP 18859	18.83	0.429	24.311	0.132	0.118

Continued on next page

HIP 19076	16.94	0.466	23.433	0.114	0.101
HIP 19205	27.6	0.147	24.021	0.036	0.032
HIP 19335	21.0	0.341	23.973	0.09	0.08
HIP 19849	4.98	0.504	25.516	0.625	0.579
HIP 19859	21.33	0.244	22.41	0.039	0.034
HIP 19884	13.04	0.19	20.397	0.024	0.02
HIP 19893	20.46	0.206	25.608	0.152	0.141
HIP 19921	18.24	0.322	25.261	0.183	0.168
HIP 19990	28.94	0.122	24.383	0.033	0.03
HIP 21421	20.43	0.039	27.351	0.17	0.166
HIP 21547	29.43	0.107	23.929	0.025	0.022
HIP 21770	20.17	0.24	25.449	0.153	0.141
HIP 21861	28.67	0.127	24.318	0.034	0.03
HIP 22263	13.28	0.635	24.402	0.243	0.218
HIP 22336	26.42	0.154	23.183	0.029	0.026
HIP 22449	8.07	0.218	26.617	0.516	0.491
HIP 23311	8.71	0.832	23.26	0.258	0.226
HIP 23482	26.08	0.185	24.074	0.047	0.042
HIP 23693	11.65	0.434	25.351	0.346	0.319
HIP 23783	26.29	0.189	24.587	0.055	0.049
HIP 23875	27.4	0.044	26.48	0.067	0.064
HIP 23941	25.46	0.208	24.364	0.057	0.051
HIP 24186	3.91	0.377	19.298	0.044	0.037
HIP 24786	25.03	0.183	23.045	0.034	0.029

Continued on next page

HIP 24813	12.63	0.458	25.207	0.311	0.285
HIP 25110	20.89	0.343	24.749	0.12	0.108
HIP 25278	14.39	0.517	24.847	0.246	0.224
HIP 25544	19.2	0.183	21.347	0.024	0.02
HIP 25623	13.02	0.163	20.148	0.02	0.017
HIP 25878	5.68	0.483	20.34	0.068	0.058
HIP 26394	18.32	0.446	24.074	0.128	0.114
HIP 26779	12.28	0.645	23.215	0.171	0.15
HIP 27072	8.93	0.256	26.326	0.474	0.448
HIP 27288	21.61	0.108	26.165	0.141	0.134
HIP 27321	19.44	0.155	26.012	0.178	0.167
HIP 27435	15.18	0.544	23.539	0.145	0.128
HIP 27628	26.73	0.081	25.936	0.071	0.066
HIP 27887	13.0	0.376	21.413	0.053	0.045
HIP 27890	26.25	0.19	24.754	0.058	0.053
HIP 28103	14.88	0.2	26.143	0.282	0.266
HIP 28360	24.87	0.031	27.217	0.098	0.096
HIP 28908	25.62	0.143	22.489	0.022	0.019
HIP 28954	15.27	0.327	21.575	0.046	0.039
HIP 29271	10.2	0.582	24.95	0.369	0.337
HIP 29295	5.75	0.401	20.008	0.051	0.043
HIP 29525	17.95	0.337	22.3	0.055	0.048
HIP 29568	16.72	0.423	22.752	0.083	0.073
HIP 29650	20.82	0.358	24.425	0.109	0.097

Continued on next page

HIP 29800	19.25	0.394	24.751	0.145	0.131
HIP 29860	19.25	0.396	23.768	0.102	0.09
HIP 30503	21.88	0.228	22.401	0.036	0.031
HIP 31592	19.75	0.225	25.568	0.163	0.151
HIP 32349	2.63	0.025	30.177	0.872	0.861
HIP 32362	18.0	0.145	26.221	0.21	0.199
HIP 32366	24.38	0.207	23.238	0.041	0.036
HIP 32439	17.87	0.465	24.414	0.152	0.136
HIP 32480	16.72	0.498	24.565	0.18	0.163
HIP 32607	29.6	0.051	26.098	0.046	0.043
HIP 32765	25.26	0.215	24.454	0.061	0.055
HIP 32984	8.71	0.777	22.753	0.205	0.179
HIP 33094	25.89	0.154	22.824	0.026	0.023
HIP 33277	17.24	0.471	23.721	0.125	0.111
HIP 33690	18.33	0.245	21.638	0.033	0.028
HIP 33817	14.65	0.425	22.086	0.071	0.061
HIP 34017	19.13	0.372	23.259	0.082	0.072
HIP 34834	21.43	0.231	25.368	0.13	0.12
HIP 35136	16.89	0.503	24.178	0.156	0.139
HIP 35296 A	14.59	0.444	22.214	0.077	0.067
HIP 36366	18.05	0.245	25.626	0.197	0.183
HIP 36399	27.24	0.132	23.032	0.024	0.021
HIP 36439	20.24	0.38	24.354	0.114	0.102
HIP 36795	25.3	0.184	25.172	0.076	0.069

Continued on next page

HIP 37279	3.51	0.063	28.816	0.796	0.778
HIP 37349	14.21	0.281	21.13	0.037	0.031
HIP 37606	24.67	0.233	24.476	0.067	0.06
HIP 37826	10.36	0.073	27.756	0.442	0.43
HIP 38784	17.19	0.358	22.262	0.059	0.051
HIP 38908	16.2	0.532	24.279	0.174	0.155
HIP 39157	16.77	0.216	21.173	0.028	0.024
HIP 39342	17.31	0.195	21.121	0.025	0.022
HIP 39757	19.48	0.083	26.621	0.184	0.177
HIP 39780	23.29	0.266	24.017	0.068	0.06
HIP 39903	19.98	0.305	25.155	0.148	0.135
HIP 40035	22.38	0.292	23.955	0.075	0.066
HIP 40693	12.49	0.674	23.689	0.205	0.181
HIP 40702	19.56	0.196	25.75	0.171	0.159
HIP 40706	28.63	0.124	25.177	0.045	0.041
HIP 40843	18.27	0.438	24.634	0.156	0.141
HIP 41211	26.62	0.159	23.493	0.033	0.029
HIP 41484	22.25	0.216	22.368	0.033	0.029
HIP 41926	12.21	0.621	22.933	0.151	0.132
HIP 42438	14.36	0.607	24.195	0.204	0.182
HIP 42808	11.14	0.631	22.574	0.141	0.123
HIP 43587	12.34	0.673	23.552	0.197	0.173
HIP 43726	17.39	0.442	23.35	0.105	0.092
HIP 43797	24.15	0.229	23.68	0.052	0.046

Continued on next page

HIP 44075	21.03	0.323	23.609	0.077	0.068
HIP 44127	14.51	0.129	26.677	0.3	0.288
HIP 44143	26.42	0.182	24.346	0.049	0.044
HIP 44897	19.19	0.377	23.372	0.086	0.076
HIP 45170	20.36	0.232	21.979	0.033	0.028
HIP 45333	19.57	0.397	24.602	0.134	0.12
HIP 45343	6.11	0.566	20.808	0.09	0.076
HIP 45617	17.27	0.131	20.537	0.016	0.014
HIP 46509	17.33	0.342	25.261	0.201	0.184
HIP 46580	12.91	0.281	20.919	0.036	0.031
HIP 46733	23.82	0.112	25.913	0.105	0.099
HIP 46843	17.79	0.161	20.93	0.021	0.018
HIP 46853	13.48	0.158	26.543	0.327	0.312
HIP 47080	11.37	0.689	24.424	0.295	0.265
HIP 47592	15.01	0.457	25.025	0.241	0.22
HIP 48113	18.37	0.425	24.727	0.159	0.143
HIP 48331	11.16	0.237	20.399	0.03	0.025
HIP 48833	28.15	0.136	24.138	0.034	0.031
HIP 49081	15.05	0.571	24.431	0.206	0.185
HIP 49593	28.24	0.137	25.074	0.047	0.043
HIP 49669	24.31	0.029	27.69	0.106	0.105
HIP 49809	27.74	0.141	23.924	0.034	0.03
HIP 49908	4.87	0.989	22.892	0.356	0.312
HIP 50075	22.85	0.198	22.331	0.03	0.026

Continued on next page

HIP 50384	22.81	0.257	23.348	0.054	0.047
HIP 50505	20.24	0.198	21.651	0.026	0.022
HIP 50564	21.37	0.309	24.921	0.119	0.108
HIP 50954	16.22	0.219	25.922	0.244	0.229
HIP 51459	12.78	0.464	25.177	0.305	0.28
HIP 51502	21.5	0.333	24.57	0.105	0.094
HIP 51523	21.81	0.298	24.914	0.112	0.102
HIP 51814	26.53	0.179	24.362	0.049	0.044
HIP 51933	25.08	0.195	23.413	0.04	0.035
HIP 53229	29.09	0.108	25.297	0.043	0.04
HIP 53253	29.13	0.101	25.391	0.044	0.041
HIP 53721	14.06	0.509	24.905	0.257	0.234
HIP 53910	24.45	0.039	26.951	0.103	0.1
HIP 54035	2.54	1.0	21.604	0.308	0.263
HIP 54182	28.99	0.125	24.696	0.037	0.033
HIP 54211	4.86	0.263	19.093	0.027	0.023
HIP 54745	21.93	0.213	22.22	0.032	0.027
HIP 54872	17.91	0.074	26.903	0.219	0.212
HIP 55691 A	13.71	0.174	20.377	0.022	0.018
HIP 55779	27.22	0.158	24.189	0.041	0.037
HIP 56445	27.23	0.133	23.075	0.024	0.021
HIP 56452	9.56	0.799	24.001	0.31	0.276
HIP 56802	26.73	0.158	23.596	0.034	0.03
HIP 56997	9.61	0.688	24.618	0.365	0.329

Continued on next page

HIP 56998	12.4	0.178	20.179	0.022	0.018
HIP 57443	9.22	0.55	25.115	0.413	0.378
HIP 57507	17.47	0.358	22.357	0.061	0.053
HIP 57632	11.0	0.088	27.443	0.417	0.404
HIP 57757	10.93	0.259	26.148	0.398	0.374
HIP 57939	9.09	0.782	22.992	0.22	0.192
HIP 58001	25.5	0.037	26.884	0.089	0.087
HIP 58345	10.16	0.549	21.707	0.093	0.08
HIP 58576	12.76	0.676	24.144	0.236	0.21
HIP 58803	25.32	0.212	24.371	0.058	0.052
HIP 58910	5.52	0.78	21.563	0.167	0.143
HIP 59072	19.76	0.204	25.689	0.166	0.154
HIP 59199	14.94	0.253	25.855	0.273	0.256
HIP 59750	22.35	0.244	22.816	0.043	0.038
HIP 59774	24.69	0.072	26.26	0.097	0.092
HIP 60965	26.63	0.051	26.407	0.075	0.071
HIP 61053	21.78	0.261	22.834	0.047	0.041
HIP 61084	27.15	0.037	26.765	0.07	0.068
HIP 61174	18.28	0.271	25.475	0.188	0.174
HIP 61291	16.18	0.248	21.274	0.033	0.028
HIP 61317	8.44	0.386	25.755	0.475	0.442
HIP 62145	14.88	0.318	21.442	0.043	0.037
HIP 62207	17.38	0.456	23.567	0.116	0.102
HIP 62523	16.93	0.418	22.789	0.083	0.073

Continued on next page

HIP 62951	7.53	0.378	20.357	0.049	0.041
HIP 62956	25.31	0.03	27.46	0.093	0.091
HIP 63076	29.29	0.112	24.085	0.028	0.025
HIP 63613	27.87	0.107	25.502	0.055	0.051
HIP 63721	4.62	0.538	20.255	0.081	0.068
HIP 64394	9.13	0.381	25.732	0.447	0.416
HIP 64408	20.67	0.337	24.857	0.127	0.115
HIP 64583	18.2	0.38	25.015	0.174	0.159
HIP 64792	17.56	0.467	24.586	0.166	0.15
HIP 64924	8.56	0.553	25.147	0.439	0.403
HIP 65109	18.02	0.076	26.859	0.216	0.209
HIP 65352	15.45	0.25	21.164	0.033	0.028
HIP 65355	16.14	0.162	20.661	0.021	0.017
HIP 65530	21.17	0.228	22.163	0.034	0.029
HIP 65721	17.99	0.426	24.802	0.169	0.153
HIP 66249	22.71	0.095	26.18	0.124	0.117
HIP 66765	15.65	0.293	21.439	0.039	0.034
HIP 67153	19.4	0.236	25.54	0.169	0.157
HIP 67155	5.41	0.319	19.535	0.036	0.03
HIP 67275	15.62	0.345	25.386	0.242	0.224
HIP 67422 A	13.41	0.362	21.413	0.05	0.043
HIP 67927	11.4	0.139	26.884	0.397	0.38
HIP 68030	24.86	0.165	22.587	0.026	0.023
HIP 68184	10.06	0.729	22.959	0.194	0.169

Continued on next page

HIP 68682	16.98	0.42	22.833	0.085	0.074
HIP 68933	18.03	0.072	26.912	0.216	0.209
HIP 69671	21.22	0.258	22.541	0.043	0.037
HIP 69701	22.24	0.194	25.491	0.121	0.112
HIP 69713	29.07	0.124	24.773	0.037	0.034
HIP 69965	18.03	0.43	23.529	0.106	0.093
HIP 69972	11.8	0.592	22.482	0.124	0.108
HIP 69989	26.1	0.181	23.903	0.043	0.038
HIP 70319	17.19	0.411	22.815	0.082	0.072
HIP 70497	14.53	0.261	25.85	0.284	0.266
HIP 70857	19.89	0.178	21.426	0.023	0.02
HIP 70873	23.74	0.172	22.267	0.025	0.022
HIP 71075	26.61	0.056	26.311	0.074	0.071
HIP 71181	13.22	0.337	21.254	0.046	0.039
HIP 71284	15.83	0.314	25.495	0.241	0.224
HIP 71855	20.0	0.203	21.649	0.027	0.023
HIP 71957	18.27	0.204	25.823	0.197	0.185
HIP 72567	18.17	0.429	23.644	0.109	0.097
HIP 72603	22.98	0.285	24.398	0.082	0.073
HIP 72622	23.24	0.062	26.537	0.119	0.114
HIP 72848	11.51	0.715	23.602	0.219	0.193
HIP 73100	25.11	0.202	23.679	0.046	0.04
HIP 73165	26.9	0.165	25.043	0.058	0.052
HIP 73996	19.55	0.347	25.001	0.15	0.136

Continued on next page

HIP 74273	24.2	0.167	22.366	0.025	0.022
HIP 74537	17.67	0.311	21.982	0.046	0.04
HIP 74605	25.34	0.211	24.386	0.059	0.053
HIP 74702	15.85	0.274	21.367	0.036	0.031
HIP 74975	25.38	0.211	24.352	0.058	0.052
HIP 75181	14.81	0.589	24.092	0.188	0.167
HIP 75718	20.58	0.139	21.214	0.018	0.015
HIP 75809	21.85	0.176	21.803	0.024	0.02
HIP 76219	28.93	0.123	24.381	0.033	0.03
HIP 76267	23.01	0.038	27.087	0.125	0.121
HIP 76829	17.44	0.34	25.26	0.198	0.182
HIP 77052	14.66	0.578	23.722	0.165	0.146
HIP 77070	22.68	0.084	26.306	0.125	0.119
HIP 77257	12.12	0.385	25.5	0.338	0.313
HIP 77358	15.35	0.525	23.372	0.132	0.117
HIP 77760	15.89	0.352	25.336	0.234	0.216
HIP 77801	17.35	0.437	23.278	0.102	0.089
HIP 77952	12.38	0.126	26.908	0.365	0.351
HIP 78072	11.25	0.272	26.058	0.385	0.361
HIP 78459	17.24	0.488	24.429	0.164	0.147
HIP 78527	21.03	0.173	25.748	0.145	0.135
HIP 78775	14.52	0.451	22.244	0.079	0.069
HIP 79190	14.67	0.304	21.331	0.041	0.035
HIP 79248	17.57	0.328	22.113	0.051	0.044

Continued on next page

HIP 79537	13.89	0.226	20.787	0.029	0.025
HIP 79578	21.55	0.168	21.662	0.022	0.019
HIP 79672	13.9	0.625	24.242	0.217	0.194
HIP 79822	29.74	0.107	24.346	0.028	0.026
HIP 80179	27.27	0.165	24.698	0.049	0.044
HIP 80331	28.23	0.053	26.202	0.058	0.055
HIP 80337	12.78	0.641	24.472	0.261	0.235
HIP 80686	12.12	0.492	25.116	0.32	0.293
HIP 81300	9.75	0.794	23.977	0.302	0.268
HIP 81935	14.26	0.166	20.386	0.021	0.017
HIP 82003	9.81	0.179	19.732	0.021	0.017
HIP 82020	26.11	0.192	24.816	0.061	0.055
HIP 82396	19.54	0.085	26.601	0.183	0.175
HIP 82587	29.19	0.111	23.885	0.026	0.023
HIP 82588	17.25	0.303	21.827	0.043	0.037
HIP 82621	26.94	0.13	22.785	0.021	0.019
HIP 82860	15.26	0.419	25.138	0.241	0.22
HIP 83000	28.04	0.084	25.743	0.056	0.052
HIP 83389	18.59	0.25	21.73	0.034	0.029
HIP 83541	17.84	0.284	21.815	0.04	0.034
HIP 83591	10.71	0.218	20.197	0.027	0.023
HIP 83601	20.67	0.317	23.214	0.067	0.058
HIP 83609	5.62	0.311	19.561	0.035	0.029
HIP 83990	13.62	0.26	20.929	0.034	0.029

Continued on next page

HIP 84143	22.53	0.104	26.117	0.126	0.119
HIP 84478	5.95	0.95	23.071	0.332	0.29
HIP 84862	14.33	0.578	24.57	0.231	0.208
HIP 85042	19.52	0.316	22.628	0.056	0.049
HIP 85235	12.8	0.588	22.853	0.136	0.119
HIP 85295	7.7	0.45	20.704	0.063	0.053
HIP 86201	23.16	0.251	25.007	0.097	0.088
HIP 86400	11.0	0.644	22.624	0.147	0.128
HIP 86486	21.45	0.29	25.037	0.121	0.11
HIP 86614	22.84	0.226	25.235	0.107	0.098
HIP 86620	23.06	0.257	23.538	0.057	0.05
HIP 86742	25.09	0.079	26.132	0.091	0.086
HIP 86796	15.51	0.512	24.744	0.215	0.195
HIP 86974	8.31	0.253	26.393	0.501	0.474
HIP 88175	23.55	0.233	25.073	0.094	0.085
HIP 88635	29.7	0.065	25.833	0.044	0.041
HIP 88694	17.55	0.439	23.382	0.104	0.092
HIP 88771	26.63	0.088	25.85	0.071	0.066
HIP 88972	11.02	0.686	23.01	0.178	0.156
HIP 89042	17.61	0.476	24.3	0.15	0.135
HIP 89348	22.92	0.28	24.79	0.094	0.085
HIP 89474	22.82	0.213	22.54	0.034	0.03
HIP 89962	18.54	0.154	26.107	0.197	0.186
HIP 90496	23.97	0.088	26.129	0.105	0.099

Continued on next page

HIP 90790	13.25	0.399	21.587	0.059	0.05
HIP 91262	7.68	0.03	29.135	0.559	0.549
HIP 91768	3.52	0.41	19.289	0.05	0.041
HIP 92024	28.55	0.136	24.804	0.041	0.037
HIP 92043	19.21	0.229	25.603	0.174	0.162
HIP 92161	28.89	0.115	25.259	0.044	0.041
HIP 92549	25.67	0.187	23.697	0.042	0.037
HIP 93747	25.46	0.055	26.449	0.088	0.084
HIP 93858	16.95	0.437	23.018	0.094	0.082
HIP 93966	21.43	0.285	23.049	0.056	0.049
HIP 94083	27.3	0.159	24.403	0.044	0.039
HIP 94376	29.87	0.06	25.889	0.043	0.04
HIP 95149	18.83	0.293	22.147	0.045	0.039
HIP 95319	15.76	0.465	22.822	0.097	0.085
HIP 95447	15.18	0.537	24.662	0.217	0.196
HIP 95501	15.53	0.158	26.357	0.269	0.256
HIP 95995 A	16.96	0.367	22.278	0.061	0.053
HIP 96100	5.75	0.532	25.374	0.576	0.531
HIP 96258	25.11	0.198	23.568	0.043	0.038
HIP 96441	18.34	0.281	25.424	0.186	0.172
HIP 96895	21.08	0.315	23.431	0.07	0.062
HIP 96901	21.21	0.284	22.947	0.054	0.047
HIP 97649	5.12	0.061	28.669	0.689	0.673
HIP 97650	27.87	0.135	23.712	0.03	0.027

Continued on next page

HIP 97675	19.19	0.403	24.679	0.143	0.129
HIP 97944	14.05	0.552	23.011	0.128	0.113
HIP 98036	13.7	0.257	25.942	0.308	0.289
HIP 98066	25.99	0.196	24.561	0.057	0.051
HIP 98470	21.25	0.322	23.721	0.078	0.069
HIP 98698	12.86	0.225	20.606	0.029	0.024
HIP 98767	15.86	0.539	23.947	0.159	0.142
HIP 98792	15.77	0.222	21.051	0.029	0.025
HIP 98819	17.77	0.453	23.791	0.122	0.108
HIP 98921	18.79	0.371	23.036	0.076	0.067
HIP 98959	17.73	0.425	23.298	0.098	0.086
HIP 99031	23.95	0.242	23.966	0.061	0.054
HIP 99137	23.43	0.197	22.533	0.031	0.027
HIP 99240	6.11	0.299	26.312	0.598	0.564
HIP 99461	6.01	0.782	24.537	0.499	0.452
HIP 99572	27.7	0.118	22.892	0.02	0.018
HIP 99701	6.2	0.402	20.137	0.052	0.044
HIP 99825	8.91	0.825	23.923	0.323	0.287
HIP 100017	17.57	0.453	23.653	0.117	0.104
HIP 100511	26.25	0.131	22.509	0.02	0.018
HIP 100925	19.52	0.216	21.657	0.029	0.025
HIP 101345	24.4	0.212	23.393	0.044	0.039
HIP 101612	27.79	0.153	24.797	0.046	0.042
HIP 101983	24.66	0.232	24.425	0.066	0.059

Continued on next page

HIP 101997	14.38	0.499	22.622	0.101	0.088
HIP 102040	20.95	0.242	22.254	0.037	0.032
HIP 102333	24.17	0.195	25.258	0.09	0.083
HIP 102422	14.27	0.201	26.191	0.299	0.282
HIP 102485	14.68	0.297	25.672	0.275	0.256
HIP 102488	22.29	0.068	26.555	0.133	0.128
HIP 103389	21.97	0.291	23.579	0.067	0.059
HIP 103458	22.14	0.176	21.863	0.024	0.02
HIP 103673	28.01	0.12	23.163	0.022	0.02
HIP 104214	3.5	0.778	24.704	0.657	0.599
HIP 104217	3.5	0.966	23.852	0.562	0.503
HIP 104239 A	17.57	0.13	20.584	0.016	0.014
HIP 105090	3.95	1.019	22.792	0.39	0.341
HIP 105199	15.04	0.077	27.164	0.291	0.282
HIP 105858	9.26	0.361	25.804	0.445	0.415
HIP 106440	4.95	0.288	19.245	0.031	0.026
HIP 106559	27.1	0.14	23.208	0.027	0.023
HIP 106696	14.62	0.283	21.212	0.037	0.032
HIP 107089	21.2	0.174	25.728	0.142	0.132
HIP 107350	17.89	0.43	23.466	0.104	0.092
HIP 107556	11.87	0.142	26.818	0.38	0.364
HIP 107649	15.99	0.539	24.202	0.173	0.154
HIP 107975	27.45	0.143	23.663	0.031	0.028
HIP 108036	26.62	0.173	24.239	0.046	0.041

Continued on next page

HIP 108870	3.62	0.625	25.183	0.688	0.633
HIP 109176	11.73	0.252	26.12	0.371	0.349
HIP 109378	21.56	0.164	21.628	0.022	0.018
HIP 109422	18.28	0.399	24.905	0.168	0.153
HIP 109427	28.3	0.071	25.894	0.055	0.052
HIP 109821	22.05	0.24	22.624	0.04	0.035
HIP 110649	20.56	0.369	24.363	0.11	0.098
HIP 111449	22.68	0.294	24.314	0.083	0.074
HIP 112117	23.64	0.22	23.07	0.042	0.037
HIP 112447	16.3	0.286	25.586	0.233	0.217
HIP 112935	27.28	0.155	24.059	0.038	0.034
HIP 113137	26.75	0.131	22.721	0.021	0.019
HIP 113283	7.61	0.849	22.821	0.242	0.211
HIP 113357	15.61	0.554	24.306	0.186	0.167
HIP 113368	7.7	0.065	28.225	0.554	0.54
HIP 113421	19.86	0.31	22.688	0.055	0.048
HIP 113576	8.22	0.273	20.018	0.033	0.028
HIP 113860	29.42	0.109	24.09	0.027	0.024
HIP 114046	3.28	1.0	21.937	0.308	0.265
HIP 114430	27.65	0.123	23.011	0.022	0.019
HIP 114570	24.59	0.192	25.221	0.085	0.077
HIP 114622	6.54	0.811	24.377	0.46	0.415
HIP 114924	20.5	0.362	24.042	0.098	0.087
HIP 114948	20.54	0.356	23.94	0.094	0.083

Continued on next page

HIP 114996	23.06	0.154	25.676	0.112	0.104
HIP 116085	16.93	0.296	21.711	0.041	0.036
HIP 116584	26.41	0.133	25.433	0.068	0.063
HIP 116727	14.1	0.186	26.3	0.305	0.29
HIP 116745	11.42	0.44	21.427	0.065	0.056
HIP 116771	13.71	0.317	25.66	0.3	0.279
HIP 120005	6.11	0.543	20.704	0.083	0.07

APPENDIX C

ANALYTICAL DS/DT

C.1 Derivation of an Analytical ds/dt

It is possible to analytically calculate the rate of change of an exoplanet's separation as a function of time (ds/dt). The process for doing this is

$$\frac{ds}{dt} = \frac{ds}{d\nu}\frac{d\nu}{dE}\frac{dE}{dM}\frac{dM}{dt}. \tag{C.1}$$

The general separation equation is

$$s = |\underline{s}| = \sqrt{X^2 + Y^2}, \tag{C.2}$$

where X and Y are the components of the planet in $\underline{r}_{k/i}$. The planet's position in XYZ is given in terms of KOE in Eqn. 5.10 After substituting Eqn. 5.10 into Eqn. C.2, we get a long expression with $\sin(\nu+\omega)^2$ and $\cos(\nu+\omega)^2$ terms. We substitute in

$$\sin(\nu+\omega)^2 = \sin(\nu)^2\cos(\omega)^2 + 2\cos(\nu)\sin(\omega) + \cos(\nu)^2\sin(\omega)^2 \text{ and} \tag{C.3}$$

$$\cos(\nu+\omega)^2 = \cos(\nu)^2\cos(\omega)^2 - 2\cos(\nu)\cos(\omega)\sin(\nu)\sin(\omega) + \sin(\nu)^2\sin(\omega)^2. \tag{C.4}$$

This isolates the expression in terms of $\cos(\nu)$ and $\sin(\nu)$ which we can now substitute in

$$\sin(\nu) = \sqrt{1-\cos(\nu)^2}, \tag{C.5}$$

to get an expression with only $\cos(\nu)$. By taking the derivative, we find $ds/d\nu$.

In the special case where $\sin(\nu) = 0$, we get

$$\frac{ds}{d\nu} = \frac{a(e-1)^2 \sin(i) \begin{pmatrix} e\sin^2(\omega) - e\sin(\omega)\cos(\nu)\cos(\omega)\left|\sin(\nu)\right| \\ -e + \dfrac{e}{\sin^2(i)} + 2\sin^2(\omega)\cos(\nu) \\ +\sin(\omega)\cos(\omega)\left|\sin(\nu)\right| - \cos(\nu) \end{pmatrix} \sin(\nu)}{(e\cos(\nu)+1)^2 \sqrt{\begin{matrix} 2\sin^2(\nu)\sin^2(\omega) - \sin^2(\nu) - \sin^2(\omega) \\ -2\sin(\omega)\cos(\nu)\cos(\omega)\left|\sin(\nu)\right| + \dfrac{1}{\sin^2(i)} \end{matrix}}}. \tag{C.6}$$

In all other cases, we can use

$$\frac{ds}{d\nu} = \frac{a(e-1)^2 \sin(i) \begin{pmatrix} e\sin^2(\omega) - \dfrac{e\sin(\omega)\cos(\nu)\cos(\omega)}{\left|\sin(\nu)\right|} - e \\ +\dfrac{2\sin^2(\nu)\sin(\omega)\cos(\omega)}{\left|\sin(\nu)\right|} - \cos(\nu) + \dfrac{e}{\sin^2(i)} \\ +2\sin^2(\omega)\cos(\nu) - \dfrac{\sin(\omega)\cos(\omega)}{\left|\sin(\nu)\right|} \end{pmatrix} \sin(\nu)}{(e\cos(\nu)+1)^2 \sqrt{\begin{matrix} 2\sin^2(\nu)\sin^2(\omega) - \sin^2(\nu) \\ -2\sin(\omega)\cos(\nu)\cos(\omega)\left|\sin(\nu)\right| \\ -\sin^2(\omega) + \dfrac{1}{\sin^2(i)} \end{matrix}}}. \tag{C.7}$$

The relationship between true anomaly and eccentric anomaly can be written as

$$\cos(\nu) = \frac{\cos(E) - e}{1 - e\cos(E)}. \tag{C.8}$$

Solving for ν and taking the derivative, we arrive at

$$\frac{d\nu}{dE} = \frac{(1-e^2)\sin(E)}{\sqrt{\frac{(1-e^2)\sin^2(E)}{(e\cos(E)-1)^2}}(e\cos(E)-1)^2}. \tag{C.9}$$

The non-invertible equation for M as a function of E and e is

$$M = E - e\sin E. \tag{C.10}$$

We are able to take the derivative with respect to E and get

$$\frac{dM}{dE} = 1 - e\cos(E). \tag{C.11}$$

Finally, the equation for mean anomaly is

$$M = \frac{2\pi}{T}t, \tag{C.12}$$

which has the derivative

$$\frac{dM}{dt} = \frac{2\pi}{T}. \tag{C.13}$$

This formulation requires us to know ν, but not time. Luckily, the exodetbox method can furnish us with ν making this calculation trivial.

The use of this formulation requires the linearization assumption of the slope at this particular point in the orbit. We know that a randomly generated planet from some non-trivial inclination distribution is highly likely to have a non-linear $ds/dt(t)$. While this may be tractable for some formulations, we do not recommend using it.